TU/e EINDHOVEN UNIVERSITY OF TECHNOLOGY

# Plasma-surface interaction in plasma-assisted atomic layer deposition

*Citation for published version (APA):*
Profijt, H. B. (2012). *Plasma-surface interaction in plasma-assisted atomic layer deposition*. [Phd Thesis 1 (Research TU/e / Graduation TU/e), Applied Physics]. Technische Universiteit Eindhoven. https://doi.org/10.6100/IR738955

*DOI:*
10.6100/IR738955

*Document status and date:*
Published: 01/01/2012

*Document Version:*
Publisher's PDF, also known as Version of Record (includes final page, issue and volume numbers)

*Please check the document version of this publication:*

• A submitted manuscript is the version of the article upon submission and before peer-review. There can be important differences between the submitted version and the official published version of record. People interested in the research are advised to contact the author for the final version of the publication, or visit the DOI to the publisher's website.
• The final author version and the galley proof are versions of the publication after peer review.
• The final published version features the final layout of the paper including the volume, issue and page numbers.

Link to publication

*General rights*
Copyright and moral rights for the publications made accessible in the public portal are retained by the authors and/or other copyright owners and it is a condition of accessing publications that users recognise and abide by the legal requirements associated with these rights.

• Users may download and print one copy of any publication from the public portal for the purpose of private study or research.
• You may not further distribute the material or use it for any profit-making activity or commercial gain
• You may freely distribute the URL identifying the publication in the public portal.

If the publication is distributed under the terms of Article 25fa of the Dutch Copyright Act, indicated by the "Taverne" license above, please follow below link for the End User Agreement:

www.tue.nl/taverne

*Take down policy*
If you believe that this document breaches copyright please contact us at:

openaccess@tue.nl

providing details and we will investigate your claim.

Download date: 05. Aug. 2022

# Plasma-Surface Interaction in Plasma-Assisted Atomic Layer Deposition

PROEFSCHRIFT

ter verkrijging van de graad van doctor aan de
Technische Universiteit Eindhoven, op gezag van de
rector magnificus, prof.dr.ir. C.J. van Duijn, voor een
commissie aangewezen door het College voor
Promoties in het openbaar te verdedigen
op dinsdag 20 november 2012 om 16.00 uur

door

Harald Benjamin Profijt

geboren te Hoogeveen

Dit proefschrift is goedgekeurd door de promotoren:

prof.dr.ir. W.M.M. Kessels
en
prof.dr.ir. M.C.M. van de Sanden

This work was financially supported by the Dutch Technology Foundation STW (TFN10018).




Enabling new technology

Printed and bound by: Printservice Technische Universiteit Eindhoven.
Cover design: Nick Meeuws, Oranje Vormgevers, Eindhoven.

A catalogue record is available from the Eindhoven University of Technology Library

ISBN: 978-90-386-3267-4

# Contents


**1 General Introduction** **1**

1.1 Ultra-Thin Films and their Applications . . . . . 1
1.2 Atomic Layer Deposition . . . . . 4
1.3 Research Project . . . . . 6
1.4 Research Questions . . . . . 7
1.5 Outline . . . . . 8
1.6 Publications . . . . . 9

**2 Plasma-Assisted Atomic Layer Deposition: Basics, Opportunities, and Challenges** **13**

2.1 Introduction . . . . . 14
2.2 Plasma Basics . . . . . 23
2.3 Plasma-Assisted ALD Configurations . . . . . 28
2.4 Merits of Plasma-Assisted ALD . . . . . 34
2.5 Challenges of Plasma-Assisted ALD . . . . . 43
2.6 Selected Applications . . . . . 50
2.7 Concluding Remarks and Outlook . . . . . 59

**3 Room-Temperature ALD of Metal-Oxide Thin Films by Energy-Enhanced ALD** **83**

3.1 Introduction . . . . . 84
3.2 Experimental . . . . . 85
3.3 Results . . . . . 88
3.4 Discussion . . . . . 90
3.5 Conclusions . . . . . 94

**4 Ion Bombardment during Plasma-Assisted Atomic Layer Deposition** **99**

4.1 Introduction . . . . . 100
4.2 Reactor Configurations . . . . . 102
4.3 Enhancing Ion Energies . . . . . 110
4.4 Influence of Ions . . . . . 111
4.5 Conclusions . . . . . 113

**5 Ion and Photon Surface Interaction during Remote Plasma ALD of Metal Oxides** **123**
5.1 Introduction . . . 124
5.2 Experimental . . . 124
5.3 Results and Discussion . . . 125
5.4 Conclusions . . . 132

**6 Substrate-Biasing during Plasma-Assisted Atomic Layer Deposition to Tailor Metal-Oxide Film Growth** **135**
6.1 Introduction . . . 136
6.2 Theoretical Aspects . . . 137
6.3 Experimental . . . 141
6.4 Results . . . 144
6.5 Conclusions . . . 154

**7 Substrate Biasing during Plasma-Assisted ALD for Crystalline Phase-Control of $TiO_2$ Thin Films** **159**
7.1 Introduction . . . 160
7.2 Experimental . . . 161
7.3 Results . . . 161
7.4 Conclusions . . . 165

**8 General Conclusions and Outlook** **173**

**Summary** **179**

**Samenvatting** **183**

**List of publications related to this work** **187**

**Dankwoord** **189**

**Curriculum Vitae** **191**

Chapter 1

# General Introduction

## 1.1 Ultra-Thin Films and their Applications

Ultra-thin films are layers of material with thicknesses ranging from several tenths up to several tens of nanometers. Due to the optical, mechanical, catalytic or electrical functionality they can possess or add to a surface, ultra-thin films are of interest to a large variety of applications. Consequently they are applied in many devices used in daily life such as computers, displays, sensors, solar cells, smart phones, other handheld devices, etc. Moreover, their importance is still vastly growing.

An extremely demanding application area of ultra-thin films lies within the field of micro- and nanoelectronics. Modern microprocessors (i.e. ICs designed to perform logic calculations), for example, are typically built up from a stack of over 20 patterned thin films, fabricated using subsequently executed deposition and patterning processes [1,2]. These structures form electrical components such as CMOS (complimentary metal-oxide-semiconductor) transistors, which are used to switch logic signals. The trend that the number of transistors on a microprocessor doubles approximately every 18 months was already predicted by Gordon Moore in 1965 [3]. Even after more than four decades, this so-called Moore's law is still applicable as it was adopted by the semiconductor industry as a roadmap in decreasing the size of the CMOS transistor with each generation [4]. Traditionally, the continuous miniaturization of transistors was purely facilitated by *lithography-enabled scaling*, while using approximately the same set of materials [5]. Since the start of the 21$^{th}$ century, new materials were introduced in order to meet the stringent requirements that came along with next step in miniaturization (see Fig. 1.1). An example of this so-called *materials-enabled scaling* is the replacement of the $SiO_2$ gate dielectric layer in CMOS transistors by a Hf-based gate oxide (i.e. $HfO_2$ or $HfSi_xO_y$) which was introduced in production in 2007 [7]. As Hf-based films possess a $\sim$60% higher dielectric constant (or $k$-value) compared to $SiO_2$, it allows for thicker dielectric films to be used and therefore for an improved device behavior [8,9]. The re-

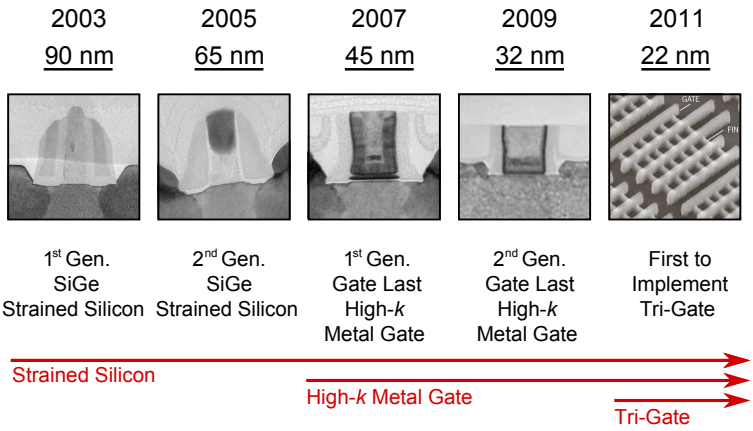



**Figure 1.1:** Illustration of materials-enabled scaling in CMOS employed by Intel to keep up with Moore's law (www.intel.com [6])

placement of $SiO_2$ was necessary, because the required thickness for the gate oxide, as dictated by the scaling, was becoming too thin (< 1 nm), resulting in too large leakage currents. Instead of being grown by an oxidation process, which was the case for $SiO_2$, the Hf-based dielectric films were deposited using atomic layer deposition (ALD), the method that is the subject of this thesis and which will be described in Sec. 1.2. A relatively new trend to keep up with Moore's law is *3D-enabled scaling*. In 2011, Intel successfully implemented a revolutionary new type of transistor in their most advanced microprocessors: the Fin-FET (referred to as Tri-Gate by Intel) [10]. This non-planar transistor consists of a Si fin around which the gate dielectric layer and the gate electrode are wrapped, as illustrated in Fig 1.2. This approach facilitates the miniaturization of the footprint of the transistor while keeping the gate surface area approximately constant. In order to fabricate reliable 2D and 3D microprocessors, the gate dielectric should be of a high quality, the growth control during deposition should be excellent to obtain the exact right film thickness, the conformality (i.e. step coverage) should be optimal for Fin-FETs, and the deposition should be uniform across the complete wafer. These are all requirements that can be fulfilled by ALD.

Also for non-IC applications, high-quality ultra-thin films are becoming increasingly important. In solar-cells, for example, surface-recombination losses can be reduced by applying an ultra-thin film of amorphous Si or $Al_2O_3$ [11]. By chemically passivating interface defects and/or by electrostatically shielding charge carriers, the solar cell efficiency can, in some cases, be improved by up to one absolute percent. Ultra-thin films are also of interest for the encapsulation of organic electronic materials to prevent the

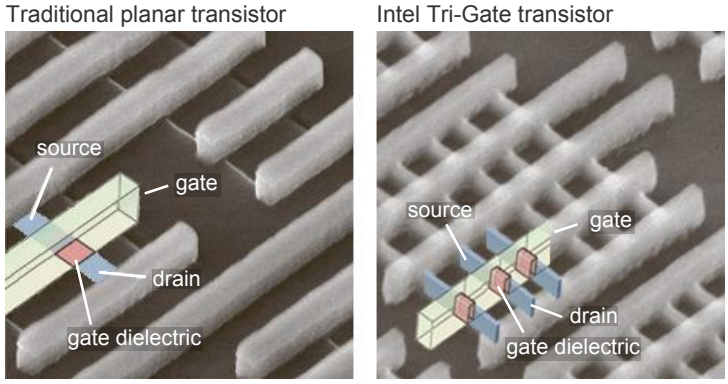



**Figure 1.2:** Illustrations of a number of (a) traditional 2D transistor and (b) 3D FinFET transistors. In the traditional implementation, the gate dielectric (drawn in red) is a planar layer, whereas in the FinFET transistor it is wrapped around a fin (drawn in blue). The gate, source and drain terminals of the transistor are indicated as well (from www.nytimes.com).

permeation of moisture and oxygen. In order to guarantee a long life-time of organic light- emitting diodes (OLEDs), for instance, these devices should be protected from moisture and oxygen as otherwise their electroluminescence decreases significantly [12]. For this application of ultra-thin films, also stacks of organic and inorganic layers can be applied, which additionally allows for decoupling of pinholes (i.e. defects that arise during the deposition process and/or during transport of the samples). Besides electronic structures, also high-precision metals parts such as bearings can be protected straightforwardly against wear and corrosion by coating them with an (ultra-)thin film [13].

The growth rate of commonly and widely used deposition techniques such as chemical vapor deposition (CVD) and physical vapor deposition (PVD) [14] depends generally on the flux of growth species and, consequently, the final film thickness is determined by the duration of the deposition process. Especially when the deposition rate is relatively high, it might be challenging to deposit relatively thin films of high quality. Furthermore, surfaces that are not in a direct line-of-sight with the source of the growth species may experience a lower (or zero) growth rate. Consequently, it is impossible to conformally coat 3D structures, such as fins or trenches, nanoparticles, etc. Moreover, when the film coverage is demanded to be uniform across a large wafer area, the growth flux is also required to be uniform with respect to the full wafer area. As it is very difficult to meet these requirements for the abovementioned applications with most deposition techniques, the popularity of atomic layer deposition (ALD) is steadily increasing.

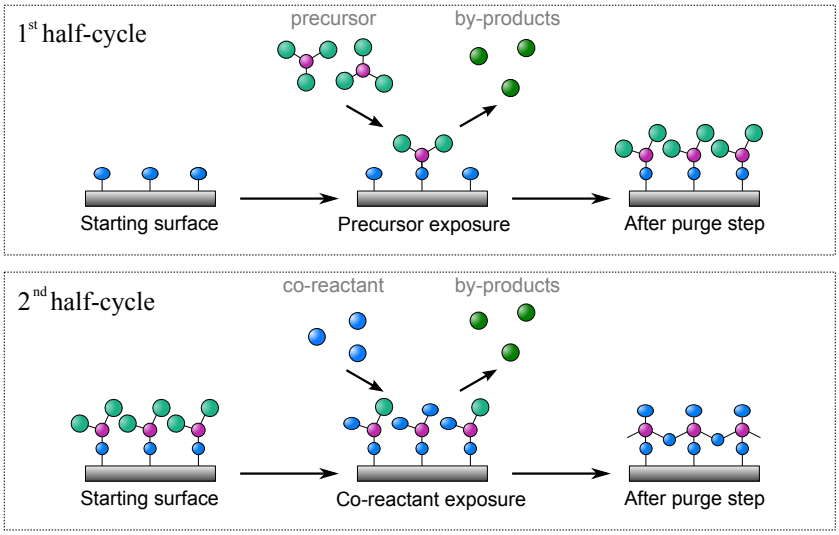



**Figure 1.3:** Schematic representation of the ALD process, where the substrate is subsequently exposed to a precursor in the first half-cycle, then pumped and/or purged, exposed to a co-reactant during the second half-cycle and again pumped and/or purged.

## 1.2 Atomic Layer Deposition

ALD is a vapor-phase deposition technique in which (ultra-)thin films are synthesized sub-monolayer by sub-monolayer by repeating two subsequently executed half-cycles [15]. Figure 1.3 illustrates the deposition process in its most basic configuration. In the first half-cycle, a precursor (typically a vapor carrying the main element of the film material) is dosed which reacts with the functional groups on the starting surface. The precursor is not reactive with the surface groups formed by itself and consequently the surface reactions stop occurring when all surface groups have reacted (i.e. the reactions are self-limiting). Then, a pump and/or purge step is executed with an inert gas (typically Ar) during which the volatile reaction by-products are removed from the reactor along with the excess of precursor. In the second half-cycle the surface is exposed to a co-reactant (typically a gas, such as $O_2$ or $NH_3$, or a vapor such as $H_2O$) which reacts with the surface groups in a self-limiting manner. After a pump and/or purge step to remove the reaction by-products and the excess of co-reactant from the reactor, one ALD cycle is completed and the surface groups are equal to those with which the cycle started. As the deposition of a sub-monolayer involves two self-limiting half-cycles, ALD offers sub-nanometer resolution of the film growth (i.e. the typical growth-per-cycle is 0.05 -

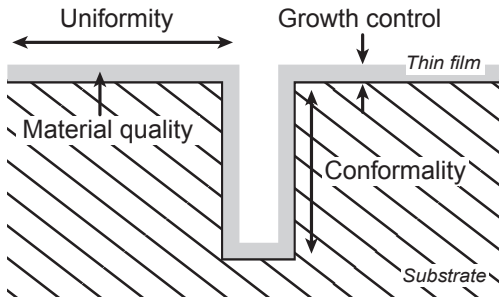



**Figure 1.4:** Illustration of the merits of ALD: high material quality, sub-nanometer growth control, high uniformity and excellent conformality.

0.1 nm) as long as the dosing and pump/purge steps are sufficiently long (i.e. the surface reactions are saturated). In addition, uniform deposition over large area substrates and conformal deposition in non-planar structures are provided (see Fig. 1.4). During ALD, the surface reactions are typically thermally-driven by elevated substrate temperatures (often 150 - 350 °C) and therefore the method is also referred to as "thermal" ALD.

Instead of a gas or a vapor, also reactive and energetic species produced in a plasma can be used as the co-reactant during the second half-cycle of the ALD process [16]. A plasma is an ionized gas which can be generated by supplying electrical power to a gas [17]. Consequently, electrons are accelerated and reactive species such as radicals (i.e. chemically reactive species), ions and photons are created upon collisions between electrons and neutral gas species. The use of plasma-generated species during the second half-cycle of the ALD process allows for more freedom in processing conditions and for a wider range of material properties and, consequently, the interest in the deposition method has increased significantly in recent years. With plasma-assisted ALD, radicals, photons and ions can all interact with the material surface and as such radicals are not the only species that provide reactivity to the surface .

Also ozone molecules can be used as alternative co-reactant species [18]. In processing environments, ozone is typically generated from molecular oxygen in a dielectric barrier discharge, which is a specific type of plasma configuration [19]. Although also radicals, ions and photons are created in a dielectric barrier discharge, only ozone molecules will be present at the output due to the geometry of the generator and the pressures typically employed. Ozone species are typically more reactive than molecular oxygen and water vapor, however less reactive than oxygen radicals. Plasmas can be generated in a variety of gases (such as $O_2$, $N_2$, $H_2$, Ar, $CO_2$, $NH_3$, $CH_4$, etc), whereas ozone is limited to oxygen as the main constituent (note that in some cases $N_2$ is admixed). It is

noted that also hydrazine ($N_2H_4$) can be employed as the co-reactant when a reducing co-reactant required, however it is less commonly used [20].

As energy is provided to the co-reactant to make the species more reactive, ozone-based and plasma-assisted ALD are also referred to as energy-enhanced ALD (EE-ALD). EE-ALD processes are mainly of interest when materials cannot be deposited using a conventional thermal ALD process, for instance in case the required deposition temperature is lower than the temperature window of thermal ALD or when the precursor is not reactive with regular co-reactant species. Alternatively, ultraviolet (UV) and vacuum ultraviolet (VUV) light can be used, for instance, to break precursor bonds during the second half-cycle of an ALD process [21]. Such a process can also be classified as EE-ALD.

## 1.3 Research Project

This dissertation work was carried out in the Plasma and Materials Processing (PMP) group at the Eindhoven University of Technology (TU/e) in the Netherlands. The project is a follow-up to a project funded by the Dutch technology foundation STW (Stichting Technische Wetenschappen) entitled "Plasma-Assisted Atomic Layer Deposition for Processing at the Nano-Scale", which started in 2003 and involved two PhD students [22,23]. The experience on plasma processing present in the PMP group allows for the investigation of plasma-assisted ALD from a unique perspective on the fundamental properties and issues related to plasma-assisted ALD, as evidenced by the relatively large number of current and finished projects on (plasma-assisted) ALD [24].

Although the interest in plasma-assisted ALD has been increasing rapidly in recent years, the plasma-surface interaction during the film growth is not fully understood yet. Especially around the topic of plasma-induced damage there is much anecdotal hearsay and the plasma generator is often considered a black-box that produces radicals. This work therefore aims at obtaining an in-depth understanding of the plasma-surface interaction during the deposition process in order to optimally benefit from the merits and to manage the challenges associated with plasma-assisted ALD.

The current research project is entitled "Atomic Layer Deposition as an Enabling Ultrathin Film Technology", part of the Thin Film Nanomanufacturing Programme by STW (TFN10018). The aim of the current project is to exploit the merits of (plasma-assisted) ALD as an enabling ultra-thin film technology for a wide range of industrial applications, by focusing on (1) understanding of the reaction mechanisms, (2) tool and process development, and (3) experimental validation of the opportunities offered by plasma-assisted

ALD. The outcome of the project is partly described in this work and in the thesis by N. Leick, which focuses on surface-reactions during (plasma-assisted) ALD of noble metals [25].

## 1.4 Research Questions

As discussed in the previous section, this thesis work aims at obtaining an in-depth understanding of the plasma-surface interaction in plasma-assisted ALD. In the initial phase of the project, the plasma-assisted ALD technique has been evaluated in detail to ultimately establish the scientific research questions. The first research question that has been posed was therefore:

***What is the present status of plasma-assisted ALD and which merits and challenges are associated with this deposition method?***

Past studies carried out within the PMP group and reported in the literature have been consulted with the aim to answer questions such as: *What is the difference between plasma-assisted ALD and conventional thermal ALD?* and *What is the status of the deposition method in terms of publications, deposition processes that have been reported and what has been adopted by the industry?* Also attention has been paid to the properties of the plasma in an ALD reactor to address *how a plasma is generated, which species are present in a plasma, the interaction between plasmas and surfaces,* and *the characteristics of typically employed reactor configurations*. With respect to the deposition process a number of questions are addressed such as: *What are the merits and challenges of plasma-assisted ALD compared to thermal ALD?; Which applications does the research on plasma-assisted ALD focus on?* and *Which aspects related to the deposition method need to be addressed in future research?* As the deposition at lower substrate temperatures is an important advantage of energy-enhanced ALD, the *challenges and criteria related to room-temperature deposition by energy-enhanced ALD* are addressed and illustrated as well.

On the basis of the findings related to this research question, the following scientific research questions have been established:

- ***Which ions and photons are present during plasma-assisted ALD and what is their influence?***

  Besides reactive radicals, also ions and photons are created in the plasma. It is inves-

tigated *how ions and photons are created in the plasma, which ions and photons are present in the plasma, what is the surface-interaction of these species during plasma-assisted ALD, and which parameters are available to limit or enhance (i.e. control) their presence and influence.* With respect to ions, answers are sought to questions such as: *What are the energies and incident angles of the ions at the substrate?* and *What are the details with respect to the presence of ions and their surface-interaction in different reactor geometries?*

- ***Can the surface-interaction of ions be exploited to tailor material properties during plasma-assisted ALD?***
  For ions present in the plasma, it is investigated *how ion energies can be enhanced* and *which ion-surface interactions possibly take place*. After implementation of the so-called substrate biasing technique, it is investigated *what the influence is of substrate biasing on the ion energies and fluxes, the plasma properties, the processing parameters and the resulting material properties.*

## 1.5 Outline

In answer to the aforementioned research questions, the plasma-surface interaction in plasma-assisted ALD will be discussed in Chapters 2 to 7. These individual Chapters have been published or have been submitted for publication (either integrally or in modified versions) as separate articles in international peer-reviewed journals. The Chapters are not ordered chronologically and there is some overlap in contents between separate Chapters. Some of the Chapters are extended with addenda to present additional or very recent results and/or information considered relevant. Chapter 8 will present the general conclusions and an outlook to future studies.

The Chapters in this dissertation can be divided in three sections, related to the research questions posed in Sec. 1.4:

(i) **Basics and status of plasma-assisted ALD:** Plasma-assisted ALD is a relative new deposition technique, which is extensively evaluated in Chapter 2. Besides the basics, also the merits and the challenges associated with the deposition method are addressed and several emerging applications are discussed. In Chapter 3, challenges and criteria for successful deposition at room-temperature are discussed, both for plasma-assisted and ozone-based ALD.

(ii) **Identification and evaluation of ions and photons during plasma-assisted ALD:** The presence and importance of ions is discussed in Chapter 4 for several reactor configurations used commonly for plasma-assisted ALD. In Chapter 5 the attention is focused on the remote plasma ALD reactor configuration, where the presence and importance of ions and photons is investigated for a wide range of process parameters. Additionally, results on the plasma parameters are discussed.

(iii) **Exploiting the presence of ions during plasma-assisted ALD using substrate biasing:** The implementation of two substrate biasing techniques in a remote plasma ALD reactor is discussed in Chapter 6, where also results are presented on the ion energy, the ion flux and the influence of substrate biasing on the plasma properties. The impact of energetic ions on the metal-oxide film growth is investigated for three metal-oxide systems. In Chapter 7 it is discussed how the crystalline phase of $TiO_2$ thin films can be tailored using substrate biasing.

## 1.6 Publications

The Chapters in this dissertation work have been published or are accepted for publication as individual articles in peer-reviewed journals. An overview is given below:

***Chapter 2: Plasma-Assisted Atomic Layer Deposition: Basics, Opportunities, and Challenges.***
This work has been published as a review article: *H. B. Profijt, S.E. Potts, M. C. M. van de Sanden, and W. M. M. Kessels, J. Vac. Sci. Technol. A 29, 050801 (2011).*

***Chapter 3: Room-Temperature ALD of Metal-Oxide Thin Films by Energy-Enhanced Atomic Layer Deposition.***
This work was presented at the 222nd Meeting of The Electrochemical Society (Honolulu, Hawaii, U.S.A., October 2012) and has been published as: *S. E. Potts, H. B. Profijt, R. Roelofs, and W. M. M. Kessels, ECS Trans. 50 (2012).*

***Chapter 4: Ion Bombardment during Plasma-Assisted Atomic Layer Deposition.***
This work was presented (invited presentation) at the 222nd Meeting of The Electrochemical Society (Honolulu, Hawaii, U.S.A., October 2012) and has been published as: *H. B. Profijt and W. M. M. Kessels, ECS Trans. 50 (2012).*

***Chapter 5: Ion and Photon Surface Interaction during Remote Plasma ALD of Metal Oxides.***
This work was presented at the 218th Meeting of The Electrochemical Society (Las Vegas, Nevada, U.S.A., October 2010) and has been published as: *H. B. Profijt, P. Kudlacek, M. C. M. van de Sanden, and W. M. M. Kessels, J. Electrochem. Soc. 158, G88 (2011).*

***Chapter 6: Substrate Biasing During Plasma-Assisted ALD to Control Metal-Oxide Film Growth.***
This work has been published in a special issue of J. Vac. Sci. Technol. A on Atomic Layer Deposition as: *H. B. Profijt, M. C. M. van de Sanden, and W. M. M. Kessels, J. Vac. Sci. Technol. A 31, 01A106 (2013).*

***Chapter 7: Substrate Biasing during Plasma-Assisted ALD for Crystalline Phase-Control of $TiO_2$ Thin Films.***
This work has been published as: *H. B. Profijt, M. C. M. van de Sanden, and W. M. M. Kessels, Electrochem. Solid-State Lett. 15, G1 (2012).*

# References

1. "From Sand to Silicon - Making of a Chip", http://download.intel.com/pressroom/kits/chipmaking/Making_of_a_Chip.pdf (May, 2009).
2. R. Doering and Y. Nishi , "Handbook of Semiconductor Manufacturing Technology ", 2nd ed. (CRC Press, New York, 2008)
3. G. Moore, Electronics 38, (1965).
4. International Technology Roadmap for Semiconductors, http://www.itrs.net, (accessed August, 2012).
5. I. Raaijmakers, "From Nano-scale Research to Nanomanufacturing of Microelectronics", Presentation at the Inaugural Symposium of Prof. W. M. M. Kessels, Eindhoven University of Technology, Eindhoven (May 11. 2012).
6. Intel website, http://www.intel.com (accessed August, 2012).
7. "Intel 32nm Disclosure", http://www.intel.com/pressroom/kits/32nm/westmere/index.htm (accessed August 2012).
8. G. D. Wilk, R. M. Wallace, and J. M. Anthony, J. Appl. Phys. 89, 5243 (2001).
9. J. Robertson, Rep. Prog. Phys. 69, 327 (2006).
10. "Intel 22nm 3-D Tri-Gate Transistor Technology", http://newsroom.intel.com/docs/DOC-2032 (accessed August 2012).

11. G. Dingemans and W. M. M. Kessels, J. Vac. Sci. Technol. A. 30, 040802 (2012).
12. J. S. Lewis and M. S. Weaver, IEEE J. Sel. Top. Quantum Electron. 10, 45 (2004).
13. R. Matero, M. Ritala, M. Leskelä, T. Salo, J. Aromaa, and O. Forsén, J. Phys. IV, 9, 493 (1999).
14. S. A. Campbell, "The Science and Engineering of Microelectronic Fabrication", 2nd ed. (Oxford University Press, New York, 2001)
15. S. M. George, Chem. Rev. 110, 111 (2010).
16. W. M. M. Kessels, S. E. Potts, H. B. Profijt, and M. C. M. van de Sanden, in Atomic Layer Deposition of Nanostructures Materials, edited by M. Knez and N. Pinna (Wiley VCH, New York, 2011).
17. M. A. Lieberman and A. J. Lichtenberg, "Principles of Plasma Discharges and Materials Processing", 2nd ed. (John Wiley & Sons, New York, 2005).
18. D. N. Goldstein, J. A. McCormick, S. M. George, J. Phys. Chem. C 112, 19530 (2008).
19. U. Kogelschatz, Plasma Chem. Plasma Process. 23, 1 (2003).
20. B. B. Burton, A. R. Lavoie, and S. M. George, J. Electrochem. Soc. 155, D508 (2008).
21. P. Bergonzo, U. Kogelschatz, and I. W. Boyd, Appl. Surf. Sci. 69, 393 (1993).
22. S. B. S. Heil, "Plasma-assisted Atomic Layer Deposition of Metal Oxides and Nitrides", PhD thesis, Eindhoven University of Technology, Eindhoven (2007).
23. E. Langereis, "Plasma-assisted Atomic Layer Deposition - an in situ diagnostic study", PhD thesis, Eindhoven University of Technology, Eindhoven (2008).
24. Website "Plasma and Materials Processing" group, http://www.phys.tue.nl/pmp/ (accessed Aug, 2012).
25. N. Leick, "Atomic layer deposition of noble metals: properties and surface reactions", PhD thesis, Eindhoven University of Technology, Eindhoven (2013).

Chapter 2

# Plasma-Assisted Atomic Layer Deposition: Basics, Opportunities, and Challenges*

**Abstract** Plasma-assisted atomic layer deposition (ALD) is an energy-enhanced method for the synthesis of ultra-thin films with Ångstrom-level resolution in which a plasma is employed during one step of the cyclic deposition process. The use of plasma species as reactants allows for more freedom in processing conditions and for a wider range of material properties compared with the conventional thermally-driven ALD method. Due to the continuous miniaturization in the microelectronics industry and the increasing relevance of ultra-thin films in also many other applications the deposition method has rapidly gained popularity in recent years, as is apparent from the increased number of articles published on the topic and plasma-assisted ALD reactors installed. To address the main differences between plasma-assisted ALD and thermal ALD, some basic aspects related to processing plasmas are presented in this Chapter. The plasma species and their role in the surface chemistry are addressed and different equipment configurations, including radical-enhanced ALD, direct plasma ALD and remote plasma ALD are described. The benefits and challenges provided by the use of a plasma step are presented and it is discussed that the use of a plasma leads to a wider choice in material properties, substrate temperature, choice of precursors, and processing conditions but that the processing can also be compromised by reduced film conformality and plasma damage. Finally several reported emerging applications of plasma-assisted ALD are reviewed. It is expected that the merits offered by plasma-assisted ALD will further increase the interest of equipment manufacturers for developing industrial-scale deposition configurations such that the method will find its use in several manufacturing applications.

*Published as: *H. B. Profijt, S. E. Potts, M. C. M. van de Sanden, and W. M. M. Kessels, J. Vac. Sci. Technol. A 29, 050801 (2011).*

## 2.1 Introduction

Atomic layer deposition (ALD) is a vapor-phase deposition technique in which ultra-thin films are typically synthesized sub-monolayer by sub-monolayer by repeating two subsequently executed half-cycles [1-10]. See Fig. 2.1 for a schematic illustration of an ALD cycle. ALD offers atomic layer precision of the growth, because the reaction of the species dosed during the two half-cycles is self-limiting. As a consequence, when sufficient precursor and reactant species are dosed, the ALD film growth is not flux-dependent, as is the case with deposition techniques such as chemical vapor deposition (CVD) and physical vapor deposition (PVD). The growth rate with respect to ALD is expressed as the growth per cycle (GPC), which is typically in the range of 0.05-0.1 nm per cycle. In order to ensure that only ALD surface reactions take place and not CVD-like reactions, which can appear when precursor and reactant are present in the reactor at the same time, a purge step is executed after each half-cycle to remove the residual precursor or reactant species. The total duration of a cycle is the sum of the precursor dosing time, the precursor purge time, the reactant dose time and the reactant purge time. Consequently, the duration of one cycle can not only be shortened by optimizing the dosing times, but also by optimizing the purge times. During ALD, the reactant is typically a gas, such as $O_2$, or a vapor, such as $H_2O$, and the surface reactions are thermally driven by slightly elevated substrate temperatures (typically 150-350 °C). Therefore, the method is also referred to as thermal ALD. Besides the atomic control over the film thickness, the self-limiting half-cycles in ALD facilitate uniform deposition over large substrates and conformal deposition in structures of high aspect ratio, as long as the dosing and purge times are sufficiently long.

The first ALD research was conducted in the 1960s and 1970s in the former USSR and Finland, and the deposition method was patented in 1977 by T. Suntola [11]. For a more extensive review on the history of ALD, the reader is referred to Puurunen *et al.* In the mid-1990s, the semiconductor industry became interested in ALD because a deposition method with atomic control over the film thickness and the ability to deposit films conformally on non-planar substrates was needed. Since then, the semiconductor industry is the key driver of the field of ALD [12]. In 2007, Intel introduced its first 45 nm microprocessor containing Hf-based gate dielectric layers fabricated by ALD. It is expected that, starting from the 22 nm technology node, ALD will be used in several key process steps [13, 14].

Plasma-assisted ALD is an energy-enhanced ALD method that is rapidly gaining popularity [15]. In plasma-assisted ALD, also referred to as plasma-enhanced ALD (PE-

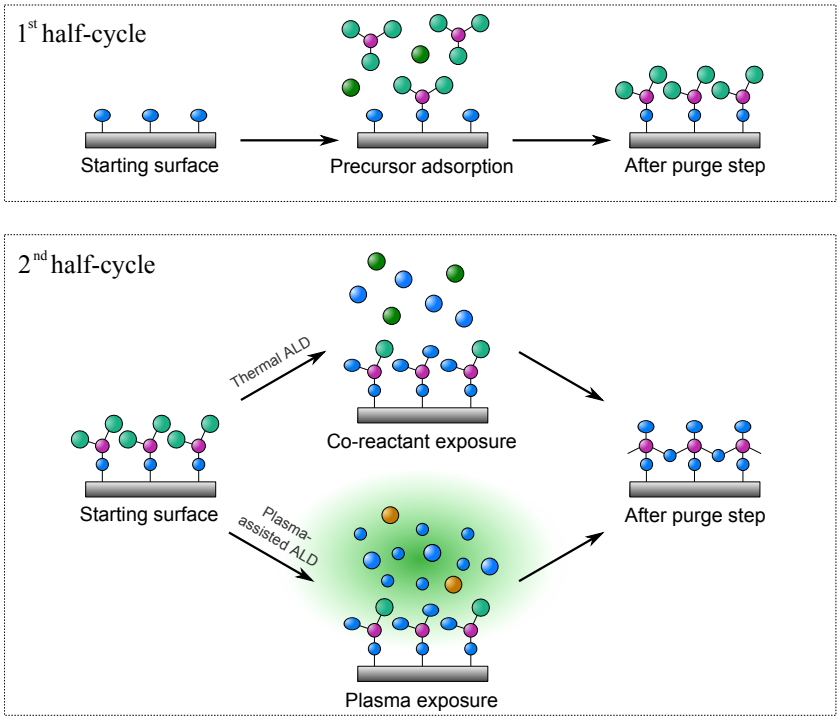



**Figure 2.1:** Schematic representation of thermal ALD and plasma-assisted ALD. During the co-reactant step of the cycle (the 2nd half-cycle), the surface is exposed to a reactant gas or vapor such as $NH_3$ or $H_2O$, or to species generated by a plasma.

ALD), plasma ALD and, in some cases, radical-enhanced ALD, the surface is exposed to the species generated by a plasma during the reactant step. This process is also illustrated in Fig. 2.1. Typical plasmas used during plasma-assisted ALD are those generated in $O_2$, $N_2$ and $H_2$ reactant gases or combinations thereof. Such plasmas can replace ligand-exchange reactions typical of $H_2O$ or $NH_3$, and they can be employed to deposit metal-oxide, metal-nitride and pure metal films. Moreover, plasmas generated in gases or vapors such as $NH_3$ and $H_2O$ have been reported, for which there can also be a combination of plasma and thermal ALD surface reactions taking place at the same time.

Plasma-assisted ALD offers several merits for the deposition of ultra-thin films over thermal ALD and other vapor-phase deposition techniques. The high reactivity of the plasma species on the deposition surface during the plasma-assisted ALD process allows for more freedom in processing conditions and for a wider range of material properties. These ideas will be addressed in detail later in this Chapter and are the primary reason

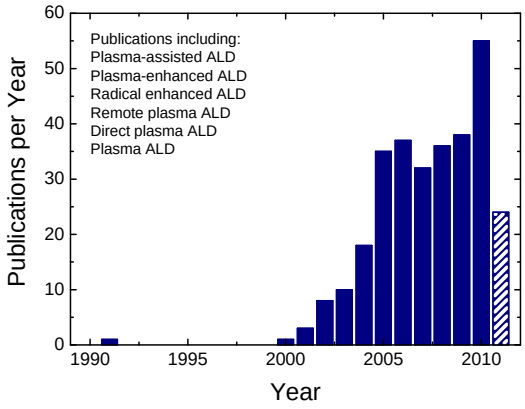



**Figure 2.2:** Number of publications per year on the subject of plasma-assisted ALD, between 1991 and 2011 (status May 31, 2011). The search was run in published abstracts using Web of Science® [23]. The search terms included "plasma-assisted ALD", "plasma-enhanced ALD", "radical enhanced ALD", "remote plasma ALD", "direct plasma ALD", and "plasma ALD". The first report of a plasma-assisted ALD process by De Keijser and Van Opdorp (Philips Research Laboratories, Eindhoven), published in 1991, is also included.

why interest in plasma-assisted ALD has increased rapidly in recent years. This interest has also been catalyzed by the many new applications of ALD that are emerging in and outside the semiconductor industry. Several non-semiconductor applications have set new requirements for the ALD parameter space, which cannot always be satisfied easily by a pure thermally-driven ALD process.

The increasing popularity of plasma-assisted ALD is manifested by the increasing number of recent publications about the topic (see Fig. 2.2), and the large set of thin film materials that have been synthesized by the method (see Table 2.1). Such is the interest and demand in the field that the number of ALD equipment manufacturers providing dedicated plasma-assisted ALD tools has increased significantly in the recent years. Currently (status May 2011), companies such as ASM (Emerald (2004) and Stellar (2006)) [16], Oxford Instruments (FlexAL (2006) and OpAL (2008)) [17], Beneq (TFS 200 (2009)) [18], Cambridge NanoTech (Fiji (2009)) [19], Applied Materials (Applied Endura iLB (2010)) [20], Tokyo Electron Limited (TELINDY PLUS IRad SA (2011)) [21], and Picosun (SUNALE (2011)) [22] provide tools for plasma-assisted ALD.

**Table 2.1:** Overview of the materials deposited by plasma-assisted ALD. The material, the precursor, the plasma gas (only the reactant gas, not the carrier gas), the reactor type ("*re*" is radical-enhanced, "*d*" is direct-plasma ALD, "*r*" is remote plasma ALD, and "-" is not specified) and the references are given for processes reported up to May 31, 2011. The search was run in published abstracts using Web of Science® [23]. acac = acetylacetonate, amd = *N,N'*-diisopropylacetamidinate, cod = 1,4-cyclooctadiene, Cp = $\eta^5$-cyclopentadienyl, Cp* = $\eta^5$-pentamethylcyclopentadienyl, $Cp^{Et}$ = $\eta^5$-ethylcyclopentadienyl, $Cp^{iPr}$ = $\eta^5$-isopropylcyclopentadienyl, $Cp^{Me}$ = $\eta^5$-methylcyclopentadienyl, dmamb = 1-dimethylamino-2-methyl-2-butanolate, dme = dimethoxyethane, Et = ethyl, fod = 6,6,7,7,8,8,8-heptafluoro-2,2-dimethyl-3,5-octanedionate, hfac = 1,1,1,5,5,5-hexafluoroacetylacetonate, $^{i}$Pr = isopropyl, Me = methyl, mp = 3-methyl-3-pentoxyl, $^{n}$Bu = butyl, Ph = phenyl, $^{t}$Bu = tertiary butyl, thd = 2,2,6,6-tetramethyl-3,5-heptanedionate, $^{t}$Pn = tertiarypentyl, vtmos = vinyltrimethoxylsilane.

| Material | Precursor | Plasma | Reactor | Refs. |
|---|---|---|---|---|
| Ag | $Ag(O_2C^tBu)(PEt_3)$ | $H_2$ | *re* | 24 |
| | $Ag(O_2C^tBu)(PnBu_3)$ | $H_2$ | *re* | 24 |
| Al | $AlH_3(NEtMe_2)$ | $H_2$ | *d* | 25,26 |
| $Al_2O_3$ | $AlH_3(MeNC_4H_4)$ | $O_2$ | *d* | 27 |
| | $AlMe_2(O^iPr)$ | $O_2$ | - | 28 |
| | $AlMe_3$ | $O_2$ | *d, r, re,* - | 28-67 |
| | | $CO_2$ | - | 68 |
| | | $N_2/O_2$ | *d*, - | 32,69-72 |
| | | $N_2O$ | d | 73 |
| AlN | $AlCl_3$ | $NH_3/H_2$ | d | 74,75 |
| | $AlMe_3$ | $NH_3$ | *d, r* | 42,76,77 |
| | | $H_2/N_2$ | *r* | 78 |
| $AlO_xN_y$ | $AlMe_3$ | $O_2/N_2$ | *d* | 30,38,79 |
| $AlSi_xO_y$ | $AlMe_3$ & $Si(OEt)_4$ | $O_2/N_2$ | *d* | 80 |
| | | $O_2$ | - | 81 |
| $AlTi_xO_y$ | $AlMe_3$ & $Ti(O^iPr)_4$ | $O_2$ | *d* | 82-85 |
| | | $N_2O$ | *d* | 85 |
| Co | $Co(amd)_2$ | $NH_3$ | *d* | 86 |
| | Co(Cp)(amd) | $NH_3$ | *d* | 87 |
| | $CO_2(CO)_8$ | $H_2$ | *r* | 88 |
| | | $H_2/N_2$ | *r* | 89 |

**Table 2.1** *Continued.*

| Material | Precursor | Plasma | Reactor | Refs. |
|---|---|---|---|---|
| Co | $CoCp_2$ | $NH_3$ | *r* | 90,91 |
| | $CoCp(CO)_2$ | $H_2$ | *r* | 92,93 |
| | | $H_2/N_2$ | *r* | 89 |
| | | $NH_3$ | *r* | 90 |
| $Co_3O_4$ | $CoCp_2$ | $O_2$ | *r* | 94 |
| $CoSi_2$ | $CoCp_2$ | $NH_3$ & $SiH_4$ | *d* | 95,96 |
| Cu | $Cu(acac)_2$ | $H_2$ | *d, re* | 97-100 |
| | Cu(hfac)(vtmos) | $H_2$ | - | 101 |
| | $Cu(thd)_2$ | $H_2$ | *r* | 102 |
| | $Cu(\eta^2\text{-}OC(Et)(Me)CH_2NMe_2)$ | $H_2$ | - | 103 |
| $Er_2O_3$ | $Er(thd)_3$ | $O_2$ | re | 104 |
| $Ga_2O_3$ | $[Ga(Me)_2NH_2]_3$ | $O_2$ | d | 105-110 |
| GaAs | $GaMe_3$ & $AsH_3$ | $H_2$ | re | 111 |
| $GaTi_xO_y$ | $[Ga(Me)_2NH_2]3$ & $Ti(NMe_2)_4$ | $O_2$ | d | 105,107,108,112 |
| $GeSb_xTe_y$ | $Ge(NMe_2)_4$ & $Sb(NMe_2)_4$ & $Te^iPr_2$ | $H_2$ | d | 113 |
| | $Ge^iBu_4$ & $Sb^iPr_3$ & $Te^iPr_2$ | $H_2$ | d | 114 |
| HfN | $Hf(NMe_2)_4$ | $H_2$ | d | 115-117 |
| | | $H_2/N_2$ | d | 117 |
| | | $N_2$ | d, r | 117,118 |
| $HfO_2$ | $Hf(NEt_2)_4$ | $O_2$ | d, r, - | 119-133 |
| | | $N_2O$ | d, - | 126,134 |
| | $Hf(NEtMe)_4$ | $O_2$ | d, r, re | 33,34,135-139 |
| | $Hf(NMe_2)_4$ | $O_2$ | d, r, - | 116,140-142 |
| | | $O_2/N_2$ | r | 143 |
| | $Hf(OH)_3NH_2$ | $O_2$ | - | 144 |
| | $Hf(mp)_4$ | $O_2$ | r | 127 |
| | $Hf(O^tBu)_4$ | $O_2$ | re | 145 |
| $HfAl_xO_y$ | $Al(Me)_3$ & $Hf(NEtMe)_4$ | $O_2$ | d | 33,34 |
| $HfO_xN_y$ | $Hf(NMe_2)_4$ | $O_2/N_2$ | r | 140,143,146 |
| | $Hf(NEt_2)_4$ | $O_2/N_2$ | r | 147 |
| $HfSi_xO_y$ | $Hf(NEtMe)_4$ & $Si(NMe_2)_3H$ | $O_2$ | r | 147 |
| | $Hf(O^tBu)_4$ & $Si(OEt)_4$ | $O_2$ | re | 148 |
| Ir | $Ir(Cp^{Et})(COD)$ | $NH_3$ | d, - | 149,150 |
| $La_2O_3$ | $La(Cp^{Et})_3$ | $O_3$ | re | 151,152 |

**Table 2.1** *Continued.*

| Material | Precursor | Plasma | Reactor | Refs. |
|---|---|---|---|---|
| $La_2O_3$ | $La(Cp^{iPr})_3$ | $O_2$ | r, re | 53,139,153,154 |
| $LaHf_xO_y$ | $La(Cp^{iPr})_3$ & $Hf(NEtMe)_4$ | $O_2$ | re | 139,155 |
| NbN | $Nb(N^tBu)(NEtMe)_3$ | $H_2$, $H_2/N_2$, $NH_3$ | r | 156,157 |
| Ni | $Ni(dmamb)_2$ | $NH_3$, $H_2$ | d | 158 |
| | "Bis-Ni(II)" | $H_2$ | - | 159 |
| | $Ni(Cp^{Et})_2$ | $H_2$ | - | 160 |
| $NiSi_2$ | $Ni(dmamb)_2$ | $NH_3/SiH_4$ | d | 95 |
| Pd | $Pd(hfac)_2$ | $H_2$ | r | 161,162 |
| | $Pd(hfac)_2$ | $H_2/N_2$ | r | 163 |
| Pt | $Pt(Cp^{Me})Me_3$ | $O_2$ | r | 164 |
| $PtO_2$ | $Pt(Cp^{Me})Me_3$ | $O_2$ | r | 164 |
| Ru | $Ru(Cp^{Et})_2$ | $NH_3$ | d, r ,- | 165-174 |
| | | $H_2/N_2$ | d,- | 175-178 |
| | $RuCp(CO)_2Et$ | $O_2$ | r | 179 |
| | $Ru(Cp)_2$ | $NH_3$ | - | 173 |
| | $Ru(Cp^{Et})(NC_4H_4)$ | $NH_3$ | d, - | 180,181 |
| | $Ru(1\text{-}^iPr\text{-}4\text{-}MeC_6H_4)(1,3\text{-}C_6H_8)$ | $NH_3$ | ăd | 182,183 |
| $SiO_2$ | $SiH_4$ | $N_2O$ | - | 184 |
| | $SiH_2(NEt_2)_2$ | $O_2$ | d | 185 |
| | $SiH_3NH_2$ | $O_2$ | d | 186 |
| | $Si(NMe_2)_4$ & $Si(NMe_2)_3Cl$ (mix) | $O_2/N_2$ | d | 187 |
| | $Si(OEt)_4$ | $O_2$ | r | 188 |
| | $[SiMe_2O\text{-}]_4$ | $O_2$ | - | 189 |
| $SiN_x$ | $SiH(N^iPrH)_3$ | $NH_3$ | d | 182 |
| $SnO_2$ | $Sn(O_2CMe)_2(^nBu)_2$ | $O_2$ | - | 190-194 |
| SrO | $Sr(C_5H_2{}^iPr_3)_2(dme)$ | $O_2$ | r | 195 |
| | $Sr(C_{11}H_{19}O_2)_2$ | $O_2$ | - | 196-198 |
| | $Sr(thd)_2$ | $O_2$ | d | 199 |
| $SrTaO_6$ | $Sr[Ta(OEt)_5(OCH_2CH_2NMe_2)]_2$ | $O_2$ | d | 200 |
| | $Sr[Ta(OEt)_5(OCH_2CH_2OMe)]_2$ | $O_2$ | d | 201,202 |
| $SrTiO_3$ | $Sr(thd)_2$ & $Ti(O^iPr)_4$ | $O_2$ | d | 196-198 |
| | $Ti(Cp^*)(OMe)_3$ & $Sr(C_5H_2{}^iPr_3)_2(dme)$ | $O_2$ | r | 195 |
| $SrBi_xTa_y$ | $Sr[Ta(OEt)_5(OCH_2CH_2OMe]_2$ & | | | |
| | $BiPh_3$ (mix) | $O_2$ | d | 202,203 |

**Table 2.1** *Continued.*

| Material | Precursor | Plasma | Reactor | Refs. |
|---|---|---|---|---|
| Ta | $TaCl_5$ | $H_2$ | r | 204-206 |
| $TaO_x$ | $Ta(NMe_2)_5$ | $O_2$ | r | 56,207-209 |
| | | $O_2/N_2$ | r | 209 |
| | $Ta(OEt)_5$ | $O_2$ | re, - | 210,211 |
| $TaC_xN_y$ | $Ta(N^tBu)(NEt_2)_3$ | $H_2$ | d | 212,213 |
| | | $NH_3$ | d | 214 |
| | | $CH_4/H_2$ | d | 215 |
| | $Ta(N^tPn)(NMe_2)_3$ | $H_2$ | d | 216 |
| | $Ta(NMe_2)_5$ | $H_2$ | r | 217 |
| $TaN_x$ | $TaCl_5$ | $H_2/N_2$ | r, - | 218-220 |
| | $TaF_5$ | $H_2/N_2$ | d | 221 |
| | $Ta(NMe_2)_5$ | $H_2$ | r, - | 207,222-224 |
| | | $N_2$ | r | 225 |
| | | $H_2/N_2$ | r | 223,226 |
| | | $NH_3$ | r, - | 174,223,225 |
| | $Ta(N^tBu)(NEt_2)_3$ | $H_2$ | d, r | 227-229 |
| | | $NH_3$ | - | 181 |
| | $Ta(N^tBu)(NEtMe)_3$ | $H_2$ | - | 230 |
| | $Ta(N^iPr)(NEtMe)_3$ | $H_2/N_2$ | r | 231 |
| | $Ta(N^tPn)(NMe_2)_3$ | $H_2$ | - | 175 |
| Ti | $TiCl_4$ | $H_2$ | r | 206,232 |
| $TiN_x$ | $TiCl_4$ | $H_2/N_2$ | d, r | 31,51,136, |
| | | | | 222,233-238 |
| | | $H_2$ , $D_2$ | re | 239 |
| | $Ti(NMe_2)_4$ | $H_2$ | d | 240 |
| | | $N_2$ | r,- | 177,241 |
| | | $H_2/N_2$ | - | 176 |
| | | $H_2$, $N_2$, $H_2/N_2$ | d, r | 242,243 |
| | | $H_2$, $N_2$, $NH_3$ | r | 244 |
| | | $NH_3$ | r | 171,245 |
| $TiO_2$ | $TiCl_4$ | $O_2$ | r | 246,247 |
| | $Ti(Cp^{Me})(O^iPr)_3$ | $O_2$ | r | 56 |
| | $Ti(Cp^*)(OMe)_3$ | $O_2$ | r | 56 |
| | $Ti(Cp^{Me})(NMe_2)_3$ | $O_2$ | r | 248 |

**Table 2.1** *Continued.*

| Material | Precursor | Plasma | Reactor | Refs. |
|---|---|---|---|---|
| $TiO_2$ | $Ti(NMe_2)_4$ | $O_2$ | d, r, - | 112,142,208, |
| | | | | 249-257 |
| | | $H_2O$ | r | 254 |
| | $Ti(O^iPr)_4$ | $O_2$ | d, r, re,- | 56,79,85,137,149 |
| | $Ti(O^iPr)_4$ | $O_2$ | d, r, re,- | 254,258-265 |
| | | $N_2O$ | d | 85,259 |
| | | $O_2/N_2$ | d, - | 79,266 |
| | | $H_2O$ | r | 254 |
| $TiO_xN_y$ | $AlMe_3$ | $O_2/N_2$ | d | 79 |
| $TiAl_xN_y$ | $TiCl_4$ & $AlCl_3$ | $H_2/N_2$ , $NH_3/H_2$ | d | 267 |
| | $Ti(NMe_2)_4$ & $AlMe_3$ | $H_2$ , $NH_3$ | d | 268 |
| $TiSi_xN_y$ | $TiCl_4$ & $SiH_4$ | $H_2/N_2$ | d | 269 |
| $TiSi_xO_y$ | $Ti(O^iPr)_4$ & $Si(OEt)_4$ | $O_2$ | d | 270 |
| $V_xO_y$ | $VO(O^iPr)_3$ | $O_2$, $H_2O$ | r | 271 |
| $WC_x$ | $W(N^tBu)_2(NMe_2)_2$ | $H_2/N_2$ | d | 272 |
| $WN_x$ | $WF_6$ | $NH_3$ | d, r | 273,274 |
| $WC_xN_y$ | $W(Cp^{Et})(CO)_2(NO)$ | $H_2$ | d | 180 |
| | $WF_6$ | $N_2/NH_3$ & $CH_4$ | d | 273 |
| $Y_2O_3$ | $Y(thd)_3$ | $O_2$ | re | 104,275 |
| $Y_2O_3$:Er | $Y(thd)_3$ & $Er(thd)_3$ | $O_2$ | re | 276-279 |
| ZnO | $ZnEt_2$ | $O_2$ | d, r, - | 37,280-283 |
| | | $N_2O$ | d | 284-286 |
| | $ZnMe_2$ | $O_2$ | d | 287,288 |
| $ZrO_2$ | $Zr(NEt_2)_4$ | $O_2$ | r, - | 289,290 |
| | $Zr(NEtMe)_4$ | $O_2$ | d | 291,292 |
| | | $O_2/N_2$ | d | 266,291-293 |
| | $Zr(O^tBu)_4$ | $O_2$ | re, - | 145,290,294 |
| | | $H_2$ | - | 295 |
| ZrN | $Zr(NEt_2)_4$ | $N_2$ | r | 296 |
| | $ZrCp_2(NMe_2)_2$ | $H_2/N_2$, $N_2$, $NH_3$, $O_2$ | r | 297 |
| | $ZrCp_2(\eta^2\text{-}MeNCH_2CH_2NMe)$ | $H_2/N_2$, $N_2$, $NH_3$, $O_2$ | r | 297 |

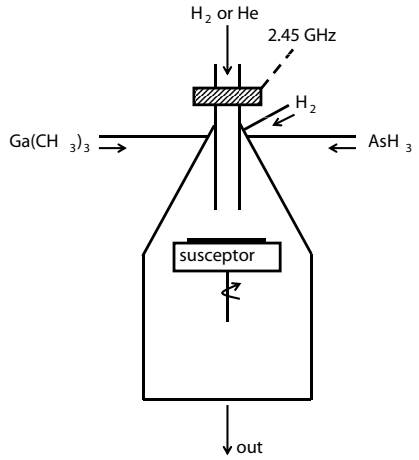



**Figure 2.3:** Reactor layout as used in the first plasma-assisted ALD experiments (Philips Research Laboratories, Eindhoven) reported in the literature [111]. An $H_2$ plasma was generated by means of a remote microwave-induced plasma source in a quartz tube. The H radicals assisted in the atomic layer epitaxy (ALE) process of GaAs. *Reprinted from M. de Keijser and C. van Opdorp, Appl. Phys. Lett.* ***58****, 1188 (1991). Copyright 1991, American Institute of Physics.*

The first case of plasma-assisted ALD was reported in 1991, when De Keijser and Van Opdorp of the Philips Research Laboratories in Eindhoven, the Netherlands, published a paper on atomic layer epitaxy (ALE) of GaAs using H radicals [111]. The hydrogen radicals were generated in a remote microwave-induced plasma and transported to the deposition surface through a quartz tube (see Fig. 2.3). The atomic hydrogen was used to drive the surface reactions after $GaMe_3$ and $AsH_3$ pulsing at substrate temperatures below 500 °C, which is close to the onset temperature for the thermal decomposition of $GaMe_3$. Subsequently, the method remained unexplored until the end of the 1990s, when the semiconductor industry became interested in ALD as mentioned earlier. Sherman filed a patent on the method in 1996 [298], after which Rossnagel and co-workers reported on plasma-assisted ALD of Ta and Ti metal films in 2000 [206]. In the latter case, the anticipated application of the technique was the deposition of Cu diffusion barriers in advanced interconnect technology, a field already very familiar with the merits and robustness of plasma-assisted processes through the broadly-applied PVD technique of sputtering. Afterwards, the number of materials, processes and applications of plasma-assisted ALD has diversified and grown rapidly.

In this Chapter, different plasma-assisted ALD configurations will be described and the merits offered by the technique will be discussed. Also the challenges that plasma-assisted ALD faces will be addressed, both in terms of limitations inherent to the use of a plasma-based process and in terms of the scale-up of the technique for industrial applications. Subsequently, the potential of plasma-assisted ALD will be illustrated by addressing some application areas of ultra-thin films. Next, an outlook will be given for the research and wide scale applicability of the plasma-assisted ALD method. However, to begin with, the next section will briefly cover some plasma basics for the typical plasma operating conditions employed during plasma-assisted ALD.

## 2.2 Plasma Basics

A plasma is a collection of free, charged particles, among other gas-phase species, which is, on average, electrically neutral [299, 300]. This so-called quasi-neutrality means that at macroscopic length scales (typically > 1 mm) the electron density is equal to the ion density, i.e. $n_e = n_i$, under the assumption that negative ions can be neglected. In most plasma configurations, plasmas are created by electrical fields which lead to acceleration and heating of the electrons. These hot electrons are able to ionize gas-phase species through electron-induced collisions and, as such, they can compensate for electron-loss collisions and consequently sustain the plasma. Typically, the average electron temperature (a measure for the kinetic electron energy), $T_e$, is $\sim 3.5 \times 10^4$ K (approximately 3 eV) while the gas temperature remains low ($T_{gas}$ = 300-500 K). This results in non-equilibrium conditions, caused by the relatively low gas pressure that is typically employed in processing plasmas, which, therefore, belong to the class of so-called "cold" plasmas. The electrons in the high-energy tail of the energy distribution are not only able to ionize species, but they can also dissociate and excite the reactant gas through electron impact collisions. This leads to the formation of reactive atomic and molecular neutrals (typically referred to as "plasma radicals"), ions, and photons. Subsequently, these species can undergo additional gas-phase reactions and they can induce surface reactions when they arrive at deposition or reactor surfaces.

Although the charged particles play a central role in sustaining the plasma, the fractional ionization or "ionization degree" of processing plasmas is very low, typically within the range $10^{-6}$-$10^{-3}$. This means that the fluxes of electrons and ions to the deposition surface are much lower than the flux of the plasma radicals. Therefore, in many cases, the surface chemistry is ruled by the interaction of the plasma radicals with the surface species. However, the energy of the ions, $E_{ion}$, arriving at the surface can be much higher

than the ion or electron temperature, as ions are accelerated within a thin positive space-charge layer, the "plasma sheath", at the boundary between the plasma and the substrate. This plasma sheath develops because the electron thermal velocity is much higher than the ion thermal velocity. To make the net current to the substrate zero, an electrical field develops between the plasma and the substrate, which retards the electrons and accelerates the ions. Therefore an electropositive plasma is (time-averaged) always at a positive potential relative to any surface in contact with it. In the rudimentary case of a floating substrate, the difference between the plasma potential, $V_p$, and the substrate potential, $V_f$, is generally given by

$$V_p - V_f = \frac{T_e}{2e} + \frac{T_e}{2e}\ln\left(\frac{m_i}{2\pi m_e}\right), \tag{2.1}$$

where $T_e$ is the electron energy in eV, and $m_e$ and $m_i$ are the electron and ion mass respectively. This means that $V_p$-$V_f$ is typically a few multiples of $T_e$. The energy gained by the ions in the plasma sheath, and consequently whether "ion bombardment" can take place or not, also depends on the collisional mean free path of the ions and the thickness of the plasma sheath. At relatively low pressures, the ion mean free path is larger than the plasma sheath thickness, such that the ions can be accelerated over the full sheath (i.e. the plasma sheath is collisionless) and consequently (i.e., $E_{ion} = e(V_p\text{-}V_f)$).

For typical processing plasmas, the potential over the plasma sheath is < 50 V; however, depending on the plasma gas, the reactor geometry and substrate stage configuration (symmetry or asymmetry of the electrodes, grounding or biasing of electrode/substrate stage, etc.), this potential can also be as high as a few hundreds of Volts. Examples of energy distributions for ions arriving at substrates for $O_2$, $N_2$ and $H_2$ plasmas under specific ALD conditions in a reactor equipped with an inductively coupled plasma are given in Fig. 2.4. At higher pressures, however, the plasma sheath becomes collisional and the net energy gained by the ions is much smaller as a result. Also note that the ions in the plasma sheath are accelerated in the direction perpendicular to the (local) surface. This means that the flux of the ions to the surface is anisotropic with the ions having an angle of incidence around the normal to the surface.

The key properties of the plasma step, executed during the synthesis of thin film materials by plasma-assisted ALD, are:

(1) The reactive species are created in the gas-phase, which means that a relatively high reactivity can be provided to the deposition surface (almost) independently of the substrate conditions (e.g. substrate temperature, substrate materials). The reactivity of the plasma can also be "selective" (e.g. in terms of reactive species produced) by tuning

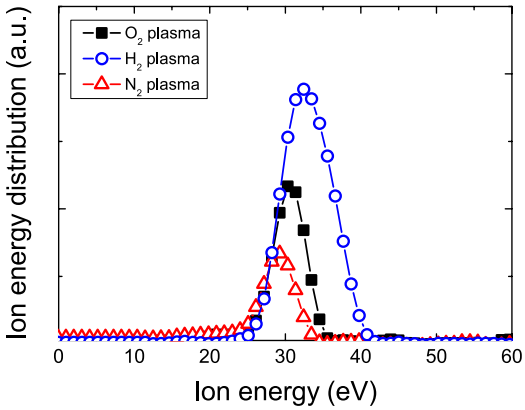



**Figure 2.4:** Ion energy distribution as measured by a retarding field energy analyzer (RFEA) in $O_2$, $H_2$ and $N_2$ plasmas (operating pressure: 8 mTorr; plasma power: 100 W) used for remote plasma-assisted ALD. The RFEA was positioned at the substrate stage. Measurements were performed in the homebuilt ALD-I reactor installed at Eindhoven University of Technology. Due to non-ideal effects such as capacitive coupling, the ion energies measured are higher than those measured in the Oxford Instruments FlexAL reactor, which are reported elsewhere [303].

its properties and composition by carefully choosing the plasma operating conditions (gases, flows, power, pressure, etc.).

(2) Typically the plasma supplies a relatively low heat flux to the surface, despite its high reactivity. The reason is that, for cold plasmas, only the electrons are heated significantly and not the other gas-phase species. Furthermore, plasma exposure takes place only during a part of the cycle (typically only for a few seconds) which does not allow the plasma to extensively heat the substrate.

(3) Through ion bombardment, additional energy can be provided to the deposition surface. This energy is locally dissipated by the surface species and can enhance surface reaction rates and processes such as surface diffusion. Possible ion-surface interactions are depicted in Fig. 2.5 for typical ranges of ion energy and ion flux towards the substrate, corresponding to various plasma-assisted techniques. Moreover, the presence and level of ion bombardment can be controlled through the plasma operating conditions (mainly the gas pressure) as well as by the choice of plasma configuration and substrate (stage) conditions (e.g. grounded substrate, stage size, substrate bias).

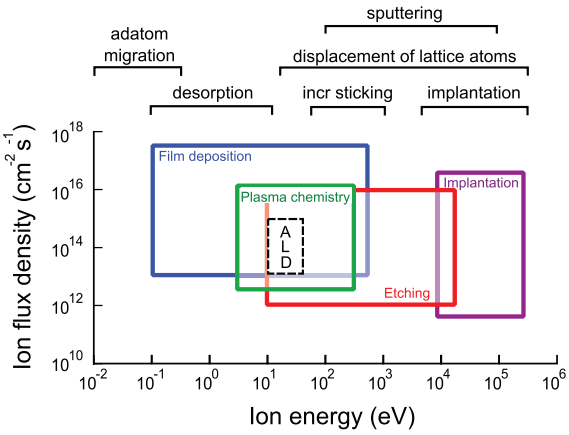



**Figure 2.5:** Ion-surface interactions during plasma processes with respect to ion flux and ion energy [345]. The typical operating windows for plasma-assisted ALD and other plasma-based processes are indicated. Reprinted with permission from *T. Tagaki, J. Vac. Sci. Technol. A* ***2****, 382 (1984). Copyright 1984 American Vacuum Society.*

These key properties can be summarized by the phrase: plasmas can deliver a high, diverse but selective reactivity to a surface without heat, and can therefore access a parameter space in materials processing, which is not easily accessible with strictly chemical methods [299, 300].

Other key differences between plasma-assisted ALD and thermal ALD include:

(1) Electron-impact collisions, as well as other reactions, which lead to the excitation of atoms and molecules. This excitation can be electronic for atoms and electronic, vibrational and rotational for molecules. When electronically excited states return to the ground state, they emit their energy as electromagnetic radiation, which can be measured using optical emission spectroscopy (OES) [42, 46, 47, 52, 119, 137, 138, 148, 223, 237, 271, 289, 301-303]. This excitation process accounts for the vacuum ultraviolet (VUV) to visible emission by the plasma as shown in the OES spectra of $O_2$, $H_2$ and $N_2$ plasmas in Fig. 2.6a-c, for example. The emission in the visible region gives the plasma its characteristic color (as illustrated by the insets of Fig. 2.6a-c) and, therefore, its spectral fingerprint can be easily used to extract information about the species present in the plasma as well as about the chemical and physical processes occurring both within the plasma and at the surface. Measuring the visible emission of the plasma also provides many opportunities for plasma-assisted ALD in terms of process monitoring and optimi-

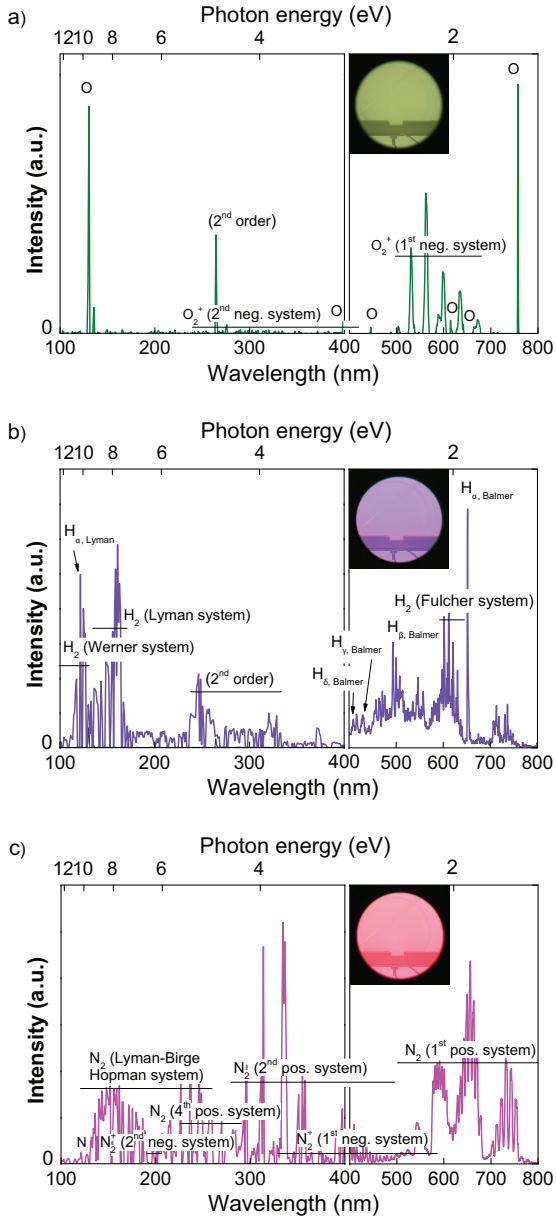



**Figure 2.6:** Optical emission spectra of plasma radiation in (a) an $O_2$ plasma, (b) an $H_2$ plasma, and (c) a $N_2$ plasma as used for plasma-assisted ALD (pressure: 8 mTorr; power: 100 W). The emission in the (vacuum) ultraviolet region was measured using a VUV monochromator and the emission in the visible by a simple spectrometer [302,303]. Emission peaks were identified using the literature [373-377]. The insets show photographs of the corresponding plasmas.

zation [302]. The emission in the ultraviolet can, however, also be sufficiently energetic to influence and induce (unfavorable) processes at surfaces or within thin films (see Sec. 2.5) [303].

(2) Creation of reactant species from the reactant gas during the plasma step, which are mainly radicals. Apart from the ALD surface reactions, these radicals can also undergo additional reactions at the surface, even at saturated surface sites. For example, radicals can recombine on wall (and deposition) surfaces to form non-reactive molecules that desorb back into the plasma. The probability of such recombination reactions, the so-called surface recombination probability, $r$, can be as small as $10^{-6}$ and as high as 1 (see Table 2.2) [304]. The value of $r$ has a direct impact on the density of the radicals in the plasma as it defines the surface loss term for the radicals. Moreover, a relatively high $r$ can also significantly reduce the flux of radicals in trenches or other high-aspect-ratio features on the substrate, for which the radicals have to undergo multiple wall collisions to reach deep inside the structures (see Sec. 2.5).

(3) The presence of a multitude of gas-phase and surface species, which makes it not possible to identify single reactant species solely responsible for the surface reactions. For example, when admixing two reactant gases in the plasma, new molecules (and related radicals) can be formed through gas-phase or surface recombination reactions [313]. Furthermore, volatile products from the ALD reactions can be excited, ionized and dissociated by the plasma when leaving the surface. All of these species can contribute to the ALD surface chemistry adding to its complexity.

To illustrate which species are typically present in a plasma, including their typical density, an overview is given in Table 2.3 for an $O_2$ plasma [314]. Data are given for two operating pressures for an inductively-coupled plasma, as typically employed for remote plasma-assisted ALD described in the next section.

## 2.3 Plasma-Assisted ALD Configurations

Several equipment configurations exist for assisting an ALD process by means of a plasma step (also see Chapter 4) [136].

### 2.3.1 Radical-Enhanced ALD

In the first configuration, a plasma generator is fitted to a thermal ALD reactor, see Fig. 2.7a. Examples of such plasma sources are microwave surfatron systems [100] and the

**Table 2.2:** Overview of recombination loss probabilities, $r$, for H, N and O radicals on the surfaces of various materials [304]. Accuracies in the values are indicated where available. The data are taken from Refs. 305-312.

| Radical | Surface | $r$ |
|---|---|---|
| H | $SiO_2$ | $0.00004 \pm 0.00003$ |
| | $Al_2O_3$ | $0.0018 \pm 0.0003$ |
| | Pyrex | $0.0058 \pm 0.0018$ |
| | Stainless steel | $0.032 \pm 0.015$ |
| | Ti | 0.35 |
| | Al | 0.29 |
| | Ni | $0.20 \pm 0.09$ |
| | Cu | 0.14 |
| | Au | $0.15 \pm 0.05$ |
| | Pd | $0.07 \pm 0.015$ |
| | Pt | 0.03 |
| N | $SiO_2$ | $0.0003 \pm 0.0002$ |
| | Stainless steel | 0.0063 |
| | Si | 0.0016 |
| | Al | 0.0018 |
| O | $SiO_2$ | $0.0002 \pm 0.0001$ |
| | Pyrex | 0.000045 |
| | $Al_2O_3$ | 0.0021 |
| | ZnO | 0.00044 |
| | $Fe_2O_3$ | 0.0052 |
| | $Co_3O_4$ | 0.0049 |
| | NiO | 0.0089 |
| | CuO | 0.043 |
| | Stainless steel | $0.070 \pm 0.009$ |

**Table 2.3:** Densities of plasma species in an $O_2$ plasma, as typically used in plasma ALD processes. Data are presented for two different pressures. The data have been compiled from the modeling results described in Ref. 314 for an inductively-coupled plasma operated at a source power of 500 W. The excited species O* and $O_2$* correspond to the lowest metastable states being O ($^1$D) and $O_2$ ($a^1\Delta_g$), respectively.

| Pressure (mTorr) | $O_2$ ($cm^{-3}$) | O ($cm^{-3}$) | $O_2$* ($cm^{-3}$) | O* ($cm^{-3}$) | $O_2^+$ ($cm^{-3}$) | $O^+$ ($cm^{-3}$) | $O^-$ ($cm^{-3}$) | $n_e$ ($cm^{-3}$) |
|---|---|---|---|---|---|---|---|---|
| 10 | $3\times10^{14}$ | $7\times10^{13}$ | $4\times10^{13}$ | $4\times10^{12}$ | $5\times10^{10}$ | $4\times10^{10}$ | $2\times10^{10}$ | $7\times10^{10}$ |
| 100 | $3\times10^{15}$ | $1\times10^{14}$ | $3\times10^{14}$ | $5\times10^{10}$ | $4\times10^{10}$ | $1\times10^{9}$ | $3\times10^{10}$ | $2\times10^{10}$ |

radio-frequency-driven R*Evolution (MKS Instruments) [315] and Litmas RPS (Advanced Energy) [316] systems, which are also commonly used for plasma-based reactor cleaning. Due to technical constraints on existing ALD reactors, plasma generation typically takes place at a relatively far distance from ALD reaction zone. Consequently, the plasma species have to flow through the reactor tubing between the plasma source and reaction chamber. This allows for many surface collisions, where ions and electrons are lost before reaching the substrate due to their recombination at surfaces. Therefore, the method is typically referred to as "radical-enhanced ALD". The many surface collisions of the plasma species can, however, also significantly reduce the flux of radicals arriving at the substrate. This is especially prominent when the choice of the inner surface of the tubing material is not harmonized with the plasma radicals to reduce surface recombination. For example, H radicals have a relatively low surface recombination probability on quartz surfaces but a very high recombination probability on most metals (see Table 2.2). In the case of metallic surfaces, very long radical exposure times might be necessary to reach saturation of the reactant step in the ALD cycle.

### 2.3.2 Direct Plasma ALD

The second configuration stems directly from the field of plasma-enhanced chemical vapor deposition (PE-CVD). In this case, a capacitively-coupled plasma is generated at radio frequency, (RF, typically 13.56 MHz), between two parallel electrodes in a so-called RF parallel plate or RF diode reactor, see Fig. 2.7b. In this case, typically one electrode is powered while the other is grounded and, generally, the substrate is positioned on the grounded electrode. As such, this ALD reactor configuration of is referred to as "direct plasma ALD" because the wafer is directly positioned at one of the electrodes which contribute to plasma generation. The gases are introduced into the reactor either through

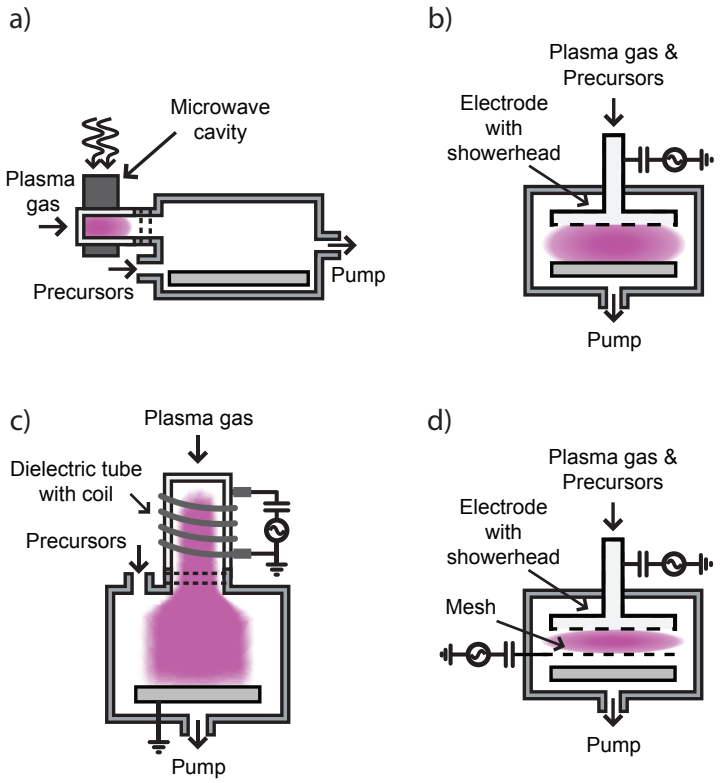



**Figure 2.7:** Various reactor configurations for plasma-assisted ALD [136]: (a) radical-enhanced ALD; (b) direct plasma-assisted ALD, (c) remote plasma ALD, and (d) direct plasma reactor with mesh. The reactor layouts and plasma sources shown serve only as examples. *Reprinted with permission from S.B.S. Heil et al., J. Vac. Sci. Technol. A **25**, 1357 (2007). Copyright 2007 American Vacuum Society.*

a shower head in the powered electrode [228] or from the side of the electrodes [199]. The first is typically referred to as "shower-head type" and the second as "flow-type" (if the pressure is sufficiently high). The ALD reactors provided by ASM (Emerald and Stellar) [16] and Beneq (TFS 200) [18] for example can be classified as direct-plasma ALD reactors. Typical operating pressures used during the plasma step in direct plasma ALD are of the order of 1 Torr [200], although these also could be <100 mTorr for an RF parallel plate reactor [25]. During direct plasma-assisted ALD, the fluxes of plasma radicals and ions towards the deposition surface can be very high, as the plasma species are created in very close proximity of the substrate surface. In principle, this enables uniform deposition over the full wafer area with short plasma exposure steps. Because

of the relatively simple reactor layout and their proven performance in other plasma processing methods, direct plasmas are extensively used in industrial tools. Depending on the voltage applied to the powered electrode and the operating pressure, the energy of the ions arriving on the substrate can, however, be substantial. In addition, the emission of high energy photons can be significant, possibly leading to plasma damage. The extent of plasma induced damage is, however, determined by the specific implementation of the plasma source and the processing conditions (see Sec. 4.2.1).

### 2.3.3 Remote Plasma ALD

A third configuration for plasma-assisted ALD equipment can be classified as "remote plasma ALD". In this case, as its name implies, the plasma source is located remotely from the substrate stage such that substrate is not involved in the generation of the plasma species, see Fig. 2.7c. This configuration can be distinguished from radical-enhanced ALD by the fact that the plasma is still present above the deposition surface, i.e., the electron and ion densities have not decreased to zero [237, 303]. As will also be shown in Chapter 5, the "downstream" plasma can be of the afterglow type (where the local electron temperature is too low to be ionizing) or can still be active (ionizing). The flux of the radicals towards the substrate can therefore be much higher than for radical-enhanced ALD. Moreover, under these circumstances, the plasma and substrate conditions can be varied (relatively) independently of each other, something which is not the case for direct plasma ALD. For example, in direct plasma-assisted ALD a change in substrate temperature affects the gas temperature and consequently the density of gas-phase species and the generation of plasma species [299]. Therefore, the remote nature of the remote plasma-assisted ALD configuration allows for more control of the plasma's composition and properties than is possible with direct-plasma ALD. The plasma properties can be optimized relatively easily by tuning the operating conditions of the plasma source and the downstream conditions at the position of the substrate. This holds specifically for the presence of ion bombardment and the influence of plasma radiation [303]. Due to their high degree of flexibility remote plasma ALD reactors are therefore well suited for process design and other R&D applications.

A variety of plasma sources can be employed for remote plasma-assisted ALD, including microwave plasmas [111], electron cyclotron resonance (ECR) plasmas [152], and RF-driven inductively-coupled plasmas (ICP) [206]. The latter type, either with a cylindrical or planar coil, is currently the most popular and it has proven itself extensively as a plasma source in plasma etching. In the Oxford Instruments FlexAL and OpAL

reactors [17], a multi-turn cylindrical coil surrounds an alumina discharge tube, while in the Cambridge NanoTech Fiji system [19] the inductor surrounds a quartz tube. The operating pressure for these ICP systems can be as high as 1 Torr [229] but, in many cases, pressures <100 mTorr are common [206]. For such low pressures, which are atypical for (thermal) ALD, the reactors are equipped with turbomolecular pumps. In remote plasma systems, the fact that the plasma source and substrate surface are separated also allows for easy use of *in situ* diagnostic techniques such as spectroscopic ellipsometry [238].

An alternative approach is provided by Beneq in their TFS 200 system [18]. Although this is, in principle, a direct ALD reactor employing a capacitively-coupled plasma, a grid can be placed between the two electrodes creating a so-called triode configuration (see Fig. 2.7d). This enables confinement of the plasma between the driven electrode and the grid such that the deposition surface is not in contact with the active plasma [62]. In essence, this leads to a lower ion energy and flux towards the deposition surface, and lower ion and photon fluxes towards the deposition surface but also to a somewhat reduced radical density.

### 2.3.4 Developments Related to Plasma-Assisted ALD Reactors

Recently, there have been a number of other developments with respect to the aforementioned reactor configurations. These initiatives mainly aim at obtaining additional control over the production of plasma species and over their interaction with the material surface. In the remote and direct-plasma configurations discussed so far, the substrate is generally placed on a grounded substrate stage. As a result, the potential over the plasma sheath and, consequently, the ion energy is relatively small. However, it is expected that some deposition processes can benefit from enhanced radical production and/or from enhanced ion energies. In that case the non-grounded substrate stage can be biased by a DC, AC, RF or pulse-shaped signal, or a combination of different signals [317]. Such methods were inspired by configurations designed for other plasma-assisted material processing techniques such as plasma etching, ion implantation, and deposition by PE-CVD or PVD [299]. One configuration recently reported is a capacitively-coupled remote plasma (a direct plasma reactor with a grid), in which a pulsed DC power was applied to the grid [138]. It was reported that for the resulting negative grid voltage, both the electron temperature and plasma density increased resulting in a higher radical and ion flux to the substrate. It was stated that this improved the electrical properties of $HfO_2$ films, such as the effective oxide thickness and the breakdown voltage. Another embodiment is the application of an RF bias or self-bias voltage to the substrate stage in a remote plasma

ICP reactor (also see Sect. 4.3 and Chapters 6 and 7) [318]. Under properly chosen operating conditions, this leads to an enhanced ion energy, therefore yielding an additional control over the plasma-surface interaction in which the ion energy can be independently controlled from the ion and radical flux.

## 2.4 Merits of Plasma-Assisted ALD

The use of plasma-assisted ALD for ultra-thin film synthesis has several potential advantages over thermal ALD, in addition to the benefits provided by the ALD technique itself. These merits can be useful for specific applications of ALD-synthesized thin films.

***A. Improved material properties***

It has been reported that, for some materials and applications, plasma-assisted ALD affords better material properties than thermal ALD in terms of, for example, film density [166, 167, 187, 207, 214, 227, 228], impurity content [120, 162, 229, 241, 245, 271, 290, 294] and electronic properties [30, 31, 50, 68, 134, 135, 154, 207, 208, 211, 228, 229, 242, 272, 290, 294, 319]. In most cases, these improved material properties are a result of the high reactivity provided by the plasma, which will be addressed in more detail below. However, more specifically, this improvement can often be attributed to kinetically-driven, selective ALD surface reactions, for example, the abstraction of surface halogen atoms by H radicals and several ion-assisted surface reactions, as illustrated in Fig. 2.5.

***B. Deposition at reduced substrate temperatures***

As high reactivity is delivered to the deposition surface by the plasma species, less thermal energy is required at the substrate to drive the ALD surface chemistry. This means that it is possible to deposit films with equivalent material properties at lower substrate temperatures than for thermal ALD [40, 56, 65, 87, 187, 233, 243, 249, 254, 320]. The reactivity delivered by the plasma species is not only provided by reactive plasma radicals but is also determined by the kinetic energy of the ions accelerated in the plasma sheath, the recombination energy of the ions and other species when recombining at the deposition surface (e.g. the ionization energy of the ions), and the energy flux caused by the plasma radiation. More details about low-temperature (i.e. room temperature) deposition, can be found in Chapter 3.

***C. Increased choice of precursors and materials***

The fact that reactive plasma radicals are delivered to the deposition surface allows for the use of precursors with relatively high thermal and chemical stabilities. A classic example is the ALD of metal oxides from $\beta$-diketonate precursors, such as those with acac (acetylacetonate) [97-100], hfac (1,1,1,5,5,5-hexafluoroacetylacetonate) [101, 161, 162] and thd (2,2,6,6,-tetramethyl-3,5-heptanedionato) [102, 104, 275-279] ligands. Such precursors require more reactive co-reactants as they show no or low reactivity with $H_2O$ (in essence, they do not readily undergo hydrolysis reactions). Although the use of $O_3$ could also provide a solution in such cases, plasma-assisted ALD processes can give even more reactivity. The plasma-assisted method can also yield solutions when depositing non-oxidic materials such as metal nitrides and metals. In addition to a wider choice of precursors, plasma-assisted ALD processes also enable the deposition of more material systems, for example, of the elemental metals Ti and Ta (see also Sec 2.6.1) [204-206, 232]. For these metals, no (thermal ALD) reactant is available to reduce the precursor. Furthermore, plasma-assisted ALD allows for a wider choice of substrate materials to be used, particularly those which are temperature-sensitive [35, 38, 38, 39, 54, 65, 163, 187, 251, 252, 256, 258, 286, 320, 321].

***D. Good control of stoichiometry and film composition***

Non-thermally-driven reactions can be induced at the deposition surface due to the non-equilibrium conditions in the plasma, which enables better control of the ALD surface chemistry and of the species incorporated into the film. Therefore, the use of a plasma provides additional variables with which to tune the stoichiometry and composition of the films. These include the operating pressure [205, 225, 245], plasma power [52, 62, 70, 151, 152, 167, 183, 213, 214, 233], plasma exposure time [164, 183, 213, 214, 221, 222, 228, 236, 237, 245], the admixing of additional gases into the plasma [30, 74, 215, 218] and the biasing voltage [138, 318]. It is, for example, relatively straightforward to incorporate N atoms into oxide thin films by the addition of $N_2$ to a plasma generated in $O_2$ [38, 73, 128, 134, 143, 146, 319]. Such controlled doping of thin film materials is difficult to achieve with strictly thermally-driven ALD reactions.

***E. Increased growth rate***

Cases exist in which the plasma species create a higher density of reactive surface sites due to the high reactivity of the plasma. Consequently, this can lead to higher growth per cycle values [31, 32, 40, 58, 60, 134, 154, 187, 207, 208, 229, 233, 254, 259, 261, 274, 294]. Moreover, the plasma can be switched on and off very rapidly, which

enables fast pulsing of the plasma reactant species [255, 273, 274, 293, 295] and reduced purge times (depending on the gas residence time in the reactor) [46, 60]. The latter is especially important for the ALD of metal oxides at low temperatures (room temperature up to 150 °C), where purging of $H_2O$, in the case of thermal ALD, requires excessively long purge times and, therefore, long cycle times [322]. Shorter cycle times have a significant impact on the net GPC (growth per cycle) and throughput of an ALD reactor. The high plasma reactivity is also beneficial in particular cases where the nucleation delay is shorter for plasma-assisted ALD than for the equivalent thermal ALD process [31, 164, 166, 168, 169, 173, 179, 183]. This aspect also contributes to an increased throughput of ALD reactors.

***F. More processing versatility in general***

The availability of a plasma source on an ALD reactor allows for several other *in situ* treatments of the deposition surface, deposited films, and reactor walls. Plasmas can be used for substrate pre-treatment (e.g. oxidation by an $O_2$ plasma [69, 70, 119, 122, 130, 132, 149] and nitridation by $NH_3$ or $N_2$ plasmas [119, 129, 132]), substrate cleaning [98], post-deposition treatments [141, 164], and reactor wall conditioning and cleaning [240]. For example, a layer of TiN covering the walls of the reactor can be removed easily by running a F-based plasma such as one generated in $NF_3$ or $SF_6$ [136].

The aforementioned merits of plasma-assisted ALD can be illustrated in more detail by several results that have been reported for various material systems in the recent years.

The first example is the remote plasma-assisted ALD of $Al_2O_3$ from $AlMe_3$ and an $O_2$ plasma, which can be compared to the thermal ALD case with $H_2O$. For both ALD processes, the dominant reaction products during the precursor dosing step are $CH_4$ molecules. During the subsequent reactant step, however, different reaction products are produced for the thermal and plasma process. For thermal ALD, only $CH_4$ is created, whereas for plasma-assisted ALD, combustion-like reactions take place which result in the production of $CO_2$ and $H_2O$. In case only mono-functional chemisorpion of $AlMe_3$ to the surface is assumed, the suggested dominant surface reactions for plasma-assisted ALD can be written as [46,47,55]:

1. $AlOH_{(ads)} + AlMe_{3\ (g)} \rightarrow AlOAlMe_{2\ (ads)} + CH_{4\ (g)}$
2. $AlMe_{(ads)} + 4\ O_{(g)} \rightarrow AlOH_{(ads)} + CO_{2\ (g)} + H_2O_{(g)}$

The process and material properties of $Al_2O_3$ films deposited by plasma-assisted ALD were compared directly with those for thermal ALD. The results in Fig. 2.8 show that the $Al_2O_3$ films can be deposited by plasma-assisted ALD at substrate temperatures between 25 and 400 °C. Data are provided for processes carried out in two ALD reactors [323], which differ in operating pressure by a factor of $\sim$10. It is clear that the GPC (growth per cycle) shows no dependence on the plasma operating pressure in this case [323]. It can also be observed that the GPC increases proportionally with decreasing substrate temperature. Although this effect can partly be attributed to a slightly reduced mass density of the films for temperatures below 150 °C, the change in GPC is predominantly caused by an increased incorporation of Al atoms into the film per cycle at lower substrate temperatures [56]. This number of Al atoms incorporated is related to a higher surface density of hydroxyl groups at lower substrate temperatures. This has been confirmed by *in situ* infrared spectroscopy, which revealed that hydroxyl groups on $Al_2O_3$ surfaces are the dominant adsorption sites for $AlMe_3$ during plasma-assisted ALD [55]. For the thermal ALD process of $AlMe_3$ and $H_2O$, the GPC values are comparable but slightly lower than for plasma-assisted ALD at temperatures > 200 °C. However, it is at temperatures < 200 °C that the main difference is observed, because here the GPC of thermal ALD drops significantly below that for plasma-assisted ALD. Apparently, the thermal energy at these temperatures is insufficient to allow for a full reaction of $H_2O$ with the surface and so, in this case, high hydroxyl surface density cannot be created. Additionally for the thermal ALD process, the purge after the $H_2O$ dose needs to be increased at low substrate temperatures to avoid parasitic CVD reactions. For temperatures > 200 °C, purge times well below 5 s are sufficient (optimized industrial ALD reactors even use sub-second purges), whereas at 58 °C, 30 s is required to completely remove residual water [322]. At room temperature, $Al_2O_3$ films can still be synthesized by thermal ALD, but the purge time required becomes impractically long (up to 180 s at 33 °C). For plasma-assisted ALD, the purge time can be kept relatively short, even at room temperature, in essence, equal to the time used at higher temperatures or only slightly extended [60]. The structural properties of $Al_2O_3$ thin films are highly comparable for both thermal and plasma-assisted ALD using $AlMe_3$ as a precursor [60, 323]. At lower substrate temperatures the film quality degrades slightly, as evidenced by a reduced mass density, an increased O/Al ratio, and a higher H concentration [60]. Furthermore, small traces of C can be found in the films deposited at room temperature. For plasma-assisted ALD the C atoms are mainly incorporated as $CO_x$ groups, the density of which can be reduced by increasing the plasma exposure time [55]. Despite the somewhat lower material quality of the $Al_2O_3$ deposited at substrate temperatures < 150 °C, these films are considered

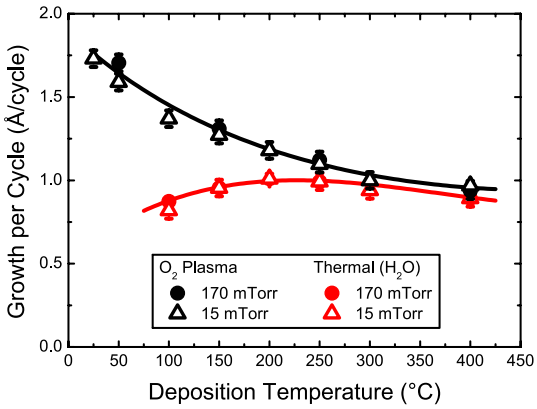



**Figure 2.8:** Growth per cycle of $Al_2O_3$ films as a function of the substrate temperature. The films were deposited by plasma-assisted ALD ($O_2$ plasma) and thermal ALD ($H_2O$). Two different ALD reactors were used; one operating at 15 mTorr and the other at 170 mTorr [43, 323]. From *S.E. Potts et al., J. Electrochem. Soc.* ***157****, 66 (2010). Reproduced by permission of ECS - The Electrochemical Society.*

very attractive for applications which require dense, amorphous and conformal $Al_2O_3$ films deposited at low temperatures. Examples are given in Sec. 2.6.

The plasma-assisted ALD of $TiO_2$ films from metal-organic precursors and an $O_2$ plasma is another case for which the merits of the plasma-based process can be illustrated. As shown in Fig. 2.9, $TiO_2$ has also been deposited at low substrate temperatures by this method, using $Ti(O^iPr)_4$, $Ti(Cp^{Me})(O^iPr)_3$, $Ti(Cp^*)(OMe)_3$ and $Ti(Cp^{Me})(NMe_2)_3$ as precursors. The films have been deposited at substrate temperatures as low as 25, 50, 100 and 100 °C, respectively [56]. Moreover, the GPC values were marginally affected by the substrate temperature over the full temperature range (up to 300 °C). For thermal ALD, with either $H_2O$ or $O_3$, the situation is quite different [324, 325]. Firstly, the GPC increases with substrate temperature, which indicates that the surface reactions are rate-limited by thermal activation. This holds for $Ti(O^iPr)_4$ with both $H_2O$ and $O_3$ (see Fig. 2.9), but also for $Ti(Cp^*)(OMe)_3$ with $O_3$ (not shown) [326]. Furthermore, for all these precursors, the GPC for the thermal process is lower than that for plasma-assisted ALD (except for the case of $Ti(O^iPr)_4$ with $O_3$ at 300 °C, where the high GPC has been attributed to thermal decomposition of the precursor [324]). This clearly demonstrates that an $O_2$ plasma is not only more reactive than $H_2O$ but is also more effective than $O_3$, particularly at lower temperatures. In addition, $O_2$ plasmas (and $O_3$) allow for the use of Cp-based Ti precursors, which show almost no reactivity against $H_2O$ in ALD processes

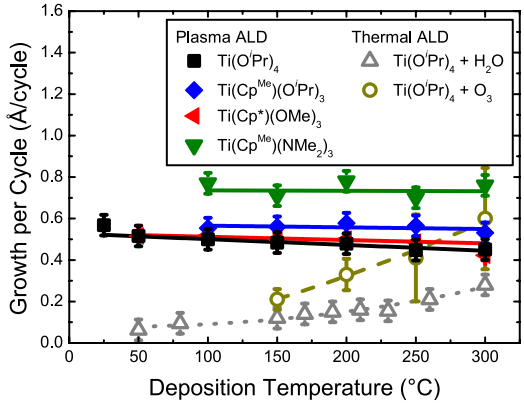



**Figure 2.9:** Growth per cycle of $TiO_2$ films as a function of the substrate temperature. Plasma-assisted ALD was carried out using Ti(O$^i$Pr)$_4$, Ti(Cp$^{Me}$)(O$^i$Pr)$_3$, Ti(Cp*)(OMe)$_3$ and Ti(Cp$^{Me}$)(NMe$_2$)$_3$ as precursors in combination with an $O_2$ plasma [56, 248]. Data for thermal ALD with $H_2O$ [325] and $O_3$ [324] using the widely-employed Ti(O$^i$Pr)$_4$ precursor are given for comparison. *From S.E. Potts et al., J. Electrochem. Soc.* ***157****, 66 (2010). Reproduced by permission of ECS - The Electrochemical Society.*

[326]. This exemplifies the fact that a wider range of precursors can be employed for use with plasma-assisted ALD. These relatively stable Cp-based precursors are currently of substantial interest for metal-insulator-metal (MIM) capacitor applications. In such capacitors the use of $SrTiO_3$ is being considered as an ultra-high-*k* dielectric, e.g., in upcoming technology nodes of DRAM devices. $SrTiO_3$ can be deposited by the combination of $TiO_2$ and SrO ALD cycles into so-called "supercycles" for which an overlap in temperature window of the two ALD processes is demanded. In order to obtain $SrTiO_3$ dielectric films with the best electrical performance, the highest possible deposition temperature within the shared temperature window should be chosen [195, 327].

The fact that plasma-assisted ALD can lead to improved material properties has also been demonstrated by results on metallic TiN films [233, 237]. The combination of $TiCl_4$ with an $H_2/N_2$ plasma yielded thin TiN films with an excellent resistivity and low impurity levels. These results greatly surpass the material quality achieved with the standard thermal process employing $TiCl_4$ and $NH_3$ [233, 237]. Alternatively, during a thermal ALD process also dimethyl hydrazine ($N_2H_2Me_2$) or hydrazine ($N_2H_4$) can be used as reactants. These reactants are, however, less common and the results obtained so far are not as good as obtained with a $H_2/N_2$ plasma.

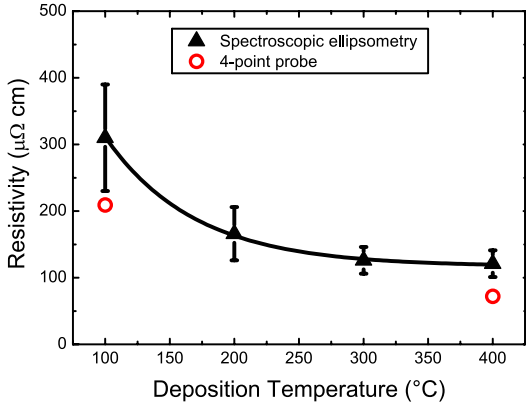



**Figure 2.10:** Resistivity (at room temperature) of TiN films obtained at 100-400 °C. The films were deposited by plasma-assisted ALD using $TiCl_4$ in combination with an $H_2/N_2$ plasma. The resistivity was determined by *in situ* spectroscopic ellipsometry (thin films, $\sim$ 10 nm) and 4-point probe measurements (thicker films, > 45 nm) [237]. *From S.B.S. Heil et al., J. Electrochem. Soc.* ***153****, G956-G965 (2006). Reproduced by permission of ECS - The Electrochemical Society.*

During a plasma-assisted ALD cycle of TiN, the simplified surface reaction scheme can be described as:

1. $TiNH_{(ads)} + TiCl_{4\ (g)} \rightarrow TiNTiCl_{3\ (ads)} + HCl_{(g)}$
2. $TiCl_{(ads)} + 2\ H_{(g)} + N_{(g)} \rightarrow TiNH_{(ads)} + HCl_{(g)}$

In terms of acceptable material quality, thermal ALD of TiN is limited to the substrate temperature range of 300-400 °C, while the plasma-assisted ALD process can yield fair material properties down to temperatures as low as 100 °C as shown in Fig. 2.10. For thicker films, resistivity values as low as 72 $\mu\Omega$ cm (400 °C) and 209 $\mu\Omega$ cm (100 °C) have been reported, which could be attributed to the low Cl concentrations of 0.1 at.% and 2.1 at.%, respectively at these temperatures [237]. This is quite a promising achievement, since TiN has numerous applications, such as an electrode material in metal-insulator-metal (MIM) capacitors and as a metal gate in CMOS devices [328].

The ability of plasma-assisted ALD to synthesize materials which cannot (or hardly) be deposited by thermal ALD is exemplified by the case of $TaN_x$. Thermal ALD processes using either metal-halide or metal-organic precursors in combination with $NH_3$ always yield the highly resistive $Ta_3N_5$ phase because the reducing power of $NH_3$ is

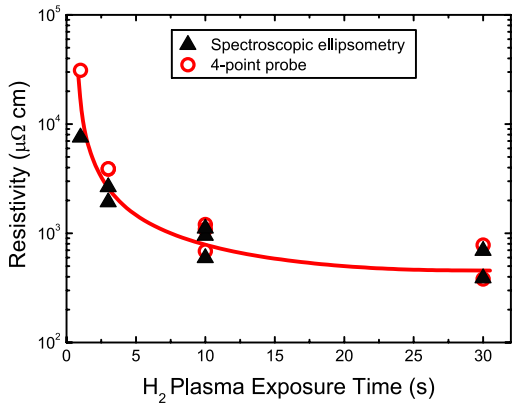



**Figure 2.11:** Resistivity (at room temperature) of TaN films as a function of $H_2$ plasma exposure time [223]. The data were obtained by *in situ* spectroscopic ellipsometry and 4-point probe measurements. *Reprinted from E. Langereis et al., J. Appl. Phys.* ***102****, 083517, (2007). Copyright 2007, American Institute of Physics.*

insufficient to reduce the Ta oxidation state from +5 to +3 [329]. Cubic TaN, can be deposited by thermal ALD when $N_2H_4$ is used as the reactant [330] or with the help of additional reducing agents such as $AlMe_3$ or elemental Zn [329, 331]. However, these processes employ relatively uncommon reactant gases or additional reducing agent dosing steps, which add significantly more complexity to the deposition process. For plasma ALD processes, it is possible to deposit conductive cubic TaN films from metal-organic precursors using an $H_2$ plasma [223, 226]. This is illustrated in Fig. 2.11, where the resistivity of TaN films, deposited using $Ta[N(Me)_2]_5$ as a precursor, as a function of the $H_2$ plasma exposure time is shown. It is clear that TaN films with resistivity values as low as 380 $\mu\Omega$ cm could be obtained for long plasma exposure times. In addition, the aforementioned highly resistive $Ta_3N_5$ films can also be synthesized by plasma-assisted ALD using the same $Ta[N(Me)_2]_5$ precursor, either by admixing a small concentration of $N_2$ into the $H_2$ plasma or by operating the plasma in $NH_3$ [223]. This process also exemplifies that plasma-assisted ALD offers good control over the film stoichiometry.

As another example, the ALD of metal films is considered; in particular the ALD of Pt. Materials from the Pt-metal group, with applications in nanoelectronics (as electrodes) and in catalysis, are among the exceptional cases of elemental metals for which thermal ALD is relatively straightforward [332]. Pt can, for example, be deposited by thermal ALD using $Pt(Cp^{Me})Me_3$ as a precursor combined with $O_2$ gas [333]. Assuming that analogous surface reactions to those reported for the thermal ALD process of Pt take

place [334], it is likely that a reaction mechanism such as the following occurs in the case of plasma-assisted ALD:

1. 2 $Pt(Cp^{Me})Me_{3\ (g)}$ + 3 $O_{(ads)} \rightarrow$ 2 $Pt(Cp^{Me})Me_{2\ (ads)}$ + $CH_{4\ (g)}$ + $CO_{2\ (g)}$ + $H_2O_{(g)}$,
2. 2 $Pt(Cp^{Me})Me_{2\ (ads)}$ + 48 $O_{(g)} \rightarrow$ 2 $Pt_{(s)}$ + 3 $O_{(ads)}$ + 16 $CO_{2\ (g)}$ + 13 $H_2O_{(g)}$,

For ALD of Pt as well as for many other noble metal processes, a relatively long nucleation delay can occur on oxides and other starting surfaces, which is especially prominent when lower operating pressures are employed. However, this nucleation delay can be almost completely eliminated when an $O_2$ plasma is used instead of $O_2$ gas [164], as shown in Fig. 2.12. The plasma-assisted step makes the ALD process and thickness control more reliable, while also reducing the consumption of an expensive Pt precursor. Furthermore, when a (seed) layer of Pt has been deposited by plasma-assisted ALD, the thermal process can be continued without disruption in the thickness increment per cycle (see Fig. 2.12). Another interesting feature of the plasma-assisted ALD process is that $PtO_2$ films can also be deposited using the same precursor and an $O_2$ plasma, the only difference (compared to the plasma-assisted ALD of Pt) being the plasma exposure time. Pt can be deposited using short plasma exposure times, whereas relatively long plasma exposure times yield $PtO_2$. For the process reported on in Fig. 2.12, these exposure times are 0.5 and 5.0 s, respectively. The GPC for $PtO_2$ is very similar to that for Pt (see Fig. 2.12) even though the number of Pt atoms per cycle is lower. So far the only thermal ALD process for $PtO_x$ that has been reported was based on a combination of $Pt(acac)_2$ and $O_3$, and was restricted to the small temperature window of 120-130 °C [335].

Another material from the Pt-group for which the nucleation delay can be reduced by the plasma-assisted process is Ru. Results obtained using $Ru(Cp^{Et})_2$ as a precursor and a $NH_3$ plasma as the reactant, for example, are reported in the literature quite extensively [165-176]. Pure and smooth films with a low resistivity were deposited with substrate-dependent growth rates and nucleation delays ($\sim$20 cycles for TiN and almost none for $SiO_2$). $NH_3$ gas is not reactive with the precursor and the thermal ALD process does not result in film growth. However, $O_2$ gas can be used for thermal ALD of Ru and results in growth rates that are up to 4 times higher compared to the plasma-assisted ALD process with $NH_3$ plasma as the reactant [166, 173]. Ru films were also deposited by employing $O_2$ gas and an $O_2$ plasma as the reactant in deposition processes using $RuCp(CO)_2Et$ [179]. These processes revealed fairly high growth rates of $\sim$1 nm/cycle after nucleation delay of $\sim$45 cycles and $\sim$85 cycles for plasma-assisted ALD and thermal ALD, respectively. The surface roughnesses were, however, somewhat higher than for the $NH_3$

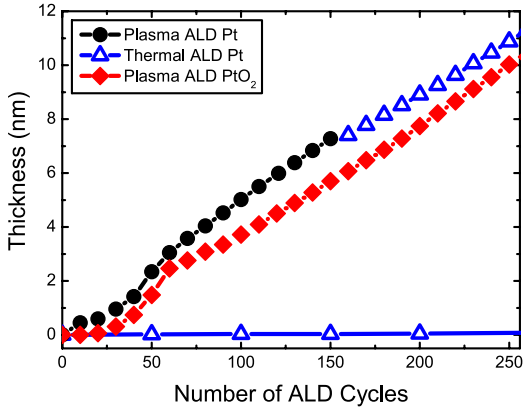



**Figure 2.12:** Thickness evolution of Pt and $PtO_2$ films deposited on an $Al_2O_3$ substrate [164]. The precursor was $Pt(Cp^{Me})Me_2$ and $O_2$ gas or an $O_2$ plasma were used as the oxidants. After 150 cycles, the plasma-assisted ALD process was stopped and film growth was continued using thermal ALD. The plasma exposure time for was 0.5 s for Pt and 5 s for $PtO_2$. *From H.C.M. Knoops et al., Electrochem. Solid-State Lett.* ***12****, G35, (2009). Reproduced with permission of ECS - The Electrochemical Society.*

plasma process. Besides the nucleation properties and the growth rate, the choice of the reactant can also depend on the other layers in the structure. $O_2$ gas or an $O_2$ plasma can oxidize a surface whereas the use a $NH_3$ plasma could lead to reduction and even nitridation of the surface [175].

## 2.5 Challenges of Plasma-Assisted ALD

Although plasma-assisted ALD can offer several benefits over thermal ALD for selected applications, the method also faces a number of challenges when compared to its thermal counterpart.

One limitation of plasma-assisted ALD that is often highlighted is the *reduced conformality* or *step coverage* that can be achieved on non-planar substrates. These can be substrates with surface structures of high aspect ratio (e.g. wafers with trenches or vias) or substrate materials with very high surface areas (e.g. porous materials and stacked particles). Thermal ALD is known to be the method of choice for depositing conformal thin films on such substrates, as film growth is self-limiting and independent of the precursor flux when the conditions are such that saturation of the ALD (half-) reactions is reached. The difference between plasma-assisted and thermal ALD, in this respect, is

that plasma-assisted ALD involves reactive species that not only undergo ALD reactions (as in thermal ALD) but can also react on saturated surface sites. As mentioned in Sec. 2.2, radicals from the plasma can react with other radicals and species residing at the surface, forming non-reactive molecules that desorb back into the plasma. In the case of high-aspect-ratio structures or porous materials, the radicals have to undergo several surface collisions in order to reach deep inside the surface features, which significantly reduces the local flux of the radicals due to the surface recombination. This has only recently been addressed qualitatively by simulations and experimentally [42, 304, 336, 337]. In many other reports, the impact of the surface recombination of plasma radicals is generalized and the poor conformality of plasma-assisted ALD films is often claimed. However, the conformality achieved by plasma-assisted ALD under certain conditions depends strongly on the value of the recombination probability, $r$, which itself depends on (a) the type of radicals responsible for film growth in a certain plasma-assisted ALD process and (b) the material being deposited (see Table 2.2). Note that the surface temperature can also affect the value of $r$, for example, a significant temperature dependence was reported for oxygen radicals on silica [305], whereas the temperature dependence of H radicals on metals was less prominent [306]. The influence of the value of $r$ can be illustrated by the results obtained from simple two-dimensional Monte Carlo simulations, in which the evolution of the deposition profile within a trench of high aspect ratio was studied as a function of the incoming radical flux [304, 337]. This was achieved by considering only the plasma exposure step during a single ALD cycle. The information on the deposition profile at the side wall of the trench was derived from the number of ALD growth events as a function of the side wall position. For $r > 0$, it was found that the deposition profiles showed a minimum thickness at the region just above the bottom of the trench (see Fig. 2.13a) and this minimum was more pronounced for larger values of $r$. The deposition profiles were clearly distinguishable from the cases in which the conformality was reaction-limited or diffusion-limited (see Fig. 2.13a) [338]. Therefore, in addition to these limiting cases (which are also observed for thermal ALD) a new recombination-limited regime was distinguished for the case of plasma-assisted ALD [304]. In order to achieve conformal deposition while in this recombination-limited regime, a longer plasma exposure time has to be employed. Compared to the case where $r = 0$, the dose required for saturation increases considerably when increasing the value of $r$, especially for high aspect ratios. The latter is illustrated in Fig. 2.13b for aspect ratios of 10 and 30 and for $r$ values ranging from 0.01 to 0.3. The "sticking" probability of the radicals on unreacted surface sites was assumed to be 0.01. From the figure it is clear that for the smaller $r$ values and reasonable aspect ratios ($\leq$10), conformal deposition can

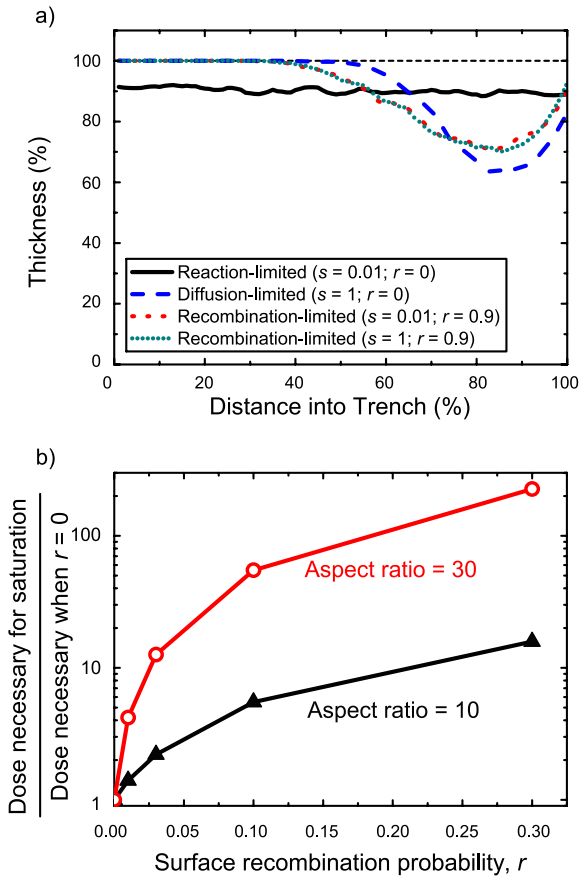



**Figure 2.13:** Results from Monte Carlo simulations to investigate the influence of surface recombination of radicals during plasma-assisted ALD [304]. (a) Equivalent thickness profile in a trench of aspect ratio 10 for different deposition regimes, obtained for various combinations of values for the sticking probability, $s$, and surface recombination probability, $r$. The positions within the trench labeled 0% and 100% correspond to the trench opening and trench bottom, respectively. Note that both recombination-limited cases show almost perfect overlap. (b) The dose required to reach saturation in trenches with aspect ratios of 10 and 30 for non-zero values of $r$. This dose is normalized to the dose required to reach saturation in these trenches when $r = 0$. For the simulations $s = 0.01$ was assumed. *From H.C.M. Knoops et al., J. Electrochem. Soc.* ***157****, G241-G249 (2010). Reproduced with permission of ECS - The Electrochemical Society.*

still be achieved relatively easily by increasing the plasma exposure time by, for example, up to 10 times longer than that required for a planar substrate. However, for very high aspect ratios (e.g. $\geq$30) plasma exposure times are necessary that are practically unfeasible. Consequently, because most current applications have reasonable aspect ratios, it can be concluded that in many practical cases, conformal deposition in high-aspect-ratio structures can certainly be achieved by plasma-assisted ALD. This is also confirmed by the results obtained for several metal oxides where the $r$ values of oxygen radicals are known to be relatively low [60, 199, 200, 210, 246, 339, 340]. For other cases, such as metals, the $r$ values of radicals are relatively high. This makes it very difficult or even impossible to achieve a good conformality, especially for aspect ratios >10. Finally, it should be noted that thermal ALD processes can also be subject to surface recombination losses of reactant species. For example, for some materials, $O_3$ also has considerable (non-zero) $r$ values, which generally increase with surface temperature [341, 342]. In this case, conformal film growth might also be recombination-limited [304, 341].

A second limitation of plasma-assisted ALD that can have an important effect on certain applications can be described as *plasma-induced damage*. During the plasma step of the ALD cycle, the deposition surface is exposed to a multitude of reactive species from the plasma that can also induce undesired surface reactions, including oxidation and nitridation of the top surface layers of the substrate [27, 62, 175]. In the case of (enhanced) surface oxidation, the interaction of oxygen atoms with the substrate during the initial ALD cycles can result in a (thicker) interfacial oxide, for example, when metal oxides are deposited on silicon (see also Sec. 2.6.2) [343]. Nitridation can take place when using $N_2$- or $NH_3$-based plasmas to deposit metal nitrides [238]. Note that nitridation is often also employed on purpose, for example, to increase the stability or the relative permittivity ($k$-value) of oxides [32, 91, 119, 129, 143, 209]. Plasma-induced damage can also manifest itself by the formation of defects inside the material or at the surface onto which the film is deposited. The bombardment of the substrate by energetic ions, accelerated in the plasma sheath, can lead to bond-breaking, displacement of atoms in the surface region and charge accumulation on dielectric layers [344, 345]. Such ion bombardment effects are particularly important during plasma-activated processes, such as reactive ion etching, where the substrate is negatively biased to give the incoming ions kinetic energies of up to several hundreds of eV [299, 300]. During plasma-assisted ALD the ion energies are typically much lower due to grounding of the substrate stage and/or the high pressures employed (i.e. when the plasma sheath is collisional), meaning that they are typically below the damage threshold (e.g. the atom displacement threshold) and cannot cause significant defect creation (also see Chapters 4 and 5). However, there is

still a significant possibility that ion bombardment may be of influence because the performance of most semiconductor devices, in which the ultra-thin ALD-synthesized films are employed, is strongly affected by their interface properties. The influence of ion bombardment was illustrated by a study in which the material properties of $HfO_2$ films deposited in a remote plasma and a direct plasma reactor were compared [124, 125]. The films deposited in the remote plasma reactor were amorphous, but showed better interface properties than the polycrystalline $HfO_2$ films deposited in the direct plasma reactor. Consequently, the electrical properties of the films, such as dielectric constant, fixed oxide charge density, and carrier mobility were superior for the remote plasma case. As exemplified by this study, the influence of plasma damage is more likely when the flux of ions is considerable, such as in direct plasma-assisted ALD. Another often neglected, but in many cases even more important, mechanism is defect creation by plasma radiation (also see Chapter 5). As mentioned earlier, a significant amount of ultraviolet (UV) radiation is formed in plasmas, the energy of which can reach up to 10 eV. Oxides, such as $SiO_2$ as well as the high-*k* oxides, have band gap values smaller than 9 eV, meaning that vacuum ultraviolet (VUV) radiation can create defects, for example, by photoemission or photoinjection of charge. Plasma-induced defect creation has been studied in great detail for the plasma processing of $SiO_2$-based gate stacks [299, 300, 346-349] and the influence of VUV exposure has also recently been studied for the high-*k* oxide $HfO_2$ [299, 300, 344, 350-352]. However, this damage mechanism has not really been highlighted for plasma-assisted ALD processes, for example, during the synthesis of metal oxides by plasma-assisted ALD itself or when depositing other materials (such as electrode materials) on top of high-*k* oxides by plasma-assisted ALD. Note that, apart from the fact that the metal oxide film might itself be affected, the interfacial $SiO_x$ layer, which is typically present (either unintentionally or prepared on purpose) between the metal oxide and the Si substrate, can also be affected. From experiments (see Fig. 2.14a), it has recently been demonstrated that the surface passivation of crystalline Si by as-deposited $Al_2O_3$ is strongly affected by defects generated by VUV photons from the $O_2$ plasma (photon energy of 9.5 eV, see Fig. 2.6) [43, 303]. To illustrate that VUV radiation is responsible for the degradation in surface passivation, a silicon wafer coated with thermal ALD-deposited $Al_2O_3$ (30 nm in thickness) was exposed to an $O_2$ plasma through 5.0 mm quartz and $MgF_2$ windows covering the sample which would either block or transmit the 9.5 eV photons, respectively. The results, which are presented in Fig 2.14b, demonstrate that no degradation in lifetime is observed when the VUV radiation was blocked by the quartz window. However, for the exposure through the $MgF_2$ window, the lifetime degraded with a rate equal to that obtained when no window was used (after correcting for the $\sim$60

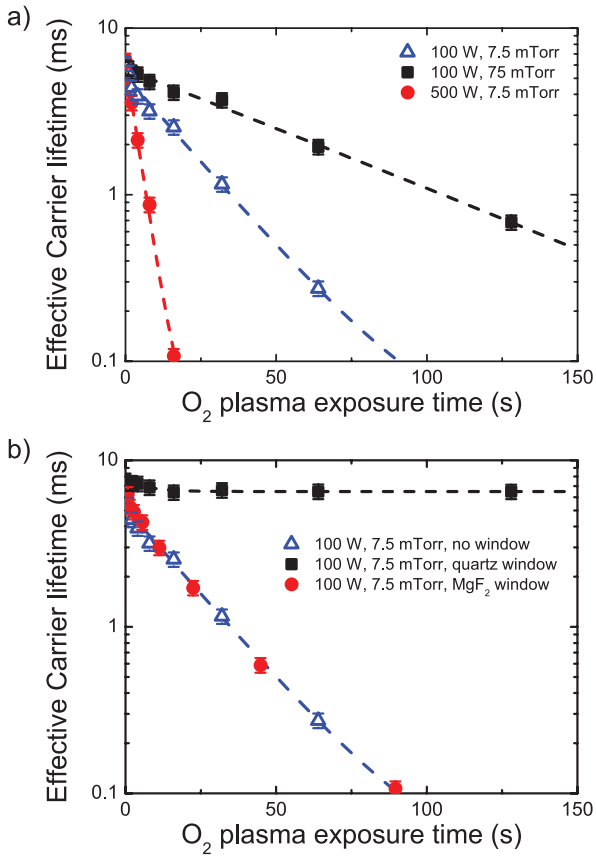



**Figure 2.14:** Experiments proving that VUV radiation from the plasma affects the surface passivation of crystalline Si by $Al_2O_3$ when deposited by plasma-assisted ALD [43, 303]. After annealing, the wafers were exposed to an $O_2$ plasma for various exposure times. (a) The effective charge carrier lifetimes degraded for increasing exposure times at a rate which increased with increasing VUV radiation present in the plasma (higher intensity for higher power and/or lower pressure). (b) Results are also given for the situation in which the substrate is covered by quartz and $MgF_2$ windows that respectively block and do not block the VUV photons of 9.5 eV. *From H.B. Profijt et al., ECS Trans.* ***33****, 61 (2010). Reproduced with permission of ECS - The Electrochemical Society.*

% transmittance of the $MgF_2$ window at 130.5 nm wavelength). The photons emitted by the $O_2$ plasma during plasma-assisted ALD induce a very high interface defect density, $D_{it}$, of $D_{it} \approx 10^{12}$ $eV^{-1}cm^{-2}$ at the mid-gap, such that extremely high surface recombination velocities of $10^7$ cm/s were obtained [43]. However, most of these surface defects can be removed by annealing the films for 10 min at 400 °C in $N_2$ ($D_{it}$ reduced to $\sim 10^{11}$ $eV^{-1}cm^{-2}$), such that excellent surface recombination velocities, as low as 1 cm/s, can be achieved on low-resistivity float-zone Si. These surface recombination velocities correspond to a surface passivation quality not yet paralleled by any other material [323]. On the other hand, as-deposited $Al_2O_3$ synthesized by thermal ALD affords reasonably low surface recombination velocities, as the films are not exposed to VUV radiation from a plasma (despite this fact, the level of surface passivation after annealing is not as good as for $Al_2O_3$ synthesized with by plasma-assisted ALD) [43]. Furthermore, it has been demonstrated that the level of surface passivation by as-deposited $Al_2O_3$ synthesized by plasma-assisted ALD can be increased by decreasing the length of the plasma exposure step, in this case, by using slightly sub-saturated ALD conditions [43].

The aforementioned challenges for plasma-assisted ALD are inherent to the plasma-surface interaction that takes place during the plasma step. To assess their possible impact on the potential applications of the plasma-assisted ALD method, a deeper investigation of the underlying surface processes, including the plasma-surface interaction, is required in order to establish whether they lead to problems for the specific applications considered. Another class of challenges is related to the development of equipment and the *industrial scale-up of the process*. The use of plasma steps during ALD cycles requires more complex equipment than that used for thermal ALD. Unless this additional complexity is compensated for by the significant advantages of plasma-assisted ALD, thermal ALD will be the method of choice. For research and development (R&D), the interest in plasma-assisted ALD equipment is hardly or not affected, as R&D equipment is required to directly compare the results obtained by plasma and thermal ALD. This is evidenced by the fact that several combined plasma and thermal ALD tools have recently been introduced onto the market. However, for industrial scale-up the situation is different. Here, plasma-assisted ALD will only be adopted when it provides major benefits over thermal ALD and when alternative deposition techniques are not available for the specific applications envisioned. The latter situation is currently prominent in the field of crystalline silicon photovoltaics, where, at the moment, mainly thermal ALD is considered by equipment manufacturers for the scale-up of $Al_2O_3$ deposition [18, 353-355], despite the fact that plasma-assisted ALD can provide significant benefits over thermal ALD in this case [356].

## 2.6 Selected Applications

In the literature a number of applications have been suggested for thin films synthesized by plasma-assisted ALD. In the semiconductor industry these applications vary from the so-called "back-end-of-line", the level in IC fabrication where individual device components are interconnected, to the "so-called" front-end-of-line, the level where the individual device components are created in and on the silicon. Over the last few years, also the application of the films as barrier and protection layers has gained significant interest.

### 2.6.1 Back-end-of-line processing

Although the first time that a plasma was used in an ALD process dates back to 1991, the research on plasma-assisted ALD primarily started around 2000, when major thin film challenges in the back-end-of-line processing were foreseen. At that time the replacement of Al by Cu as the interconnect material was imminent and plasma-assisted ALD processes for the deposition of Ta and Ti liners were developed [206]. Such liner materials became necessary to prevent Cu diffusion into the low-k dielectric and to promote the adhesion of Cu to the diffusion barrier layer [357]. For this application, typically a stack of materials, such as TaN/Ta or TiN/Ti, needs to be employed and these materials need to be deposited in the trenches and vias before filling them with Cu. Therefore, in addition to the good barrier and adhesion properties, other requirements for the liner materials include a high conformality of the films in nanoscale structures, a deposition temperature compatible with back-end-of-line processing ($\leq$400 °C), as well as a high chemical and thermal stability. Also the resistivity should be low to keep the total resistance of the interconnects as low as possible and to allow for metal layers to be connected through the barrier layers. In particular cases, a low-resistivity barrier and adhesion layer could also simultaneously act as a seed-layer for the electrochemical deposition process of Cu [161, 166, 180-183, 220, 240].

Triggered by these challenges, Rossnagel and co-workers at IBM developed plasma-assisted ALD processes of Ta and Ti using the metal-halides $TiCl_4$ and $TaCl_5$ as precursors and an $H_2$ plasma as a reducing agent [206]. As mentioned in Sec. 2.4, no thermal ALD processes exist for these metals, but the deposition of Ta and Ti films by plasma-assisted ALD was successful (see Fig. 2.15). As a follow-up of this work, the IBM group, as well as others, also developed plasma-assisted ALD processes for other liner materials, including the metal-nitrides TaN and TiN. The development of these processes was intended to facilitate the switching from metal-halide precursors to metal-organic precursors (e.g., $Ta(NMe_2)_5$, $Ta(N^tBu)(NEt_2)_3$, $Ti(NMe_2)_4$ to name a few) due to com-

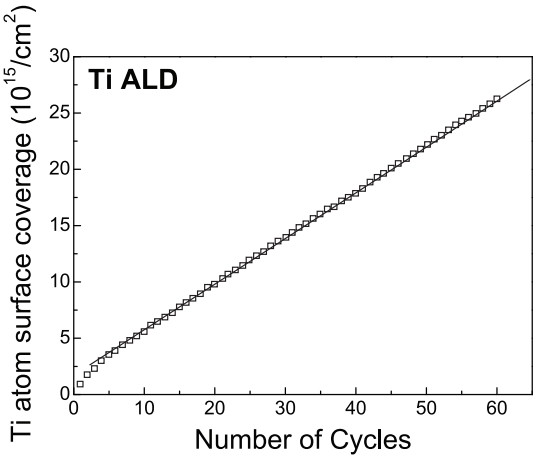



**Figure 2.15:** Surface coverage of Ti atoms as a function of the number of ALD cycles, as measured by a quartz crystal micro-balance at room temperature [232]. The precursor employed was $TiCl_4$ and the reactant was an $H_2$ plasma. For deposition on the as-received crystal, the growth showed a linear trend after ∼5 cycles. *Reprinted with permission from H. Kim et al., J. Vac. Sci. Technol. A **20**, 802 (2002). Copyright 2002 American Vacuum Society.*

patibility issues of the former, caused by halide impurities in the films. The plasmas employed were typically generated in $H_2$, $H_2/N_2$ and $NH_3$. Research on a combined Cu diffusion barrier and Cu seed layer triggered the development of plasma-assisted processes of refractory metals, most prominently Ru, e.g. from $Ru(Cp^{Et})_2$ as the precursor and an $NH_3$ plasma as the reactant [165-174]. A comprehensive overview of the metal and metal nitride films deposited by (plasma-assisted) ALD for Cu interconnect applications can be found in the review paper by Kim [328].

The suitability of plasma-assisted ALD-deposited Ta, TaN, Ti and TiN films as diffusion barriers was investigated and reported in a number of articles [175, 204, 219, 222, 225, 226]. In an early report, Kim *et al.* demonstrated that the barrier films should preferably be amorphous, in order to avoid Cu leakage along the grain boundaries [226, 357]. They demonstrated that plasma-assisted ALD Ta films showed superior Cu diffusion barrier properties compared to their PVD counterpart, especially for thicknesses below 10 nm, due to the amorphous structure of the films [204]. For TaN films deposited by plasma-assisted ALD and PVD, a similar performance was found with both materials basically showing the same barrier failure temperatures as a function of thickness [219]. These results are summarized in Fig. 2.16. For a process involving the metal-organic

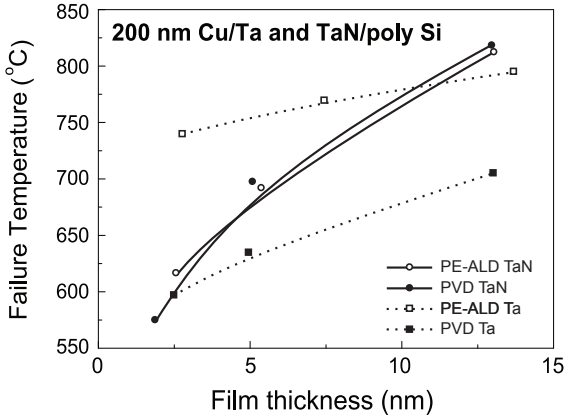



**Figure 2.16:** Barrier failure temperatures for TaN and Ta films deposited by PVD and plasma-assisted ALD [204, 219]. After deposition the TaN and Ta layers were capped by 200 nm thick Cu films using the PVD technique. Barrier failure temperatures were determined by monitoring the disappearance of the Cu (111) peak by X-ray diffraction measurements. The ALD films were deposited using an $H_2/N_2$ plasma for TaN and an $H_2$ plasma for Ta. *From H. Kim et al., J. Appl. Phys.* ***95****, 5848-5855 (2004). Reprinted with permission. Copyright 2004, American Institute of Physics.*

precursor $Ta(NMe_2)_5$ and a $N_2$ plasma, it was demonstrated that TaN films of only 0.6 nm thick possessed a barrier failure temperature of > 800°C [226]. This temperature is one of the higher values reported with the enhancement in diffusion barrier properties being mostly attributed to an increased nitrogen content in the film.

Another interesting issue addressed by Kim *et al.*, is the fact that the barrier material should not penetrate into the porous low-*k* dielectric layer. Therefore, penetration of TaN during deposition with thermal and plasma-assisted ALD using $Ta(NMe_2)_5$ as the precursor and $NH_3$ or an $H_2/N_2$ plasma as reactants was investigated [357]. For the thermal ALD case, the TaN layer penetrated the porous dielectric material as both the precursor as the reactant species were able to enter the pores and to participate in the ALD growth process. However, for the plasma-assisted case, no evidence of film growth was found deep in the pores. While the precursor is able to travel a significant distance into the pores, the plasma radicals can not, as they will eventually recombine after undergoing several surface collisions [357].

Despite these efforts in the early 2000s, the interest and research on plasma-assisted (and thermal) ALD on liner materials declined after several years. The reason was that continuous improvements in PVD technology for Cu interconnects, for example by ad-

vances in ionized PVD, reduced the need for the adaption of a completely new film technology in the back-end-of-line processing. However, the research on ALD materials for back-end-of-line processing is currently increasing again, as it is inevitable that new thin film technologies will need to be implemented to deal with the challenges presented by future technology nodes [13, 357].

### 2.6.2 Front-end-of-line processing

#### High-*k* dielectric layers

Since the advent of Moore's law, the downscaling of CMOS transistors requires a continuous decrease in the thickness of the gate dielectric. By the end of the 1990s, it was realized that the required thickness of the standard $SiO_2$ layer would eventually be too thin to prevent large leakage currents [358]. This led to an increase in interest, within the semiconductor industry, in ALD of dielectric thin films as a viable alternative to growing $SiO_2$ by thermal oxidation. It resulted in the screening of all kinds of high-*k* dielectrics, especially $HfO_2$ and $ZrO_2$, and associated ALD processes to find a material with a physically higher thickness but a lower equivalent oxide thickness (EOT). Eventually it led to the implementation of ALD-deposited Hf-based oxides in the 45 nm technology node in 2007 [12, 359]. In addition to thermal ALD processes, it also resulted in many investigations of plasma-assisted ALD processes for high-*k* oxides, again putting a considerable effort into $HfO_2$ and related oxides. For example, Park *et al.* demonstrated that a plasma step can be beneficial as it can result in $HfO_2$ films with a higher density, a lower impurity level and a higher interface quality [135]. The films were deposited from $Hf(NEtMe)_4$ with an $O_2$ plasma as the reactant. Compared to thermally-deposited layers, the interface layer was thicker (2.0 nm vs. 1.5 nm, see Fig. 2.17), but because it consisted of Hf-Si-O mixed with $SiO_2$, the total film had a higher *k*-value than the thermal ALD layer with a $SiO_2$ interface layer. Moreover, the leakage current density of the plasma deposited samples was three times lower than that for the thermally deposited samples, but the fixed oxide charge density was higher.

The fact that the availability of a plasma source also offers the possibility to use plasmas *in situ* before, during or after deposition was also exploited. In a number of studies, it was demonstrated that a thin $SiO_2$ layer grown by an $O_2$ plasma pre-treatment can retard the formation of a Hf-silicate interface layer, resulting in films with improved *k*-values and related electrical properties [122, 130, 132]. The use of a $CF_4$ plasma for 60 s was also proven to be beneficial prior to the deposition process [141]. Maeng *et al.* reported on interface defect passivation by Si-F bonds resulting in a decrease in the

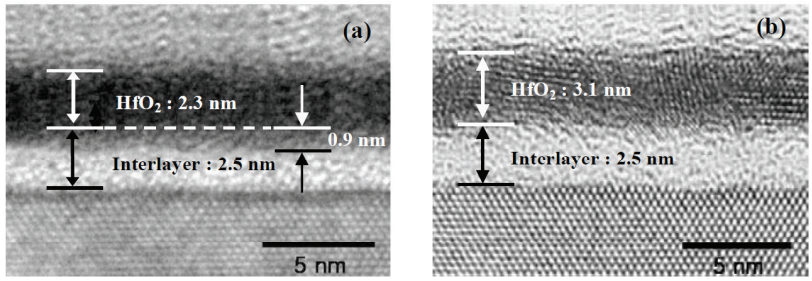



**Figure 2.17:** Cross-sectional high-resolution transmission electron microscopy (HR-TEM) images of as-grown $HfO_2$ films deposited by (a) remote-plasma ALD and (b) direct-plasma ALD [124, 125]. The films were deposited on Si at a deposition temperature of 250 °C using $Hf(NEt_2)_4$ as the precursor and an $O_2$ plasma as the reactant. A gradual transition from the interface layer to the $HfO_2$ layer can be observed for the remote-plasma ALD film, whereas the film deposited using a direct-plasma shows an abrupt transition. The film deposited using a direct-plasma was partially crystallized, whereas using a remote plasma afforded an amorphous film. *From J. Kim et al., Appl. Phys. Lett.* ***87****, 53108 (2005). Reprinted with permission. Copyright 2005, American Institute of Physics.*

flatband voltage and a lower leakage current density. The deposition of $HfO_2$ on a 1.0 nm thick plasma-nitrided $HfO_2$ or $Al_2O_3$ layer was found to result in a thinner interfacial layer, a lower EOT, a lower leakage current density and a reduced charge defect density [129].

Exploring variations in plasma composition, Lee *et al.* reported a lower fixed oxide charge density when using a $N_2O$ plasma instead of an $O_2$ plasma [134]. Maeng *et al.* observed a slightly higher fixed oxide charge density and interface state charge density when using a $N_2/O_2$ plasma [134, 140]. It was also shown that the use of a $N_2O$ plasma resulted in randomly-oriented polycrystalline films, instead of amorphous films obtained with $N_2O$ gas. Also, the growth per cycle was higher [134]. Maeng *et al.* also reported two different experiments in which a $HfO_xN_y$ layer was incorporated within an $HfO_2$ film by varying the plasma composition during the ALD process [116, 143]. In this case the precursor was $Hf(NMe_2)_4$, whereas the reactant was varied from an $O_2$ plasma to an $H_2$ plasma or an $O_2/N_2$ plasma. The films possessed a higher $k$-value, a lower interface defect density $D_{it}$ and a lower or comparable leakage current density. The latter was attributed to the presence of N-H bonds, which block leakage paths and suppress conduction

band lowering and reduce trap sites [116]. Besides the plasma composition, the reactor choice can also influence the material properties, as already mentioned in Sec. 2.5. Kim *et al.* reported polycrystalline $HfO_2$ films deposited from $Hf(NEt_2)_4$ and an $O_2$ plasma in a direct plasma reactor compared to amorphous films obtained with the same ALD chemistry in a remote plasma [123,125]. In addition to better dielectric properties, MOSFET devices that were prepared using remote-plasma ALD $HfO_2$ showed better interface properties and a lower fixed oxide charge density. The difference in material properties was attributed to the increased physical reactivity of the direct plasma, in terms of ion bombardment (also see Sec. 2.5). On the other hand, a beneficial effect of some (mild) ion bombardment was also demonstrated in a recent study. $HfO_2$ was deposited using $Hf(NEtMe)_4$ and an $O_2$ plasma in a capacitively-coupled remote plasma reactor (see Sec. 2.3) in which the grid between the driven electrode and the substrate carrier was biased. Films deposited with a 30 W bias power resulted in films with a lower EOT and a higher breakdown electric field than those in an unbiased situation [138].

Although the plasma-assisted ALD processes to Hf-based and the many other high-*k* oxides investigated are currently not considered for adaptation into process flows for advanced gate stacks, there are still many research efforts on plasma-assisted ALD of high-*k* oxides ongoing. Several other applications also exist for which high-*k* and other oxides deposited by plasma-assisted ALD are interesting candidates. In particular, the manufacture of high-density capacitors, for which ultrahigh-*k* oxides (e.g. $SrTiO_3$ [195-198]) are being considered [327], might require energy-enhanced ALD processes as certain classes of precursors do not react with $H_2O$ under ALD conditions (see Sec. 2.4) [360].

**Spacer-defined double patterning**

As discussed in the previous sections, plasma-assisted ALD is generally able to deposit thin films at lower temperatures than thermal ALD. In several cases, films of reasonably high quality can even be deposited at temperatures of 100 °C and lower. This merit of plasma-assisted ALD has recently led to a development of high interest to the semiconductor industry. In order to keep up with the future demands of miniaturization, extreme-UV lithography (wavelength = 13.5 nm) is being developed. However, methods such as immersion lithography [361] and double exposure or double patterning [362] are being adopted in the interim to extend the versatility of current lithography methods (wavelength = 193 nm) while allowing for still smaller structures to be defined. Recently an alternative form of double patterning, requiring only one lithography step instead of two, has been developed. This spacer-defined double patterning method, which is being introduced in DRAM manufacturing and which is likely to be introduced in the manufacture

of the next generation of logic devices, employs a low temperature plasma-assisted ALD step [13, 321, 363].

In spacer-defined double patterning, a photoresist layer is deposited and patterned on top of the target layer, as shown in Fig. 2.18. Then, a highly conformal $SiO_2$ spacer layer is deposited directly onto the photoresist pattern. This requires a low temperature plasma-assisted ALD process, as the photoresist is temperature-sensitive. Next, the structure is anisotropically etched and the photoresist is removed, resulting in a patterned layer with narrow spacer features. These then function as a mask for the second anisotropic etching step, in which the pattern is transferred to the target layer. Finally, the $SiO_2$ masking material can be removed. Obviously, the deposition of $\sim$20 nm thick $SiO_2$ layers with an excellent uniformity and deposition temperatures < 100 °C is key in this process. Plasma-assisted ALD is well-suited for this application and is, therefore, an enabling technology for the spacer-defined double patterning method. Several low-temperature plasma-assisted ALD processes of $SiO_2$ have recently been reported [184,186,187]. In the literature, a successful spacer-defined double patterning process was demonstrated for 32 nm half-pitch polysilicon lines [321]. It has also been reported that pre-deposition plasma treatments are useful for further widening of the space between lines and/or to reform the resist shape. Spacer-defined double patterning does not suffer from overlay issues, which is common for the double patterning technique. High throughputs can be achieved in mini-batch systems which are essentially multi-single-wafer systems [13].

### 2.6.3 Encapsulation

Another promising application of plasma-assisted ALD processes is the encapsulation of polymeric and/or organic devices by thin films. It has been demonstrated that metal oxide films (e.g. $Al_2O_3$ and $TiO_2$) prepared by plasma-assisted ALD can serve as good barrier layers against $H_2O$ and $O_2$ permeation [38,39,54,251,256]. For $Al_2O_3$ it was reported that the material can provide very low water vapor transmission rates for the encapsulation of organic LEDs while also significantly reducing the pinhole density [38, 39, 54]. The advantage of ALD processes for this application is that dense, high quality thin films can be prepared that outperform films prepared by other vapor phase deposition methods (such as PE-CVD and PVD) even when those layers are much thicker [54,364,365]. The main advantage of the plasma-based process is that short cycle times can be maintained at low substrate temperatures, including room temperature. Moreover, Langereis *et al.* reported the striking result that, for $Al_2O_3$ films deposited by remote plasma-assisted ALD, the best barrier performance was obtained for films deposited at room temperature

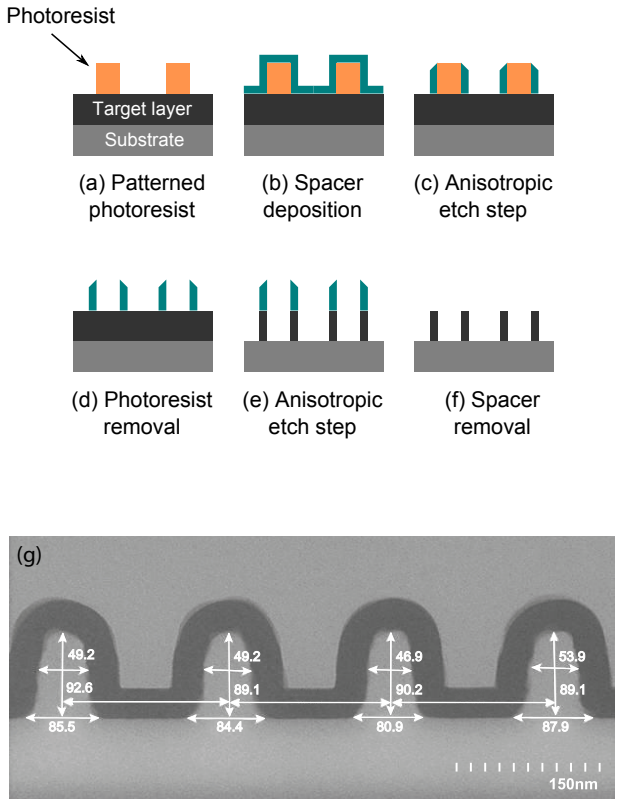



**Figure 2.18:** The spacer-defined double patterning process [321], in which (a) a photoresist layer is deposited on top of the target layer (i.e. the layer to be patterned) and patterned by UV exposure and photoresist development. In the next step (b) a $SiO_2$ spacer layer is deposited at a low temperature using plasma-assisted ALD, after which an anisotropic etch is carried out. Subsequently, the photoresist is removed in step (d) after which the pattern can be transferred into the target layer. Finally, in step (f) the $SiO_2$ spacers are removed, after which narrow features at half-pitch are left. Between steps (a) and (b), an optional plasma-treatment can be carried out in order to additionally reduce the feature thickness of the photo resist. In (g) a scanning-electron microscopy image is shown, illustrating a photoresist pattern covered by a conformal $SiO_2$ spacer layer (corresponding to the situation in (b)). Courtesy of ASM International N.V.

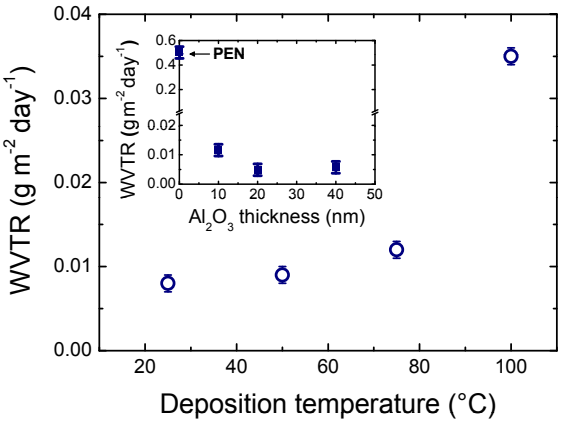



**Figure 2.19:** Water vapor transmission rate (WVTR) of a 20 nm thick $Al_2O_3$ films on poly(2,6-ethylenenaphthalate) (PEN) substrates as a function of the deposition temperature [54]. The $Al_2O_3$ films were deposited by plasma-assisted ALD using $AlMe_3$ as the precursor and an $O_2$ plasma as the reactant. The inset shows the WVTR as a function of the film thickness for a film deposited at room temperature. The WVTR values were determined using a standard calcium test [378] and include water permeation through pinholes which are possibly present. *From E. Langereis et al., Appl. Phys. Lett.* ***89****, 081915 (2006). Reprinted with permission. Copyright 2006, American Institute of Physics.*

(see Fig. 2.19) [54].

A related application of low temperature ALD-synthesized films is the protection of high-precision and high-purity metal parts against corrosion by water (liquid or vapor); acidic, basic or saline solutions; or organic solvents [366-369]. For this application, ultra-thin, dense and defect-free coatings are also desired and, in most cases, they need to be deposited at reduced substrate temperatures to maintain the mechanical properties of the substrates and to reduce the possibility of premature surface oxidation. $Al_2O_3$ is again among the most important candidate materials although for the final application a stack of materials might be required. A recent study revealed that plasma-assisted ALD with an $O_2$ plasma produced $Al_2O_3$ encapsulation layers that showed a better film nucleation and lower porosity than films deposited by thermal ALD using $H_2O$ vapor [65]. For this application, but also for the application of $Al_2O_3$ as an $H_2O$ and $O_2$ barrier, the advantage of plasma-assisted ALD over thermal ALD was most prominent for the thinnest films ($\sim$10 nm) deposited at room temperature. Considering the growing importance of thin film encapsulation and the increasing number of applications of temperature sensitive

materials, plasma-assisted ALD has the potential to become a prominent technology in this field.

## 2.7 Concluding Remarks and Outlook

With the growing need for high quality ultra-thin and conformal films, in and outside the semiconductor industry, the number of applications of ALD will grow substantially in the next decade. As a consequence, the requirements on process conditions and material properties will increase and diversify, requiring new experimental approaches and a variety of ALD equipment configurations. As plasma-assisted ALD can provide some unique merits over the thermal ALD method, it is expected that the interest in this method will also keep growing considerably. This increase in interest is already currently manifested by the number of ALD equipment manufacturers providing dedicated plasma-assisted ALD tools, which has increased significantly in the last few years. The demand for plasma-assisted ALD equipment from industrial R&D laboratories has, in particular, appeared to be high. It is likely that this is fueled by the fact that industrial labs are particularly focused on equipment that provides a high degree of flexibility in combination with a robustness of the equipment and processes. In this respect, plasma-based techniques have been well-accepted in thin film and device manufacturing. Nevertheless, plasma-assisted ALD also faces several challenges. In order to address the question whether and when aspects inherent to the plasma-based process will provide principal limitations for certain applications, a deeper understanding of film growth by plasma-assisted ALD is required. Therefore, more insight into the underlying surface reactions and the role of the plasma-surface interaction needs to be obtained. This is quite a challenging task but, consequently, also an appealing one, considering the complexity of plasma processes. Also of vital importance is that plasma-assisted ALD equipment for high volume manufacturing will be developed and implemented. In the case where (multiple) single wafer reactors are used, the implementation of a plasma source is relatively easy [13]. Recently, however, the first results were presented on plasma-assisted ALD an inline spatial ALD system [66], while also the first results obtained in a multi wafer ALD batch reactor equipped with plasma source were presented [370]. Furthermore, in 2007 a patent was filed on roll-to-roll ALD using an atmospheric plasma [371] by Fuji-Film Manufacturing Europe [372]. Generally for plasma-assisted ALD, it would be best to focus initially on applications for which no alternative deposition techniques exist, or on applications for which the merits of plasma-assisted ALD are substantial and critical. Once established, the method will certainly find more applications and plasma-assisted

ALD will complement existing thin film manufacturing techniques.

## Acknowledgements

The current and past ALD team members of the Eindhoven University are thanked for their contribution to the measurements and the many fruitful discussions. This work was supported financially by the Dutch Technology Foundation STW (Thin Film Nanomanufacturing (TFN) programme) and by the NanoNextNL programme.

## Addendum

This addendum presents updated information (status September 2012) on the number of publications per year on plasma-assisted ALD (see Fig. 2.20), the materials deposited by plasma-assisted ALD (see Fig. 2.21), and the equipment manufacturers providing plasma-assisted ALD tools (see Table 2.4).

In Sec 2.5 it was discussed that reduced conformality on nonplanar substrates is one of the challenges associated with plasma-assisted ALD. Using Monte Carlo simulations, Knoops *et al.* have shown that the conformality of films deposited in structures of high aspect ratio by plasma-assisted depends strongly on the surface recombination probability $r$ [304]. Recently, conformal deposition by plasma-assisted ALD has been reported for an increased number of materials (see Table 2.5).

The various results obtained by modeling and experiments allow for the following "rule of thumb":

- For plasma-assisted ALD of metal oxides (i.e. small $r$), conformal deposition in structures with aspect ratio < 30 is easy
- For plasma-assisted ALD of metals (i.e. high $r$), conformal deposition in structures with aspect ratio > 10 is difficult

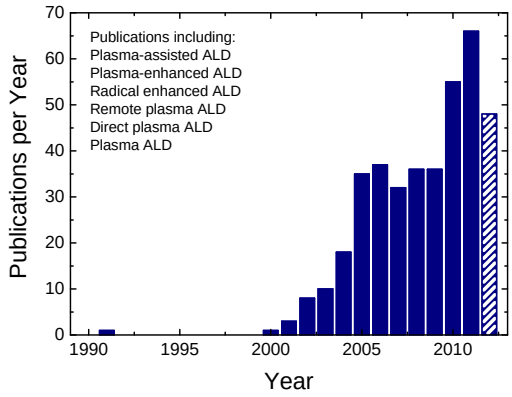



**Figure 2.20:** Number of publications per year on the subject of plasma-assisted ALD, between 1991 and 2012 (status September 2012). The search was run in abstracts using Web of Science® (Ref. 23).

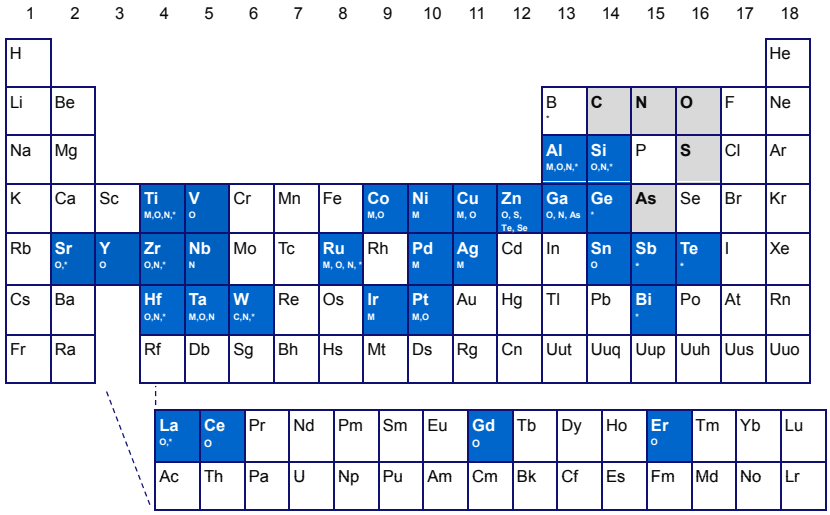



**Figure 2.21:** Periodic table showing the elements (dark background) which have been part of films synthesized by plasma-assisted ALD. "M" means that the pure elements were deposited; compounds with oxygen, nitrogen and other elements are indicated by their symbols ("O", "N", etc.). Asterisks denote ternary or other compounds. The search was run in abstracts using Web of Science® (Ref. 23).)

**Table 2.4:** Equipment manufacturers providing plasma-assisted ALD tools.

| Manufacturer | Type |
|---|---|
| Genitech | Experimental system (2001) |
| ASM | EmerALD (2004) and Stellar (2006) |
| Jusung Engineering | Cyclone (2004) |
| Novellus | INOVA NExT (2005) |
| Oxford Instruments | FlexAL (2006) and OpAL (2008) |
| Beneq TFS 500 (2006) | TFS 200 (2008) |
| Cambridge NanoTech | Fiji (2009) |
| SNTEK | ALD5008 (2010) |
| Tokyo Electron | TELINDY PLUS iRAD SA (2010) |
| Applied Materials | Endura iLB (2011) |
| Picosun | SUNALE (2011) |
| Sentech | Experimental system (2011) |
| SVT-Northstar | ALD-P-200B (2011) |
| NCD Technology | Lucida M (2011) |
| MES AFTY | Experimental system (2011) |
| Kurt J. Lesker | 150LX (2011) |
| Wuxi | MNT-100P (2012) |

**Table 2.5:** Overview of materials deposited by plasma-assisted ALD for which conformal films in high aspect ratios (AR) have been achieved. Data are given only for maximum aspect ratio reported. acac = acetylacetonate, Et = ethyl, Me = methyl, $^{i}$Pr = isopropyl, $^{t}$Bu = tertiary butyl.

| Material | Precursor | Plasma | AR | Ref. |
|---|---|---|---|---|
| $Al_2O_3$ | $AlMe_3$ | $O_2$ | 30 | 379 |
| $SiO_2$ | $SiH(NMe_2)_3$ | $O_2$ | 60 | 380 |
| $SiO_2$ | $Si(NEt_2)_2H_2$ | $O_2$ | 30 | 379 |
| $HfO_2$ | $Hf(NEtMe)_4$ | $O_2$ | 60 | 380 |
| $TaO_2$ | $Ta(OEt)_5$ | $O_2$ | 20 | 380 |
| $TiO_2$ | $Ti(O\,^{i}Pr)_4$ | $O_2$ | 27 | 380 |
| Ag | $Ag(O_2C\,^{t}Bu)(PEt_3)$ | $H_2$ | 9 | 24 |
| Cu | Cu-acac | $H_2$ | 9 | 99 |
| Ta | $TaCl_5$ | $H_2$ | 15 | 204 |
| TaN | $Ta(N\,^{t}Bu)(NEt_2)_3$ | $H_2$ | 10 | 228 |
| TiN | $Ti(NMe_2)_4$ | $NH_3$ | 10 | 244 |

# References


1. S. M. George, A. W. Ott, and J. W. Klaus, J. Phys. Chem. 100, 13121 (1996).
2. S. M. George, Chem. Rev. 110, 111 (2010).
3. C. H. L. Goodman and M. V. Pessa, J. Appl. Phys. 60, R65 (1986).
4. M. Leskelä and M. Ritala, J. Phys. IV 9, Pr8/837 (1999).
5. M. Leskelä and M. Ritala, Thin Solid Films 409, 138 (2002).
6. L. Niinisto, M. Ritala, and M. Leskelä, Mater. Sci. Eng. B 41, 23 (1996).
7. R. L. Puurunen, J. Appl. Phys. 97, 121301 (2005).
8. M. Ritala and M. Leskelä, Nanotechnology 10, 19 (1999).
9. T. Suntola, Mater. Sci. Rep. 4, 261 (1989).
10. S. Haukka, E. L. Lakooma, and T. Suntola, Stud. Surf. Sci. Catal. 120A, 715 (1999).
11. T. Suntola and J. Antson, U.S. Patent No. 4,058,430 (15 November 1977).
12. International Technology Roadmap for Semiconductors, http://www.itrs.net, (May 31, 2011).
13. M. Verghese, J. W. Maes, and N. Kobayashi, Solid State Tech. 53 (2010).
14. Intel website, http://www.intel.com, (May 31, 2011).
15. W. M. M. Kessels, S. E. Potts, H. B. Profijt, and M. C. M. van de Sanden, in "Atomic Layer Deposition of Nanostructures Materials", edited by M. Knez and N. Pinna (Wiley VCH, 2011)
16. ASM International website, http://www.asm.com, (May 31, 2011).
17. Oxford Instruments website, http://www.oxford-instruments.com, (May 31, 2011).
18. Beneq website, http://www.beneq.com, (May 31, 2011).
19. Cambridge NanoTech website, http://www.cambridgenanotech.com, (May 31, 2011).
20. Applied Materials website, http://www.appliedmaterials.com, (May 31, 2011).
21. Tokyo Electron Limited website, http://www.tel.com/, (May 31, 2011).
22. Picosun website, http://www.picosun.com, (May 31, 2011).
23. Web of Knowledge, http://apps.isiknowlegde.com, (May 31, 2011).
24. A. Niskanen, T. Hatanpaa, K. Arstila, M. Leskelä, M. Ritala, Chem. Vap. Dep. 13, 408 (2007).
25. C. W. Jeong, B. I. Lee, and S. K. Joo, Mater. Sci. Eng. C 16, 59 (2001).
26. C. W. Jeong, J. S. Lee, and S. K. Joo, Jpn. J. Appl. Phys. , Part 1 40, 285 (2001).
27. B. H. Kim, W. S. Jeon, S. H. Jung, and B. T. Ahn, Electrochem. Solid-State Lett. 8, G294 (2005).

28. J. Koo, S. Kim, S. Jeon, H. Jeon, Y. Kim, and Y. Won, J. Korean. Phys. Soc. 48, 131 (2006).
29. M. T. Seman, D. N. Richards, P. Rowlette, and C. A. Wolden, Chem. Vap. Dep. 14, 296 (2008).
30. J. W. Lim and S. J. Yun, Jpn. J. Appl. Phys. , Part 2 42, L663 (2003).
31. S. W. Choi, C. M. Jang, D. Y. Kim, J. S. Ha, H. S. Park, W. Koh, and C. S. Lee, J. Korean. Phys. Soc. 42, S975 (2003).
32. J. W. Lim and S. J. Yun, Electrochem. Solid-State Lett. 7, F45 (2004).
33. P. K. Park and S. W. Kang, Appl. Phys. Lett. 89, 192905 (2006).
34. P. K. Park, E. S. Cha, and S. W. Kang, Appl. Phys. Lett. 90, 232906 (2007).
35. J. W. Lim, J. B. Koo, S. J. Yun, and H. T. Kim, Electrochem. Solid-State Lett. 10, J136 (2007).
36. K. Y. Park, H. I. Cho, H. C. Choi, Y. H. Bae, C. S. Lee, J. L. Lee, and J. H. Lee, Jpn. J. Appl. Phys. , Part 2 43, L1433 (2004).
37. S. M. Yoon, S. H. K. Park, C. W. Byun, S. H. Yang, and C. S. Hwang, J. Electrochem. Soc. 157, H727 (2010).
38. S. J. Yun, Y. W. Ko, and J. W. Lim, Appl. Phys. Lett. 85, 4896 (2004).
39. W. S. Kim, D. Y. Moon, B. W. Kang, J. W. Park, and J. G. Park, J. Korean. Phys. Soc. 55, 55 (2009).
40. A. Niskanen, K. Arstila, M. Ritala, and M. Leskelä, J. Electrochem. Soc. 152, F90 (2005).
41. M. Caymax, G. Brammertz, A. Delabie, S. Sioncke, D. Lin, M. Scarrozza, G. Pourtois, W. E. Wang, M. Meuris, and M. Heyns, Microelectron. Eng. 86, 1529 (2009).
42. J. Dendooven, D. Deduytsche, J. Musschoot, R. L. Vanmeirhaeghe, and C. Detavernier, J. Electrochem. Soc. 157, G111 (2010).
43. G. Dingemans, N. M. Terlinden, D. Pierreux, H. B. Profijt, M. C. M. Van de Sanden, and W. M. M. Kessels, Electrochem. Solid-State Lett. 14, H1 (2010).
44. G. Dingemans, R. Seguin, P. Engelhart, M. C. M. van de Sanden, and W. M. M. Kessels, Phys. Status Solidi RRL 4, 10 (2010).
45. J. J. H. Gielis, P. M. Gevers, I. M. P. Aarts, M. C. M. van de Sanden, and W. M. M. Kessels, J. Vac. Sci. Technol. A 26, 1519 (2008).
46. S. B. S. Heil, P. Kudlacek, E. Langereis, R. Engeln, M. C. M. van de Sanden, and W. M. M. Kessels, Appl. Phys. Lett. 89, 131505 (2006).
47. S. B. S. Heil, J. L. van Hemmen, M. C. M. van de Sanden, and W. M. M. Kessels, J. Appl. Phys. 103, 103302 (2008).

48. B. Hoex, S. B. S. Heil, E. Langereis, M. C. M. van de Sanden, and W. M. M. Kessels, Appl. Phys. Lett. 89, 042112 (2006).
49. B. Hoex, J. Schmidt, R. Bock, P. P. Altermatt, M. C. M. van de Sanden, and W. M. M. Kessels, Appl. Phys. Lett. 91, 112107 (2007).
50. B. Hoex, J. Schmidt, P. Pohl, M. C. M. van de Sanden, and W. M. M. Kessels, J. Appl. Phys. 104, 044903 (2008).
51. D. Hoogeland, K. B. Jinesh, F. Roozeboom, W. F. A. Besling, M. C. M. van de Sanden, and W. M. M. Kessels, J. Appl. Phys. 106, 114107 (2009).
52. H. Kim, S. Woo, J. Lee, H. Lee, and H. Jeon, J. Phys. D: Appl. Phys. 43, 505301 (2010).
53. Y. Kim, S. Woo, H. Kim, J. Lee, H. Kim, H. Lee, and H. Jeona, J. Mater. Res. 25, 1898 (2010).
54. E. Langereis, M. Creatore, S. B. S. Heil, M. C. M. Van de Sanden, and W. M. M. Kessels, Appl. Phys. Lett. 89, 081915 (2006).
55. E. Langereis, J. Keijmel, M. C. M. Van de Sanden, and W. M. M. Kessels, Appl. Phys. Lett. 92, 231904 (2008).
56. S. E. Potts, W. Keuning, E. Langereis, G. Dingemans, M. C. M. van de Sanden, and W. M. M. Kessels, J. Electrochem. Soc. 157, 66 (2010).
57. V. R. Rai, V. Vandalon, and S. Agarwal, Langmuir 26, 13732 (2010).
58. S. Sioncke, A. Delabie, G. Brammertz, T. Conard, A. Franquet, M. Caymax, A. Urbanzcyk, M. Heyns, M. Meuris, J. L. van Hemmen, W. Keuning, and W. M. M. Kessels, J. Electrochem. Soc. 156, H255 (2009).
59. N. M. Terlinden, G. Dingemans, M. C. M. van de Sanden, and W. M. M. Kessels, Appl. Phys. Lett. 96, 112101 (2010).
60. J. L. Van Hemmen, S. B. S. Heil, J. H. Klootwijk, F. Roozeboom, C. J. Hodson, M. C. M. Van de Sanden, and W. M. M. Kessels, J. Electrochem. Soc. 154, G165 (2007).
61. H. S. Yun and K. H. Kim, J. Korean. Phys. Soc. 54, 707 (2009).
62. T. O. Kaariainen and D. C. Cameron, Plasma Process. Polym. 6, S237 (2009).
63. K. Lambert, J. Dendooven, C. Detavernier, and Z. Hens, Chemistry of Materials 23, 126 (2011).
64. K. B. Jinesh, J. L. van Hemmen, M. C. M. van de Sanden, F. Roozeboom, J. H. Klootwijk, W. F. A. Besling, and W. M. M. Kessels, J. Electrochem. Soc. 158, G21 (2011).

65. S. E. Potts, L. Schmalz, M. Fenker, B. Diaz, J. Swiatowska, V. Maurice, A. Seyeux, P. Marcus, G. Radnoczi, L. Toth, and W. M. M. Kessels, J. Electrochem. Soc. 158, C132 (2011).
66. P. Poodt, B. Kniknie, A. Branca, H. Winands, and F. Roozeboom, Phys. Status Solidi RRL 5, 165 (2011).
67. O. M. Nayfeh, T. Marr, and M. Dubey, IEEE Electron. Dev. Lett. 32, 473 (2011).
68. A. Ali, H. S. Madan, A. P. Kirk, D. A. Zhao, D. A. Mourey, M. K. Hudait, R. M. Wallace, T. N. Jackson, B. R. Bennett, J. B. Boos, and S. Datta, Appl. Phys. Lett. 97 (2010).
69. Y. H. Kim, J. Moon, C. H. Chung, S. J. Yun, D. J. Park, J. W. Lim, Y. H. Song, and J. H. Lee, IEEE Electron. Dev. Lett. 27, 896 (2006).
70. D. J. Park, J. W. Lim, and B. O. Park, Solid-State Electron. 54, 323 (2010).
71. Y. H. Kim, C. Y. Sohn, J. W. Lim, S. J. Yun, C. S. Hwang, C. H. Chung, Y. W. Ko, and J. H. Lee, IEEE Electron. Dev. Lett. 25, 550 (2004).
72. J. Moon, Y. H. Kim, D. J. Park, C. H. Chung, S. Y. Kang, and J. H. Lee, Solid-State Electron. 54, 1326 (2010).
73. S. Lee and H. Jeon, Electron. Mater. Lett. 3, 17 (2007).
74. Y. J. Lee and S. W. Kang, Thin Solid Films 446, 227 (2004).
75. Y. J. Lee, J. Cryst. Growth 266, 568 (2004).
76. M. Bosund, P. Mattila, A. Aierken, T. Hakkarainen, H. Koskenvaara, M. Sopanen, V. M. Airaksinen, and H. Lipsanen, Appl. Surf. Sci. 256, 7434 (2010).
77. M. Bosund, T. Sajavaara, M. Laitinen, T. Huhtio, M. Putkonen, V. M. Airaksinen, and H. Lipsanen, Appl. Surf. Sci. 257, 7827 (2011).
78. K. H. Kim, N. W. Kwak, and S. H. Lee, Electron. Mater. Lett. 5, 83 (2009).
79. J. W. Lim and S. J. Yun, Electrochem. Solid-State Lett. 7, H33 (2004).
80. J. W. Lim, S. J. Yun, and J. H. Lee, Electrochem. Solid-State Lett. 8, F25 (2005).
81. J. W. Lim, S. J. Yun, and J. H. Lee, Electrochem. Solid-State Lett. 9, F8 (2006).
82. J. W. Lim, S. J. Yun, and H. T. Kim, J. Electrochem. Soc. 154, G239 (2007).
83. J. W. Lim, S. J. Yun, and H. T. Kim, Jpn. J. Appl. Phys. 47, 6934 (2008).
84. J. W. Lim, S. J. Yun, and S. H. Lee, J. Korean. Phys. Soc. 56, 96 (2010).
85. G. J. Choi, S. K. Kim, S. J. Won, H. J. Kim, and C. S. Hwang, J. Electrochem. Soc. 156, G138 (2009).
86. H. B. R. Lee, J. Kim, H. Kim, W. H. Kim, J. W. Lee, and I. Hwang, J. Korean. Phys. Soc. 56, 104 (2010).
87. J. M. Kim, H. B. R. Lee, C. Lansalot, C. Dussarrat, J. Gatineau, and H. Kim, Jpn. J. Appl. Phys. 49, 05FA10 (2010).

88. K. Kim, K. Lee, S. Han, W. Jeong, and H. Jeon, J. Electrochem. Soc. 154, H177 (2007).
89. K. Kim, K. Lee, S. Han, T. Park, Y. Lee, J. Kim, S. Yeom, and H. Jeon, Jpn. J. Appl. Phys. , Part 2 46, L173 (2007).
90. H. B. R. Lee and H. Kim, Electrochem. Solid-State Lett. 9, G323 (2006).
91. H. B. R. Lee, J. Y. Son, and H. Kim, Appl. Phys. Lett. 90, 213509 (2007).
92. K. Lee, K. Kim, T. Park, H. Jeon, Y. Lee, J. Kim, and S. Yeom, J. Electrochem. Soc. 154, H899 (2007).
93. K. Lee, K. Kim, H. Jeon, Y. Lee, J. Kim, and S. Yeom, J. Korean. Phys. Soc. 50, 1141 (2007).
94. M. E. Donders, H. C. M. Knoops, M. C. M. van de Sanden, W. M. M. Kessels, and P. H. L. Notten, J. Electrochem. Soc. (2011).
95. H. B. R. Lee, G. H. Gu, J. Y. Son, C. G. Park, and H. Kim, Small 4, 2247 (2008).
96. H. B. R. Lee and H. Kim, J. Cryst. Growth 312, 2215 (2010).
97. L. Wu and E. Eisenbraun, J. Vac. Sci. Technol. B 25, 2581 (2007).
98. L. Wu and E. Eisenbraun, Electrochem. Solid-State Lett. 11, H107 (2008).
99. L. Wu and E. Eisenbraun, J. Electrochem. Soc. 156, H734 (2009).
100. A. Niskanen, A. Rahtu, T. Sajavaara, K. Arstila, M. Ritala, and M. Leskelä, J. Electrochem. Soc. 152, G25 (2005).
101. D. Y. Moon, W. S. Kim, T. S. Kim, B. W. Kang, J. W. Park, S. J. Yeom, and J. H. Kim, J. Korean. Phys. Soc. 54, 1330 (2009).
102. C. Jezewski, W. A. Lanford, C. J. Wiegand, J. P. Singh, P. I. Wang, J. J. Senkevich, and T. M. Lu, J. Electrochem. Soc. 152, C60 (2005).
103. D. Y. Moon, D. S. Han, S. Y. Shin, J. W. Park, B. M. Kim, and J. H. Kim, Thin Solid Films 519, 3636 (2011).
104. T. T. Van and J. P. Chang, Appl. Surf. Sci. 246, 250 (2005).
105. G. X. Liu, F. K. Shan, W. J. Lee, G. H. Lee, I. S. Kim, and B. C. Shin, Integr. Ferroelec. 85, 155 (2006).
106. G. X. Liu, F. K. Shan, W. J. Lee, B. C. Shin, S. C. Kim, H. S. Kim, and C. R. Cho, Integr. Ferroelec. 94, 11 (2007).
107. N. J. Seong, S. G. Yoon, and W. J. Lee, Appl. Phys. Lett. 87, 082909 (2005).
108. N. J. Seong, E. T. Kim, and S. G. Yoon, Integr. Ferroelec. 74, 181 (2005).
109. F. K. Shan, G. X. Liu, W. J. Lee, G. H. Lee, I. S. Kim, and B. C. Shin, J. Appl. Phys. 98, 023504 (2005).
110. F. K. Shan, G. X. Liu, W. J. Lee, G. H. Lee, I. S. Kim, and B. C. Shin, Integr. Ferroelec. 80, 197 (2006).

111. M. De Keijser and C. Van Opdorp, Appl. Phys. Lett. 58, 1187 (1991).
112. G. X. Liu, F. K. Shan, J. J. Park, W. J. Lee, G. H. Lee, I. S. Kim, B. C. Shin, and S. G. Yoon, J. Electroceram. 17, 145 (2006).
113. J. Lee, S. Choi, C. Lee, Y. Kang, and D. Kim, Appl. Surf. Sci. 253, 3969 (2007).
114. B. J. Choi, S. Choi, T. Eom, S. W. Ryu, D. Y. Cho, J. Heo, H. J. Kim, C. S. Hwang, Y. J. Kim, and S. K. Hong, Chemistry of Materials 21, 2386 (2009).
115. S. Consiglio, W. X. Zeng, N. Berliner, and E. T. Eisenbraun, J. Electrochem. Soc. 155, H196 (2008).
116. W. J. Maeng, G. H. Gu, C. G. Park, K. Lee, T. Lee, and H. Kim, J. Electrochem. Soc. 156, G109 (2009).
117. E. J. Kim and D. H. Kim, Electrochem. Solid-State Lett. 9, C123 (2006).
118. W. Jeong, Y. Ko, S. Bang, S. Lee, and H. Jeon, J. Korean. Phys. Soc. 56, 905 (2010).
119. J. Choi, S. Kim, J. Kim, H. Kang, H. Jeon, and C. Bae, J. Vac. Sci. Technol. A 24, 900 (2006).
120. S. Choi, J. Koo, H. Jeon, and Y. Kim, J. Korean. Phys. Soc. 44, 35 (2004).
121. H. Hong, S. Kim, S. Woo, H. Kim, H. Kim, W. Jeong, S. Jeon, S. Bang, S. Lfe, and H. Jeon, J. Korean. Phys. Soc. 52, 1114 (2008).
122. H. Kang, S. Kim, J. Choi, J. Kim, H. Jeon, and C. Bae, Electrochem. Solid-State Lett. 9, G211 (2006).
123. I. Kim, S. Kuk, S. Kim, J. Kim, H. Jeon, M. H. Cho, and K. B. Chung, Appl. Phys. Lett. 90, 222101 (2007).
124. J. Kim, S. Kim, H. Kang, J. Choi, H. Jeon, M. Cho, K. Chung, S. Back, K. Yoo, and C. Bae, J. Appl. Phys. 98, 094509 (2005).
125. J. Kim, S. Kim, H. Jeon, M. H. Cho, K. B. Chung, and C. Bae, Appl. Phys. Lett. 87, 053108 (2005).
126. S. Kim, J. Kim, J. Choi, H. S. Kang, H. Jeon, and C. Bae, J. Vac. Sci. Technol. B 24, 1088 (2006).
127. S. Kim, J. Kim, J. Choi, H. Kang, H. Jeon, W. Cho, K. S. An, T. M. Chung, Y. Kim, and C. Bae, Electrochem. Solid-State Lett. 9, G200 (2006).
128. S. Kim, S. Woo, H. Kim, W. Jeong, T. Park, H. Kim, S. B. Kim, and H. Jeon, J. Vac. Sci. Technol. B 25, 1922 (2007).
129. S. Kim, S. Woo, H. Hong, H. Kim, H. Jeon, and C. Bae, J. Electrochem. Soc. 154, H97 (2007).
130. S. Kim, S. Woo, H. Kim, I. Kim, K. Lee, W. Jeong, T. Park, and H. Jeon, J. Korean. Phys. Soc. 52, 1103 (2008).

131. Y. Won, S. Park, J. Koo, S. Kim, J. Kim, and H. Jeon, Appl. Phys. Lett. 87, 262901 (2005).
132. S. Woo, H. Hong, S. Kim, H. Kim, J. Kim, H. Jeon, C. Bae, T. Okada, K. Sawada, and M. Ishida, Jpn. J. Appl. Phys. 47, 6196 (2008).
133. Y. C. Byun, C. H. An, J. Y. Choi, C. Y. Kim, M. H. Cho, and H. Kim, J. Electrochem. Soc. 158, G141 (2011).
134. Y. Lee, S. Kim, J. Koo, I. Kim, J. Choi, H. Jeon, and Y. Won, J. Electrochem. Soc. 153, G353 (2006).
135. P. K. Park, J. S. Roh, B. H. Choi, and S. W. Kang, Electrochem. Solid-State Lett. 9, F34 (2006).
136. S. B. S. Heil, J. L. van Hemmen, C. J. Hodson, N. Singh, J. H. Klootwijk, F. Roozeboom, M. C. M. van de Sanden, and W. M. M. Kessels, J. Vac. Sci. Technol. A 25, 1357 (2007).
137. J. Joo and S. M. Rossnagel, J. Korean. Phys. Soc. 54, 1048 (2009).
138. H. Kim, S. Woo, J. Lee, Y. Kim, H. Lee, I. J. Choi, Y. D. Kim, C. W. Chung, and H. Jeon, J. Electrochem. Soc. 158, H21 (2011).
139. W. S. Kim, S. K. Park, D. Y. Moon, T. S. Kim, B. W. Kang, J. K. Seo, H. D. Kim, and J. W. Park, J. Korean. Phys. Soc. 53, 3334 (2008).
140. W. J. Maeng and H. Kim, J. Electrochem. Soc. 155, H267 (2008).
141. W. J. Maeng, J. Y. Son, and H. Kim, J. Electrochem. Soc. 156, G33 (2009).
142. W. J. Maeng, W. H. Kim, J. H. Koo, S. J. Lim, C. S. Lee, T. Lee, and H. Kim, Appl. Phys. Lett. 96 (2010).
143. W. J. Maeng and H. Kim, Appl. Phys. Lett. 91, 092901 (2007).
144. H. Jeon and Y. Won, Appl. Phys. Lett. 93, 124104 (2008).
145. S. X. Lao, R. M. Martin, and J. P. Chang, J. Vac. Sci. Technol. A 23, 488 (2005).
146. W. J. Maeng and H. Kim, J. Appl. Phys. 104, 064111 (2008).
147. H. Kim, S. Kim, S. Woo, H. Y. Chung, H. Kim, J. Park, and H. Jeon, J. Electrochem. Soc. 155, G299 (2008).
148. J. R. Liu, R. M. Martin, and J. P. Chang, J. Vac. Sci. Technol. A 26, 1251 (2008).
149. D. K. Joo, J. S. Park, and S. W. Kang, Electrochem. Solid-State Lett. 12, H77 (2009).
150. S. W. Kim, S. H. Kwon, S. J. Jeong, J. S. Park, and S. W. Kang, Electrochem. Solid-State Lett. 11, H303 (2008).
151. B. Y. Kim, M. G. Ko, E. J. Lee, M. S. Hong, Y. J. Jeon, and J. W. Park, J. Korean. Phys. Soc. 49, 1303 (2006).

152. E. J. Lee, M. G. Ko, B. Y. Kim, S. K. Park, H. D. Kim, and J. W. Park, J. Korean. Phys. Soc. 49, 1243 (2006).
153. H. Kim, S. Woo, J. Lee, H. Kim, Y. Kim, H. Lee, and H. Jeon, J. Electrochem. Soc. 157, H479 (2010).
154. W. H. Kim, W. J. Maeng, K. J. Moon, J. M. Myoung, and H. Kim, Thin Solid Films 519, 362 (2010).
155. W. S. Kim, S. K. Park, D. Y. Moon, B. W. Kang, H. D. Kim, and J. W. Park, Thin Solid Films 517, 3900 (2009).
156. J. Hinz, A. J. Bauer, and L. Frey, Semicond. Sci. Technol. 25, 045009 (2010).
157. J. Hinz, A. J. Bauer, T. Thiede, R. A. Fischer, and L. Frey, Semicond. Sci. Technol. 25, 075009 (2010).
158. H. B. R. Lee, S. H. Bang, W. H. Kim, G. H. Gu, Y. K. Lee, T. M. Chung, C. G. Kim, C. G. Park, and H. Kim, Jpn. J. Appl. Phys. 49, 05FA11 (2010).
159. K. M. Lee, C. Y. Kim, C. K. Choi, S. W. Yun, J. B. Ha, J. H. Lee, and J. Y. Lee, J. Korean. Phys. Soc. 55, 1153 (2009).
160. J. H. Lee, I. N. Lund, E. T. Eisenbraun, and R. E. Geer, Nanotechnology 22 (2011).
161. N. E. Lay, G. A. T. Eyck, D. J. Duquette, and T. M. Lu, Electrochem. Solid-State Lett. 10, D13 (2007).
162. G. A. Ten Eyck, J. J. Senkevich, F. Tang, D. L. Liu, S. Pimanpang, T. Karaback, G. C. Wang, T. M. Lu, C. Jezewski, and W. A. Lanford, Chem. Vap. Dep. 11, 60 (2005).
163. G. A. Ten Eyck, S. Pimanpang, J. S. Juneja, H. Bakhru, T. M. Lu, and G. C. Wang, Chem. Vap. Dep. 13, 307 (2007).
164. H. C. M. Knoops, A. J. M. Mackus, M. E. Donders, M. C. M. van de Sanden, P. H. L. Notten, and W. M. M. Kessels, Electrochem. Solid-State Lett. 12, G34 (2009).
165. M. G. Ko, W. S. Kim, S. K. Park, H. D. Kim, and J. W. Park, J. Korean. Phys. Soc. 53, 2123 (2008).
166. O. K. Kwon, S. H. Kwon, H. S. Park, and S. W. Kang, J. Electrochem. Soc. 151, C753 (2004).
167. O. K. Kwon, S. H. Kwon, H. S. Park, and S. W. Kang, Electrochem. Solid-State Lett. 7, C46 (2004).
168. S. H. Kwon, O. K. Kwon, J. H. Kim, H. R. Oh, K. H. Kim, and S. W. Kang, J. Electrochem. Soc. 155, H296 (2008).
169. S. S. Yim, M. S. Lee, K. S. Kim, and K. B. Kim, Appl. Phys. Lett. 89 (2006).
170. S. S. Yim, D. J. Lee, K. S. Kim, M. S. Lee, S. H. Kim, and K. B. Kim, Electrochem. Solid-State Lett. 11, K89 (2008).

171. J. Musschoot, Q. Xie, D. Deduytsche, K. De Keyser, D. Longrie, J. Haemers, S. Van den Berghe, R. L. Van Meirhaeghe, J. D'Haen, and C. Detavernier, Microelectron. Eng. 87, 1879 (2010).
172. B. H. Choi, Y. H. Lim, J. H. Lee, Y. B. Kim, H. N. Lee, and H. K. Lee, Microelectron. Eng. 87, 1391 (2010).
173. S. J. Park, W. H. Kim, H. B. R. Lee, W. J. Maeng, and H. Kim, Microelectron. Eng. 85, 39 (2008).
174. Q. Xie, Y. L. Jiang, J. Musschoot, D. Deduytsche, C. Detavernier, R. L. Van Meirhaeghe, S. Van den Berghe, G. P. Ru, B. Z. Li, and X. P. Qu, Thin Solid Films 517, 4689 (2009).
175. S. W. Kim, S. H. Kwon, S. J. Jeong, and S. W. Kang, J. Electrochem. Soc. 155, H885 (2008).
176. S. H. Kwon, O. K. Kwon, J. S. Min, and S. W. Kang, J. Electrochem. Soc. 153, G578 (2006).
177. S. J. Jeong, D. I. Kim, S. O. Kim, T. H. Han, J. D. Kwon, J. S. Park, and S. H. Kwon, J. Nanosci. Nanotechnol. 11, 671 (2011).
178. C. C. Chang and F. M. Pan, J. Electrochem. Soc. 158, G97 (2011).
179. N. Leick, R. O. F. Verkuijlen, E. Langereis, S. Rushworth, F. Roozeboom, M. C. M. van de Sanden, and W. M. M. Kessels, J. Vac. Sci. Technol. A 29, 021016 (2011).
180. D. Greenslit, T. Chakraborty, and E. Eisenbraun, J. Vac. Sci. Technol. B 27, 631 (2009).
181. S. Kumar, D. Greenslit, T. Chakraborty, and E. T. Eisenbraun, J. Vac. Sci. Technol. A 27, 572 (2009).
182. T. K. Eom, S. H. Kim, K. S. Park, S. Kim, and H. Kim, Electrochem. Solid-State Lett. 14, D10 (2011).
183. W. Sari, T. K. Eom, S. H. Kim, and H. Kim, J. Electrochem. Soc. 158, D42 (2011).
184. T. Murata, Y. Miyagawa, Y. Nishida, Y. Yamamoto, T. Yamashita, M. Matsuura, K. Asai, and H. Miyatake, Jpn. J. Appl. Phys. 49, 04DB11 (2010).
185. S. J. Won, S. Suh, M. S. Huh, and H. J. Kim, IEEE Electron. Dev. Lett. 31, 857 (2010).
186. A. Kobayashi, N. Tsuji, A. Fukazawa, and N. Kobayashi, "Temperature dependence of GPC with PE-ALD SiO", in Book of abstracts, 10th International conference on atomic layer deposition, Seoul, Korea, 20 June 2010.
187. J. W. Lim, S. J. Yun, and J. H. Lee, ETRI J. 27, 118 (2005).

188. Y. B. Jiang, N. G. Liu, H. Gerung, J. L. Cecchi, and C. J. Brinker, J. Am. Chem. Soc. 128, 11018 (2006).
189. A. Cacciato, L. Breuil, H. Dekker, M. Zahid, G. S. Kar, J. L. Everaert, G. Schoofs, X. Shi, G. Van den Bosch, M. Jurczak, I. Debusschere, J. Van Houdt, A. Cockburn, L. Date, L. Q. Xa, M. Le, and W. Lee, Electrochemical and Solid State Letters 14, H271 (2011).
190. G. Choi, L. Satyanarayana, and J. Park, Appl. Surf. Sci. 252, 7878 (2006).
191. D. H. Kim, W. S. Kim, S. B. Lee, and S. H. Hong, Sens. Actuators. B 147, 653 (2010).
192. W. Lee, K. Hong, Y. Park, N. H. Kim, Y. Choi, and J. Park, Electron. Lett. 41, 475 (2005).
193. W. Lee, Y. Choi, K. Hong, N. H. Kim, Y. Park, and J. Park, J. Korean. Phys. Soc. 46, L756 (2005).
194. D. H. Kim, J. H. Kwon, M. Kim, and S. H. Hong, J. Cryst. Growth 322, 33 (2011).
195. E. Langereis, R. Roijmans, F. Roozeboom, M. C. M. van de Sanden, and W. M. M. Kessels, J. Electrochem. Soc. 158, G34 (2011).
196. J. H. Ahn, J. Y. Kim, and S. W. Kang, Appl. Phys. Lett. 91, 062910 (2007).
197. J. H. Ahn, S. W. Kang, J. Y. Kim, J. H. Kim, and J. S. Roh, J. Electrochem. Soc. 155, G185 (2008).
198. J. H. Ahn, J. Y. Kim, J. H. Kim, J. S. Roh, and S. W. Kang, Electrochem. Solid-State Lett. 12, G5 (2009).
199. J. H. Lee, Y. J. Cho, Y. S. Min, D. Kim, and S. W. Rhee, J. Vac. Sci. Technol. A 20, 1828 (2002).
200. W. J. Lee, I. K. You, S. O. Ryu, B. G. Yu, K. I. Cho, S. G. Yoon, and C. S. Lee, Jpn. J. Appl. Phys. , Part 1 40, 6941 (2001).
201. W. C. Shin, S. O. Ryu, I. K. You, B. G. Yu, W. J. Lee, K. J. Choi, and S. G. Yoon, J. Electrochem. Soc. 151, C292 (2004).
202. W. J. Lee, W. C. Shin, B. G. Chae, S. O. Ryu, I. K. You, S. M. Cho, B. G. Yu, and B. C. Shin, Integr. Ferroelec. 46, 275 (2002).
203. W. C. Shin, S. O. Ryu, I. K. You, S. M. Yoon, S. M. Cho, N. Y. Lee, K. D. Kim, B. G. Yu, W. J. Lee, K. J. Choi, and S. G. Yoon, Electrochem. Solid-State Lett. 7, F31 (2004).
204. H. Kim, C. Cabral, C. Lavoie, and S. M. Rossnagel, J. Vac. Sci. Technol. B 20, 1321 (2002).
205. H. Kim and S. M. Rossnagel, Thin Solid Films 441, 311 (2003).

206. S. M. Rossnagel, A. Sherman, and F. Turner, J. Vac. Sci. Technol. B 18, 2016 (2000).
207. W. J. Maeng, S. J. Park, and H. Kim, J. Vac. Sci. Technol. B 24, 2276 (2006).
208. W. J. Maeng and H. Kim, Electrochem. Solid-State Lett. 9, G191 (2006).
209. W. J. Maeng, J. W. Lee, J. M. Myoung, and H. Kim, Jpn. J. Appl. Phys. , Part 1 46, 3224 (2007).
210. A. Niskanen, U. Kreissig, M. Leskelä, and M. Ritala, Chem. Mater. 19, 2316 (2007).
211. D. F. Gu, J. Li, S. K. Dey, H. De Waard, and S. Marcus, J. Vac. Sci. Technol. B 24, 2230 (2006).
212. C. Hossbach, S. Teichert, J. Thomas, L. Wilde, H. Wojcik, D. Schmidt, B. Adolphi, M. Bertram, U. Muhle, M. Albert, S. Menzel, B. Hintze, and J. W. Bartha, J. Electrochem. Soc. 156, H852 (2009).
213. M. K. Song and S. W. Rhee, Chem. Vap. Dep. 14, 334 (2008).
214. M. K. Song and S. W. Rhee, J. Electrochem. Soc. 155, H823 (2008).
215. G. H. Cho and S. W. Rhee, Electrochem. Solid-State Lett. 13, H426 (2010).
216. T. J. Park, J. H. Kim, J. H. Jang, K. D. Na, C. S. Hwang, J. H. Kim, G. M. Kim, J. H. Choi, K. J. Choi, and J. H. Jeong, Appl. Phys. Lett. 91, 252106 (2007).
217. Q. Xie, D. Deduytsche, J. Musschoot, R. L. Van Meirhaeghe, C. Detavernier, S. F. Ding, and X. P. Qu, Microelectron. Eng. 88, 646 (2011).
218. H. Kim, A. J. Kellock, and S. M. Rossnagel, J. Appl. Phys. 92, 7080 (2002).
219. H. Kim, C. Lavoie, M. Copel, V. Narayanan, D. G. Park, and S. M. Rossnagel, J. Appl. Phys. 95, 5848 (2004).
220. C. C. Chang, F. M. Pan, and C. W. Chen, J. Electrochem. Soc. 157, G62 (2010).
221. H. S. Chung, J. D. Kwon, and S. W. Kang, J. Electrochem. Soc. 153, C751 (2006).
222. H. C. M. Knoops, L. Baggetto, E. Langereis, M. C. M. van de Sanden, J. H. Klootwijk, F. Roozeboom, R. A. H. Niessen, P. H. L. Notten, and W. M. M. Kessels, J. Electrochem. Soc. 155, G287 (2008).
223. E. Langereis, H. C. M. Knoops, A. J. M. Mackus, F. Roozeboom, M. C. M. Van de Sanden, and W. M. M. Kessels, J. Appl. Phys. 102, 083517 (2007).
224. A. Furuya, H. Tsuda, and S. Ogawa, J. Vac. Sci. Technol. B 23, 979 (2005).
225. Q. Xie, J. Musschoot, C. Detavernier, D. Deduytsche, R. L. Van Meirhaeghe, S. Van den Berghe, Y. L. Jiang, G. P. Ru, B. Z. Li, and X. P. Qu, Microelectron. Eng. 85, 2059 (2008).
226. H. Kim, C. Detavernier, O. Van der Straten, S. M. Rossnagel, A. J. Kellock, and D. G. Park, J. Appl. Phys. 98 (2005).

227. J. S. Park, M. J. Lee, C. S. Lee, and S. W. Kang, Electrochem. Solid-State Lett. 4, C17 (2001).
228. J. S. Park, H. S. Park, and S. W. Kang, J. Electrochem. Soc. 149, C28 (2002).
229. J. Y. Kim, K. W. Lee, H. O. Park, Y. D. Kim, H. Jeon, and Y. Kim, J. Korean. Phys. Soc. 45, 1069 (2004).
230. D. K. Kim, B. H. Kim, H. G. Woo, D. H. Kim, and H. K. Shin, J. Nanosci. Nanotechnol. 6, 3392 (2006).
231. R. Sreenivasan, T. Sugawara, K. C. Saraswat, and P. C. McIntyre, Appl. Phys. Lett. 90, 102101 (2007).
232. H. Kim and S. M. Rossnagel, J. Vac. Sci. Technol. A 20, 802 (2002).
233. K. E. Elers, J. Winkler, K. Weeks, and S. Marcus, J. Electrochem. Soc. 152, G589 (2005).
234. J. D. Kwon and J. S. Park, J. Korean. Phys. Soc. 57, 806 (2010).
235. J. S. Park, S. W. Kang, and H. Kim, J. Vac. Sci. Technol. B 24, 1327 (2006).
236. S. B. S. Heil, E. Langereis, A. Kemmeren, F. Roozeboom, M. C. M. van de Sanden, and W. M. M. Kessels, J. Vac. Sci. Technol. A 23, L5 (2005).
237. S. B. S. Heil, E. Langereis, F. Roozeboom, M. C. M. Van de Sanden, and W. M. M. Kessels, J. Electrochem. Soc. 153, G956 (2006).
238. E. Langereis, S. B. S. Heil, M. C. M. Van de Sanden, and W. M. M. Kessels, J. Appl. Phys. 100, 023534 (2006).
239. F. Greer, D. Fraser, J. W. Coburn, and D. B. Graves, J. Vac. Sci. Technol. A 21, 96 (2003).
240. P. Caubet, T. Blomberg, R. Benaboud, C. Wyon, E. Blanquet, J. P. Gonchond, M. Juhel, P. Bouvet, M. Gros-Jean, J. Michailos, C. Richard, and B. Iteprat, J. Electrochem. Soc. 155, H625 (2008).
241. J. Y. Kim, Y. Kim, and H. Jeon, Jpn. J. Appl. Phys. , Part 2 42, L414 (2003).
242. D. H. Kim, Y. J. Kima, J. H. Park, and J. H. Kim, Mater. Sci. Eng. C 24, 289 (2004).
243. J. Y. Kim, S. Seo, D. Y. Kim, H. Jeon, and Y. Kim, J. Vac. Sci. Technol. A 22, 8 (2004).
244. J. Y. Kim, D. Y. Kim, H. O. Park, and H. T. Jeon, J. Electrochem. Soc. 152, G29 (2005).
245. J. Y. Kim, D. Y. Kim, H. O. Park, and H. Jeon, J. Korean. Phys. Soc. 45, 1639 (2004).
246. N. G. Kubala, P. C. Rowlette, and C. A. Wolden, J. Phys. Chem. C 113, 16307 (2009).

247. N. G. Kubala and C. A. Wolden, Thin Solid Films 518, 6733 (2010).
248. A. Sarkar, S. E. Potts, S. A. Rushworth, F. Roozeboom, M. C. M. van de Sanden, and W. M. M. Kessels, ECS Trans. 33, 385 (2010).
249. G. X. Liu, F. K. Shan, W. J. Lee, and B. C. Shin, J. Korean. Phys. Soc. 50, 1827 (2007).
250. J. J. Park, W. J. Lee, G. H. Lee, I. S. Kim, B. C. Shin, and S. G. Yoon, Integr. Ferroelec. 68, 129 (2004).
251. B. W. Kang, W. S. Kim, C. M. Hwang, D. Y. Moon, J. J. Kim, J. G. Park, and J. W. Park, Jpn. J. Appl. Phys. 49, 08JG05 (2010).
252. C. S. Lee, J. Kim, J. Y. Son, W. Choi, and H. Kim, Appl. Catal. B 91, 628 (2009).
253. C. S. Lee, J. Kim, G. H. Gu, D. H. Jo, C. G. Park, W. Choi, and H. Kim, Thin Solid Films 518, 4757 (2010).
254. Q. Xie, J. Musschoot, D. Deduytsche, R. L. Van Meirhaeghe, C. Detavernier, S. Van den Berghe, Y. L. Jiang, G. P. Ru, B. Z. Li, and X. P. Qu, J. Electrochem. Soc. 155, H688 (2008).
255. J. H. Kim, W. J. Lee, and S. G. Yoon, Integr. Ferroelec. 68, 63 (2004).
256. W. S. Kim, M. G. Ko, T. S. Kim, S. K. Park, Y. K. Moon, S. H. Lee, J. G. Park, and J. W. Park, J. Nanosci. Nanotechnol. 8, 4726 (2008).
257. Y. K. Moon, S. H. Kim, D. Y. Moon, W. S. Kim, and J. W. Park, J. Korean. Phys. Soc. 51, 1732 (2007).
258. H. Y. Jeong, Y. I. Kim, J. Y. Lee, and S. Y. Choi, Nanotechnology 21, 115203 (2010).
259. S. J. Won, S. Suh, S. W. Lee, G. J. Choi, C. S. Hwang, and H. J. Kim, Electrochem. Solid-State Lett. 13, G13 (2010).
260. V. R. Rai and S. Agarwal, J. Phys. Chem. C 113, 12962 (2009).
261. A. Niskanen, K. Arstila, M. Leskelä, and M. Ritala, Chem. Vap. Dep. 13, 152 (2007).
262. H. Y. Jeong, J. Y. Lee, M. K. Ryu, and S. Y. Choi, Phys. Status Solidi RRL 4, 28 (2010).
263. S. Kim, S. L. Brown, S. M. Rossnagel, J. Bruley, M. Copel, M. J. P. Hopstaken, V. Narayanan, and M. M. Frank, J. Appl. Phys. 107, 054102 (2010).
264. J. W. Park, D. Lee, H. Kwon, S. Yoo, and J. Huh, IEEE Electron. Dev. Lett. 30, 739 (2009).
265. J. W. Park, D. Y. Lee, H. Kwon, and S. Yoo, IEEE Electron. Dev. Lett. 30, 362 (2009).
266. W. S. Yang and S. W. Kang, Thin Solid Films 500, 231 (2006).

267. Y. J. Lee and S. W. Kang, Appl. Phys. Lett. 86, 071919 (2005).
268. Y. J. Lee and S. W. Kang, Electrochem. Solid-State Lett. 6, C70 (2003).
269. J. S. Park and S. W. Kang, Electrochem. Solid-State Lett. 7, C87 (2004).
270. J. W. Lim, S. J. Yun, and J. H. Kim, ETRI J. 31, 675 (2009).
271. J. Musschoot, D. Deduytsche, H. Poelman, J. Haemers, R. L. Van Meirhaeghe, S. Van den Berghe, and C. Detavernier, J. Electrochem. Soc. 156, 122 (2009).
272. D. H. Kim, Y. J. Kim, Y. S. Song, B. T. Lee, J. H. Kim, S. Suh, and R. Gordon, J. Electrochem. Soc. 150, C740 (2003).
273. Y. T. Kim and J. H. Park, Phys. Status Solidi A 202, R164 (2005).
274. H. S. Sim, S. I. Kim, H. Jeon, and Y. T. Kim, Jpn. J. Appl. Phys. , Part 1 42, 6359 (2003).
275. T. T. Van and J. P. Chang, Surf. Sci. 596, 1 (2005).
276. J. Hoang, T. T. Van, M. Sawkar-Mathur, B. Hoex, M. C. M. van de Sanden, W. M. M. Kessels, R. Ostroumov, K. L. Wang, J. R. Bargar, and J. P. Chang, J. Appl. Phys. 101, 123116 (2007).
277. T. T. Van and J. P. Chang, Appl. Phys. Lett. 87, 011907 (2005).
278. T. T. Van, J. R. Bargar, and J. P. Chang, J. Appl. Phys. 100, 023115 (2006).
279. T. T. Van, J. Hoang, R. Ostroumov, K. L. Wang, J. R. Bargar, J. Lu, H. O. Blom, and J. P. Chang, J. Appl. Phys. 100, 073512 (2006).
280. S. H. K. Park, C. S. Hwang, H. S. Kwack, J. H. Lee, and H. Y. Chu, Electrochem. Solid-State Lett. 9, G299 (2006).
281. C. R. Kim, C. M. Shin, J. Y. Lee, J. H. Heo, T. M. Lee, J. H. Park, H. Ryu, C. S. Son, and J. H. Chang, Current Appl. Phys. 10, S294 (2010).
282. S. J. Lim, J. M. Kim, D. Kim, C. Lee, J. S. Park, and H. Kim, Electrochem. Solid-State Lett. 13, H151 (2010).
283. D. Kim, H. Kang, J. M. Kim, and H. Kim, Appl. Surf. Sci. 257, 3776 (2011).
284. D. A. Mourey, D. L. A. Zhao, and T. N. Jackson, IEEE Electron. Dev. Lett. 31, 326 (2010).
285. D. A. Mourey, D. A. L. Zhao, J. Sun, and T. N. Jackson, IEEE Trans. Electron Devices 57, 530 (2010).
286. D. L. Zhao, D. A. Mourey, and T. N. Jackson, IEEE Electron. Dev. Lett. 31, 323 (2010).
287. P. C. Rowlette, C. G. Allen, O. B. Bromley, and C. A. Wolden, J. Vac. Sci. Technol. A 27, 761 (2009).
288. P. C. Rowlette, C. G. Allen, O. B. Bromley, A. E. Dubetz, and C. A. Wolden, Chem. Vap. Dep. 15, 15 (2009).

289. J. Y. Kim, S. H. Kim, H. Seo, J. H. Kim, and H. Jeon, Electrochem. Solid-State Lett. 8, G82 (2005).
290. Y. Kim, J. Koo, J. W. Han, S. Choi, H. Jeon, and C. G. Park, J. Appl. Phys. 92, 5443 (2002).
291. S. J. Yun, J. W. Lim, and J. H. Lee, Electrochem. Solid-State Lett. 7, F81 (2004).
292. S. J. Yun, J. B. Koo, J. W. Lim, and S. H. Kim, Electrochem. Solid-State Lett. 10, H90 (2007).
293. S. J. Yun, J. W. Lim, and J. H. Lee, Electrochem. Solid-State Lett. 8, F47 (2005).
294. J. Koo, Y. Kim, and H. Jeon, Jpn. J. Appl. Phys. , Part 1 41, 3043 (2002).
295. Y. Tak and K. Yong, Surface Review and Letters 12, 215 (2005).
296. S. Cho, K. Lee, P. Song, H. Jeon, and Y. Kim, Jpn. J. Appl. Phys. , Part 1 46, 4085 (2007).
297. S. E. Potts, C. J. Carmalt, C. S. Blackman, F. Abou-Chahine, N. Leick, W. M. M. Kessels, H. O. Davies, and P. N. Heys, Inorg. Chim. Acta 363, 1077 (2010).
298. A. Sherman, Patent No. US 5916365 (1996).
299. M. A. Lieberman and A. J. Lichtenberg, Principles of plasma discharges and materials processing, 2nd edition (John Wiley & Sons, New York, 2005).
300. A. Grill, Cold Plasmas in Materials Fabrication: From Fundamentals to Applications (Wiley-IEEE Press, New York, 1994).
301. S. B. S. Heil, F. Roozeboom, M. C. M. van de Sanden, and W. M. M. Kessels, J. Vac. Sci. Technol. A 26, 472 (2008).
302. A. J. M. Mackus, S. B. S. Heil, E. Langereis, H. C. M. Knoops, M. C. M. Van de Sanden, and W. M. M. Kessels, J. Vac. Sci. Technol. A 28, 77 (2010).
303. H. B. Profijt, P. Kudlacek, M. C. M. Van de Sanden, and W. M. M. Kessels, J. Electrochem. Soc. 158, G88 (2011).
304. H. C. M. Knoops, E. Langereis, M. C. M. van de Sanden, and W. M. M. Kessels, J. Electrochem. Soc. 157, G241 (2010).
305. J. C. Greaves and J. W. Linnett, Trans. Faraday Soc. 55, 1346 (1959).
306. B. J. Wood and H. Wise, J. Appl. Chem. 65, 1976 (1961).
307. Y. C. Kim and M. Boudart, Langmuir 7, 2999 (1991).
308. A. D. Tserepi and T. A. Miller, J. Appl. Phys. 75, 7231 (1994).
309. J. Abrefah and D. R. Olander, Surf. Sci. 209, 291 (1989).
310. A. Bouchoule and P. Ranson, J. Vac. Sci. Technol. A 9, 317 (1991).
311. S. F. Adams and T. A. Miller, Plasma Sources Sci. Technol. 9, 248 (2000).
312. M. Mozetic and A. Zalar, Appl. Surf. Sci. 158, 263 (2000).

313. H. C. M. Knoops, E. Langereis, M. C. M. van de Sanden, and W. M. M. Kessels, Submitted to J. Vac. Sci. Technol. (2011).
314. J. T. Gudmundsson, I. G. Kouznetsov, K. K. Patel, and M. A. Lieberman, J. Phys. D: Appl. Phys. 34, 1100 (2001).
315. MKS website, http://www.mksinst.com, (May 31, 2011).
316. Advanced Energy website, http://www.advanced-energy.com/, (May 31, 2011).
317. E. Kawamura, V. Vahedi, M. A. Lieberman, and C. K. Birdsall, Plasma Sources Sci. Technol. 8, R45 (1999).
318. H. B. Profijt, M. C. M. van de Sanden, and W. M. M. Kessels, To be Published (2011).
319. J. W. Lim, S. J. Yun, and J. H. Lee, Electrochem. Solid-State Lett. 7, F73 (2004).
320. S. J. Yun, J. W. Lim, and J. H. Lee, Electrochem. Solid-State Lett. 7, C13 (2004).
321. J. Beynet, P. Wong, A. Miller, S. Locorotondo, D. Vangoidsenhoven, T. H. Yoon, M. Demand, H. S. Park, T. Vandeweyer, H. Sprey, Y. M. Yoo, and M. Maenhoudt, Proc. SPIE 7520, 75201J (2009).
322. M. D. Groner, F. H. Fabreguette, J. W. Elam, and S. M. George, Chem. Mater. 16, 639 (2004).
323. G. Dingemans, M. C. M. van de Sanden, and W. M. M. Kessels, Electrochem. Solid-State Lett. 13, H76 (2010).
324. P. Williams, A. Kingsley, T. Leese, Y. Otsuka, and K. Uotani, in Book of abstracts, 8th International Conference on Atomic Layer Deposition, Bruges, Belgium, 7 February 2008.
325. Q. Xie, Y. L. Jiang, C. Detavernier, D. Deduytsche, R. L. Van Meirhaeghe, G. P. Ru, B. Z. Li, and X. P. Qu, J. Appl. Phys. 102, 083521 (2007).
326. R. Katamreddy, Z. Wang, V. Omarjee, P. Venkateswara Raoa, C. Dussarrat, and C. Blasco, ECS Trans. 25, 217 (2009).
327. J. A. Kittl, K. Opsomer, M. Popovici, N. Menou, B. Kaczer, X. P. Wang, C. Adelmann, M. A. Pawlak, K. Tomida, A. Rothschild, B. Govoreanu, R. Degraeve, M. Schaekers, M. Zahid, A. Delabie, J. Meersschaut, W. Polspoel, S. Clima, G. Pourtois, W. Knaepen, C. Detavernier, V. V. Afanas'ev, T. Blomberg, D. Pierreux, J. Swerts, P. Fischer, J. W. Maes, D. Manger, W. Vandervorst, T. Conard, A. Franquet, P. Favia, H. Bender, B. Brijs, S. van Elshocht, M. Jurczak, J. Van Houdt, and D. J. Wouters, Microel. Eng. 86, 1789 (2009).
328. H. Kim, J. Vac. Sci. Technol. B 21, 2231 (2003).
329. M. Ritala, P. Kalsi, D. Riihela, K. Kukli, M. Leskelä, and J. Jokinen, Chem. Mater. 11, 1712 (1999).

330. B. B. Burton, A. R. Lavoie, and S. M. George, J. Electrochem. Soc. 155, D508 (2008).
331. P. Alen, M. Juppo, M. Ritaka, T. Sajavaara, J. Keinonen, and M. Leskelä, J. Electrochem. Soc. 148, G566 (2001).
332. T. Aaltonen, Atomic layer deposition of noble metal thin films, Ph.D. thesis (University of Helsinki, Finland, 2005).
333. T. Aaltonen, M. Ritala, T. Sajavaara, J. Keinonen, and M. Leskelä, Chem. Mater. 15, 1924 (2003).
334. W. M. M. Kessels, H. C. M. Knoops, S. A. F. Dielissen, A. J. M. Mackus, and M. C. M. van de Sanden, Appl. Phys. Lett. 95, 013114 (2009).
335. J. Hämäläinen, F. Munnik, M. Ritala, and M. Leskelä, Chem. Mater. 20, 6840 (2008).
336. J. Dendooven, D. Deduytsche, J. Musschoot, R. L. Vanmeirhaeghe, and C. Detavernier, J. Electrochem. Soc. 156, 63 (2009).
337. W. M. M. Kessels, in Book of abstracts, Baltic Conference on Atomic Layer Deposition 2006, Oslo, Norway, 19 June 2006.
338. J. W. Elam, D. Routkevitch, P. P. Mardilovich, and S. M. George, Chem. Mater. 15, 3507 (2003).
339. J. Y. Kim, J. H. Kim, J. H. Ahn, P. K. Park, and S. W. Kang, J. Electrochem. Soc. 154, H1008 (2007).
340. O. S. Kwon, S. K. Kim, M. Cho, C. S. Hwang, and J. Jeong, J. Electrochem. Soc. 152, C229 (2005).
341. H. C. M. Knoops, J. W. Elam, J. A. Libera, and W. M. M. Kessels, Chem. Mater. 23, 2381 (2011).
342. S. T. Oyama, Cat. Rev. Sci. Eng. 42, 279 (2000).
343. S. C. Ha, E. Choi, S. H. Kim, and J. S. Roh, Thin Solid Films 476, 252 (2005).
344. H. Ren, Y. Nishi, and J. L. Shohet, Electrochem. Solid-State Lett. 14, H107 (2011).
345. T. Takagi, J. Vac. Sci. Technol. A 2, 382 (1984).
346. C. Cismaru and J. L. Shohet, Appl. Phys. Lett. 74, 2599 (1999).
347. K. G. Druijf, J. M. M. Denijs, E. Vanderdrift, E. H. A. Granneman, and P. Balk, Appl. Phys. Lett. 65, 347 (1994).
348. H. L. Hughes and J. M. Benedetto, IEEE Trans. Nucl. Sci. 50, 500 (2003).
349. S. Samukawa, Y. Ishikawa, S. Kumagai, and N. Okigawa, Jpn. J. Appl. Phys. , Part 2 40, L1346 (2001).
350. J. L. Lauer, J. L. Shohet, and Y. Nishi, Appl. Phys. Lett. 94, 162907 (2009).

351. H. Ren, S. L. Cheng, Y. Nishi, and J. L. Shohet, Appl. Phys. Lett. 96, 192904 (2010).
352. G. S. Upadhyaya and J. L. Shohet, Appl. Phys. Lett. 90, 072904 (2007).
353. Levitech website, http://www.levitech.nl, (May 31, 2011).
354. TNO website, http://www.tno.nl, (May 31, 2011).
355. SolayTec website, http://www.solaytec.com, (May 31, 2011).
356. G. Dingemans and W. M. M. Kessels, Proc. 25th EU PVSEC (Valencia, Spain, 6-10 September 2010), 1083 (2010).
357. H. Kim, Surf. Coat. Technol. 200, 3104 (2006).
358. J. Robertson, Rep. Prog. Phys. 69, 327 (2005).
359. J. H. Choi, Y. Mao, and J. P. Chang, Mater. Sci. Eng. R (2011).
360. M. Vehkamaki, T. Hatanpaa, T. Hanninen, M. Ritala, and M. Leskelä, Electrochem. Solid-State Lett. 2, 504 (1999).
361. S. Owa, H. Nagasaka, K. Nakano, and Y. Ohmura, Proc. SPIE 6154, 615408 (2006).
362. Y. Borodovky, Proc. SPIE 6153, 615301 (2006).
363. "Below 22nm, spacers get unconventional: Interview with ASM", in Solid State Tech., Vol. 54 (2011).
364. P. F. Carcia, R. S. Mclean, M. H. Reilly, M. D. Groner, and S. M. George, Appl. Phys. Lett. 89, 031915 (2006).
365. S. H. K. Park, J. Oh, C. S. Hwang, J. I. Lee, Y. S. Yang, and H. Y. Chu, Electrochem. Solid-State Lett. 8, H21 (2005).
366. X. Du, K. Zhang, K. Holland, T. Tombler, and M. Moskovits, Appl. Optics 48, 6470 (2009).
367. R. Matero, M. Ritala, M. Leskelä, T. Salo, J. Aromaa, and O. Forsen, J. Phys. IV 9, 493 (1999).
368. C. X. Shan, X. Hou, and K. L. Choy, Surf. Coat. Technol. 202, 2399 (2007).
369. K. Sugioka, J. F. Fan, K. Toyoda, H. Waki, and H. Takai, J. Mater. Res. 7, 185 (1992).
370. W. Lehnert, G. Ruhl, and A. Gschwandtner, "Plasma enhanced ALD of high k dielectrics in a batch system", in Book of abstracts, Baltic ALD 2010 & GerALD 2, Hamburg, Germany, 16 September 2010.
371. H. W. de Vries, WO Patent No. 2007145513 (2007).
372. FujiFilm Manufacturing Europe website, http://www.fujitilburg.nl, (May 31, 2011).
373. J. M. Ajello, S. K. Srivastava, and Y. L. Yung, Phys. Rev. A 25, 2485 (1982).

374. A. C. Fozza, A. Kruse, A. Hollander, A. Ricard, and M. R. Wertheimer, J. Vac. Sci. Technol. A 16, 72 (1998).
375. R. Henck, C. Fuchs, and E. Fogarassy, J. Appl. Phys. 79, 2259 (1996).
376. J. A. Young, C. P. Malone, P. V. Johnson, J. M. Ajello, X. Liu, and I. Kanik, J. Phys. B 43, 135201 (2010).
377. Z. Lianzhu, Z. Shuxia, and M. Xiulan, Plasma Sci. Technol. 10, 455 (2008).
378. P. C. P. Bouten, G. Nisato, P. J. Slikkerveer, H. F. van Tongeren, H. E. Itzhak, and P. van der Sluis, U.S. Patent No. 6,993,956 (2006).
379. G. Dingemans, C. A. A. van Helvoirt, D. Pierreux, W. Keuning, and W. M. M. Kessels, J. Electrochem. Soc. 159, H277 (2012).
380. M. Kariniemi, J. Niinistö, M. Vehkamäki, M. Kemell, M. Ritala, and Markku Leskelä, J. Vac. Sci. Technol. A 30, 01A115 (2012).

Chapter 3

# Room-Temperature ALD of Metal-Oxide Thin Films by Energy-Enhanced ALD*

**Abstract** Room-temperature ALD (RT-ALD) processes are of interest for applications using temperature-sensitive substrates, yet they are not so commonly reported. The challenges associated with RT-ALD arise when surface groups and incoming precursors are not sufficiently reactive towards each other, the precursors are not sufficiently volatile, and purge times become impractically long. In several cases, these challenges can be overcome using energy-enhanced ALD. We demonstrate here viable energy-enhanced RT-ALD (25 °C) processes for $Al_2O_3$, $TiO_2$ and $SiO_2$ from TMA, TTIP, and BDEAS precursors, enabled using an $O_2$ plasma or $O_3$ as co-reactants. Saturated ALD growth was obtained at room temperature for the TMA/$O_2$ plasma, TMA/$O_3$, BDEAS/$O_2$ plasma, and TTIP/$O_2$ plasma processes, whereas the BDEAS/$O_3$ process gave no growth and the TTIP/$O_3$ process gave negligible growth at room temperature. Using these results, the essential and desirable criteria that are necessary for viable RT-ALD processes are discussed.

*A part of this work has been published as: *S. E. Potts, H. B. Profijt, R. Roelofs, and W. M. M. Kessels, ECS Trans. 50 (2012).*

## 3.1 Introduction

Atomic layer deposition (ALD) is known for its ability to deposit high-quality, uniform and conformal thin films. As, in many cases, ALD relies on ligand-exchange reactions rather than precursor decomposition, relatively low deposition temperatures ($\leq$ 200 °C) can be employed [1], which is important for applications requiring temperature-sensitive substrates and materials [2-11], for example those employing polymeric or organic materials. In several cases, it is essential to keep the deposition temperature as low as possible to prevent damage, such as a change in composition, or a distortion of the substrates; therefore, room-temperature ALD (RT-ALD) is highly desired.

Despite the apparent need for RT-ALD, it is not so commonly reported. Generally, depositions at room temperature described in the literature (summarized in Table 3.1) are an extension of a temperature series and room-temperature saturation of the surface reactions is rarely mentioned. Additionally, the literature outlines two key challenges for RT-ALD:

1. *Low growth-per-cycle (GPC) values* as a result of insufficient thermal energy for reactions between the surface groups and the precursors.
2. *The requirement for extremely long purge times*, predominantly where water is employed as the co-reactant.

The majority of the examples in Table 3.1 are energy-enhanced ALD processes, so-called because energy is not supplied to the substrate as heat, but to the co-reactant gas to give a reactive species. Therefore, energy-enhanced ALD encompasses ozone-based and plasma-assisted ALD [30-32]. This extra energy is important for driving the reactions that would otherwise not (or hardly) proceed at such low substrate temperatures. In addition, there are examples where a catalyst, such as an amine [23,24] or UV light [29] was used to enhance the reactivity of traditionally "thermal" processes. In the cases where thermal processes were not hindered by the lack of energy (generally where water was used as the co-reactant) the purge times required were of the order of minutes in order to reach proper ALD conditions [12,13,25].

Taking these observations into account, the following criteria should ideally be met to afford viable RT-ALD processes:

- Desirable: the metal precursor should have a high vapor pressure at room temperature, ideally $\geq$5 Torr ($\sim$667 Pa, 6.7 mbar).

- Desirable: purge times should be short.
- Essential: the surface reactions should be viable.

This Chapter aims to show that viable, saturated ALD processes can be carried out at room temperature, and examine why and how the aforementioned points can be addressed, using the RT-ALD of $Al_2O_3$, $SiO_2$ and $TiO_2$ as examples.

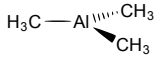
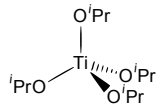
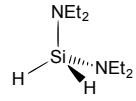
**Table 3.1:** Examples of metal oxides deposited at room temperature by ALD. Me = methyl, Et = ethyl, $^i$Pr = isopropyl, $^t$Bu = tert-butyl.

| Material | Metal Precursor | Reactant | Lowest Reported Temp. ( °C) | Ref. |
|---|---|---|---|---|
| $Al_2O_3$ | $Al(CH_3)_3$ | $H_2O$ | 25 | 12,13 |
| $Al_2O_3$ | $Al(CH_3)_3$ | $O_3$ | 25 | 14, this work |
| $Al_2O_3$ | $Al(CH_3)_3$ | $O_2$ plasma | 25 | 1-3, 15-20, this work |
| $Al_2O_3$ | $[Al(CH_3)_2(O\ ^iPr)]_2$ | $O_2$ plasma | 25 | 21 |
| $B_2O_3$ | $BBr_3$ | $H_2O$ | 20 | 22 |
| $SiO_2$ | $Si(OEt)_4$ | $H_2O$ + $NH_3$ cat. | 25 | 34,24 |
| $SiO_2$ | $Si(NCO)_4$ | $H_2O$ | 25 | 25 |
| $SiO_2$ | $SiH_2(NEt_2)_2$ | $O_2$ plasma | 25 | This work |
| $TiO_2$ | $Ti(O\ ^iPr)_4$ | $O_2$ plasma | 25 | 1, this work |
| $TiO_2$ | $Ti(NMe_2)_4$ | $H_2O$ | 25 | 13 |
| $TiO_2$ | $Ti(NMe_2)_4$ | $O_2$ plasma | 25 | 13 |
| $Ta_2O_5$ | $Ta(NMe_2)_5$ | $O_2$ plasma | 25 | 1 |
| ZnO | $Zn(CH_2CH_3)_2$ | $H_2O$ | 25 | 13,26,27 |
| ZnO | $Zn(CH_2CH_3)_2$ | $H_2O_2$ | 25 | 28 |
| $ZrO_2$ | $Zr(O\ ^tBu)_4$ | $H_2O$ + UV light | 25 | 29 |

## 3.2 Experimental

The RT-ALD experiments were carried out using an Oxford Instruments FlexALTM reactor, described in detail elsewhere [16,33]. The base pressure was $\sim 10^{-6}$ Torr and the operating pressure was set to 25 mTorr for plasma-assisted ALD and 250 mTorr for $O_3$ ALD. The metalorganic precursors are detailed in Table 3.2. For the deposition of $Al_2O_3$, trimethylaluminium ($AlMe_3$, purity 99.99%, AkzoNobel) was used as the precursor, held in an unheated stainless steel bubbler. Titanium(IV) tetraisopropoxide (TTIP, purity 99.999%, Sigma Aldrich) was used for the deposition of $TiO_2$ and held at a bubbler temperature of

**Table 3.2:** Examples of metal oxides deposited at room temperature by ALD. Me = methyl, Et = ethyl, $^{i}$Pr = isopropyl, $^{t}$Bu = tert-butyl.

| Property | TMA | TTIP | BDEAS |
|---|---|---|---|
| Structural Formula |  |  |  |
| Melting Point | 15 °C | 14 °C | <-10 °C |
| Boiling Point | 125 °C | 232 °C | 188 °C |
| Vapor Pressure at 25 °C | ∼13 Torr | ∼0.13 Torr | ∼2 Torr |

45 °C. For the deposition of $SiO_2$, bis(diethylamino)silane (BDEAS*, purity >99.99%, Air Liquide) was held at a bubbler temperature of 50 °C. $O_2$ (purity >99.999%, 100 sccm) was used to generate the plasma and Ar (purity >99.999%, 100 sccm was employed as the purge gas. The plasma power was 200 W. $O_3$ was generated from pure $O_2$ (purity >99.999%) using an Atlas 25 ozone Generator (Absolute Ozone), which comprised a dielectric barrier discharge setup running at 150 W. The generator was allowed to warm up for 15 min prior to depositions and was run continuously throughout the ALD processes. The $O_3$ was pulsed directly into the reactor at a flow rate of 250 sccm. To obtain the saturation curves for each ALD process, n-type Si(100) wafers (100 mm diameter) were used, which were covered with a thin native oxide ($SiO_2$) layer and did not undergo any additional cleaning steps. The optimized (viable) ALD process cycles (precursor - purge - co-reactant - purge) were as follows: TMA/$O_2$ plasma 0.02-2-(2 pre-plasma)-3-2 s; TMA/$O_3$ 0.02-2-5-2 s; TTIP/$O_2$ plasma 4-2-(2 pre-plasma)-5-5 s; BDEAS/$O_2$ plasma 0.05-2-(2 pre-plasma)-5-3 s. The pre-plasma step allowed for stabilization of the gas flows and ensured the correct pressure was reached before igniting the plasma.

The film growth was monitored by *in situ* spectroscopic ellipsometry (SE), carried out using a J. A. Woollam Inc. M2000 rotating compensator ellipsometer over a photon energy range of 1.2-6.5 eV [15,34]. The atomic composition of the films was determined by Rutherford backscattering spectroscopy (RBS) with 2 MeV $^{4}He^{+}$ ions, except for the hydrogen concentration, which was obtained by elastic recoil detection (ERD) analysis using the same apparatus. The mass density of the films was calculated using a combination of the RBS and SE data.

*BDEAS is also known as SAM.24, which is the trade name used by Air Liquide

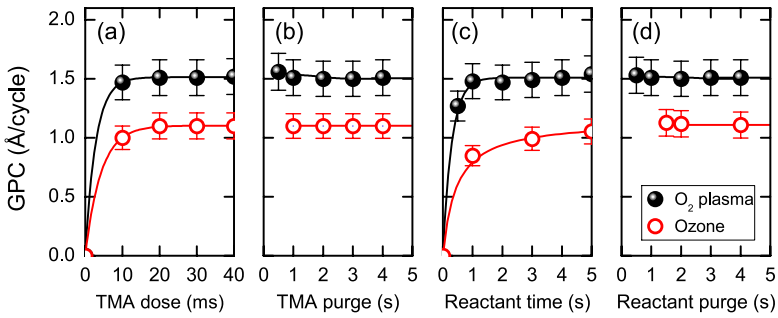



**Figure 3.1:** Saturation curves for the RT-ALD $Al_2O_3$ process from TMA and either an $O_2$ plasma or $O_3$. Lines serve as a guide to the eye.

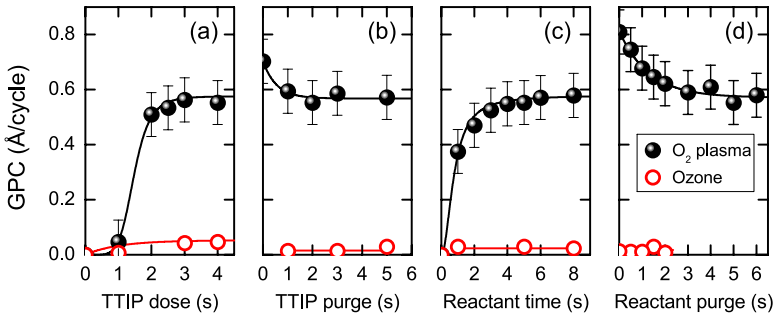



**Figure 3.2:** Saturation curves for the RT-ALD $TiO_2$ process from TTIP and either an $O_2$ plasma or $O_3$. Lines serve as a guide to the eye.

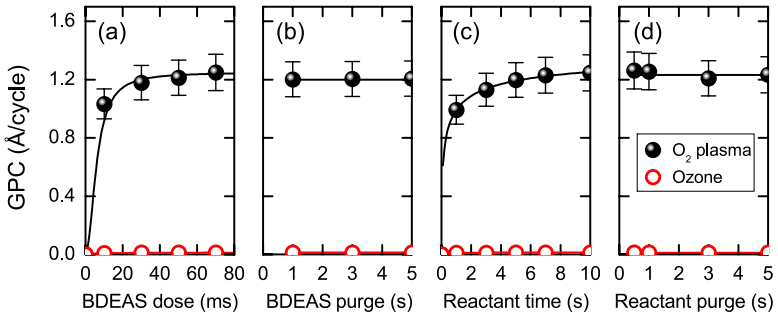



**Figure 3.3:** Saturation curves for the RT-ALD $SiO_2$ process from BDEAS and either an $O_2$ plasma or $O_3$. Lines serve as a guide to the eye.

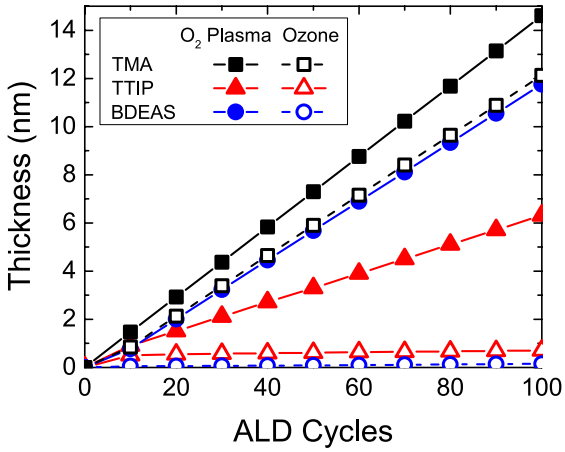



**Figure 3.4:** Summary of the RT-ALD processes for $Al_2O_3$ (black squares), $TiO_2$ (red triangles), and $SiO_2$ (blue circles). Datapoints for the plasma-assisted process are shown as filled symbols and datapoints for the ozone-based process are shown as open symbols. All plasma-assisted RT-ALD processes and the $Al_2O_3$ ozone-based RT-ALD process showed a linear increase in thickness with the number of ALD cycles.

## 3.3 Results

Figures 3.1, 3.2 and 3.3 show that ALD behavior occurred at room temperature for TMA, TTIP and BDEAS with an $O_2$ plasma, with GPC values of 1.5, 0.6 and 1.2 $\pm$ 0.1 Å/cycle, respectively. For the TTIP/$O_2$ plasma case no growth was obtained for a TTIP dose of 1 s. This delay in growth was attributed to the relatively low vapor pressure of the precursor (see below) combined with the design of the precursor dosing system. The precursor dose, co-reactant dose, and purges were all saturated. Saturation was also achieved for the TMA/$O_3$ RT-ALD process, which afforded a GPC of 1.1 $\pm$ 0.1 Å/cycle. Furthermore, these aforementioned processes showed a linear increase in film thickness (Fig. 3.4) as a function of ALD cycles with no nucleation delay, which was an indication of a good ALD process and suggests that (significant) precursor condensation did not occur over time. For the TTIP/$O_3$ RT-ALD process (Figs. 3.2 and 3.4) only $\sim$0.5 nm of growth was observed during the initial cycle, which is probably because there is some adsorption of TTIP on the surface hydroxyl (s-OH) groups initially present on the substrate. No growth was observed for the BDEAS/$O_3$ RT-ALD process (Figs. 3.3 and 3.4), which was surprising, as BDEAS is a sufficiently reactive precursor with -OH groups [35].

**Table 3.3:** Material properties for $Al_2O_3$, $TiO_2$, and $SiO_2$ thin films deposited by energy-enhanced ALD at room temperature and at 200 °C. All films had thicknesses of 30-40 nm, except for the $SiO_2$ film deposited at room temperature which was ∼70 nm. The relative errors in the [O]/[M] ratio (the oxygen-to-metal ratio), the mass density, the C content, and the number of metal atoms deposited per cycle (all determined by RBS) were 4%, 4% 6% and 5%, respectively. For the H content (determined by ERD), the relative error was 10%.

| Material | Co-reactant | Deposition temp. | [O]/[M] ratio | C content (at.%) | H content (at.%) | Mass density (g $cm^{-3}$) | M at. deposited (at. $nm^{-2}$ $cycle^{-1}$) |
|---|---|---|---|---|---|---|---|
| $Al_2O_3$ | $O_2$ plasma | RT | 2.0 | 2.8 | 15.2 | 2.7 | 4.2 |
| | | 200 °C | 1.5 | < 1.0 | 2.5 | 3.1 | 3.4 |
| $Al_2O_3$ | $O_3$ | RT | 2.1 | 9.0 | 20.8 | 2.4 | 1.9 |
| | | 200 °C | 1.7 | < 2.0 | 8.1 | 3.0 | 2.2 |
| $TiO_2$ | $O_2$ plasma | RT | 2.2 | 4.2 | 16.9 | 2.7 | 0.9 |
| | | 200 °C | 2.0 | < 1.0 | < 5.0 | 3.7 | 1.2 |
| $SiO_2$ | $O_2$ plasma | RT | 2.0 | < 5.0 | 7.8 | 1.9 | 2.8 |
| | | 200 °C | 2.1 | < 5.0 | 7.1 | 2.0 | 2.3 |

Table 3.3 summarizes RBS and ERD data obtained for the TMA/$O_2$ plasma, TMA/$O_3$, TTIP/$O_2$ plasma, and BDEAS/$O_2$ plasma processes carried out at room temperature and at a substrate temperature of 200 °C. The $Al_2O_3$ and $TiO_2$ films deposited at room temperature, either with $O_2$ plasma or $O_3$ as the co-reactant, contained more oxygen and had higher C and H contents compared to the films deposited at 200 °C [1]. For the $Al_2O_3$ films the [Al]/[O] ratios were 2.0 and 2.1 for room-temperature processes with $O_2$ plasma and $O_3$ as co-reactants, respectively. For the $TiO_2$ film deposited at room temperature, a [Ti]/[O] ratio of 2.2 was found whereas the sample deposited at 200 °C was stoichiometric. The higher C-contents of the $Al_2O_3$ and $TiO_2$ films deposited at room temperature reflect the presence of carbonaceous species, such as formates and carbonates, in the material, whereas the higher level of H is related to an increased amount of OH species incorporated [17,18,37-40]. The incorporation of such species explains for the excess oxygen and the lower mass density of the films. For the plasma-based process of $Al_2O_3$, the number of Al atoms deposited per unit area was higher for deposition at room temperature compared to deposition at 200 °C (4.2 and 3.4 at. $nm^{-2}$ $cycle^{-1}$, respectively). This is due to the increased surface coverage of OH groups of the films deposited at room temperature [17,18]. For the TMA/$O_3$ and TTIP/$O_2$ plasma processes, the number of metal atoms (Al and Ti, respectively) deposited per unit area was lower for the films deposited at room temperature compared to the films deposited at 200 °C. This

is expected to be due to the increased presence of carbonaceous species in these films which are less reactive or non-reactive with the precursor.

For $SiO_2$ the material properties for films deposited at room temperature and 200 °C were very similar. Both films has a [O]/[Si] ratio and mass density that were approximately equal, the C content was below the RBS detection limit of 5 at.% and the H content was similar with 8 and 7 at.% for room temperature and 200 °C, respectively. Interestingly, the number of Si atoms deposited per unit area was higher for the room-temperature deposition (2.8 at. $nm^{-2}$ $cycle^{-1}$, compared to 2.3 at. $nm^{-2}$ $cycle^{-1}$ at 200 °C), probably due to a higher surface coverage of OH groups after $O_2$ plasma exposure at room temperature.

## 3.4 Discussion

From the results, it can be seen that saturating ALD reactions can occur at room temperature. Analysis of the TMA, TTIP, and BDEAS processes allows for the formulation of the following "rules of thumb" for successful RT-ALD processes.

***Vapor Pressure of the Metal Precursors***

The vapor pressures for TMA, TTIP, and BDEAS are shown in Table 3.2 and Fig. 3.4. For RT-ALD to be viable, the precursor needs to have a sufficiently high vapor pressure to be carried easily to the reactor and such that any excess can be rapidly purged away. Therefore, the vapor pressure should ideally be $\geq$5 Torr at room temperature. For precursors that do not meet this criterion, the bubbler can be heated to give a higher vapor pressure. The need for (significant) heating can be avoided by bubbling with an inert gas, typically Ar. With precursors that require heating of the bubbler to considerably higher temperatures than 50 °C, however, there is a significant risk of precursor condensation. For example, condensation could occur on the substrate, which can lead to non-uniformity, and on the colder parts of the reactor, which makes the purging of excess precursor and reaction products difficult. In principle, a combination of a low degree of heating and bubbling could allow for precursors with even lower vapor pressures to be employed at room temperature.

TMA has a vapor pressure of $\sim$13 Torr at 25 °C and therefore it is not required to heat the bubbler. The high vapor pressure also accounts for the rapid ALD saturation observed (Fig. 3.1a). TTIP and BDEAS, however, are not as volatile at room temperature with vapor pressures of 0.13 Torr and 2 Torr, respectively. In order to obtain a similar vapor pressure to TMA, the BDEAS bubbler was heated to 50 °C, giving a vapor pres-

sure of ∼9 Torr, which resulted in similarly quick saturation to TMA (Fig. 3.3a). For TTIP, heating to 50 °C would result in a vapor pressure of only 0.9 Torr, which would be too low to obtain an acceptable saturation time. Therefore, the bubbler was heated to 45 °C and additionally 50 sccm Ar bubbling was employed, which resulted in a reasonable precursor dosing time of 2 s (Fig. 3.2a).

***Purge Times***

Ideally, purge times should be short to keep the overall process time low, which is simply not possible for most thermal RT-ALD processes employing $H_2O$, some of which require purging of the order of minutes to properly saturate [13]. However, all the viable energy-enhanced RT-ALD processes reported here showed GPC saturation within 2 to 3 s for all purge steps (Figs. 3.1b, 3.1d, 3.2b, 3.2d, 3.3b and 3.3d). The main reason for this is that the energy-enhanced RT-ALD processes involve gaseous co-reactants (plasmas and $O_3$) that are quickly removed from the reaction chamber. The reactive species disappear very quickly after the plasma power or the $O_3$ dosing is stopped. For example, in a plasma ions and electrons disappear almost instantly and radicals can recombine at the reactor walls [32,43] or are pumped away at typical timescales of < 1s. Also $O_3$ can recombine at reactor walls [44]. Furthermore, water can be a reaction product of $O_2$ plasma and $O_3$-based ALD processes but the quantity produced during a typical cycle is very small compared to the amount delivered in a typical water pulse (∼ 10 ms) in thermal ALD. Moreover, the water produced in an energy-enhanced ALD process can undergo thermal ALD reactions with the surface groups [16], which therefore contributes to the surface chemistry, meaning there is less likely to be a significant excess of water to purge. Therefore, the use of energy-enhanced ALD processes allows for substantially reduced cycle times at room temperature.

***Surface Reactions***

Surface reactions are the driving force of ALD and it is therefore essential that these occur easily at room temperature for RT-ALD to be viable. In other words, the following conditions should be met:

1. The metalorganic precursor should be sufficiently reactive with the surface groups left by the oxygen source. This applies for all ALD chemistries, irrespective of thermal ALD and energy-enhanced ALD processes.

2. The oxygen source, or co-reactant, should react with the surface groups left by the metalorganic precursor.

TMA, TTIP and BDEAS are known to react with surface hydroxyl (s-OH) groups [16-18,35,37-40,45,46], which are the dominant surface species after $H_2O$ doses for thermal ALD and $O_2$ plasma exposures for plasma-assisted ALD. In an earlier study, the creation of s-OH by an $O_2$ plasma during the ALD of $Al_2O_3$ was demonstrated in the FTIR difference spectra taken after the plasma exposure (Fig. 5). The density of s-OH on $Al_2O_3$ [18], $TiO_2$ [39,46], and $SiO_2$ [47,48] is temperature dependent; as the temperature increases, two adjacent s-OH species can combine to form water, which is removed from the film (known as dehydroxylation). This is manifested in the fact that, in general, the s-OH density is highest at low substrate temperatures [18,38,46-48], demonstrated in Fig. 3.5 for $Al_2O_3$, whereby the peak at 3100-3600 $cm^{-1}$ (OH) is visibly larger at 25 °C than 150 °C (this could also reflect some adsorbed water at this temperature). Furthermore, this higher density of s-OH promotes bifunctional reactions at room temperature with the incoming metalorganic precursor [18,47,48], as opposed to monofunctional binding at higher temperatures, which has been observed for TMA-based ALD processes [16,49].

Regarding ozone-based ALD, the reaction of $O_3$ with surface methyl groups during $Al_2O_3$ ALD has been shown to result in s-OH [37], whereas no s-OH was observed for the reaction of $O_3$ with surface isopropoxide during ALD of $TiO_2$ [50]. Carbonaceous surface groups, such as alkoxy (in this case methoxy [$OCH_3$]), formate [$HCO_2$] and carbonate [$CO_3$] groups, are observed with both ozone-based and plasma-assisted ALD of $Al_2O_3$ and $TiO_2$. In the case of plasma-assisted ALD, however, they are a more transient species and are rapidly replaced by s-OH at higher temperatures such as $\geq$ 150 °C [40,38]. At room temperature a small concentration of carbonates is still present in the films resulting from the incorporation of carbonate surface groups (Fig. 3.6, feature at $\sim$1650 $cm^{-1}$) [18]. TMA is able to react with such carbonaceous groups at room temperature [37,38,40], as also evidenced by the relatively high GPC (1.1 $\pm$ 0.1 Å/cycle) obtained in the ozone-based process. TTIP is also reactive with the carbonaceous surface groups at higher temperatures, resulting in a feasible ALD process, probably even in the absence of surface-hydroxyl groups [39,50]. At room temperature, however, no growth was observed for the ozone-based $TiO_2$ process, which could indicate that Al-Me is more reactive than Ti-O towards carbonaceous species at room temperature. It is also possible that BDEAS is not reactive with carbonaceous groups, but there is probably still sufficient s-OH, certainly on the initial substrate, to initiate a reaction. Therefore, the surface groups created by the $O_3$ are not likely the only reason for the lack of growth in the BDEAS/$O_3$ RT-ALD process.

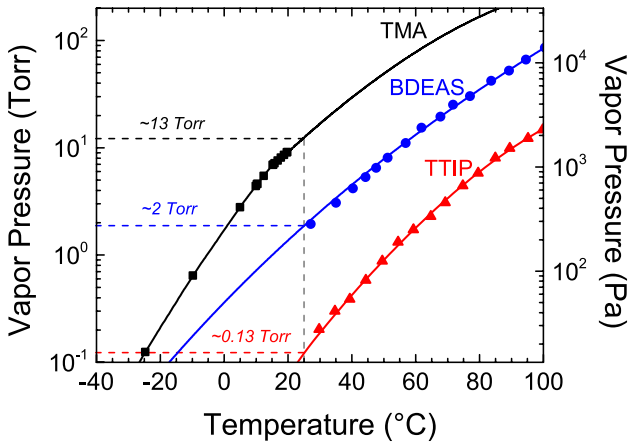



**Figure 3.5:** Vapor pressures for TMA [36], TTIP [41], and BDEAS [42] precursors as a function of temperature. Lines serve as a guide to the eye.

Water, ozone, and $O_2$ plasma all react with the surface methyl groups remaining after the precursor pulse in the ALD of $Al_2O_3$ [16-18,35]. Surface isopropoxide is also able to react with $O_2$ plasma room temperature [1,39,50]. However, it is possible that $O_3$ is not sufficiently reactive towards surface isopropoxide in the case of room-temperature deposition of $TiO_2$. BDEAS adsorption leaves either surface amino species (in this case, s-Si-$NEt_2$) and/or hydride species (s-Si-H) on the surface. For aminosilane compounds, mass spectroscopy [35], FT-IR [45], and DFT calculation studies [51,52] have all shown that amines are the preferred reaction product when the aminosilane precursor reacts with s-OH, and that s-Si-H always remains. The main reasons given were that amino ligands can form hydrogen bonds with s-OH, which reduces the activation energy for the ligand-exchange reaction, and that $H_2$ production from s-OH and s-Si-H is energetically very unlikely. Therefore, as the density of s-OH is high at room temperature and promotes bifunctional chemisorption of the BDEAS [47,48], it can be assumed that there will only be a s-Si-H surface left after BDEAS dose. The $O_2$ plasma must be sufficiently reactive toward these s-Si-H groups at room temperature, forming s-OH, as ALD growth was observed. However, this is probably not the case for $O_3$. This suggests that there is insufficient energy for a full reaction between s-Si-H and $O_3$ at room temperature. At higher substrate temperatures the BDEAS binding is more monofunctional such that s-Si-$NEt_2$

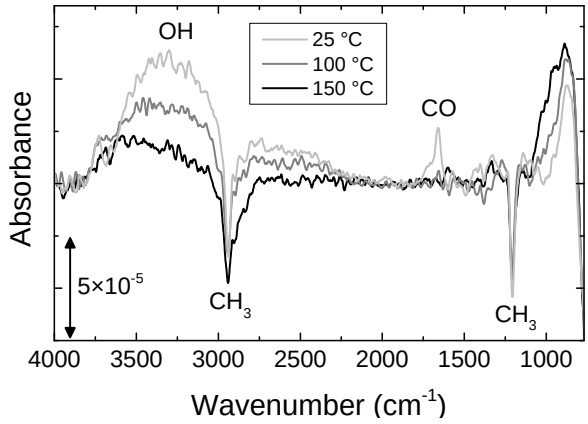



**Figure 3.6:** *In situ* FT-IR difference spectra of the surface of $Al_2O_3$ films representing changes caused by the $O_2$ plasma dose during plasma-assisted ALD using TMA, adapted from Ref. 18. The difference spectra comprise an FT-IR spectrum taken after the $O_2$ plasma dose and divided by the reference spectrum taken before the plasma exposure.

can remain. Surface amino species are more reactive with the incoming $O_3$ whereas also reactions between s-Si-H and $O_3$ might become more feasible at higher temperatures. Both aspects may therefore help drive the ALD reactions.

## 3.5 Conclusions

Taking $Al_2O_3$, $SiO_2$, and $TiO_2$ energy-enhanced ALD processes as examples, the following criteria for successful, saturating room-temperature (RT-)ALD have been identified and discussed. Concerning the practicalities of the RT-ALD process, we determined that the metalorganic precursors used must ideally have a high vapor pressure at room temperature and that purge times can be kept short by using energy-enhanced co-reactants that can be switched on and off, and hence removed from the reactor, within a short time frame. It was also discussed that the precursor must be reactive with the surface groups left by the co-reactant and that the co-reactant has to be reactive with the surface groups left by the precursor molecules. The case of the BDEAS/$O_3$ and TTIP/$O_3$ RT-ALD processes, where no or negligible growth was observed, show that fulfilling these requirements is not trivial. However, if all the aforementioned criteria (vapor pressure, purging, and reactivity) are taken into consideration for a desired material, then a viable RT-ALD process for that material should be possible.

## Acknowledgements

This work was carried out within the Thin Film Nanomanufacturing (TFN) programme and is supported financially by the Dutch Technology Foundation STW. The work of S.E.P. is supported by NanoNextNL, a micro and nanotechnology programme of the Dutch ministry of economic affairs, agriculture and innovation (ELI) and 130 partners. The authors also thank W. Keuning, C. A. A. van Helvoirt, J. J. L. M. Meulendijks, J. J. A. Zeebregts and M. J. F. van de Sande (all TU/e) for their technical assistance, support and advice.

## References

1. S. E. Potts, W. Keuning, E. Langereis, G. Dingemans, M. C. M. van de Sanden, and W. M. M. Kessels, J. Electrochem. Soc., 157, P66 (2010).
2. E. Langereis, M. Creatore, S. B. S. Heil, M. C. M. van de Sanden, and W. M. M. Kessels, Appl. Phys. Lett., 89, 081915 (2006).
3. W. Keuning, P. van de Weijer, H. Lifka, W. M. M. Kessels, and M. Creatore, J. Vac. Sci. Technol. A, 30, 01A131 (2012).
4. D. H. Levy, D. Freeman, S. F. Nelson, P. J. Cowdery-Corvan, and L. M. Irving, Appl. Phys. Lett., 92, 192101 (2008).
5. S. Bang, S. Lee, S. Jeon, S. Kwon, W. Jeong, H. Kim, I. Shin, H. J. Chang, H. Park, and H. Jeon, Semicond. Sci. Technol., 24, 025008 (2009).
6. T. Murata, Y. Miyagawa, Y. Nishida, Y. Yamamoto, T. Yamashita, M. Matuura, K. Asai, and H. Miyatake, Jpn. J. Appl. Phys., 49, 04DB11 (2010).
7. J. Beynet, P. Wong, A. Miller, S. Locorotondo, D. Vangoidsenhoven, T.-H. Yoon, M. Demand, H.-S. Park, T. Vandeweyer, H. Sprey, Y.-M. Yoo, and M. Maenhoudt, Proc. SPIE, 7520, 75201J (2009).
8. J. Haisma, M. Verheijen, K. van den Heuvel, and J. van den Berg, J. Vac. Sci. Technol. B, 14, 4124 (1996).
9. J. Viheriälä, J. Tommila, T. Leinonen, M. Dumitrescu, L. Toikkanen, T. Niemi, and M. Pessa, Microelectron. Eng., 86, 321 (2009).
10. L. Sainiemi, J. Viheriälä, T. Sikanen, J. Laukkanen, and T. Niemi, J. Micromech. Eng., 20, 077001 (2010).
11. C. Peroz, S. Dhuey, M. Cornet, M. Vogler, D. Olynick, and S. Cabrini, Nanotechnology, 23, 015305 (2012).

12. M. D. Groner, F. H. Fabreguette, J. W. Elam, and S. M. George, Chem. Mater., 16, 639 (2004).
13. T. Nam, J.-M. Kim, M.-K. Kim, H. Kim, and W.-H. Kim, J. Korean Phys. Soc., 59, 452 (2011).
14. S. K. Kim, S. W. Lee, C. S. Hwang, Y.-S. Min, J. Y. Won, and J. Jong, J. Electrochem. Soc., 153, F69 (2006).
15. J. L. van Hemmen, S. B. S. Heil, J. H. Klootwijk, F. Roozeboom, C. J. Hodson, M. C. M. van de Sanden, and W. M. M. Kessels, J. Electrochem. Soc., 154, G165 (2007).
16. S. B. S. Heil, J. L. van Hemmen, M. C. M. van de Sanden, and W. M. M. Kessels, J. Appl. Phys., 103, 103302 (2008).
17. E. Langereis, M. Bouman, J. Keijmel, S. B. S. Heil, M. C. M. van de Sanden, and W. M. M. Kessels, ECS Trans., 16, 247 (2008).
18. E. Langereis, J. Keijmel, M. C. M. van de Sanden, and W. M. M. Kessels, Appl. Phys. Lett., 92, 231904 (2008).
19. A. Niskanen, K. Arstila, M. Ritala, and M. Leskelä, J. Electrochem. Soc., 152, F90 (2005).
20. X. Tang, L. A. Francis, P. Simonis, M. Haslinger, R. Delamare, O. Deschaume, D. Flandre, P. Defrance, A. M. Jonas, J. P. Vigneron, and J. P. Raskin, J. Vac. Sci. Technol. A, 30, 01A146 (2012).
21. S. E. Potts, G. Dingemans, C. Lachaud, and W. M. M. Kessels, J. Vac. Sci. Technol. A, 30, 021505 (2012).
22. M. Putkonen and L. Niinistö, Thin Solid Films, 514, 145 (2006).
23. J. W. Klaus and S. M. George, Surf. Sci., 447, 81 (2000).
24. J. D. Ferguson, E. R. Smith, A. W. Weimer, and S. M. George, J. Electrochem. Soc., 151, G528 (2004).
25. W. Gasser, Y. Uchida, and M. Matsumura, Thin Solid Films, 250, 213 (1994).
26. C.-S. Ku, J.-M. Huang, C.-M. Lin, and H.-Y. Lee, Thin Solid Films, 518, 1373 (2009).
27. Y.-M. Chang, J. Shieh, P.-Y. Chu, H.-S. Lee, C.-M. Lin, and J.-Y. Juang, ACS Appl. Mater. Interfaces, 3, 4415 (2011).
28. D. M. King, X. Liang, P. Li, and A. W. Weimer, Thin Solid Films, 516, 8517 (2008).
29. B. H. Lee, S. Cho, J. K. Hwang, S. H. Kim, and M. M. Sung, Thin Solid Films, 518, 6432 (2010).

30. W. M. M. Kessels, H. B. Profijt, S. E. Potts, and M. C. M. van de Sanden, Plasma Atomic Layer Deposition, p. 131, Wiley-VCH (2011).
31. W. M. M. Kessels and M. Putkonen, MRS Bull., 36, 907 (2011).
32. H. B. Profijt, S. E. Potts, M. C. M. van de Sanden, and W. M. M. Kessels, J. Vac. Sci. Technol. A, 29, 050801 (2011).
33. S. B. S. Heil, J. L. van Hemmen, C. J. Hodson, N. Singh, J. H. Klootwijk, F. Roozeboom, M. C. M. van de Sanden, and W. M. M. Kessels, J. Vac. Sci. Technol. A, 25, 1357 (2007).
34. E. Langereis, S. B. S. Heil, H. C. M. Knoops, W. Keuning, M. C. M. van de Sanden, and W. M. M. Kessels, J. Phys. D: Appl. Phys., 42, 073001 (2009).
35. G. Dingemans, C. A. A. van Helvoirt, D. Pierreux, W. Keuning, and W. M. M. Kessels, J. Electrochem. Soc., 159, H277 (2012).
36. M. Fulem, K. Ruzicka, V. Ruzicka, E. Hulicius, T. Simecek, K. Melichar, J. Pangrác, S. A. Rushworth, and L. M. Smith, J. Cryst. Growth, 248, 99 (2003).
37. D. M. Goldstein, J. A. McCormick, and S. M. George, J. Phys. Chem. C, 112, 19530 (2008).
38. V. R. Rai, V. Vandalon, and S. Agarwal, Langmuir, 28, 350 (2012).
39. V. R. Rai and S. Agarwal, J. Phys. Chem. C, 113, 12962 (2009).
40. V. R. Rai, V. Vandalon, and S. Agarwal, Langmuir, 26, 13732 (2010).
41. K. L. Siefering and G. L. Griffin, J. Electrochem. Soc, 137, 1206 (1990).
42. Air Liquide, private communication (2011).
43. H. C. M. Knoops, E. Langereis, M. C. M. van de Sanden, and W. M. M. Kessels, J. Electrochem. Soc. 157, G241 (2010).
44. H. C. M. Knoops, J. W. Elam, J. A. Libera, and W. M. M. Kessels, Chem. Mater., 23, 2381 (2011).
45. B. B. Burton, S. W. Kang, S. W. Rhee, and S. M. George, J. Phys. Chem. C, 113, 8249 (2009).
46. M. Ritala, M. Leskela, E. Nykanen, E. Soininen, and L. Niinisto, Thin Solid Films, 255, 288 (1993).
47. S. Haukka, E.-L. Lakomaa, and T. Suntola, Appl. Surf. Sci., 82/83, 548 (1994).
48. S. Haukka and T. Suntola, Interface Sci., 5, 119 (1997).
49. A. Rahtu, T. Alaranta, and M. Ritala, Langmuir, 17, 6506 (2001).
50. V. R. Rai and S. Agarwal, J. Phys. Chem. C, 112, 9552 (2008).
51. B. Han, Q. Zhang, J. Wu, B. Han, E. J. Karwacki, A. Derecskei, M. Xiao, X. Lei, M. L. O'Neill, and H. Cheng, J. Phys. Chem. C, 116, 947 (2012).
52. J. Li, J. Wu, C. Zhou, B. Han, E. J. Karwacki, M. Xiao, X. Lei, and H. Cheng, J. Phys. Chem. C, 113, 9731 (2009).

Chapter 4

# Ion Bombardment during Plasma-Assisted Atomic Layer Deposition*

**Abstract** The presence and influence of ions in several reactor configurations used for plasma-assisted atomic layer deposition (ALD) are discussed. It is shown that the ion energies are often moderate or even negligible in direct plasma and remote plasma ALD reactors under processing conditions typically employed. Plasma-induced damage by ion bombardment is therefore not a major issue during most processes. It has furthermore been demonstrated that ion energies can be enhanced using substrate biasing, which can be used to tailor the material properties as demonstrated for several metal oxides.

*Published as: *H. B. Profijt and W. M. M. Kessels, ECS Trans. 50 (2012).*

## 4.1 Introduction

The interest in plasma-assisted ALD has increased significantly in recent years, which is mainly because of the additional freedom in process parameters and material properties compared to thermal ALD [1]. A plasma contains a large variety of species, such as ions, photons and radicals, which can all contribute to the growth process and resulting film properties [2]. The presence and importance of ions during the ALD process, however, have not extensively been addressed yet. In this contribution we will therefore consider the presence of ions for the reactor configurations commonly used for plasma-assisted ALD (see Fig. 4.1). Also, the influence of ions with enhanced energies on thin film material properties will be demonstrated and discussed.

Before discussing the presence of ions in a number of different reactor configurations, some basic properties of processing plasmas will be described:

(*i*) Plasmas are quasi-neutral when looking at macroscopic length scales (typically > 1 mm). This means that the density of electrons, $n_e$, equals the density of ions, $n_i$, when the presence of negative ions can be neglected.

(*ii*) Processing plasmas are generated by supplying ac electrical power (typically at radio frequency, RF, 13.56 MHz) to a gas to accelerate and therefore heat electrons. These hot electrons are able to dissociate, ionize, and excite gas-phase species during the collisions they undergo. The electron temperature, $T_e$, is a measure for the mean kinetic energy of the electrons in the plasma and its magnitude is such that the production of species in the plasma balances the loss. A typical value of the electron temperature is $\sim 3.3 \times 10^4$ K (approximately 3 eV). The temperature of ions and gas species typically remains in the order of 300 - 500 K for low operating pressures, due to ineffective energy transfer by collisions between heavy species and hot electrons.

(*iii*) A positive space charge layer is formed between the plasma and surfaces in contact with it (see Fig. 4.2). This so-called plasma sheath is deficient in electrons and develops after ignition of the plasma because thermal velocity of the electrons is much higher than the thermal velocity of the (much heavier) ions. To balance the flux of ions and electrons (such that the net electrical current towards floating surfaces is zero), an electrical field develops between the plasma and surfaces, which retards the electrons and accelerates the ions. The kinetic energy of ions arriving at surfaces (such as the reactor walls and the substrate) can be much higher than their thermal energy in the plasma because they are accelerated in the plasma sheath. For processing plasmas, the typical sheath thickness is in the range of $10^{-4}$ - $10^{-2}$ m, for a sheath voltage of several 10s up

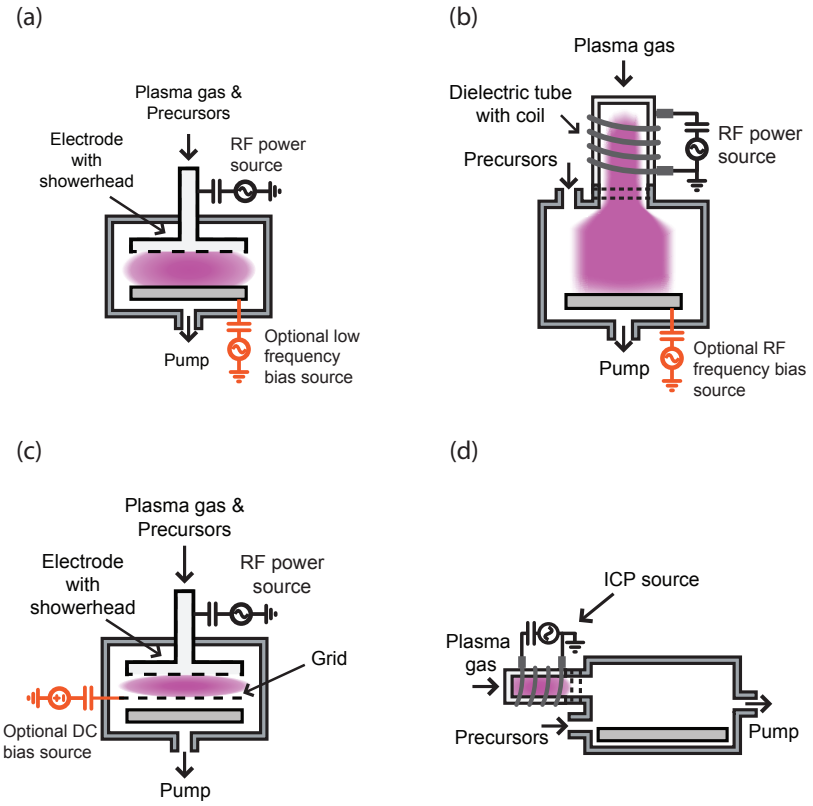



**Figure 4.1:** Reactor configurations commonly used for plasma-assisted ALD [1,3]: (a) direct plasma reactor with a capacitively-coupled plasma (CCP) source, (b) remote plasma reactor with an inductively-coupled plasma (ICP) source, (c) reactor in a remote capacitively-coupled plasma (CCP) configuration and (d) reactor equipped with an inductively-coupled plasma used as radical source for radical-enhanced ALD. Reactors (a) and (b) can be equipped with optional substrate bias sources (denoted in orange) to increase the ion energy and in reactor (c) the ion energy (amongst other plasma parameters) can be controlled by a bias voltage applied to the grid [4]. In (d) no ions are present above the substrate due to the large physical distance between the plasma source and the substrate.

to several 100s of Volts. Consequently, the plasma sheath does not follow the profile of 3D structures (e.g. trenches and vias) with $\mu$m and nm dimensions, in which films are often deposited by (plasma-assisted) ALD. Ions will only impact on surfaces parallel to the sheath, i.e. the planar substrate surface and the bottom of a 3D structure, however not on the sidewalls.

(*iv*) The energy and angle with which ions arrive at the substrate surface depends on the voltage across the plasma sheath and whether the ions undergo collisions while passing the sheath. In a collisionless plasma sheath (i.e. the mean free path of the ions is larger than the sheath thickness), ions will obtain a kinetic energy equal to $E_{\text{ion}} = e \cdot V_{\text{sheath}} = e \cdot (V_{\text{plasma}} - V_{\text{surface}})$ and arrive at an angle $\sim 0^\circ$ with respect to the normal to the film surface. In the equation, $V_{\text{sheath}}$ is the voltage across the sheath, $V_{\text{plasma}}$ is the plasma potential, and $V_{\text{surface}}$ is the surface potential. In a collisional plasma sheath, however, a portion of the ions will collide with neutral gas species and, consequently, new ions will be created by charge exchange collisions. These newly created ions will arrive at the substrate surface with lower energies and at higher angles with respect to the surface normal (see Fig. 4.3). With respect to ALD it is important to realize that the ions with relatively high energies will not impact on the walls of a trench due to their low angle with respect to the surface normal, whereas ions with lower energies will arrive at higher angles and therefore impact on the walls of a trench to some extent. Consequently, for both collisionless and collisional plasma sheaths, effects involving high-energy ions (such as the ones discussed in Sec. 4.4) will take place at the substrate surface, however not on the sidewalls. Whether ion-induced effects can take place at the bottom of a 3D structure depends on whether the ions lose energy during collisions with neutral gas species before reaching the bottom. Under the gas pressures usually employed ($\sim$10 mTorr up to $\sim$1 Torr), the mean free path of the ions is in the order of $10^{-4}$ - $10^{-2}$ m. For example, an Ar plasma with a sheath thickness of 1.2 mm ($V_{\text{sheath}}$ = 50 V, $T_{\text{e}}$ = 3 eV, and $n_{\text{e}} = 5 \times 10^9$ cm$^{-3}$) has a collisional sheath for gas pressures higher than 140 mTorr ($T_{\text{gas}}$ = 300 °C).

(*v*) The ion flux at the substrate can be enhanced straightforwardly by increasing the plasma power and reduced by increasing the gas pressure. Typically, the ion flux is in the order of $10^{11}$ - $10^{14}$ cm$^{-2}$ s$^{-1}$.

## 4.2 Reactor Configurations

In this section four reactor configurations used commonly for plasma-assisted ALD will be discussed.

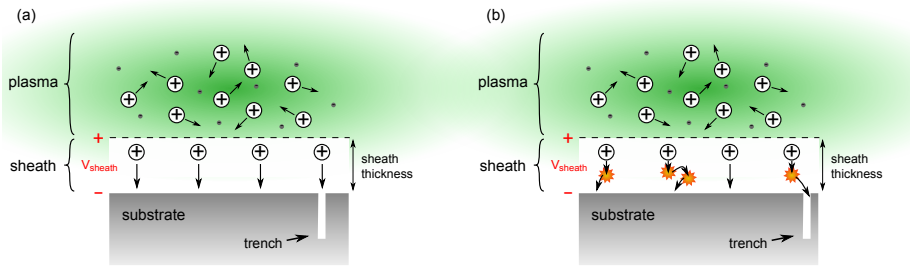



**Figure 4.2:** Illustrations of (a) a collisionless plasma sheath, in which ions are anisotropically accelerated towards the substrate surface, and (b) a collisional plasma sheath, in which ions are also accelerated however can lose energy and directionality during collisions with neutral gas species. The sheath thickness is orders of magnitude larger than the dimensions of trenches typically deposited by (plasma-assisted) ALD and therefore the sheath does not follow the profile of such trenches. In case the sheath is collisionless, ions will only impact on the planar substrate surface and the bottom of the trench, whereas in the case of a collisional sheath low-energy ions might also impact on the walls of the trench to some extent.

### 4.2.1 Direct CCP Reactor

The capacitively-coupled plasma (CCP) reactor is relatively straightforward and easy to scale up while allowing for uniform radical and ion fluxes at substrates with diameters of 300 mm and beyond. These properties make it a popular configuration for a variety of plasma processing techniques [2]. In a CCP reactor the plasma is generated between two planar electrodes, where typically one is powered by a radio frequency (RF, typically 13.56 MHz) signal while the other one is electrically grounded. The substrate is placed (or clamped) directly on one of the electrodes. Being basically a part of the electrode, the substrate contributes to the plasma generation and therefore this configuration is referred to as a "direct plasma" reactor. Consequently, it is not straightforward to vary the plasma and substrate conditions independently of each other, because, for example, a change in the substrate temperature will affect the gas temperature between the electrodes and consequently also changes the generation and density of the plasma species. Typically, CCP reactors used for plasma-assisted ALD operate at pressures of several hundreds of mTorr up to several Torr, with inter-electrode distances of a few mm up to a few cm and electrode areas which scale with the substrate size up to several tens of cm. It is noted that the substrate stage is usually a few percent larger than the substrate to allow for uniform plasma exposures. Generally, the electron temperature is in the range of 1 - 5 eV (often

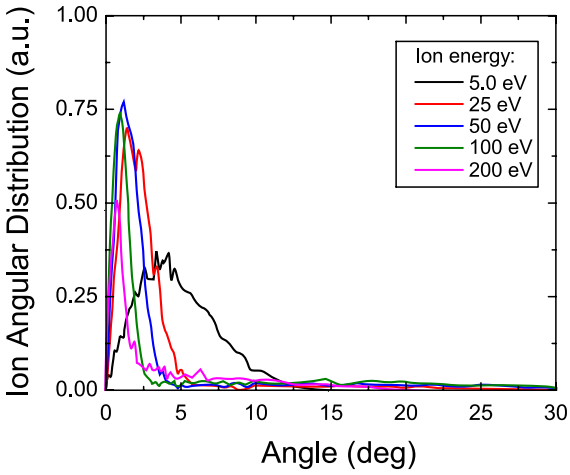



**Figure 4.3:** Ion angular distributions (IADs) for an Ar plasma with a collisional plasma sheath. The electrode is DC-biased at -200 V and the gas pressure is 300 mTorr. The data has been simulated by Kratzer *et al.* using a hybrid fluid dynamic/Monte Carlo model [5]. An electron temperature of 2.5 eV, an ion flux of 3.1 $\times$ $10^{16}$ $cm^{-2}$ $s^{-1}$, and a gas temperature of 500 K have been used as the input parameters for the model. Copyright 2001, The American Institute of Physics.

$\sim$3 eV) and the electron density can be in the range of $10^9$ - $10^{10}$ $cm^{-3}$ [2]. Depending on the area of the electrodes, typically 0.05 - 0.5 W $cm^{-2}$ (which corresponds to 50 - 300 W power) is supplied to the plasma which results in voltages of several hundreds of volts across the electrodes depending on the type of gas mixture used, the pressure, the power, and the reactor geometry.

In the case where the plasma is confined between two equally-sized electrodes, the sheath voltage (and thickness) is in principle equal at both electrodes (see Fig. 4.4a). Consequently, the sheath voltage is also the same for both electrodes and, on average, equal to half the amplitude of the RF voltage. In reality, however, capacitively-coupled plasmas are often not fully confined between the electrodes [6]. As such, the plasma also interacts with the grounded reactor walls (see Fig. 4.4b) such that the effective grounded electrode is much larger than the powered electrode. In order to balance the flux of charged particles within the RF cycle, the voltage across the plasma sheath at the powered electrode increases whereas the voltage across the grounded electrode decreases. The effect of the reactor walls becomes less important for smaller inter-electrode gap distances and larger sized of the electrodes.

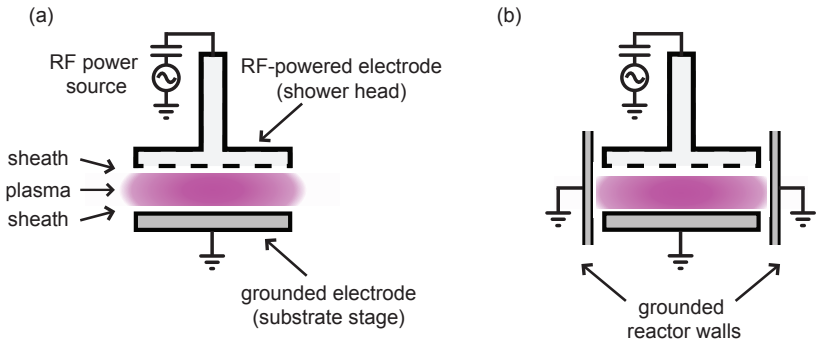



**Figure 4.4:** Illustrations of (a) a capacitively-coupled plasma (CCP) reactor where the plasma is confined between the two electrodes. Although the electrodes are symmetric the configuration is in reality often asymmetric because the plasma is additionally in contact with the grounded reactor walls. Configuration (b) represents therefore a realistic situation. The effect of the reactor walls decreases with decreasing inter-electrode gap distances and increasing size of the electrodes.

In Figs. 4.5a and 4.5b it is illustrated that the ion energies at the grounded substrate can be one order of magnitude lower compared to the powered electrode [7]. At 23 mTorr, the ion energy distribution (IED) for the grounded electrode reveals a peak at 16 eV, which is equal to $e \cdot V_{\mathrm{sheath}}$ (where $V_{\mathrm{sheath}}$ is the average voltage across the plasma sheath). The smooth mono-modal distribution furthermore reveals that the plasma sheath is collisionless. At the powered electrode, on the other hand, the ion energies are much higher and the multitude of peaks in the distribution reveal that the plasma sheath is collisional. This plasma sheath is much thicker compared to the one at the grounded electrode, because the sheath thickness increases with the voltage across it. In case no collisions would take place in the plasma sheath between ions and neutral gas species, the ions would obtain energies between 260 and 315 eV as indicated by the arrows in the graph. The peaks in the IED at lower energies correspond to ions created in the plasma sheath by charge-exchange collisions between ions and neutral gas species. When the pressure is increased, the ion energy at the grounded electrode initially increases due to an increasing sheath voltage, however it eventually decreases due to collisions in the sheath. At 225 mTorr, the IED shows that the mean ion energy is 11 eV whereas the area under the curve reveals that the ion flux, which is in the order of $10^{13}$ $cm^{-2}$ $s^{-1}$, has decreased with a factor $\sim$4. At the powered electrode the effect of a pressure increase is also obvious. As the pressure increases, the number of peaks decreases and eventually

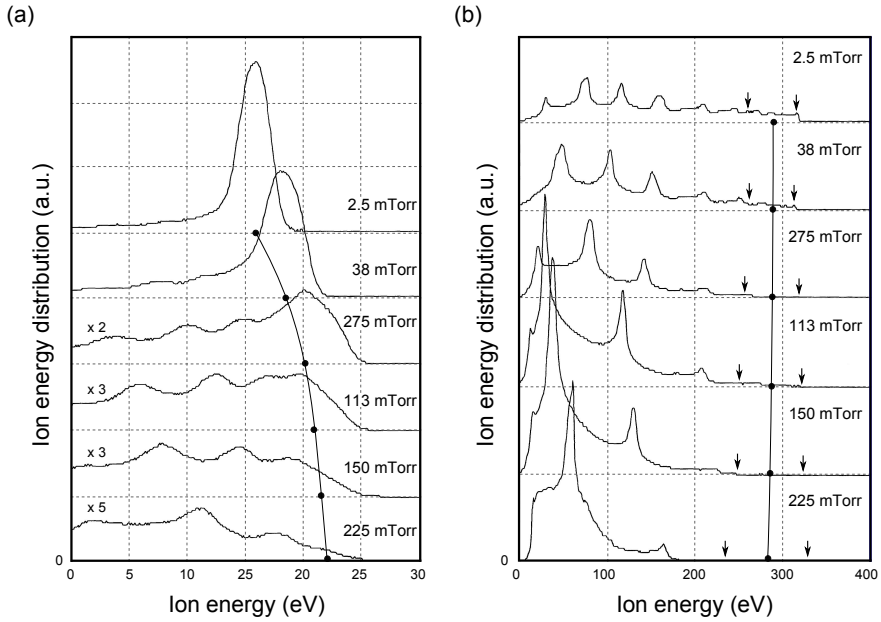



**Figure 4.5:** Ion energy distributions (IEDs) for an Ar plasma in a CCP configuration measured at (a) the grounded electrode and (b) at the powered electrode. The voltage across the sheaths is indicated by dots in both plots, whereas the minimum and maximum energy of ions that would cross the sheath without collisions is indicated by arrows in the right figure only. The amplitude of the RF signal applied to the powered electrode is 285 V, the inter-electrode distance is 5 cm and the diameter of the electrodes is 40 cm. The IEDs were measured by Zeuner *et al.* using a differentially-pumped quadrupole mass spectrometer with an electrostatic energy analyzer to filter the ions by their energy. Reproduced with permission from [7]. Copyright 1997, The Japanese Society of Applied Physics.

at 225 mTorr the main contribution comes from ions with an energy of 62 eV. It is noted that the area under the curve has increased by a factor two which indicates that the ion flux has doubled.

In this example, the gap distance between the electrodes (5 cm) is relatively large compared to the diameter of the electrodes (40 cm), which is typical for direct plasma reactors used for research purposes on plasma-assisted ALD. Commercial direct plasma reactors, designed for plasma-assisted ALD in a manufacturing environment, however, often have large electrode diameters (up to 300 mm and beyond) and small inter-electrode gap distances (down to 0.5 cm). Consequently, the contact area between the plasma and the grounded reactor walls is relatively small and therefore the voltage across the plasma sheath at the grounded substrate stage can be high [8]. However, the operating pressure for such tools is typically 1 Torr or higher and the RF voltage applied to the electrodes does not need to be very high due to the small gap distance. In reality, the ion energies in these tools are therefore typically still moderate and typically several tens of eV at maximum.

### 4.2.2 Remote ICP Reactor

In a remote plasma reactor, the plasma source is located at a distance from the substrate stage and the substrate is not involved in the generation of plasma species. Often, inductively-coupled plasma (ICP) sources operating at radio frequency (RF, 13.56 MHz) are used in this configuration in which electrical power is supplied to a coil wrapped around a dielectric tube (helical coil configuration) or placed on top of a dielectric window (planar coil configuration). Time-varying currents in the coil induce magnetic fields, which, in turn, induce electric fields that accelerate electrons in the gas kept inside the reactor to generate and sustain a plasma. The plasma potential of a plasma that is purely inductively-coupled does not vary in time and typically has a value of several tens of volts. Consequently, the ion energy at the grounded substrate is several tens of eV. In practice, however, the plasma is often also partly generated by capacitive coupling of the power into the plasma (i.e. the coil and a reactor part act as electrodes) and consequently the plasma potential and ion energy can have time-varying and power-dependent components superimposed on their static values. Capacitive-coupling can be eliminated using a Faraday shield placed between the coil and the dielectric tube or window [9]. The ICP source belongs to the class of high-density sources and typically has an electron temperature in the range of 1 - 5 eV (often $\sim$3 eV) and an electron density in the range of $10^{10}$ -

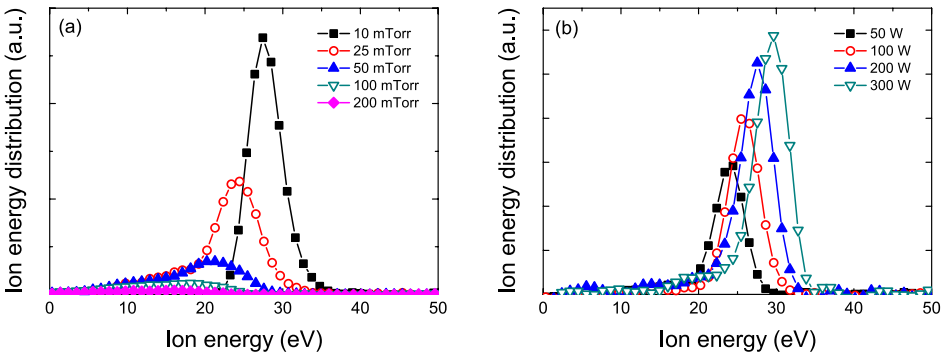



**Figure 4.6:** Ion energy distributions (IEDs) for ions in an Ar plasma generated in a reactor equipped with an ICP source for (a) various gas pressures (at power of 200 W) and (b) various plasma powers (at a pressure of 8 mTorr). The IEDs were recorded using a compact retarding field energy analyzer (RFEA) [11], placed directly on the substrate stage to measure the energy of ions arriving at the substrate surface. It is noted that the data for 100 and 200 mTorr might be affected by collisions between ions and neutrals within the RFEA.

$10^{12}$ cm$^{-3}$ [2]. The electron density is, however, often one or two orders of magnitude lower at the level of the substrate, especially when the distance between the plasma source and the substrate stage is relatively large. Despite being generated remotely, the plasma can still be ionizing directly above the substrate stage which is beneficial for the presence of plasma species at the substrate surface [10]. In a remote plasma configuration, the substrate and plasma conditions can be varied quite independently from each other, which for example allows for control over the ion energy by substrate biasing. The ion flux can be controlled at the same time by adjusting the plasma power. The remote plasma configuration furthermore allows for easy access for diagnostic tools to study material properties during deposition (e.g. thickness and optical properties using spectroscopic ellipsometry [12]) or plasma properties (e.g. $T_e$ and $n_e$ using a Langmuir probe [10] or excited plasma species using optical emission spectroscopy [13]).

Figures 4.6a and 4.6b show IEDs for ions from an Ar plasma measured in a plasma-assisted ALD reactor equipped with a ICP source (helical coil configuration) [14]. The ion energy is mono-modally distributed with an average value that decreases from 27 to 16 eV with increasing pressure and increases with increasing power from 24 to 30 eV [10]. For the lower pressures (i.e. 10, 25 and 50 mTorr), the decrease of the energy with

the pressure can be attributed mainly to a decrease of the plasma potential due to a lowered electron temperature resulting from reduced ion- and electron loss with increasing pressure. For higher pressures (i.e. 100 and 200 mTorr), collisions in the plasma sheath also play a role and consequently the ion energy decreases further. The modest increase of the ion energy with the plasma power for constant pressure is an indication of parasitic capacitive coupling causing the ion energy to increase from 24 to 30 eV when the power is increased from 50 to 300 W. The ion flux is in the range of $10^{13}$ - $10^{14}$ $cm^{-2}$ $s^{-1}$ and decreases with a factor $\sim$26 when the pressure is increased from 10 to 200 mTorr and increases with a factor $\sim$2 when the power is increased from 50 to 300 W, as calculated from the areas under the IEDs.

### 4.2.3 Remote CCP Reactor

A relatively new embodiment for plasma-assisted ALD is the remote CCP reactor (also known as the "triode" configuration) [15,16]. In this configuration, remote plasma conditions can be obtained in a CCP reactor by placing a grid between the two electrodes. The plasma is now generated between the powered top electrode and the grid [15] to avoid contact between the plasma and the substrate surface. Consequently, the substrate stage is not involved in the plasma generation, contrary to in a CCP reactor. For a grounded grid, the electron temperature and the electron density above the grid are comparable to a direct CCP reactor with a grounded substrate. Below the grid no active plasma is present when the diameter of the holes in the grid is smaller than twice the plasma sheath thickness at the grid, such that hot electrons, which are able to generate plasma, cannot penetrate the region below the grid [17]. For a plasma with an electron temperature of 3 eV and a plasma potential of 50 V the diameter of the holes in the grid need to be $\leq$5.3 mm and $\leq$1.7 mm to keep the plasma above the grid for typical electron densities of $10^{9}$ $cm^{-3}$ and $10^{10}$ $cm^{-3}$, respectively. When the grid is grounded, ions are still able to penetrate into the area under the grid by simply passing through the holes. Under pressures typically employed (i.e. hundreds of mTorr) and for relatively large gap distances between the grid and the substrate, the ions will, however, undergo several collisions before reaching the substrate. Consequently, the ion energy at the substrate surface is negligible. It is noted that even when the grid has many holes, the grid can still have a relatively large surface area on which radicals can recombine when colliding with the grid material. Placing a grid between the two electrodes therefore can have a significant effect on the radical flux to the substrate surface.

### 4.2.4 Radical-Enhanced Reactor

A radical-enhanced ALD reactor is often a thermal ALD reactor to which a commercially available plasma generator is fitted. The plasma source can be of any type including ICP and microwave plasma sources. Plasma generation typically takes place at a relatively far distance from the substrate and consequently the plasma species undergo many surface and gas-phase collisions when passing though the reactor tubing to reach the substrate. Ions and electrons can get lost easily during these collisions, which is why this type of configuration is typically referred to as a "radical-enhanced" ALD reactor. Due to their non-zero surface recombination probability also radicals can get lost when undergoing collisions with the walls while flowing through the tubing [18]. The surface recombination probability depends on the type of radical and the wall material. Hydrogen radicals, for example, have a low surface recombination probability on silica, whereas their recombination probability on most metals is relatively high. For metallic reactor tubing, hydrogen radical densities can therefore be considerably reduced above the substrate surface and consequently saturation of the second ALD half-cycle might take relatively long.

## 4.3 Enhancing Ion Energies in Plasma-Assisted ALD Reactors

In the Introduction of this Chapter it was discussed that the sheath voltage is equal to the potential difference between the plasma and the electrode at which the substrate is placed. A straightforward way to increase the voltage across the sheath, and consequently the ion energy, would be to apply a bias signal with a negative average voltage to a non-grounded substrate stage [4,19-21]. This can, for instance, be a DC, AC, or a pulse-shaped signal [22]. DC signals are, however, not appropriate when non-conducting thin films and non-conducting substrates are employed.

In a direct plasma CCP reactor, both electrodes are actively involved in the plasma generation and therefore it is complicated to enhance the ion energy using substrate biasing without affecting other plasma properties. Applying a RF signal to the substrate stage, for example, will also result in additional generation of plasma and/or interference with the RF signal applied to the adjacent powered electrode. By using a signal with a frequency much lower than that of the RF power signal (e.g. 10 - 100s of kHz), however, ion energies can be enhanced without substantially affecting the plasma properties. By

varying the phase or the amplitude of the substrate bias signal, control over the ion energy can be obtained [23]. In a remote plasma ICP reactor, the ion energy can be tuned relatively easily using substrate biasing as the region where the plasma is generated and the substrate stage are geometrically separated. Consequently, a bias signal can be applied to the substrate stage to enhance the ion energy without affecting the plasma properties. Substrate biasing can also be used in a remote CCP reactor to enhance the ion energy. Alternatively, the grid can be biased to tune the electron temperature and the electron and ion density, as reported in the literature [16,22,24].

Figure 4.7 shows an ion energy distribution (IEDs) for a remote plasma ALD reactor equipped with substrate biasing (either RF biasing or substrate-tuned biasing). At a bias voltage of 0 V, the data shows that the ion energy is mono-modally distributed with a mean value of 53 $\pm$ 1 eV. When the average substrate voltage is now enhanced (e.g. by applying RF power to the substrate stage or by tuning the impedance of the substrate stage with respect to the ground), the ion energy increases and the distribution becomes bimodal. The two peaks in the distribution represent ions that travel through the plasma sheath at different time-instances of the RF cycle, i.e. ions that pass the sheath when the voltage difference between the plasma and substrate is relatively low will obtain a lower energy compared to ions that pass the sheath when the voltage difference is relatively high. The width of the distribution increases with the bias voltage and at an average bias voltage of -200 V, the average ion energy is 246 $\pm$ 1 eV and the minimum and maximum values are 219 $\pm$ 1 and 272 $\pm$ 1 eV, respectively. The ion flux is in the order of $10^{14}$ $cm^{-2}$ $s^{-1}$ and remains relatively constant when varying the bias voltage, as can be concluded from the areas under the IEDs.

## 4.4 Influence of Ions on Metal-Oxide Films Deposited by Plasma-Assisted ALD

As discussed in this Chapter, the ion energy is in the order of several tens of eV under processing conditions typically used for remote and direct plasma ALD. This energy is well below the threshold for typical ion-induced damage processes, whereas the additional energy provided to the deposition surface can be sufficiently high to stimulate processes such as ligand-desorption and adatom migration [20,25]. In case the ion energies would be increased using substrate biasing, additional physical surface reactions could be expected to play a role during ALD [20,25].

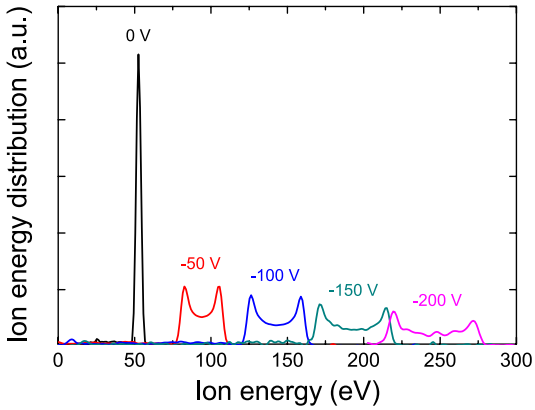



**Figure 4.7:** Ion energy distributions measured in an $O_2$ plasma, generated in a remote ICP reactor equipped with substrate biasing [19,20]. The gas pressure and ICP power were 8 mTorr and is 550 W. The ion energy was enhanced by substrate-tuned biasing in this example, which enables control of the impedance between the substrate stage and the ground potential and, consequently, allows for average bias voltages of up to -200 V.

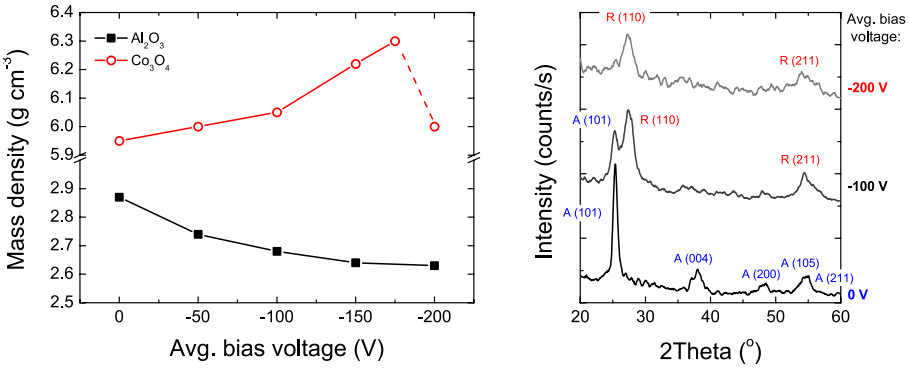



**Figure 4.8:** The influence of substrate biasing during plasma-assisted ALD on (a) the density of $Al_2O_3$ (200 °C) and $Co_3O_4$ (300 °C) films as measured by x-ray reflectivity (XRR), and (b) the crystallinity of $TiO_2$ (300 °C) films as measured by x-ray diffraction (XRD). The peaks corresponding to the anatase and rutile phase of $TiO_2$ were identified in the XRD scans and indicated by "A" and "R", respectively.

To investigate the impact of high-energy ions on the material properties of ALD-synthesized films, $Al_2O_3$, $Co_3O_4$, and $TiO_2$ films were deposited using plasma-assisted ALD with substrate biasing. The deposition processes involved trimethylaluminium [$Al(CH_3)_3$], cobaltocene [$CoCp_2$], and Star-Ti [$Ti(Cp^{Me5})(OMe)_3$], as the precursors respectively [26-28], in combination with $O_2$ plasmas (8 mTorr, 200 W). Substrate-tuned biasing was employed to obtain bias voltages of up to -100 V, whereas 0-24 W RF substrate biasing was used to obtain a voltage of up to -200 V at the substrate stage. In Fig. 4.8a, experimental results are shown for $Al_2O_3$ and $Co_3O_4$ thin films. For $Al_2O_3$, the mass density decreases monotonically when the bias voltage is increased from 0 V to -200 V, which demonstrates that the impact of high energy ions is detrimental to the material quality. At the same time the growth-per-cycle (GPC, measured by spectroscopic ellipsometry) increases with increasing bias voltage (data not shown). For the $Co_3O_4$ film, on the other hand, the mass density and the GPC show different trends; the films become considerably denser and the GPC is lower when the bias voltage is increased up to -175 V. At an average substrate bias voltage of -200 V, however, the GPC is the lowest, whereas the mass density of the films is comparable to the situation without biasing. For this latter case it is expected that the high ion energy facilitates sputtering of the film, while suppressing the beneficial effect of film densification. The third example of the impact of high energy ions is shown in Fig. 4.8b where it is illustrated that the crystallinity of $TiO_2$ thin films can be gradually tuned from the anatase phase to the rutile phase by increasing the substrate bias voltage from 0 to -200 V. Usually, the anatase phase is obtained by plasma-assisted or thermal ALD of $TiO_2$ at substrate temperatures of 300 °C. Specific starting layers or a high temperature anneal are required to obtain the rutile phase under such conditions [29]. These results in Fig. 4.8b reveal, however, that it is possible to obtain the rutile phase of $TiO_2$ at 300 °C by only increasing the ion energy. The anatase and rutile phases of $TiO_2$ offer different optical, catalytic, and dielectric properties and consequently tuning the crystallinity during deposition is interesting for many applications.

## 4.5 Conclusions

In this Chapter, the influence of ions during plasma-assisted ALD was discussed. The presence of ions during the plasma step, as characterized by the ion energy and the ion flux, was discussed for four reactor configurations commonly used for plasma-assisted ALD. It has been illustrated that during plasma-assisted ALD in both remote and direct plasma reactors the ion energies are moderate and in the order of several tens of eV un-

der processing conditions typically used. The ion energy is typically below the damage threshold and beneficial effects such as ligand-desorption and adatom migration can be expected. Moreover, the possibility to tune the ion energy using substrate-tuned biasing and RF substrate biasing was demonstrated for a remote plasma reactor equipped with an inductively-coupled plasma (ICP) source. Using ions accelerated up to $272 \pm 1$ eV, it was shown that thin film properties can be tuned by varying the bias voltage. For $Al_2O_3$ it has been shown that the mass density decreased as a result of the high ion energy, a detrimental effect which can be classified as ion-induced damage. For $Co_3O_4$ is has been demonstrated that the density can be increased by high energy ions, although at too high energies sputtering can start to play a role. For $TiO_2$ films it was shown that the crystallinity could be tuned gradually from the anatase to the rutile phase using substrate biasing. The latter two examples, i.e. densification and tuning of the crystallinity, illustrate that ion energy control can be beneficial for tailoring thin film material properties.

# Acknowledgements

Dr. T. Fernández Landaluce, W. Keuning, J. J. A. Zeebregts, M. J. F. van de Sande, J. J. L. M. Meulendijks, C.A.A. van Helvoirt, and H. M. M. de Jong (all TU/e) are acknowledged for their assistance. Dr. A. C. Bronneberg is acknowledged for performing the PIM measurements (see Addendum). This work is carried out within the Thin Film Nanomanufacturing (TFN) programme and is supported financially by the Dutch Technology Foundation STW.

# Addendum

In this addendum it is discussed how electrical power is coupled into inductively-coupled plasmas (ICPs) and capacitively-coupled plasmas (CCPs).

## 4.5.1 Inductively-Coupled Plasma Source

Figure 4.9a shows an electrical equivalent circuit of an inductively-coupled plasma (ICP), the power source, the matching network and the coaxial cable of a typical remote plasma ALD reactor. The home-built "ALD-I" reactor has been taken as an example. The real and equivalent electrical components are summarized in Table 4.1. The plasma source itself consists of a coil wrapped around a dielectric tube (helical ICP configuration). From an electrical point of view, the ignited plasma behaves like a coil, $L_p$, in series with a

**Table 4.1:** Overview of the real and equivalent components given in the electrical circuits in Fig. 4.1a. For the ICP source, $C_{i1}$ and $C_{i2}$ were measured using a *LC*-meter for the plasma in a matched condition (i.e. $Z_{match}$ = 50 Ω), from which $R_{pi}$ and $L_p$ were calculated. The range of $C_{i1}$ and $C_{i2}$ was printed on the capacitors in the matching network. $R_{src}$ and $Z_{coax}$ were obtained from Refs. 37 and 38.

| Plasma source | Component | Description | Value |
|---|---|---|---|
| ICP | $R_{pi}$ | plasma resistance | 11.2 Ω |
| | $L_p$ | ICP coil inductance | 2.5 μH |
| | $C_{i1}$ | parallel variable capacitor in matching network | 5 -500 pF |
| | $C_{i2}$ | series variable capacitor in matching network | 5 - 125 pF |
| | $R_{src}$ | output resistance of power source | 50 Ω |
| | $Z_{coax}$ | characteristic impedance coax cable | 50 Ω |

resistor, $R_{pi}$ [30]. The coil accounts for the physical coil wrapped around the dielectric tube (or placed on top of the dielectric window, in case of a planar ICP source) and the induced electron current which generates the plasma. The plasma resistance represents the dissipation of electrical power by the plasma [30]. For an $O_2$ plasma generated in the "ALD-I" at 100W ICP power and 7.5 mTorr pressure, a plasma impedance, $Z_{plasma}$, of 11.2 + j 213.3 Ω was calculated which means that $R_{pi}$ = 11.2 Ω and $L_p$ = 2.5 μH.

The RF (radio frequency) power source has a frequency, *f*, and output resistance, $R_{src}$, of 13.56 MHz and 50 Ω, respectively. In order to deliver the maximum power into the load (i.e. the plasma), the load impedance, $Z_{load}$, should be equal to $R_{src}$ [31]. This is the purpose for adding a matching network to the circuit.

Due to the relatively high frequency of the power signal, the electromagnetic behavior of the signal in the coaxial cable should be taken into account (i.e. transmission line theory should be applied) [32,33]. Consequently, the coaxial cable responds like an electrical network that consists of capacitors and inductances (See Fig. 4.10). The characteristic impedance, $Z_{coax}$, of the cable (type: RG-213) is 50 Ω, which means that it is designed to transfer signals with a voltage to current ratio of 50 (Ω) [32]. The coaxial cable has a solid polyethylene dielectric and therefore the wave propagation speed is 66% of the speed of light. Consequently, the wavelength, λ, of the signal is 14.8 m [34]. In case $Z_{match}$ is not 50 Ω, then $Z_{load}$ is a function of the cable length *l* [33]:

$$Z_{load} = Z_{coax}\frac{Z_{match} + jZ_{coax}\tan(2\pi\lambda^{-1}l)}{Z_{coax} + jZ_{match}\tan(2\pi\lambda^{-1}l)}, \tag{4.1}$$

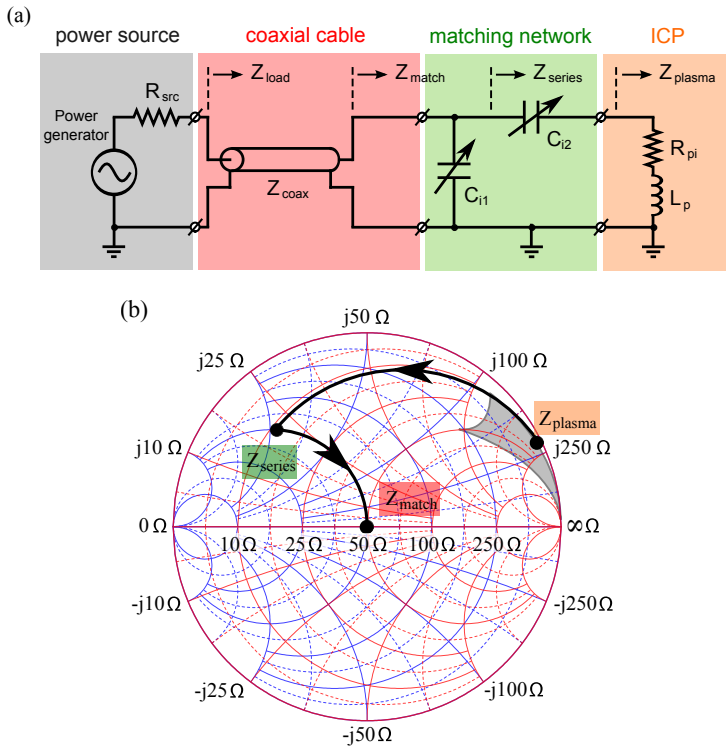



**Figure 4.9:** (a) Equivalent electrical circuit of an inductively-coupled plasma (ICP) source, connected to a power source via a coaxial cable and a matching network. See Table 4.1 for a description of the real and equivalent electrical components. (b) Smith chart that illustrates how $Z_{\text{plasma}}$ is matched into $Z_{\text{match}}$. The gray area marks the range of values for $Z_{\text{plasma}}$ that can be matched to 50 Ω using this matching network.

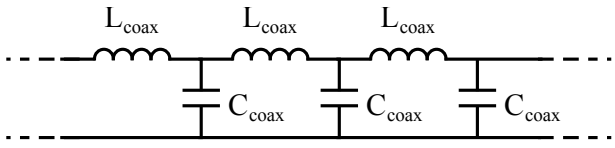



**Figure 4.10:** Simplified equivalent electrical circuit of a coaxial cable. The resistance in the cable is neglected.

**Table 4.2:** Overview of the real and equivalent components given in the electrical circuits in Fig. 4.3a. For the CCP plasma, the phase and the absolute impedance of the plasma have been measured using a Plasma Impedance Monitor (PIM) [36], from which $R_{pc}$ and $C_p$ were calculated. The range of $C_{c1}$ and $C_{c2}$, and the static value of $L_c$ were measured using a *LC*-meter. $R_{src}$ and $Z_{coax}$ were obtained from Refs. 37 and 38.

| Plasma source | Component | Description | Value |
|---|---|---|---|
| CCP | $R_{pc}$ | plasma resistance | 7.4 Ω |
| | $C_p$ | sheath capacitances | 253 pF |
| | $C_{c1}$ | parallel variable capacitor in matching network | 173 - 932 pF |
| | $C_{c2}$ | series variable capacitor in matching network | 45 - 136 pF |
| | $L_c$ | series coil in matching network | 2.5 $\mu$H |
| | $R_{src}$ | output resistance of power source | 50 Ω |
| | $Z_{coax}$ | characteristic impedance coax cable | 50 Ω |

The equation illustrates that $Z_{load} = Z_{match}$ when $l = 1/2\lambda$ mod$(1/2\lambda)$ and $Z_{load} = Z^2_{coax}/Z_{match}$ when $l = 1/4\lambda$ mod$(1/4\lambda)$. The length of the cable is not important when $Z_{load} = Z_{match} = Z_{coax}$. For $l << 1/4\ \lambda$, which was the case for the configuration in this specific example, $Z_{load}$ is not influenced too much by the cable length.

To transform $Z_{plasma}$ impedance to 50 Ω, a so-called *L*-type matching network with two variable capacitors, $C_{i1}$ and $C_{i2}$, is used (see Fig. 4.9a). The Smith chart in Fig. 4.9b illustrates how the matching network transforms the complex plasma impedance into 50 Ω : first series capacitor $C_{i2}$ (value 61 pF) transforms $Z_{plasma}$ to $Z_{series}$ ( = 11.2 + j 20.8 Ω ) after which parallel capacitor $C_{i1}$ (value 437 pF) transforms $Z_{series}$ into $Z_{match}$ which is equal to 50 Ω. For more details on how to use Smith charts, see Ref. 5.

### 4.5.2 Capacitively-Coupled Plasma Source

The electrical equivalent circuit of a capacitively-coupled plasma (CCP) is shown in Fig. 4.11a. The real and equivalent electrical components are summarized in Table 4.2. The home-built "a$\mu$se" reactor has been taken as an example. A CCP plasma behaves like a capacitor, $C_p$, and a resistor, $R_{pc}$, in series, which account for the plasma sheath capacitance and the dissipation of electrical power by the plasma, respectively [30]. For an $H_2$ plasma generated in the home-built "a$\mu$se" setup (1 cm gap distance, 10 cm$^2$ electrode area [35]) at 100 W power and 10 Torr pressure, the plasma impedance, $Z_{plasma}$, was measured to be 7.4 - j 46.4 Ω. This means that $R_{pc}$ = 7.4 Ω and $C_p$ = 253 pF.

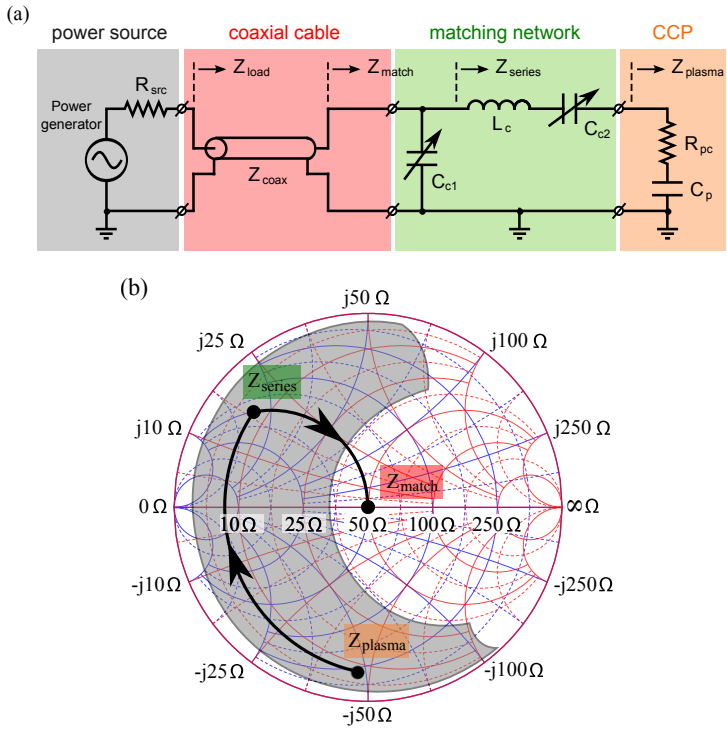



**Figure 4.11:** (a) Equivalent electrical circuit of a capacitively-coupled plasma (CCP) source, connected to a power source via a coaxial cable line and a matching network. See Table 4.2 for a description of the real and equivalent electrical components. (b) Smith chart that illustrates how $Z_{\text{plasma}}$ is matched into $Z_{\text{match}}$. The gray area marks the range of values for $Z_{\text{plasma}}$ that can be matched to 50 Ωusing this matching network.

As was the case with the ICP plasma, a coaxial cable (type: RG-213) with a length $<<$ 1/4 $\lambda$ was used to connect the 13.56 MHz power source with a *L*-type matching network. Again a matching network with two capacitors, $C_{c1}$ and $C_{c2}$, is used, however also a coil, $L_c$, is present with a self-inductance of 2.5 $\mu$H (see Fig. 4.11a). As illustrated in the Smith chart (see Fig. 4.11b.), the matching network transforms $Z_{\text{plasma}}$ into $Z_{\text{match}}$. $Z_{\text{match}}$ is 50 Ω when $C_{c1}$ and $C_{c2}$ are 564 and 79 pF, respectively.

# References

1. H. B. Profijt, S. E. Potts, M. C. M. van de Sanden, and W. M. M. Kessels, J. Vac. Sci. Technol. A, 29, 050801 (2011).

2. M. A. Lieberman and A. J. Lichtenberg, Principles of Plasma Discharges and Materials Processing, 2nd ed., John Wiley Sons, New York, (2005).
3. S. B. S. Heil, J. L. van Hemmen, C. J. Hodson, N. Singh, J. H. Klootwijk, F. Roozeboom, M. C. M. van de Sanden, and W. M. M. Kessels, J. Vac. Sci. Technol. A 25, 1357 (2007).
4. E. A. Edelberg, A. Perry, N. Benjamin, and E. S. Aydil, J. Vac. Sci. Technol. A, 17, 506 (1999).
5. M. Kratzer, R. P. Brinkmann, W. Sabisch, and H. Schmidt, J. Appl. Phys. 90, 2169 (2001).
6. H. R. Koenig and L. I. Maissel, IBM J. Res. Develop. 14, 168 (1970).
7. M. Zeuner, Horst Neumann, and J. Meichsner, Jpn. J. Appl. Phys. 36, 4711 (1997).
8. J. W. Coburn and E. Kay, J. Appl. Phys. 43, 4965 (1972).
9. J. Hopwood, Plasma Sources Sci. Technol. 1, 109 (1992).
10. H. B. Profijt, P. Kudlacek, M. C. M. van de Sanden, and W. M. M. Kessels, J. Electrochem. Soc. 158, G88 (2011).
11. D. Gahan, B. Dolinaj, and M. B. Hopkins, Rev. Sci. Instrum. 79, 033502 (2008).
12. E. Langereis, S. B. S. Heil, H. C. M. Knoops, W. Keuning, M. C. M van de Sanden, and W. M. M. Kessels, J. Phys. D: Appl. Phys. 42, 073001 (2009).
13. A. J. M. Mackus, S. B. S. Heil, E. Langereis, H. C. M. Knoops, M. C. M. van de Sanden, and W. M. M. Kessels, J. Vac. Sci. Technol. A 28, 77 (2010).
14. E. Langereis, H. C. M. Knoops, A. J. M. Mackus, F. Roozeboom, M. C. M. van de Sanden, and W. M. M. Kessels, J. Appl. Phys. 102, 083517 (2007).
15. T. O. Kääriäinen and D. C. Cameron, Plasma Process. Polym. 6, S237 (2009).
16. H. Kim, S. Woo, J. Lee, Y. Kim, H. Lee,I.-J. Choi, Y.-D. Kim,C.-W. Chung, and H. Jeon, J. Electrochem. Soc. 158, H21 (2011).
17. J. I. Hong, S. H. Seo, S. S. Kim, N. S. Yoon, C. S. Chang, and H. Y. Chang, Physics of Plasmas 6, 1017 (1999).
18. H. C. M. Knoops, E. Langereis, M. C. M. van de Sanden, and W. M. M. Kessels, J. Electrochem. Soc. 157, G241 (2010).
19. H. B. Profijt, M. C. M. van de Sanden, and W. M. M. Kessels, Electrochem. Solid-State Lett., 15, G1-G3 (2012).
20. H. B. Profijt, M. C. M. van de Sanden, and W. M. M. Kessels, J. Vac. Sci. Technol. A, submitted to J. Vac. Sci. Technol. A. (2012).
21. E. Kawamura, V. Vahedi, M. A. Lieberman, and C. K. Birdsall, Plasma Sources Sci. Technol. 8, R45 (1999).

22. P. Kudlacek, R. F. Rumphorst, and M. C. M. van de Sanden, J. Appl. Phys. 106, 073303 (2009).
23. P. C. Boyle, A. R. Ellingboe and M. M. Turner, J. Phys. D: Appl. Phys. 37, 697 (2004).
24. K. Kato, S. Iizuka, and N. Sato, Appl. Phys. Lett. 65, 816 (1994).
25. T. Takagi, J. Vac. Sci. Technol. A., 2, 382 (1984).
26. S. K. Kim, W. -D. Kim, K. -M. Kim, C. S. Hwang, and J. Jeong, Appl. Phys. Lett. 85, 4112 (2004).
27. M.E. Donders, H.C.M. Knoops, M.C.M. van de Sanden, W.M.M. Kessels, and P.H.L. Notten, J. Electroch. Soc. 158, G92 (2011).
28. E. Langereis, R. Roijmans, F. Roozeboom, M. C. M. van de Sanden, and W. M. M. Kessels, J. Electrochem. Soc. 158, G34 (2011).
29. S. K. Kim,W. -D. Kim, K. -M. Kim, C. S. Hwang, and J. Jeong, Appl. Phys. Lett., 85, 4112 (2004).
30. M. A. Lieberman and A. J. Lichtenberg, "Principles of Plasma Discharges and Materials Processing", 2nd ed. (John Wiley & Sons, New York, 2005).
31. H.W. Jackson (1959) Introduction to Electronic Circuits, Prentice-Hall.
32. D. F. Brown, "Radio Frequency Fundamentals: An Intuitive Approach" (Comdel, 2004).
33. "Transmission line", http://en.wikipedia.org/wiki/Transmission_line, (accessed August 2012).
34. "Smith Chart Tutorial", http://www.fourier-series.com/rf-concepts/smithchart.html, (accessed August 2012).
35. A. C. Bronneberg, "Plasma Processing of Microcrystalline Silicon: Filling in the Gaps", PhD thesis, Eindhoven University of Technology, Eindhoven (2012).
36. J. Beckers, "Dust particle(s) (as) Diagnostics in Plasmas", PhD thesis, Eindhoven University of Technology, Eindhoven (2011).
37. Website RFVII, http://www.rfvii.com/, (accessed August 2012).
38. Website Farnell, http://nl.farnell.com/, (accessed August 2012).

Chapter 5

# Ion and Photon Surface Interaction during Remote Plasma ALD of Metal Oxides*

**Abstract** The influence of ions and photons during remote plasma atomic layer deposition (ALD) of metal-oxide thin films was investigated for different $O_2$ gas pressures and plasma powers. The ions have kinetic energies of $\leq$35 eV and fluxes of $\sim 10^{12}$ - $10^{14}$ $cm^{-2}$ $s^{-1}$ toward the substrate surface: low enough to prevent substantial ion-induced film damage, but sufficiently large to potentially stimulate the ALD surface reactions. It is further demonstrated that 9.5 eV vacuum ultraviolet photons, present in the plasma, can degrade the electrical performance of electronic structures with ALD-synthesized metal-oxide films.

*Published as: *H. B. Profijt, P. Kudlacek, M. C. M. van de Sanden, and W. M. M. Kessels, J. Electrochem. Soc. 158, G88 (2011).*

## 5.1 Introduction

The interest in plasma-assisted atomic layer deposition (ALD) has grown considerably over the last few years, as evidenced by the increased number of plasma-assisted ALD reactors installed and processes developed. This is a result of several studies that demonstrated the merits offered by plasma-assisted ALD, such as improved material properties, higher throughput, additional control over material properties, more freedom in precursors and processes, and facilitated deposition at reduced substrate temperatures [1-3]. For thermal ALD of metal oxides typically $H_2O$ vapor, $O_2$ gas or $O_3$ are employed for the oxidation reactions, whereas during plasma-assisted ALD the oxidation reaction of the surface and ligands is driven by reactive radical species present in the $O_2$ plasma. However, besides radicals, additional species such as electrons, ions and photons are present in the plasma. Their densities and energies vary with the reactor geometry, the plasma source type, the gas pressure and flow, and the plasma power [4]. Plasma-surface interaction during plasma-based thin film processing is a topic addressed extensively in the literature, but not for the specific case of plasma-assisted ALD. Therefore, the presence of ions and photons during the plasma exposure step of plasma-assisted ALD was studied to identify the interactions of ions and photons with the surface and the potential effect on the ALD growth process. Experiments were carried out under conditions typical for remote plasma ALD of metal oxides in three inductively coupled plasma (ICP) setups used for ALD: the Oxford Instruments FlexAL and OpAL reactors, and the home-built ALD-I reactor. In this Chapter it is demonstrated that, although not always taken into account, the ions and photons present in plasmas during plasma-assisted ALD can influence the deposition process and the material quality significantly.

## 5.2 Experimental

The kinetic energy $E_i$ and flux $\Gamma_i$ of ions accelerated to the substrate surface were studied using an Impedans Semion retarding field energy analyzer (RFEA) [5] and a tungsten planar current collecting probe, respectively. Using the RFEA the flux of ions passing through a system of biased grids was measured, from which the ion energy distribution (IED) was determined. The planar probe with an area of 1 $cm^2$ was used to measure the total ion current to the substrate, from which the ion flux $\Gamma_i$ was calculated. Additionally, measurements were conducted with a double Langmuir probe at 5 mm above the center of the substrate stage to non-intrusively measure the electron temperature $T_e$ and the electron density $n_e$ in the plasma.

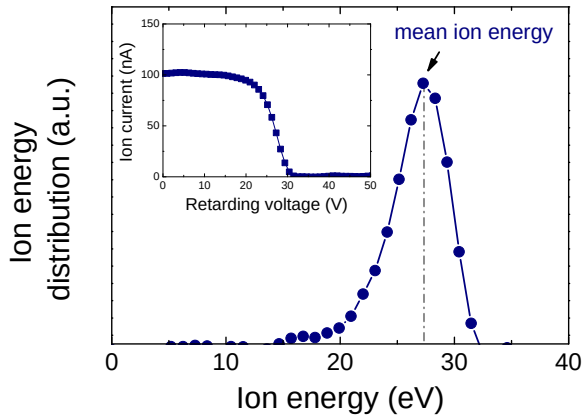



**Figure 5.1:** Ion energy distribution (IED) as measured for an $O_2$ plasma at standard conditions in the FlexAL reactor, with the RFEA placed at the substrate stage. The dashed line indicates the mean ion energy $\hat{E}_i$ of 27.3 $\pm$ 1.0 eV. The inset shows the data from the original *I*-*V* measurement from which the IED was derived.

The visible emission in the 400-800 nm range was recorded with an OceanOptics USB2000+ spectrometer, whereas vacuum ultraviolet (VUV) and ultraviolet (UV) emission in the 100-400 nm range was detected by a differentially pumped McPherson 234/302 monochromator. The relative emission intensities were recorded from the position directly above the substrate stage.

Most plasma measurements were carried out in the Oxford Instruments FlexAL and OpAL reactors, for $O_2$ pressures of 3.8-187.5 mTorr and powers in the 100-500 W range. Only the emission study was carried out in the home-built ALD-I reactor, at pressures of 3.8-37.5 mTorr and powers of 100-300 W. A gas $O_2$ pressure $p$ of 7.5 mTorr and a plasma power $P$ of 100 W were used as standard conditions.

## 5.3 Results and Discussion

### 5.3.1 Ions and their Surface Interaction

A typical ion energy distribution (IED) measured by the RFEA is displayed in Fig. 5.1. The majority of the ions arrive at the substrate surface with a kinetic energy $\hat{E}_i$ of 27.3 $\pm$ 1.0 eV, which is the ion energy where the IED is at its maximum value. The kinetic energy obtained by the ions in the plasma sheath is determined by the difference between the plasma potential $V_p$ and the substrate potential $V_s$. The energy has a mean value equal

to $e \cdot V_p$ for a grounded substrate stage and it is distributed due to fluctuations in $V_p$ and collisions between the ions and other plasma species in the sheath. The corresponding average ion flux $\Gamma_i$ is (5.0 $\pm$ 0.3) $\times$ $10^{13}$ $cm^{-2}$ $s^{-1}$. The energy and flux of the ions can be attributed mainly to singly ionized $O_2$ molecules, as reported by Gudmundsson *et al.* [6]. The values of $T_e$ and $n$ are 3.4 $\pm$ 1.0 eV and (3.0 $\pm$ 0.6) $\times$ $10^8$ $cm^{-3}$ respectively. The electron density directly above the substrate stage is approximately two orders of magnitude lower compared to the density in the plasma bulk [6].

The pressure $p$ and power $P$ dependence of $\hat{E}_i$, $T_e$, $\Gamma_i$ and $n_e$ is illustrated in Fig. 5.2. For pressures up to 22.5 mTorr, measurements were carried out in the FlexAL reactor, whereas for pressures $\geq$ 85 mTorr data was obtained from measurements in the OpAL reactor. $\hat{E}_i$ is given only for $p \leq$ 22.5 mTorr, because at higher pressures the ion current was too low to be measured by the RFEA. The change in the mean ion energy and the electron temperature show a similar trend upon a change in $p$ and $P$, because the plasma potential depends on the electron temperature. Obviously, the electron density and the ion flux are also related. In electropositive processing plasmas, such as the one used in this work, the electron density and ion density in the bulk plasma are equal and a change in the electron density directly affects the ion flux. Upon a pressure increase, both $\hat{E}_i$ and $T_e$ decrease due to the fact that more electron-molecule collisions take place at higher pressures increasing the ionization rate. As a result, the plasma can be sustained at a lower electron temperature explaining its decrease with increasing pressure. The electron density and ion flux also decrease at higher pressures for the position directly above the substrate stage, possibly due to a slightly reduced out-diffusion of the plasma species from the plasma source. At higher plasma powers, more power is coupled into the plasma, which also results in a higher ionization rate and lower $T_e$. Obviously, the ion flux and density increase with increasing power as well. The magnitude of $T_e$ indicates that, although the plasmas in the FlexAL and OpAL are generated remotely, they are still ionizing above the substrate over the complete pressure and power range measured in this study.

The amount of energy the ions provide to the substrate surface can be illustrated by comparing the growth-per-cycle, in terms of atoms deposited per unit area, with the ion dose to the surface within one cycle. Table 5.1 summarizes this data for four metal-oxide systems deposited in the FlexAL reactor. These materials were deposited under saturated and optimized plasma-assisted ALD conditions as previously reported by Potts *et al.* and Heil *et al.* [3,4]. The ion dose per cycle and the average energy per atom deposited are provided for a plasma generated at 15 mTorr $O_2$ gas pressure and 300 W plasma power ($\hat{E}_i$ = 17.8 eV, $\Gamma_i$ = 3.2 $\times$ $10^{13}$ $cm^{-2}$ $s^{-1}$). Consequently, for every few

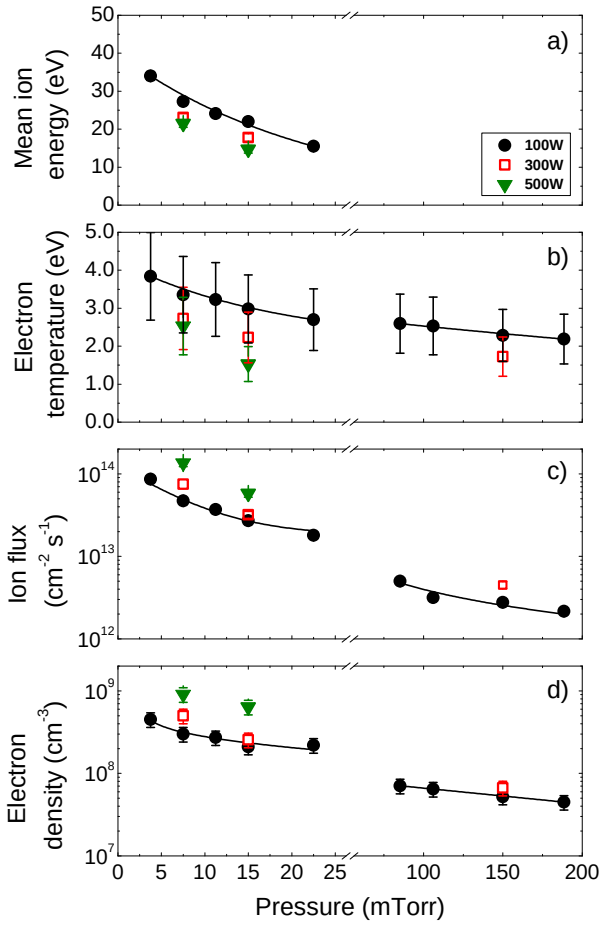



**Figure 5.2:** Pressure and power dependence of a) the mean ion energy $\hat{E}_\mathrm{i}$, b) the electron temperature $T_\mathrm{e}$, c) the ion flux $\Gamma_i$ and d) the electron density $n_\mathrm{e}$ in an $O_2$ plasma used for plasma-assisted ALD. For $p \leq 22.5$ mTorr, measurements were performed in the FlexAL reactor, whereas for $p > 75$ mTorr, measurements were carried out in the OpAL. Lines serve as a guide to the eye.

**Table 5.1:** A comparison between the growth-per-cycle in terms of atoms deposited and the ion dose for four metal oxides deposited under optimized ALD conditions in the FlexAL reactor [3,4]. The precursor [Me is methyl, $CH_3$; Et is ethyl, $C_2H_5$; and $^i$Pr is isopropyl, $CH(CH_3)_2$], the plasma dosing time per cycle ($t_{plasma}$), the growth-per-cycle and the average energy provided to an atom deposited ($\hat{E}_i$-per-atom) are given for depositions performed at $p$ = 15 mTorr and $P$ = 300 W. The data demonstrates that the energy provided by the ions can be significant, depending on the growth-per-cycle obtained and/or plasma dosing time required for the process.

| Material | Precursor | $t_{plasma}$ (s) | Growth-per-cycle (cm$^{-2}$ cycle$^{-1}$) | Ion dose per cycle (at. cm$^{-2}$ cycle$^{-1}$) | $\hat{E}_i$-per-atom (eV) |
|---|---|---|---|---|---|
| $Al_2O_3$ | $Al(Me)_3$ | 2 | $1.1 \times 10^{15}$ | $6.4 \times 10^{13}$ | 1.1 |
| $HfO_2$ | $Hf(NMeEt)_4$ | 3 | $8.5 \times 10^{14}$ | $9.6 \times 10^{13}$ | 2.0 |
| $TiO_2$ | $Ti(O\ ^iPr)_4$ | 12 | $3.7 \times 10^{14}$ | $3.8 \times 10^{14}$ | 18.4 |
| $Ta_2O_5$ | $Ta(NMe_2)_5$ | 5 | $6.3 \times 10^{14}$ | $1.6 \times 10^{14}$ | 4.6 |

atoms deposited there is one ion leading to an average ion energy dose of one or a few eV per atom. The dose is highest for deposition processes such as $TiO_2$ that provide only a low atomic growth-per-cycle and require a relatively long plasma dosing time. From the data and the fact that good material properties were reported by Potts *et al.* and Heil *et al.* [3,4], it can also be concluded that the ion doses and energies are not high enough to induce substantial ion-induced damage. On the other hand, as reported by Takagi the ion energies and fluxes are within the range to potentially stimulate the ALD surface reactions, e.g., through ligand desorption and adatom migration [7]. As illustrated in Fig. 5.2, the potential influence of the ions can be limited mainly by increasing the $O_2$ gas pressure.

### 5.3.2 Photons and their Surface Interaction

Emission spectra in the VUV (100-200 nm), UV (200-400 nm) and visible (400-800 nm) range of the optical spectrum were recorded at standard conditions. Figures 5.3a and 5.3b show a number of emission peaks corresponding to photons emitted after decay of electronically excited atoms and ions. In the visible range (Fig. 5.3b), the spectrum is similar to what was observed and described in more detail by Mackus *et al.* [9]. In the UV and VUV range (Fig. 5.3a), an intense peak was observed at 130.5 $\pm$ 0.1 nm, corresponding to 9.5 eV photons (transition: $3s\ ^3S^0 \rightarrow 2p^4\ ^3P$). Besides this emission peak, this spectral range does not reveal other intense emission lines (the peak at 261.0 $\pm$ 0.1 nm is

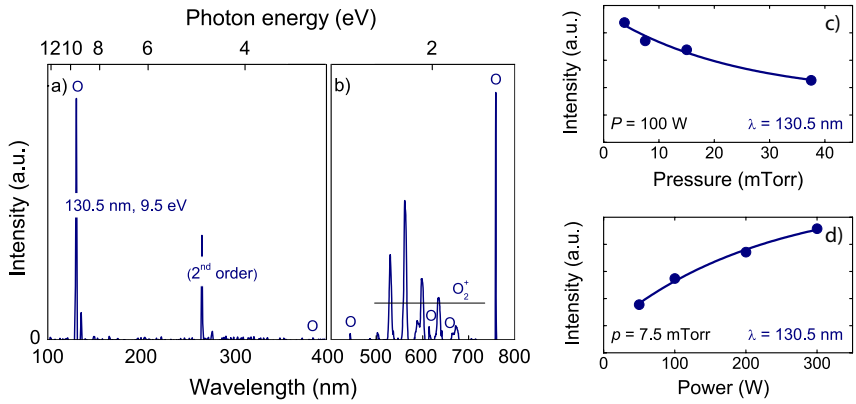



**Figure 5.3:** Emission spectrum of an $O_2$ plasma as measured in a) the VUV and UV region (100-400 nm) and b) the visible region (400-800 nm). The wavelength $\lambda$ and the photon energy $E_p$ are given on the lower and upper horizontal axis, respectively. The second order peak is caused by the diffraction grating in the monochromator and is associated with the 130.5 $\pm$ 0.1 nm emission line. Additionally, the emission intensity at $\lambda$ = 130.5 $\pm$ 0.1 nm peak is given as a function of c) the $O_2$ gas pressure $p$ and d) the plasma power $P$.

a second order effect of the diffraction grating used in the monochromator). High energy VUV photons are likely to be re-absorbed by the plasma [8], so it is expected that the photons emitted towards the substrate surface are produced directly above the substrate surface, e.g., by de-excitation of O atoms in the plasma or by ion-electron recombination at or near the sample surface. The intensity of the 130.5 nm peak, a qualitative measure for its photon flux, decreases when going to higher pressures and increases at higher powers, as illustrated in Figs. 5.3c and 5.3d respectively.

It has been reported that high energy VUV photons have the ability to negatively affect the performance of electronic devices with metal-oxide thin films during plasma processing [9-14]. To investigate the influence of VUV photons on the material properties of films prepared by ALD, a number of plasma exposure experiments were conducted in the FlexAL reactor. During the experiments the minority charge carrier lifetime of c-Si wafers passivated by $Al_2O_3$ was monitored using a Sinton WCT-100 tool [16]. This parameter is very sensitive to electrical defects near the c-Si/$Al_2O_3$ interface [11-13] whereas $Al_2O_3$ is a commonly-applied dielectric prepared by ALD. For the experiment, double side polished float-zone <100> c-Si wafers (3.5 $\mu$cm, n-type) were used, double side deposited with a 30 nm $Al_2O_3$ passivation layer and annealed for 10 minutes at 400

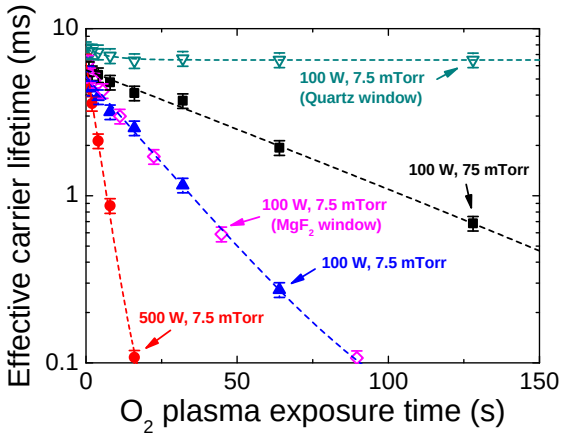



**Figure 5.4:** Effective lifetime $\tau_{\text{eff}}$ measured for a float-zone <100> c-Si wafer (3.5 $\mu$cm, n-type), polished and deposited with 30 nm $Al_2O_3$ at both sides, as a function of the $O_2$ plasma exposure time tplasma. The decrease in lifetime is demonstrated for different pressure and power levels. Results are also given with the substrate covered by windows blocking (Quartz) and not blocking ($MgF_2$, $\sim$ 60% transmission corrected) the VUV emission at 130.5 nm. The $Al_2O_3$ film was deposited by thermal ALD and annealed for 10 min at 400 °C before plasma exposure. Lines serve as a guide to the eye.

°C. These $Al_2O_3$ layers were deposited by thermal ALD to avoid the influence of plasma photons at the initial stage of the experiment. The resulting effective lifetimes $\tau_{\text{eff}}$, the minority charge carrier lifetimes at a charge injection level of $10^{15}$ $cm^{-3}$, in the Si substrates were measured to be $\sim$6 ms. The high lifetime is a result of the excellent passivation of silicon by the ALD-prepared $Al_2O_3$ films [17]. The effect of the high energy VUV radiation was demonstrated by exposing the samples to an $O_2$ plasma for different time intervals. The resulting effective lifetime versus the plasma exposure time is illustrated in Fig. 5.4, for three samples exposed at different plasma conditions. The results clearly show a decrease in the effective lifetimes for samples under plasma exposure. The decrease in lifetime depends on the intensity of the VUV radiation (see Figs. 5.3c and 5.3d) as it is evident that the lifetime decreases faster for exposures at higher plasma powers, but slower when higher gas pressures are employed. This automatically also implies that the effect of plasma radiation on the lifetime can be controlled by choosing the right plasma parameters.

The experiments were repeated under standard conditions for the situation in which samples were exposed to the radiation through 5.0 mm thick $MgF_2$ and quartz windows

(blocking plasma radiation < 110 nm and < 140 nm, respectively). In this way the potential influence of ion bombardment on the lifetime degradation can be excluded and the role of the 9.5 eV photons can be identified. The transparency of the $MgF_2$ window for 130.5 nm radiation is approximately 60%, and after correcting for the resulting lower photon flux through this window the results were included in Fig. 5.4. For sample exposure through the $MgF_2$ window, the lifetime as a function of the plasma exposure time is comparable to the situation in which no window was used at all. For the case with the quartz window virtually no lifetime degradation was observed. Therefore it is obvious that the VUV photons are responsible for the plasma exposure damage.

According to the literature 9.5 eV photons have enough energy to depassivate hydrogen-passivated Si dangling bonds at the interface between the Si and the $Al_2O_3$ and/or to create charge traps in dielectric materials whose bandgap is lower than the VUV photon energy [10,11]. For 9.5 eV photons, the latter holds for the $Al_2O_3$ but also for the 1-2 nm thick interfacial $SiO_x$ layer that generally forms between the Si and the $Al_2O_3$. The decrease in the minority charge carrier lifetime, observed during the experiments reported on in this work, can therefore be attributed to an increased density of defect states at the interface, induced by VUV photons. These results explain the observations by Dingemans *et al.* who compared the lifetime of as-deposited c-Si substrates coated with $Al_2O_3$ films deposited by thermal ALD and by plasma-assisted ALD [12]. In this work, lifetimes in the $\mu$s range were found for substrates coated with $Al_2O_3$ deposited by plasma-assisted ALD whereas lifetimes in the ms range were observed for $Al_2O_3$ deposited by thermal ALD. The difference in lifetimes can therefore be attributed to the fact that the plasma-assisted ALD samples were exposed to VUV radiation. After a post-deposition anneal the lifetimes were similar for the plasma-assisted and thermal ALD deposited substrates [12] which implies that the photon-induced lifetime degradation can be repaired by such a post-deposition anneal. It was verified that this holds for the thermal ALD $Al_2O_3$ samples (shown in Fig. 5.4) degraded by the VUV radiation as well. This confirms that the results in Fig. 5.4 reflect the influence of VUV photons during plasma-assisted ALD, despite the fact that the experiments reported in this work were carried out on substrates with thermally deposited $Al_2O_3$ films. More evidence for the detrimental influence of VUV photons during plasma-assisted ALD of $Al_2O_3$ (as-deposited) on silicon is also provided by the recent observation that the lifetime degradation during plasma-assisted ALD is lower for shorter plasma exposure steps [13].

## 5.4 Conclusions

The potential influence of ions and photons during plasma-assisted ALD was investigated for different $O_2$ gas pressures and plasma powers. The ions present in the remote $O_2$ plasma have kinetic energies of $\leq$35 eV and fluxes of $\sim 10^{12}$-$10^{14}$ $cm^{-2}$ $s^{-1}$. The energy provided by the ions can vary from one up to a few eV per atom deposited, depending on the growth-per-cycle of the process and the plasma exposure time required to reach saturation of the ALD cycle. The energy dose is low enough to prevent substantial ion-induced film damage, but sufficiently large to potentially stimulate the ALD surface reactions. The electron temperature and electron density reveal that for the remote plasma systems employed, the plasma still is ionizing at the substrate stage level for the pressure (7.5-187.5 mTorr) and power (100-500 W) range studied. The emission spectrum of the plasma revealed the presence of photons with energies of 9.5 eV in the plasma. These VUV photons are energetic enough to create electrical defects during plasma-assisted ALD processes, which has unambiguously been demonstrated in this work. The plasma-induced damage can be reduced by tuning the gas pressure and plasma power.

## Acknowledgements

G. Dingemans, C. van Helvoirt, M. J. F. van de Sande, J. J. L. M. Meulendijks, J. J. A. Zeebregts, and H. M. M. de Jong are acknowledged for assisting with the experiments. This work is carried out within the Thin Film Nanomanufacturing (TFN) programme and is supported financially by the Dutch Technology Foundation STW.

## References

1. S. B. S. Heil, E. Langereis, F. Roozeboom, M. C. M. van de Sanden, and W. M. M. Kessels, J. Electrochem. Soc. 153, G956 (2006).
2. W. M. M. Kessels, S. B. S. Heil, E. Langereis, J. L. van Hemmen, H. C. M. Knoops, and M. C. M. van de Sanden, ECS Trans. 3, 183 (2007).
3. S. E. Potts, W. Keuning, E. Langereis, G. Dingemans, M. C. M. van de Sanden, and W. M. M. Kessels, J. Electrochem. Soc. 157, P66 (2010).
4. S. B. S. Heil, J. L. van Hemmen, C. J. Hodson, N. Singh, J. H. Klootwijk, F. Roozeboom, M. C. M. van de Sanden, and W. M. M. Kessels, J. Vac. Sci. Technol. A. 25, 1357 (2007).
5. D. Gahan, B. Dolinaj, and M. B. Hopkins, Rev. Sci. Instrum. 79, 033502 (2008).

6. J. T. Gudmundsson, I. G. Kouznetsov, K. K. Patel, and M. A. Lieberman, J. Phys. D: Appl. Phys. 34, 1100 (2001).
7. T. Takagi, J. Vac. Sci. Technol. A. 2, 382 (1984).
8. A. C. Fozza, A. Kruse, A. Hollander, A. Ricard, and M. R. Wertheimer, J. Vac. Sci. Technol. A 16, 72 (1998).
9. A. J. M. Mackus, S. B. S. Heil, E. Langereis, H. C. M. Knoops, M. C. M. van de Sanden, and W. M. M. Kessels, J. Vac. Sci. Technol. A 28, 77-87 (2010)
10. C. Cismaru, J. L. Shohet, J. L. Lauer, R. W. Hansen, and S. Ostapenko, Appl. Phys. Lett. 77, 3914 (2000).
11. A. Stesmans and V. V. Afanasev, Appl. Phys. Lett. 80, 1957 (2002).
12. G. Dingemans, R. Seguin, P. Engelhart, M. C. M. van de Sanden, and W. M. M. Kessels, Phys. Status Solidi RRL 4, 10 (2010).
13. G. Dingemans, N. M. Terlinden, D. Pierreux, H. B. Profijt, M. C. M. van de Sanden, and W. M. M. Kessels, Electrochem. and Solid State Lett. 14, H1 (2011).
14. A. W. Flounders, S. A. Bel, and D. W. Hess, J. Electrochem. Soc. 140, 1414- 1424 (1993).
15. G. S. Upadhyaya and J. L. Shohet, Appl. Phys. Lett. 90, 072904 (2007).
16. R. A. Sinton and A. Cuevas, Appl. Phys. Lett. 69, 2510 (1996).
17. B. Hoex, S. B. S. Heil, E. Langereis, M. C. M. van de Sanden, and W. M. M. Kessels, Appl. Phys. Lett. 89, 042112 (2006).

Chapter 6

# Substrate-Biasing during Plasma-Assisted Atomic Layer Deposition to Tailor Metal Oxide Film Growth*

**Abstract** Two substrate-biasing techniques, i.e. substrate-tuned biasing and RF biasing, have been implemented in a remote plasma configuration, enabling control of the ion energy during plasma-assisted atomic layer deposition (ALD). With both techniques, substrate bias voltages up to -200 V have been reached, which allowed for ion energies up to 272 eV. Besides the bias voltage, the ion energy and the ion flux, also the electron temperature, the electron density, and the optical emission of the plasma have been measured. The effects of substrate biasing during plasma-assisted ALD have been investigated for $Al_2O_3$, $Co_3O_4$ and $TiO_2$ thin films. The growth per cycle, the mass density, and the crystallinity have been investigated and it was found that these process and material properties can be tailored using substrate biasing. Additionally, the residual stress in substrates coated with $Al_2O_3$ films varied with the substrate bias voltage. The results reported in this Chapter demonstrate that substrate biasing is a promising technique to tailor the material properties of thin films synthesized by plasma-assisted ALD.

*Published as: *H. B. Profijt, M. C. M. van de Sanden, and W. M. M. Kessels, J. Vac. Sci. Technol. A 31, 01A106 (2013).*

## 6.1 Introduction

For certain materials and processes, plasma-assisted atomic layer deposition (ALD) allows for an increased level of freedom in processing conditions and material properties. This is facilitated by the reactive species generated in the plasma and present during the deposition process [1]. These species include radicals, electrons, ions and photons. The extent to which ions can contribute to the ALD process depends on their energy and flux, parameters that can be controlled by many variables including the plasma gas mixture, the gas pressure, the power coupled in to the plasma, the reactor design, the type of plasma source and the possible presence of substrate biasing [1-5].

A number of ion-induced effects have been reported which may also be relevant for plasma-assisted ALD. One of those is adatom migration, which is known to enhance (initial) film nucleation [6-8]. In the case of ALD, nucleation delays may be reduced and for poly-crystalline films the crystallinity may be enhanced when adatom migration is promoted. Another ion-induced effect is the desorption of surface species [7], which can possibly assist ligand-desorption during the second half-cycle of an ALD process. Subplantation (i.e. subsurface-implantation) is another process which may take place, during which the top few mono-layers of the ALD film or the substrate are modified by shallow implantation effects [6,7]. Consequently, the physical or chemical properties of thin films can be affected, which potentially results in a higher film density or the promotion of crystallization of the films at relatively low deposition temperatures [7,8]. It has furthermore been reported that energetic ions can induce or enhance compressive film stress by the subplantation of energetic ions [6,9].

In our recent work, we discussed that during remote-plasma ALD, the energies and fluxes of the ions are typically sufficiently high to play a role during the deposition process, e.g. by stimulating ligand-removal and enhancing adatom migration [2]. In a follow-up paper the successful implementation of substrate biasing in a remote plasma ALD reactor was reported, which allows for controlling of the average ion energy [10]. Accordingly, it was demonstrated that the crystalline phase of $TiO_2$ films can be tailored from anatase to rutile by varying the substrate bias voltage from 0 to -200 V. Also the concentration of hydroxyl groups in the $TiO_2$ films was shown to be affected by substrate biasing. Moreover, in an independent study the effects of higher radical and ion fluxes were shown by Kim *et al.* for a plasma-assisted ALD reactor with a remote capacitively-coupled plasma [11]. In this reactor configuration, the plasma was generated between an electrode and a grid with a pulsed negative DC voltage applied to it. The substrate was placed downstream with respect to the grid. The authors reported on $HfO_2$ dielectric

films with a decreased equivalent oxide thickness and an increased dielectric breakdown voltage.

Notwithstanding the fact that substrate biasing has been used for many years during plasma-processing techniques such as plasma-enhanced chemical vapor deposition (CVD) and plasma-enhanced physical vapor deposition (PVD), the impact of high-energy ions on thin films deposited by ALD is still largely unexplored. Since ALD is a different deposition method during which the sample is alternately exposed to the precursor and the plasma, it is interesting to study the influence of substrate biasing specifically for this deposition method.

This Chapter discusses the implementation of substrate-tuned biasing and RF substrate biasing in a remote plasma ALD reactor. The impact of substrate biasing on the ion energy distribution and the plasma properties are reported, as well as the effects of substrate biasing during plasma-assisted ALD of metal oxides. The results demonstrate that substrate biasing is a promising technique to tailor the material properties of thin films synthesized by plasma-assisted ALD.

## 6.2 Theoretical Aspects

### 6.2.1 Ion-bombardment during Plasma Processing

Processing plasmas are typically generated by supplying AC electrical power (mostly at radio frequency, RF, 13.56 MHz) to a gas which leads to the acceleration and heating of electrons. The hot electrons are able to dissociate, ionize, and excite gas-phase species during the collisions they undergo. The density of these electrons is equal to the density of ions, when looking at length scales larger than the Debye length (i.e. the screening length of the charge carriers, typically $10^{-4}$ - $10^{-3}$ m for remote plasma ALD conditions) and when the presence of negative ions can be neglected. However, between the plasma and a surface, a positive space charge layer builds up because the thermal velocity of the electrons is much higher than the thermal velocity of the (much heavier) ions. The voltage across this so-called plasma sheath is such that the flux of ions and electrons is balanced by retarding electrons and accelerating ions [3,5]. This means, for example, that for a floating substrate the net electrical current to electrically floating surfaces in contact with the plasma is zero. In the case of a collisionless plasma sheath, the pressure in the reactor is sufficiently low to prevent collisions between ions and neutral gas species in the plasma sheath. Consequently, ions are accelerated over the full sheath and the ion

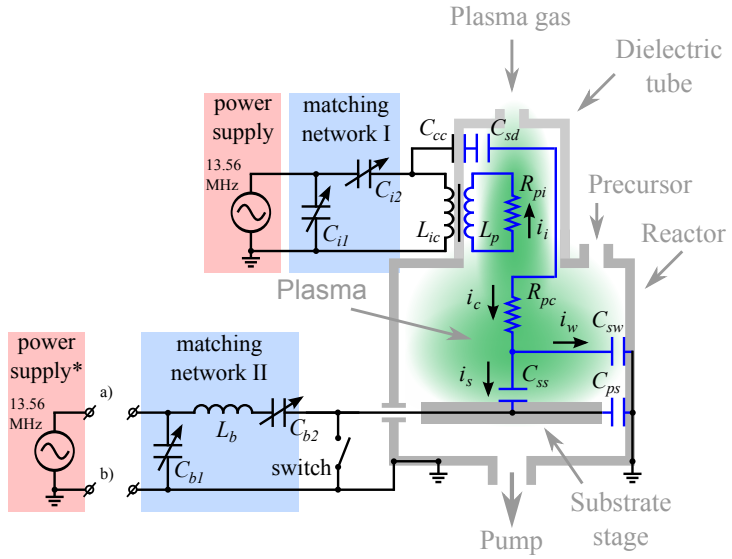



**Figure 6.1:** Remote plasma ALD reactor equipped with an inductively-coupled plasma source. Real electrical components are drawn in black whereas equivalent electrical components describing the plasma behavior are drawn in blue (see also Table 6.1). Matching network II is connected to the substrate stage to control the substrate potential by substrate-tuned biasing. The corresponding RF power supply (denoted with an asterisk) can additionally be connected to the matching network at nodes "a)" and "b)" for RF biasing. The substrate stage can be electrically grounded by closing the switch.

energy, $E_{\text{ion}}$ (expressed in [eV]), at the substrate surface is given by

$$E_{\text{ion}} = e \cdot V_{\text{sheath}} = e \cdot (V_{\text{plasma}} - V_{\text{subs}}) \tag{6.1}$$

where $e$ is the electron charge, $V_{\text{sheath}}$ is the voltage across the plasma sheath, $V_{\text{plasma}}$ is the plasma potential and $V_{\text{subs}}$ is the substrate potential. For a grounded substrate stage (i.e. $V_{\text{subs}}$ = 0 V) the sheath voltage is equal to the plasma potential. The equation furthermore illustrates that the energy of the ions can be increased by applying a voltage to the substrate stage that is, on average, negative. Usually this negative bias voltage is applied using DC, AC, RF or more complex signals [4,12].

### 6.2.2 Substrate-Tuned Biasing and RF Biasing

Substrate-tuned biasing (or substrate-tuning) is a technique to vary the voltage across the plasma sheath at the substrate stage, without the need for an external bias source. The

**Table 6.1:** Overview of the electrical components given in the electrical circuit in Fig. 6.1. To distinguish real components from equivalent electrical components, the latter are marked with an asterisk.

| Part of the circuit | Symbol | Component |
|---|---|---|
| Inductive coupling | $L_{\mathrm{icp}}$ | coil inductance |
| | $L_{\mathrm{p}}$ | plasma inductance* |
| | $R_{\mathrm{pi}}$ | plasma resistance* |
| Capacitive coupling | $C_{\mathrm{ccp}}$ | capacitance across dielectric tube* |
| | $C_{\mathrm{sd}}$ | sheath capacitance at dielectric tube* |
| | $C_{\mathrm{sw}}$ | sheath capacitance at wall* |
| | $C_{\mathrm{ss}}$ | sheath capacitance at substrate* |
| | $C_{\mathrm{ps}}$ | stray capacitance at substrate* |
| | $R_{\mathrm{pc}}$ | plasma resistance* |
| Matching network I | $C_{\mathrm{i1}}$ | variable parallel capacitor |
| | $C_{\mathrm{i2}}$ | variable series capacitor |
| Matching network II | $C_{\mathrm{b1}}$ | variable parallel capacitor |
| | $C_{\mathrm{b2}}$ | variable series capacitor |
| | $L_{\mathrm{b}}$ | series coil |

mechanism behind this technique is the tuning of the impedance between the substrate stage and the ground, using an external electrical circuit [13, 14]. In Fig. 6.1, a remote plasma ALD reactor equipped with substrate-tuned biasing is shown. The electrical circuit of real and equivalent components in the setup is also drawn in this figure, which makes it possible to evaluate the substrate-tuned biasing technique electrically. In Table 6.1, the components are summed up and described, while a more detailed description is given in this Section.

The electrical power used to generate the inductively-coupled plasma (ICP) plasma is provided by a RF (radio frequency, 13.56 MHz) power supply. The power source is connected to the ICP coil through a *L*-type matching network with two variable capacitors $C_{\mathrm{i1}}$ and $C_{\mathrm{i2}}$, designed to match inductive loads. The inductive coupling of the power is represented by a 5:1 transformer, where $L_{\mathrm{ic}}$ is the five-turn Cu coil wrapped around the dielectric tube on top of the reactor and $L_{\mathrm{p}}$ accounts for the induced electron current which generates the plasma. ICP sources are typically non-ideal and electrical power is also partly capacitively-coupled through $C_{\mathrm{cc}}$ which is the capacitance across the walls of the dielectric tube. The resistors $R_{\mathrm{pi}}$ and $R_{\mathrm{pc}}$ represent the dissipation of electrical power by the plasma, whereas $C_{\mathrm{sd}}$, $C_{\mathrm{sw}}$ and $C_{\mathrm{ss}}$ denote the plasma sheath capacitances

between the plasma and the dielectric tube, the plasma and the grounded reactor wall and the plasma and the substrate stage, respectively. Furthermore, the parasitic capacitance present between the substrate stage and the reactor walls is represented by $C_{\mathrm{ps}}$. A matching network, designed to match capacitive loads using two variable capacitors, $C_{\mathrm{b1}}$ and $C_{\mathrm{b2}}$, and a coil, $L_{\mathrm{b}}$, is connected to the substrate stage to control the substrate voltage $V_{\mathrm{subs}}$ by substrate-tuned biasing. $i_{\mathrm{c}}$ and $i_{\mathrm{i}}$ denote the flow of electrical RF current into the plasma as a result of capacitive and inductive coupling, respectively, whereas $i_{\mathrm{w}}$ and $i_{\mathrm{s}}$ are the RF currents towards the grounded reactor wall and the substrate stage, respectively.

The impedance of the substrate-ground branch (i.e. the current path from the plasma to the ground via the substrate stage), $Z_{\mathrm{subs}}$, and the impedance to the wall, $Z_{\mathrm{wall}}$, determine the RF current flow to the substrate, $i_{\mathrm{s}}$, and the RF current flow to the wall, $i_{\mathrm{w}}$. These currents can be expressed as

$$i_{\mathrm{s}} = i_{\mathrm{c}} \cdot \frac{|Z_{\mathrm{wall}}|}{|Z_{\mathrm{wall}}| + |Z_{\mathrm{subs}}|}, \tag{6.2}$$

and

$$i_{\mathrm{w}} = i_{\mathrm{c}} \cdot \frac{|Z_{\mathrm{subs}}|}{|Z_{\mathrm{wall}}| + |Z_{\mathrm{subs}}|}, \tag{6.3}$$

where

$$Z_{\mathrm{subs}} = \mathrm{j}X_{\mathrm{subs}} = \frac{\frac{-\mathrm{j}}{\omega C_{\mathrm{ps}}} \cdot \left(\omega L_{\mathrm{b}} - \frac{1}{\omega C_{\mathrm{b}}}\right)}{\omega L_{\mathrm{b}} - \frac{1}{\omega C_{\mathrm{b}}} - \frac{1}{\omega C_{\mathrm{ps}}}} - \frac{\mathrm{j}}{\omega C_{\mathrm{ss}}}, \tag{6.4}$$

and

$$Z_{\mathrm{wall}} = \mathrm{j}X_{\mathrm{wall}} = \frac{-\mathrm{j}}{\omega C_{\mathrm{sw}}}. \tag{6.5}$$

$X_{\mathrm{subs}}$ is the reactance of the substrate-ground branch, i.e. the imaginary part of $Z_{\mathrm{subs}}$, and $C_{\mathrm{b}}$ is assumed $(C_{\mathrm{b1}} \cdot C_{\mathrm{b2}})/(C_{\mathrm{b1}} + C_{\mathrm{b2}})$. The higher $i_{\mathrm{s}}$, the higher the average voltage across the plasma sheath at the substrate, $V_{\mathrm{ss,avg}}$, will become to keep the net flux of ions and electrons to the substrate zero. For $V_{\mathrm{ss,avg}} > V_{\mathrm{plasma}}$, the average substrate voltage, $V_{\mathrm{subs,avg}}$, will be negative (see Eq. 6.1). The sheath capacitance at the substrate, $C_{\mathrm{ss}}$, can be expressed as [14,15]

$$C_{\mathrm{ss}} = \frac{dQ_{\mathrm{ss}}}{dV_{\mathrm{ss}}} = Aen_{\mathrm{e}}\frac{dt_{\mathrm{ss}}}{dV_{\mathrm{ss}}} = \frac{0.76A\sqrt{\epsilon_0 n_{\mathrm{e}} e}}{(T_{\mathrm{e}}V_{\mathrm{ss}})^{1/4}}, \tag{6.6}$$

where $Q_{\mathrm{ss}}$ is the charge in the plasma sheath at the substrate, $A$ is the substrate stage area, $t_{\mathrm{ss}}$ is the sheath thickness at the substrate, $\epsilon_0$ is the vacuum permittivity, $n_{\mathrm{e}}$ is the electron

density, $k$ is the Boltzmann constant and $T_e$ is the electron temperature (expressed in [eV]).

The impedance of the substrate-ground branch, $Z_{subs}$, can be tuned by varying $C_b$. For relatively low values of $C_b$, the value of $Z_{subs}$ is negative (i.e. the impedance is capacitive). An increase of $C_b$ will decrease $|Z_{subs}|$ (i.e. $Z_{subs}$ becomes less negative) and increase $i_s$. Consequently, $V_{ss}$ will increase in order to balance the fluxes of ions and electrons to the substrate stage. According to Eq. 6.6, an increase of $V_{ss}$ will decrease $C_{ss}$ (assuming that $n_e$ and $T_e$ remain relatively constant) and $|Z_{subs}|$ will then increase (i.e. $Z_{subs}$ becomes more negative) thereby stabilizing $V_{ss}$. Therefore, $V_{ss}$ can be controlled continuously by varying $C_b$, as long as $Z_{subs}$ is negative (i.e. for every value of $C_b$ there is a $V_{ss}$). $V_{ss}$ is at its maximum when $Z_{subs} = 0\ \Omega$, which is when the substrate-ground branch is in series resonance. For values of $C_b$ higher than for the resonance condition, $Z_{subs}$ is positive (i.e. the impedance is inductive). An increase of $C_b$ will increase $|Z_{subs}|$ (i.e. $Z_{subs}$ becomes more positive), $V_{ss}$ will decrease and $C_{ss}$ will increase. Because an increase in $C_{ss}$ will increase $|Z_{subs}|$ (i.e. $Z_{subs}$ becomes more positive) even more, no stable situation will be reached and $Z_{subs}$ will keep increasing. $i_s$ will become low and, consequently, $V_{ss}$ will also be low.

In order to allow for the use of the substrate-tuned biasing technique, the components and variables in Eq. 6.4 and 6.6 should have values such that $Z_{subs}$ can be tuned to values (significantly) lower than $Z_{wall}$. If, for example, the substrate stage area, $A$, is too large, then $C_{ss}$ is too large and $Z_{subs}$ is positive (i.e. the impedance is inductive) for the full tunable range of $C_b$ and, consequently, $V_{ss}$ cannot be controlled. In this situation, or when the maximum $V_{ss}$ obtainable by substrate-tuned biasing is not sufficient for a specific application, an external RF power source can be used. This power source is connected to nodes a) and b) in Fig. 6.1. By supplying RF power to the substrate, $i_s$ can be controlled and, as a result, $V_{ss}$ can be increased. RF biasing is addressed extensively in the literature, the reader is for example referred to Refs. 3 - 5.

## 6.3 Experimental

### 6.3.1 Plasma-Assisted ALD Reactor

All experiments were carried out in the home-built remote plasma ALD reactor which is schematically illustrated in Fig. 6.1 [16]. The inductively-coupled plasma (ICP) source mounted on top of the reactor was used to generate plasmas in gases such as Ar, $H_2$, $N_2$, $O_2$, and $NH_3$, which were supplied via the dielectric tube. The base pressure of the sys-

tem was $\sim 10^{-6}$ Torr, which was achieved by using a rotary vane pump and a maglev turbo molecular pump. Typical values for the gas pressure and the ICP power were 7.5 mTorr and 200 W, respectively. For some of the experiments reported in this Chapter, however, ICP powers up to 550 W were used, during which the ICP coil was cooled by an additional air flow. The substrate temperature was monitored by a thermocouple connected to the substrate stage and controllable up to 400 °C by a PID-controller (proportional-integral-derivative controller). The temperature of the reactor walls (typically 80 °C), the precursor containers (up to 100 °C, depending on the precursor) and the corresponding precursor lines (typically 15 °C higher than the precursor container, to prevent precursor condensation in the lines) were individually controlled by temperature regulators. The system hardware was operated using a National Instruments compact Fieldpoint programmable automation controller and in-house developed LabVIEW software.

### 6.3.2 Substrate-Tuned Biasing and RF Biasing

In order to have the possibility to apply a bias voltage to it, the substrate stage was electrically isolated from the grounded reactor wall using ceramic insulators. A flange with two electrical feed-throughs was connected to the reactor, where one was connected to a *L*-type matching network, whereas the other was connected to an oscilloscope via a 100:1 probe to measure the substrate bias voltage. During the experiments, $C_{\mathrm{b1}}$ and $L_{\mathrm{b}}$, present in the matching network, were kept constant at 136 $\pm$ 7 pF and 1.5 $\pm$ 0.1 $\mu$H, whereas $C_{\mathrm{b2}}$ was varied between 173 $\pm$ 9 and 932 $\pm$ 47 pF. The capacitances and self-inductance were measured using a LC-meter. It was furthermore possible to electrically ground the substrate stage through a switch.

During plasma exposure with substrate-tuned biasing or RF biasing enabled, the power supply to the resistive heating element integrated in the substrate stage was temporarily disabled by a relays. This was essential, as the additional impedance from the power source of the heater prevented the use of the substrate-tuned biasing technique for high substrate bias voltages. Since relatively short plasma exposures are usually required during the ALD deposition process (several seconds at maximum, which is typically $\sim$25% of the cycle time), the substrate temperature was hardly affected by temporarily disabling the substrate heating. The latter was also facilitated by the well-calibrated PID temperature controller.

A home-built double Langmuir probe with Pt tips was aligned at approximately 1 cm above the substrate stage to measure IV-curves from which the electron temperature, $T_{\mathrm{e}}$, and the electron density, $n_{\mathrm{e}}$, were calculated using the method described by Peterson and

Talbot [17]. The signal was filtered by a *LC* electrical network to remove unwanted RF components. For the ion energy and ion flux measurements, an Impedans Semion retarding field energy analyzer (RFEA) was employed, placed on the substrate stage [18]. Optical emission measurements were performed using an OceanOptics UBS4000-UV-VIS spectrometer (200 - 850 nm wavelength range) through a quartz window, aligned at approximately 1 cm above the substrate stage [19]. It is noted that it was verified that the plasma did not significantly heat the samples during the deposition process using a thermocouple connected to the substrate stage.

### 6.3.3 Thin Film Deposition and Characterization

The effects of substrate-tuned biasing and RF substrate biasing were evaluated for $Al_2O_3$, $Co_3O_4$ and $TiO_2$ thin films deposited by plasma-assisted ALD. In the case of a grounded substrate, the switch in Fig. 6.1 was closed. Substrate-tuned biasing was used for bias voltages of -50 and -100 V and RF biasing was employed for -150 and -200 V (see Sec. 6.4.1 for more details on these choices). During the plasma exposure step, the power supply to the substrate heater was switched off, to allow for a substrate bias signal to be applied to the substrate stage (see Sec. 6.3.2). During deposition of the metal-oxide films, $O_2$ [> 99.999% purity] was provided through the quartz tube continuously, as none of the precursors showed a reaction with $O_2$ gas at the conditions employed. The operating pressure was 7.5 mTorr and 200 W ICP power was supplied during the second half-cycle of the deposition process. Unless noted otherwise, 1x1 inch substrates with $\sim$2 nm native oxide cut from n-type c-Si (100) wafers with resistivity 10-20 $\mu\Omega$cm have been used. For the deposition of $Al_2O_3$, trimethylaluminium [$AlMe_3$, purity 99.99%, purchased from Akzo Nobel] was used as the precursor [20]. The precursor container was not heated and no Ar bubbling was required, as the vapor pressure of $AlMe_3$ was sufficiently high at room temperature. The precursor dose time, precursor purge time, plasma dose time, and plasma purge time were set to 50 ms, 3 s, 2 s and 3 s, respectively. $Al_2O_3$ films of approximately 25 nm thick were deposited at 25 and 200 °C. The $Co_3O_4$ films were deposited from cobaltocene [$CoCp_2$, purity 98%, purchased from Strem Chemicals] as the precursor, kept in a precursor container that was heated to 80 °C. Additionally, Ar bubbling [> 99.999% purity] was used [21]. During processing, the dose and purge times were 2 s, 5 s, 5 s and 5 s, respectively. $Co_3O_4$ films of approximately 25 nm thick were deposited at 300 °C. For the deposition of the $TiO_2$ films, Star-Ti [$Ti(Cp^{Me5})(OMe)^3$, purity > 99%, donated by Air Liquide] was used as the precursor [22]. The precursor container was heated to 78 °C and Ar bubbling was used. During

processing, all dose and purge times were set to 5 s. $TiO_2$ films of approximately 30 nm thick were deposited at 300 °C. Several techniques were used for the characterization of the thin films properties. The film thickness was measured *ex situ* by spectroscopic ellipsometry (SE) using a J.A. Woollam M2000D rotating compensator ellipsometer and CompleteEASE software. As proposed by Langereis *et al.*, a Cauchy oscillator was used for the optical model of $Al_2O_3$, whereas two Tauc-Lorentz oscillators were used to parameterize $TiO_2$ [23]. For the optical model of the $Co_3O_4$ films, a combination of a Gauss, a Tauc-Lorentz and two Lorentz oscillators was used, as reported by Donders *et al.* [21]. The mass density and the crystallinity of the films were determined by x-ray reflectometry (XRR) and grazing-incidence x-ray diffraction (GI-XRD), respectively. For both techniques, the PANalytical's X'Pert PRO MRD system was used. The composition of the $Al_2O_3$ and $Co_3O_4$ films was studied by X-ray photoelectron spectroscopy (XPS) using a Thermo Scientific K-Alpha KA1066 spectrometer. Additionally, wafer-curvature tests were carried out at room temperature with a kSA MOS Ultra-Scan system to determine the curvature of 4 inch wafers before and after deposition of the $Al_2O_3$ films. From the difference in curvature, the stress of the $Al_2O_3$ films was calculated using the Stoney equation [24].

## 6.4 Results

### 6.4.1 Substrate-Tuned Biasing and RF Biasing

In Fig. 6.2a, the substrate-tuned bias voltage, $V_{\text{subs}}$, is displayed as a function of time and in Fig. 6.2b the corresponding ion energy distributions (IEDs) are shown. The voltage waveforms were measured by an oscilloscope for various settings of $C_{\text{b2}}$. The frequency of the voltage signals is 13.56 MHz, which is equal to the frequency applied to the ICP source. Also the voltage signal for which the substrate stage was electrically grounded (i.e. the switch in Fig. 6.1 is closed and $V_{\text{subs}} = 0$ V) is included. In all cases, the average substrate voltage, $V_{\text{subs,avg}}$, (also referred to as the DC-self bias voltage) is negative and has a value for which the net flux of ions and electrons to the substrate stage is zero within one RF cycle. Most of the time, the substrate voltage is negative and ions are accelerated towards the substrate stage. During a short fraction of the RF cycle, however, the bias signal approaches the positive plasma potential and a flux of electrons is incident on the substrate. The IEDs demonstrate that the ion energy increases when the bias voltage is increased. When the substrate stage is electrically grounded, the IED is mono-modal and $E_{\text{ion}} = 53 \pm 1$ eV, from which it can be deduced that $V_{\text{plasma}}$ is $53 \pm 1$ V. When a substrate-

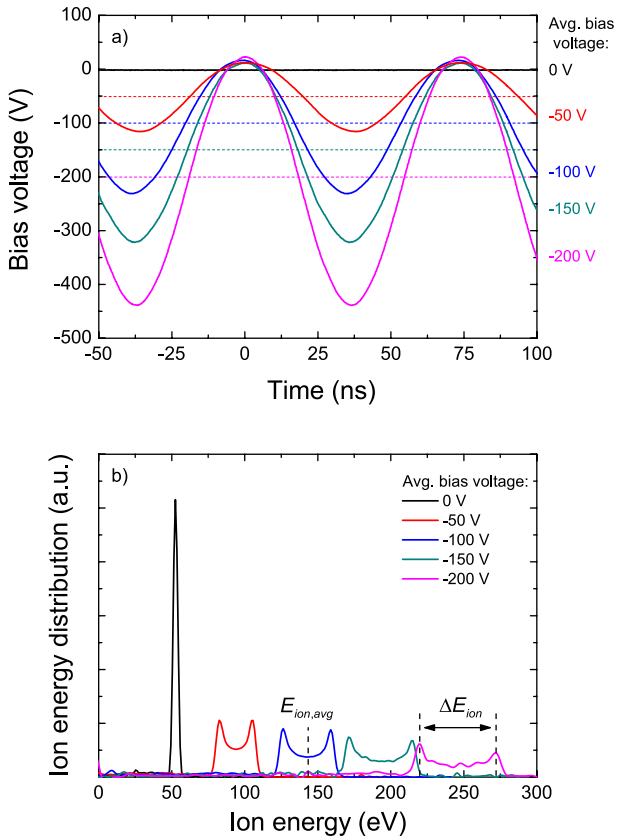



**Figure 6.2:** Substrate-tuned bias voltage as a function of time and b) corresponding ion energy distributions (IEDs). The plasmas were generated in $O_2$ at 550 W ICP power and 7.5 mTorr pressure. Data are given for substrate-tuned bias voltages of 0 to -200 V, obtained by varying $C_{b2}$ in the matching network connected to the substrate stage. The average bias voltages are also displayed with the curves, to link the voltage waveforms in a) with the IEDs in b). The average ion energy, $E_{ion,avg}$, and the ion energy distribution width, $\Delta E_{ion}$, are indicated. It is noted that the phase of the voltage-signals also varies with the substrate-ground impedance. The information about the phase is, however, not visible in the graph since signal-triggering was used on the oscilloscope.

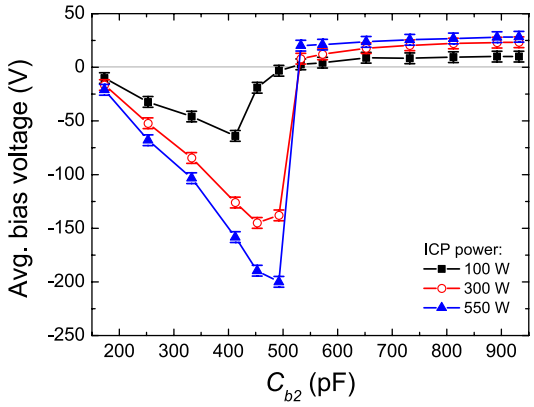



**Figure 6.3:** Average substrate-tuned bias voltage as a function of $C_{b2}$, given for different ICP powers. The plasmas were generated in $O_2$ at a pressure 7.5 mTorr. The maximum substrate-tuned bias voltage for a given power is obtained when the substrate-branch is in resonance.

tuned bias voltage is applied, the ion energy distribution becomes bimodal. The average ion energy, $E_{ion,avg}$, remains approximately equal to $e \cdot (V_{plasma} - V_{subs,avg})$, which indicates that $V_{plasma}$ stays relatively constant (see also Eq. 6.1). When a substrate-tuned bias voltage is applied, the ion energy distribution width, $\Delta E_{ion}$, increases as the ion transit time through the plasma sheath is smaller than the RF cycle time [3-5]. Consequently, the ions respond to the voltage across the sheath at the instant they pass the sheath and for that reason some ions obtain more energy than others, resulting in a bimodal IED. When a substrate-tuned bias voltage of -200 V is applied, $E_{ion,avg}$ is 246 $\pm$ 1 eV and $\Delta E_{ion}$ is 52 $\pm$ 1 eV, with minimal and maximum energies of 219 $\pm$ 1 and 272 $\pm$ 1 eV, respectively. The ion flux has been determined from the ion current measured by the RFEA and its value is (1.7 $\pm$ 0.1) $\times$ $10^{14}$ $cm^{-2}$ $s^{-1}$ for a grounded substrate stage, whereas it decreases slightly to (1.0 $\pm$ 0.1) $\times$ $10^{14}$ $cm^{-2}$ $s^{-1}$ for an average bias voltage of -200 V.

Data illustrating the relation between $V_{subs,avg}$ and $C_{b2}$ are shown in Fig. 6.3a, obtained by gradually increasing $C_{b2}$ from its minimum to its maximum value for different ICP powers. For values of $C_{b2}$ lower than a certain threshold value, $V_{subs,avg}$ increases in magnitude (i.e. its value becomes more negative) with increasing $C_{b2}$. The impedance of the substrate-ground branch is negative and consequently there belongs a $V_{subs,avg}$ for every value of $C_{b2}$, as long as $C_{b2}$ stays below the threshold value (see Sec. 6.2.2). For values of $C_{b2}$ higher than the threshold value, $V_{subs,avg}$ decreases rapidly in magnitude

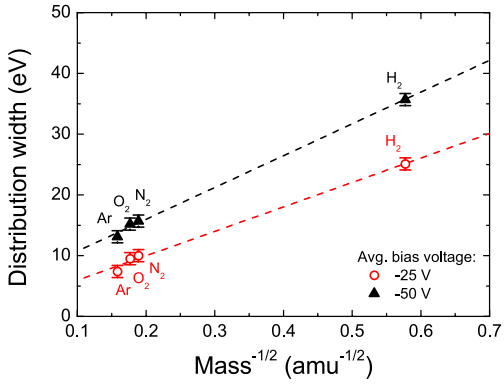



**Figure 6.4:** Ion energy distribution width $\Delta E_{ion}$ vs. the square root of the reciprocal mass of the dominant ions in the plasma. Datapoints are given for different plasmas and substrate-tuned bias voltages of -25 and -50 V. The plasmas were generated at an ICP power of 200 W and a pressure 7.5 mTorr. The data points were fitted linearly.

and eventually becomes positive when the impedance of the substrate-ground branch has become relatively high. The maximum attainable $V_{subs,avg}$ increases with increasing ICP power as a result of enhanced capacitive coupling of power into the plasma at higher powers (i.e. $i_c$ in Fig. 6.1. increases) [14]. The threshold value for $C_{b2}$ is affected by the ICP power as well, because the substrate sheath capacitance, $C_{ss}$, is a function of $n_e$ (see Eq. 4.). Although not shown, it is noteworthy that the maximum $V_{subs,avg}$ will be found for a different $C_{b2}$, when the capacitor value is decreased from its maximum value to its minimum value. This is due to the non-linear behavior of the substrate-ground branch with respect to variations in $V_{ss}$, $T_e$ and $n_e$.

IEDs have also been measured for plasmas generated in Ar, $O_2$, $N_2$ and $H_2$ for substrate-tuned bias voltages of -25 and -50 V, at an ICP power of 200 W and a gas pressure 7.5 mTorr. According to the literature, the dominant ions in plasmas operated under the present conditions are $Ar^+$, $O_2^+$, $N_2^+$ and $H_2^+$, respectively [24 - 26]. For each IED, $\Delta E_{ion}$ is derived and plotted in Fig. 6.4 against the root of the reciprocal ion mass. $\Delta E_{ion}$ is higher for ions with a lower mass, because these ions have a higher velocity and therefore a lower ion transit time. Although $\Delta E_{ion}$ is also affected by possible variations in $T_e$ and $n_e$ with changing plasma gases, such variations are probably minor as the data points can be fitted well by a linear curve [5] for each bias voltage.

The influence of substrate-tuned biasing on the electron temperature $T_e$ and the electron density $n_e$ has also been investigated. Plots illustrating the relation between $V_{subs,avg}$

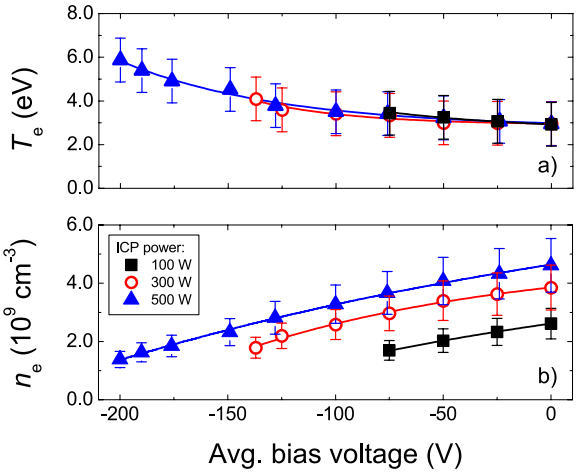



**Figure 6.5:** a) Electron temperature, $T_e$, and b) electron density, $n_e$, as a function of the average substrate-tuned bias voltage. The plasmas were generated in $O_2$ at 7.5 mTorr pressure and 100 - 550 W ICP power. Lines serve as a guide to the eye.

and $T_e$ and $n_e$ are shown in Fig. 6.5a and b. For a grounded substrate stage, $T_e$ is 2.9 $\pm$ 1.0 eV and $n_e$ is (2.6 $\pm$ 0.5) $\times$ $10^9$ cm$^{-3}$ at 100 W ICP power. Data are also given for higher ICP powers. Evidently $T_e$ is hardly influenced by the power, whereas $n_e$ increases to (4.6 $\pm$ 0.9) $\times$ $10^9$ cm$^{-3}$ when the power is increased to 550 W, as expected for inductively-coupled plasmas [3]. When the substrate-tuned bias voltage is increased, $T_e$ increases from 2.9 $\pm$ 1.0 eV at 0 V to 5.9 $\pm$ 1.0 eV at -200 V, when the power is 550 W. The increasing value of $T_e$ indicates that the plasma becomes more ionizing at the substrate level as a result of enhanced capacitive coupling. The electron density is affected by the substrate-tuned bias voltage as well, as it decreases from (4.6 $\pm$ 0.9) $\times$ $10^9$ cm$^{-3}$ at 0 V to (1.4 $\pm$ 0.3) $\times$ $10^9$ cm$^{-3}$ for -200 V, at a plasma power of 550 W. The decrease in the ion density can explain for the decrease in the ion flux with increasing bias voltage.

Also the plasma emission has been monitored. The integrated optical emission spectrum (200 - 850 nm range) is plotted against the substrate-tuned bias voltage in Fig. 6.6. Data are given for different ICP powers and, as illustrated, the integrated optical emission intensity increases with increasing ICP power. This originates from an increase in $n_e$ with the ICP power, resulting in a higher number of electron-induced excitation reactions. The optical emission intensity also increases with $V_{subs}$, despite the fact that $n_e$

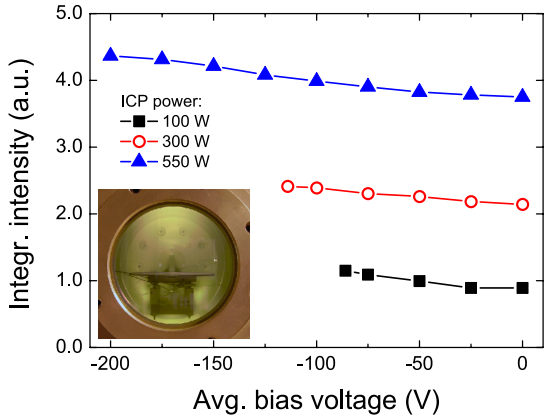



**Figure 6.6:** Integrated optical emission intensity (200 - 850 nm) provided for different substrate-tuned bias voltages. The plasmas were generated in $O_2$ at 100 - 550 W ICP power and 7.5 mTorr pressure. The optical emission was recorded directly above the substrate stage. The inset shows the substrate stage in the remote plasma ALD reactor, surrounded by the characteristic green glow of an $O_2$ plasma.

showed to decrease with $V_{subs}$ in Fig 6.5b. The emission intensity is enhanced because the excitation rate of the atoms and molecules in the plasma is highly affected by $T_e$ (as shown in Fig. 6.5a), which increases with $V_{subs}$. The increase in emission intensity as a function of the ICP power and the bias voltage can also be confirmed by observations made by the naked eye, as exemplified in the photograph in the inset of Fig. 6.6. An increased emission intensity around the substrate stage for increased bias voltages has also been reported by Smets *et al.* in a remote expanding thermal plasma (ETP) setup used for plasma-enhanced CVD of a-Si:H [27].

As discussed in Sec. 6.2.2, RF biasing can be used to obtain higher substrate bias voltages than achievable with substrate-tuned biasing only. In Fig. 6.7, $V_{subs,avg}$ is plotted as a function of the RF bias power for both the substrate-tuned biasing and the RF biasing techniques. The plasma is generated in $O_2$ employing an ICP power of 200 W and an $O_2$ pressure of 7.5 mTorr. As shown, the maximum obtainable $V_{subs,avg}$ with substrate-tuned biasing for this ICP power is -116 V. With the RF bias source connected to the matching network, the maximum attainable substrate-tuned bias voltage decreases to -75 V. This is a result of a change in the impedance of the substrate-branch. When the bias power source is switched on and $C_{b1}$ and $C_{b2}$ are properly adjusted, $V_{subs}$ can be increased. An average RF bias voltage of -200 V is obtained for a bias power of 24 W. The resulting

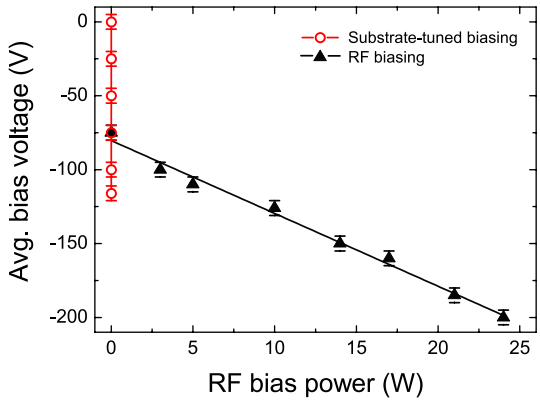



**Figure 6.7:** Graph showing the range of average substrate bias voltages that were achieved when substrate-tuned biasing or RF biasing was used for an ICP power of 200 W. The plasmas were generated in $O_2$ at 7.5 mTorr pressure. A RF power supply was additionally connected in the case of RF biasing to supply 0 - 24 W bias power to the substrate stage. Lines serve as a guide to the eye.

substrate voltage signals and ion energy distributions are comparable to those measured for substrate-tuned biasing (see Figs. 6.2a and 6.2b).

### 6.4.2 The Effects of Substrate Biasing on Metal-Oxide Film Growth

#### $Al_2O_3$ films

In Fig. 6.8a, the growth per cycle (GPC) and mass density of the $Al_2O_3$ films are shown as a function of the average bias voltage. For a substrate bias voltage of 0 V, the GPC is 1.46 $\pm$ 0.05 Å and the film density is 2.9 $\pm$ 0.1 g cm$^{-3}$. The growth per cycle increases to 1.55 $\pm$ 0.05 Å and 1.57 $\pm$ 0.05 Å for bias voltages of -100 and -200 V, respectively. The mass density, however, shows a decreasing trend with increasing bias voltage, which might explain for the increased growth rate. At -100 V bias voltage, the mass density is 2.7 $\pm$ 0.1 g cm$^{-3}$ and at -200 V the mass density has decreased to 2.6 $\pm$ 0.1 g cm$^{-3}$. According to the compositional data obtained by XPS, the film that has been deposited at 0 V is virtually stoichiometric with an [O]/[Al] ratio of 1.51 $\pm$ 0.05 and no observable amount of C in the bulk. For substrate bias voltages of -100 and -200 V, the [O]/[Al] ratio increases to 1.55 $\pm$ 0.05 and 1.56 $\pm$ 0.05, respectively, as a result of excess hydroxyl groups into the films. Furthermore, a C content of 0.5 at.% has been measured for the

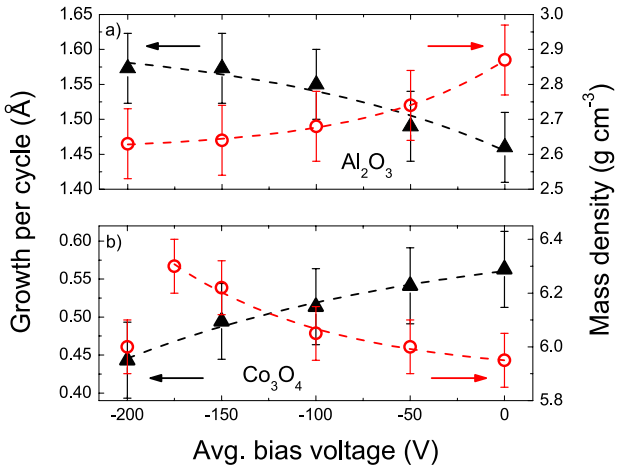



**Figure 6.8:** Growth per cycle and mass density of a) $Al_2O_3$ films and b) $Co_3O_4$ films deposited with bias voltages ranging from 0 to -200 V. Substrate-tuned biasing was employed for 0 to -100 V, whereas 0-24 W RF substrate biasing was applied for -150 and -200 V. Lines serve as a guide to the eye.

film deposited at -100 V, whereas the C content is 0.6 at.% for the film deposited at -200 V. The C incorporated in the films is expected to originate from the methyl ligands in the precursor which have been decomposed by the impact of high-energy ions from the plasma. The $Al_2O_3$ films are amorphous for the full range of bias voltages employed.

Figure 6.9 shows the residual stress of the $Al_2O_3$ films on the Si substrates for substrate temperatures of 25 and 200 °C. In the absence of a substrate bias voltage, a residual stress of -630 $\pm$ 25 MPa has been found for the film deposited at 25 °C, whereas 153 $\pm$ 25 MPa has been found for 200 °C. The stress in the $Al_2O_3$ is compressive for 25 °C and most likely induced by the ions from the plasma [9]. For the film deposited at 200 °C, however, a tensile residual stress has been measured which agrees with the results reported by Puurunen *et al.* for $Al_2O_3$ films deposited by thermal ALD [28]. The tensile stress most likely originates from the difference in thermal expansion coefficients of the Si substrate and the $Al_2O_3$ film [29,30], however the stress might also be partly present in the $Al_2O_3$ layer itself. When the substrate bias voltage is increased, the stress in the film deposited at 200 °C becomes compressive and the stress values become comparable to what has been measured for the film deposited at 25 °C. This might indicate that the impact of ions on the film stress has become stronger than the effect of the elevated substrate temperature. The magnitude of the compressive stress decreases with increasing

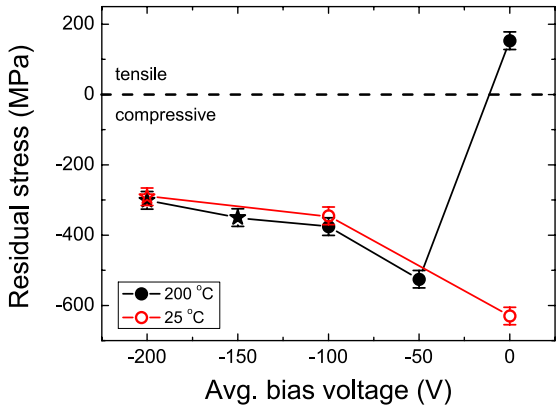



**Figure 6.9:** Residual film stress as a function of the average bias voltage for $Al_2O_3$ films deposited at 25 and 200 °C. Substrate-tuned biasing was employed for 0 to -100 V (circles), whereas 14 and 24 RF substrate biasing was applied to obtain substrate bias voltages of -150 and -200 V (stars).

bias voltage for both deposition temperatures, probably because the stress relaxes as a result of the reduced film density. At -200 V, residual stress values of -291 $\pm$ 25 MPa and -301 $\pm$ 25 MPa have been found for the films deposited at 25 and 200 °C, respectively.

Non-stoichiometric $Al_2O_3$ films with a reduced mass density are probably of limited interest, as generally high quality dielectric films are required. The fact that the stress in the films allows to be tailored from tensile to compressive, however, may be of interest for applications in the mechanical domain or when the films serve as protective layers.

### $Co_3O_4$

The GPC and mass density of the $Co_3O_4$ films are illustrated in Fig. 6.8b and show a different trend than for $Al_2O_3$. When the bias voltage increases, the GPC decreases while the mass density increases. Only the data point for the mass density obtained for -200 V deviates from this trend. For a grounded substrate stage, the GPC and mass density were found to be 0.56 $\pm$ 0.05 Å and 6.0 $\pm$ 0.1 g $cm^{-3}$, respectively, which agrees well with the values reported by Donders *et al.* [20]. When the bias voltage is increased to -100 V, the growth per cycle decreases to 0.51 $\pm$ 0.05 Å and the film density increases to 6.1 $\pm$ 0.1 g $cm^{-3}$. At a bias voltage of -175 V, the mass density of the films has been found to be 6.3 $\pm$ 0.1 g $cm^{-3}$, which is the highest value found within the range of bias voltages. For -200 V, the growth per cycle further decreases to 0.44 $\pm$ 0.05 Å, however the mass density for

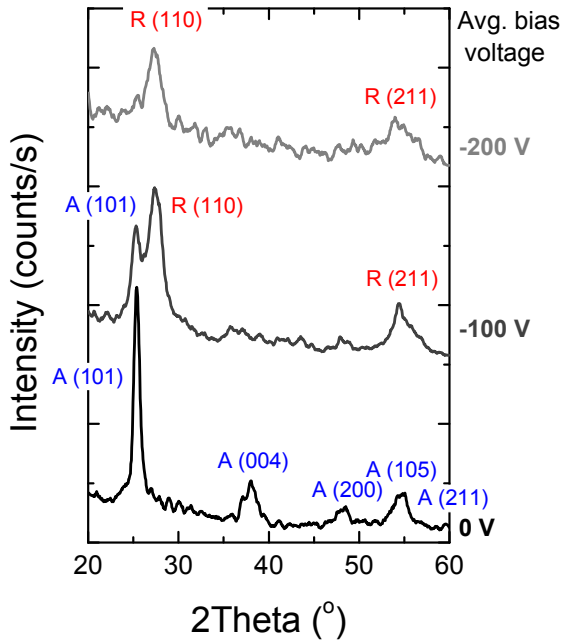



**Figure 6.10:** X-ray diffraction spectra for $TiO_2$ films deposited with bias voltages ranging from 0 to -200 V. Substrate-tuned biasing was employed for 0 to -100 V, whereas 24 W RF substrate biasing was applied for to obtain a substrate bias voltage of -200 V. Peaks corresponding to the anatase and rutile crystalline phases are denoted with "A" and "R", respectively.

this film does not fit the trend and drops to 6.0 $\pm$ 0.1 g $cm^{-3}$, which is approximately equal to the case with a grounded substrate. For the film that has been deposited at -200 V, it is hypothesized that the impact of high-energy ions has led to removal of material by sputtering which might explain for the reduced mass density. Stoichiometric $Co_3O_4$ films with no detectable amount of C were obtained for a grounded substrate stage. The films deposited at -100 and -200 V, however, are slightly oxygen-deficient ([O]/[Co] ratio = 1.25 $\pm$ 0.05 for both samples) while no C has been observed. The $Co_3O_4$ films are polycrystalline for every substrate bias voltage. For more details on the GI-XRD results the reader is referred to Ref. 21.

For many materials, the electrical, mechanical, optical, or catalytic properties improve when the mass density is higher. Therefore, these results reveal that substrate-biasing may be of interest for many more materials than $Co_3O_4$.

### $TiO_2$

For $TiO_2$, a GPC of 0.41 $\pm$ 0.05 Å has been measured for the films deposited without a substrate bias, which is $\sim$24% lower than the GPC reported by Langereis *et al.* [21]. The GPC increases for an increasing bias voltage and at -100 and -200 V, GPCs of 0.45 Å and 0.57 Å are obtained. In Fig. 6.10, XRD spectra are shown for $TiO_2$ films deposited with average bias voltages of 0, -100 and -200 V. In the absence of substrate biasing, the XRD spectrum shows the (101), (004), (200), (105), and (211) diffraction peaks which belong to anatase $TiO_2$. When the bias voltage is increased, however, most peaks corresponding to the anatase phase disappear and two new diffraction peaks, i.e. (110) and (211), appear in the spectrum which correspond to the rutile phase. At -200 V, the anatase peaks have disappeared and only peaks corresponding to the rutile phase are visible. The change in the crystalline phase with a variation in the bias voltage was also previously reported for $TiO_2$ deposited in the same remote plasma ALD reactor using $Ti(Cp^{Me})(NMe_2)_3$ and $O_2$ plasma [10]. That study also showed that the film density decreased with $\sim$10% as a result of the impact of high-energy ions, an effect that is also expected to be partly responsible for the higher GPC observed in this study.

The results reported for $TiO_2$ show that it is possible to obtain the rutile phase of $TiO_2$ at 300 °C, whereas usually amorphous or anatase $TiO_2$ is obtained unless specific starting layers or post-deposition annealing is employed.

## 6.5 Conclusions

Substrate-tuned biasing and RF biasing have been implemented in a remote plasma reactor to control the ion energy during thin film deposition by plasma-assisted ALD. Using the substrate-tuned biasing technique, the impedance between the substrate stage and the ground was tuned and, consequently, the substrate bias voltage could be controlled. With the RF substrate biasing technique, an additional power source is connected to the substrate stage via a matching network to control the voltage at the substrate stage. The maximum average substrate-tuned bias voltage has been shown to scale with the ICP power and is -125 V for 200 W and -200 V for 550 W. When the average substrate bias voltage is -200 V, the maximum ion energy is 272 eV. The influence of substrate-tuned biasing on the electron density, the electron temperature, and the optical emission of the plasma have been studied. Alternatively, for RF biasing at 24 W with 200 W ICP power the ion energy has been enhanced up to 272 eV.

The effects of substrate biasing on the material properties have been demonstrated

for $Al_2O_3$, $Co_3O_4$ and $TiO_2$ deposited by plasma-assisted ALD. The ion-induced effects have turned out to be material and/or process-specific. For $Al_2O_3$ it has been found that the growth per cycle increased while the mass density decreased with higher bias voltages. This effect is expected to originate from increased incorporation of OH groups and C impurities into the films. It has also been shown that the residual stress of $Al_2O_3$ films on Si can be tailored from the tensile to the compressive regime by controlling the substrate bias voltage. For $Co_3O_4$ the growth per cycle decreased and the film density increased for higher bias voltages, as the films became slightly oxygen-deficient. Using substrate biasing, the crystalline-phase of $TiO_2$ films can be tailored gradually from anatase to rutile. This effect may be of interest for a variety of applications as it is not trivial to obtain as-deposited rutile $TiO_2$ by (plasma-assisted) ALD.

The results reported in this Chapter demonstrate that the material properties of thin films synthesized by plasma-assisted ALD can be tailored by enhancing the ion energy using substrate biasing. Improved control over the ion energy distribution may, however, be beneficial to tailor ion-induced effects even more precisely. Bias signals that result in narrower ion energy distributions, e.g. those with higher frequencies or pulsed signals are of interest. Alternatively, the bias signal can be ramped up or down, and the timing can be varied such that substrate biasing is only enabled during part of a plasma exposure step or only during every couple of cycles. It can finally also be of interest to decouple the physical and chemical effects of the plasma exposure step, for example by first exposing the sample to a reactive plasma (e.g., $O_2$ plasma) with substrate biasing disabled and subsequently to a noble gas plasma with substrate biasing enabled. These are probably just a few of the many possibilities that exist to gain more control over the ALD process and the film properties obtained.

## Acknowledgements

Dr. T. Fernández Landaluce, W. Keuning, J. J. A. Zeebregts, M. J. F. van de Sande, J. J. L. M. Meulendijks, C.A.A. van Helvoirt, and H. M. M. de Jong (all TU/e) are acknowledged for their assistance. This work is carried out within the Thin Film Nanomanufacturing (TFN) programme and is supported financially by the Dutch Technology Foundation STW.

# References


1. H. B. Profijt, S. E. Potts, M. C. M. van de Sanden, and W. M. M. Kessels, J. Vac. Sci. Technol. A 29, 050801 (2011).
2. H. B. Profijt, P. Kudlacek, M. C. M. van de Sanden, and W. M. M. Kessels, J. Electrochem. Soc., 158, G88 (2011).
3. M. A. Lieberman and A. J. Lichtenberg, Principles of Plasma Discharges and Materials Processing, 2nd ed. (John Wiley & Sons, New York, 2005).
4. E. A. Edelberg, A. Perry, N. Benjamin, and E. S. Aydil, J. Vac. Sci. Technol. A 17, 506 (1999).
5. E. Kawamura, V. Vahedi, M. A. Lieberman, and C. K. Birdsall, Plasma Sources Sci. Technol. 8, R45 (1999).
6. Y. Lifshitz, S. R. Kasi, and J. W. Rabalais, Phys. Rev. B 41, 10468 (1990).
7. T. Takagi, J. Vac. Sci. Technol. A. 2, 382 (1984).
8. L. M. Williams, and D. W. Hess, J. Vac. Sci. Technol. A 1, 1810 (1983).
9. C. A. Davis, Thin Solid Films 226, 30 (1993).
10. H. B. Profijt, M. C. M. van de Sanden, and W. M. M. Kessels, Electrochem. Solid-State Lett. 15, G1-G3 (2012).
11. H. Kim, S. Woo, J. Lee, Y. Kim, J. Lee, I.-J. Choi, Y.-D. Kim, C.-W. Chung, and H. Jeon, J. Electrochem. Soc. 158, H21 (2011).
12. P. Kudlacek, R. F. Rumphorst, and M. C. M. van de Sanden, J. Appl. Phys. 106, 073303 (2009).
13. J. S. Logan, IBM J. Res. Dev. 14, 172 (1970).
14. Z. F. Ding, W. G. Huo, and Y. N. Wang, Plasma Sci. Technol. 6, 2549 (2004).
15. B. M. Oliver, R. M. Clements, and P. R. Smy, J. Appl. Phys 44, 4511 (1973).
16. E. Langereis, H.C.M. Knoops, A.J.M. Mackus, F. Roozeboom, M.C.M. van de Sanden, and W.M.M. Kessels, J. Appl. Phys. 102, 083517 (2007).
17. E. W. Peterson and L. Talbot, Aiaa journal 8, 2215 (1970).
18. D. Gahan, B. Dolinaj, and M. B. Hopkins, Rev. Sci. Instrum. 79, 033502 (2008).
19. A. J. M. Mackus, S. B. S. Heil, E. Langereis, H. C. M. Knoops, M. C. M. van de Sanden, and W. M. M. Kessels, J. Vac. Sci. Technol. A 28, 77 (2010).
20. J. W. Lim and S. J. Yun, Jpn. J. Appl. Phys., Part 2 42, L663 (2003).
21. M. E. Donders, H.C.M. Knoops, M.C.M. van de Sanden, W.M.M. Kessels, and P.H.L. Notten, J. Electroch. Soc. 158, G92 (2011).
22. E. Langereis, R. Roijmans, F. Roozeboom, M. C. M. van de Sanden, and W. M. M. Kessels, J. Electrochem. Soc. 158, G34 (2011).

23. E. Langereis, S. B. S. Heil, H. C. M. Knoops, W. Keuning, M. C. M. van de Sanden, and W. M. M. Kessels, J. Phys. D 42, 073001 (2009).
24. L. B. Freund and S. Suresh, Thin Film Materials: Stress, Defect Formation and Surface Evolution, (Cambridge University Press, Cambridge, U.K., 2004).
25. N. Kang, F. Gaboriau, S. -G. Oh, and A. Ricard, Plasma Sources Sci. Technol. 20, 045015 (2011).
26. A. T. Hjartarson, E. G. Thorsteinsson, and J. T. Gudmundsson, Plasma Sources Sci. Technol. 19, 065008 (2010).
27. J. T. Gudmundsson, I. G. Kouznetsov, K. K. Patel, and M. A. Lieberman, J. Phys. D: Appl. Phys. 34, 1100 (2001).
28. A. H. M. Smets, W. M. M. Kessels, and M. C. M. van de Sanden, J. Appl. Phys. 102, 073523 (2007).
29. R. Puurunen, J. Saarilahti, and H. Kattelus, ECS Transactions 11, 3-14 (2007).
30. J. A. Thornton and D. W. Hoffman, Thin Solid Films 171, 5 (1989).

Chapter 7

# Substrate Biasing during Plasma-Assisted ALD for Crystalline Phase-Control of $TiO_2$ Thin Films*

**Abstract** Substrate biasing has been implemented in a remote plasma atomic layer deposition (ALD) reactor, enabling control of the ion energy up to 260 eV. For $TiO_2$ films deposited from $Ti(Cp^{Me})(NMe_2)_3$ and $O_2$ plasma it is demonstrated that the crystalline phase can be tailored by tuning the ion energy. Rutile $TiO_2$ was obtained at 200 and 300 °C, typically yielding amorphous and anatase films without biasing. Aspects such as film mass density, [O]/[Ti] ratio and growth per cycle under biased conditions are addressed. The results demonstrate that substrate biasing is a viable method for ALD to tailor ultra-thin film properties.

*Published as: *H. B. Profijt, M. C. M. van de Sanden, and W. M. M. Kessels, Electrochem. Solid-State Lett. 15, G1 (2012).*

## 7.1 Introduction

For certain thin film materials and applications, plasma-assisted atomic layer deposition (ALD) can offer an increased level of freedom in material properties and processing conditions compared to thermal ALD [1]. This freedom can be attributed to the presence of reactive radicals and ions which interact with the material surface during deposition. The use of a plasma furthermore offers an increased number of process parameters that can be varied to influence the properties of the thin films deposited. A parameter that has, however, not yet been explored for plasma-assisted ALD is the substrate potential which directly affects the ion energy [4]. In electropositive processing plasmas, the average potential of the plasma is positive with respect to the grounded reactor walls and substrate stage. As a result, positive ions are accelerated in a thin space charge layer, the plasma sheath, towards the grounded reactor walls and the substrate stage. For the case of a collisionless plasma sheath (i.e. at relatively low pressures), the kinetic energy of the ions $E_i$ can be expressed by $E_i = e(V_p - V_s)$, where $V_p$ is the plasma potential and $V_s$ is the substrate potential. This expression illustrates that the energy with which the ions arrive at the substrate surface is increased for a more negatively biased substrate stage. Recently, we illustrated that during remote plasma ALD under regular conditions (i.e. with a grounded substrate stage) the ion energy can be sufficiently high to play a role during the ALD process, e.g. by enhancing adatom migration and ligand removal [5]. With substrate biasing even higher ion energies can be reached and an increased number of physical surface reactions can be expected to play a role during ALD [6].

For plasma-enhanced chemical vapor deposition (PECVD), substrate biasing has already proven its value in tailoring thin film material properties. For the deposition process of Si, for example, the microstructure, density and crystallinity can be affected by controlling the substrate bias voltage [7, 8]. For PECVD of $TiO_2$ the effect of substrate biasing has been confirmed as well - the deposition rate and the crystalline phase are affected by a bias voltage applied to the substrate stage [9-11]. Also for $ZnO_2$, the influence of RF substrate biasing was demonstrated and the preferred orientation, the crystal size, and the thermal stability of the films were shown to be affected by the bias power [12]. Being a different deposition method ruled by surface chemistry, it is also interesting to study the influence of substrate biasing for the case of plasma-assisted ALD.

In this Chapter, we demonstrate that substrate biasing is a viable technique during plasma-assisted ALD to tailor material properties of ultra-thin films. More specifically, it is shown that substrate biasing allows for control over the phase composition of $TiO_2$ thin films deposited at relatively low substrate temperatures. It is also revealed that substrate

biasing affects the mass density, the [O]/[Ti] ratio and the growth per cycle (GPC).

## 7.2 Experimental

The experiments were carried out in a remote plasma ALD reactor equipped with an inductively-coupled plasma (ICP) source. The reactor is schematically illustrated in Fig. 7.1. During the plasma step of the ALD cycle, the substrate stage was electrically grounded or biased by substrate-tuned biasing [13] or RF biasing [4]. With substrate-tuned biasing, only a matching network was connected to the substrate stage (4 inch diameter) and the bias voltage was controlled by adjusting the impedance between the substrate stage and the ground potential [13]. In the case of RF biasing, a power supply (denoted by the asterisk in Fig. 7.1) was connected to the matching network. The substrate can be grounded by closing a switch that electrically connects the substrate stage and the grounded reactor wall. Films were deposited on 1x1 inch substrates, cut from a n-type c-Si (100) wafer with a resistivity of 0.004-0.007 $\mu\Omega$·cm. During $TiO_2$ deposition, the substrate was alternately exposed to $Ti(Cp^{Me})(NMe_2)_3$ (purity 98%, SAFC Hitech Ltd.) and a 200 W $O_2$ plasma with dosing times of 5 and 10 s, respectively, separated by 5 s purge steps. The chamber was continuously purged by $O_2$ at 7.5 mTorr provided through the ICP source, which was possible since no reaction between $O_2$ and the precursor was observed under the conditions employed. Films were deposited at 100, 200, and 300 °C. Substrate-tuned biasing was utilized to achieve bias voltages of -50 and -100 V and RF biasing was used for -100, -150 and -200 V. A retarding field energy analyzer (RFEA) was employed to determine the ion energy distribution function (IEDF) for the $O_2$ plasma [4, 14].

## 7.3 Results

Figure 7.2 displays the IEDFs measured for substrate-tuned bias voltages between 0 and -100 V. The inset of this figure shows the average ion energy deduced from the IEDFs. For the case of a grounded substrate stage (i.e. with the switch closed), the ion energy is mono-modally distributed and peaks at 33 $\pm$ 1 eV. The value for the ion energy is somewhat higher than reported earlier for an $O_2$ plasma in the Oxford Instruments FlexAL reactor [5]. In that case the plasma was operated at a higher gas pressure and in a reactor with a different geometry, both reducing the ion energy. When the substrate stage is biased, the ion energy distribution becomes bi-modal. This is a result of the fact that the ion transit time (i.e. the time it takes for an ion to travel through the plasma sheath) is lower

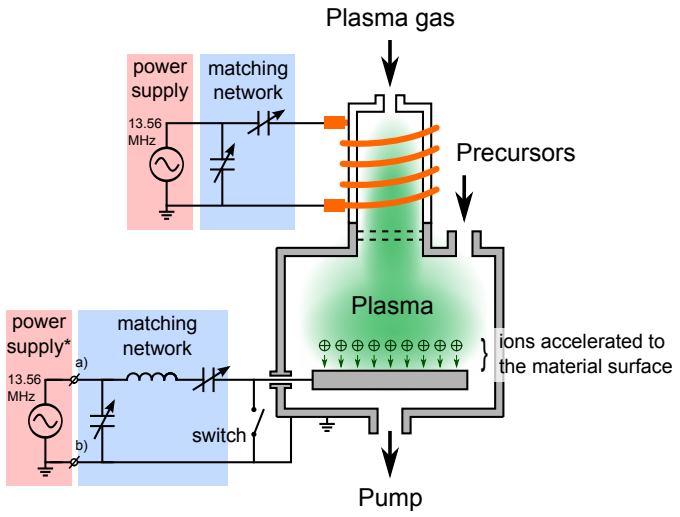



**Figure 7.1:** Remote plasma ALD reactor equipped with an inductively coupled plasma source. A matching network is connected to the substrate stage to control the substrate potential by substrate-tuned biasing. The asterisk denotes the power supply that is additionally connected (at nodes "a)" and "b)") to the matching network in the case of RF biasing. The substrate stage also can be directly connected to the grounded reactor wall by closing the switch.

than the RF cycle time (being 73.7 ns) of the plasma source. Consequently, ions that pass the plasma sheath at different time instances within one RF cycle obtain different energies since the sheath voltage drop is different. For a detailed explanation on the origin of the bimodal distribution, the reader is referred to Edelberg et al. [4].

In the case the substrate is biased at -100 V, the ion energy is distributed between 121 and 155 $\pm$ 1 eV and the average value is 138 $\pm$ 1 eV. Since the pressure is relatively low, the plasma sheath is collisionless, which is confirmed by the absence of low-energy tails in the ion energy distributions. When the power supply is connected to the matching network, a power of 4 W is needed to bias the substrate at -100 V. The bias voltage can be further increased to -150 and -200 V by setting the power to 14 and 24 W, respectively. For these biasing conditions, average ion energies of 197 and 260 $\pm$ 1 eV were found by extrapolating the average ion energies obtained for substrate-tuned biasing. Planar probe measurements confirmed that the ion flux to the substrate surface is hardly affected by substrate-tuned biasing and is in the order of $10^{14}$ $cm^{-2}$ $s^{1}$.

Grazing-incidence X-ray diffraction measurements (XRD) were carried out on $\sim$30

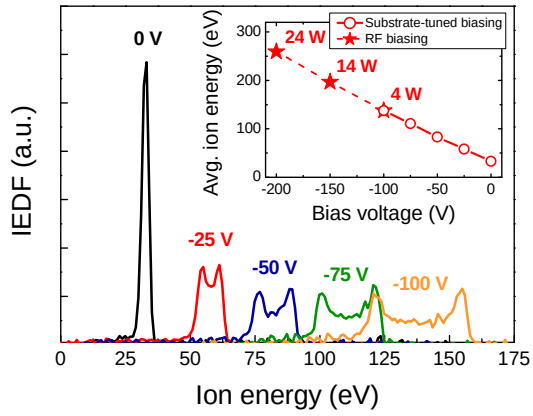



**Figure 7.2:** Ion energy distribution functions (IEDFs) for bias voltages of 0 to -100 V, obtained by substrate-tuned biasing. The inset shows the average ion energy as a function of the bias voltage. For substrate-tuned biasing, the average ion energies are derived from the IEDFs, whereas the values for RF biasing are extrapolated values.

nm (200 °C series) and ∼50 nm (300 °C series) thick $TiO_2$ films and the spectra are shown in Fig. 7.3. For films deposited at 300 °C and a substrate potential of 0 V, the XRD spectrum includes the (101), (004), (200), (105), and (211) diffraction peaks corresponding to the anatase $TiO_2$ phase. When a bias voltage of -50 V is applied, the magnitude of these peaks decreases, while the (110) peak related to the rutile $TiO_2$ phase starts appearing. When the bias voltage is further increased, the anatase diffraction peaks gradually disappear and the (110), (101), (111), and (211) diffraction peaks, corresponding to the rutile phase, increase in magnitude. At -200 V solely peaks related to the rutile phase are visible in the spectrum. A difference can be observed between the spectra for -100 V substrate-tuned biasing and -100 V RF-biasing. This difference is expected to originate from a change in the plasma density and electron temperature as a result of the increase in power delivered to the plasma with RF biasing. $TiO_2$ films deposited at 200 °C are amorphous, however when -100 V biasing is applied the (110) rutile phase peak appears in the XRD spectrum. Films deposited at 100 °C remain amorphous even when substrate biasing is applied (not shown). It is noted that we verified that substrate biasing does not significantly heat the samples, by monitoring the substrate temperature using a thermocouple connected to the substrate stage.

The impact of substrate biasing was furthermore evaluated by Rutherford backscattering spectroscopy (RBS), elastic recoil detection (ERD), and X-ray photoelectron spec-

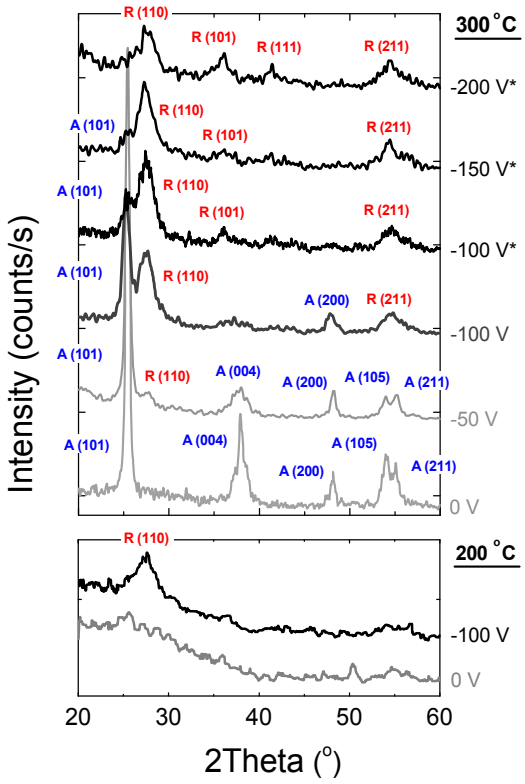



**Figure 7.3:** X-ray diffraction spectra for $TiO_2$ films deposited at 200 and 300 °C for different bias voltages. Peaks corresponding to the anatase and rutile crystalline phases are denoted with "A" and "R", respectively. Substrate-tuned biasing was employed for -50 and -100 V, whereas RF substrate biasing was applied for -100, -150 and -200 V (labeled by asterisks).

troscopy (XPS). Table 7.1 shows that films deposited without substrate biasing are stoichiometric, have a mass density typical for ALD-prepared $TiO_2$ films and contain < 2 at.% H. The film properties for $TiO_2$ deposited at a bias voltage of -50 V are very similar, however $TiO_2$ films deposited at higher bias voltages show a pronounced change in the compositional material properties. The [O]/[Ti] ratio increases and the mass density decreases with increasing bias voltage. From in-depth analysis of the ERD results, the knowledge is gained that for bias voltages of 0 and -50 V the 1.4 at.% H in the films is mainly present at the $TiO_2$ interface as well as at the $TiO_2$ interface with the substrate. For films deposited at higher bias voltages a considerable amount of H seems to be present in

**Table 7.1:** Influence of the bias voltage on the material properties of ∼50 nm thick $TiO_2$ films deposited at 300 °C. Substrate-tuned biasing was employed for -50 and -100 V, whereas RF substrate biasing was applied for -100, -150 and -200 V (voltages labeled by asterisks). The relative errors in the [O]/[Ti] ratio, the mass density and the number of Ti atoms deposited, (all determined by RBS) are 4%, 4% and 3%, respectively. For the H content (determined by ERD), the relative error is 7%.

| Bias voltage (V) | [O]/[Ti] ratio | Mass density (g $cm^{-3}$) | H content (at.%) | Ti atoms deposited ($nm^{-2}$ $cycle^{-1}$) |
|---|---|---|---|---|
| 0 | 2.0 | 3.7 | 1.4 | 2.4 |
| -50 | 2.0 | 3.7 | 1.4 | 2.6 |
| -100 | 2.2 | 3.4 | 5.2 | 2.3 |
| -100* | 2.3 | 3.5 | 4.4 | 2.2 |
| -150* | 2.3 | 3.3 | 4.0 | 2.3 |
| -200* | 2.4 | 3.3 | 6.1 | 2.2 |

the bulk, particularly as -OH groups, as confirmed by X-ray photoelectron spectroscopy (XPS) measurements. These OH groups are apparently more incorporated under biased conditions and are the reason for lower density films obtained for higher bias voltages. Using *ex situ* spectroscopic ellipsometry (SE) the average GPC for the $TiO_2$ films was determined to be 0.86 Å/cycle without biasing, and 0.89 and 0.94 Å/cycle for a -100 V and -200 V RF biased substrate stage, respectively. The growth in terms of Ti atoms per cycle is approximately constant over the range of bias voltages applied (see Table 7.1) and therefore the increased GPC can be attributed to the lower density of the films under these conditions. The N and C impurity levels are respectively 0.1 and 0.5 at.% for films deposited without biasing, comparable to $TiO_2$ films previously deposited using the same precursor [15]. When -200 V RF biasing is applied, the N and C contents increased to 0.8 and 1.0 at.%. These higher impurity levels are expected to originate from precursor ligands decomposed by the impact of high energy ions.

## 7.4 Conclusions

This study demonstrates that substrate biasing allows for additional control over thin film material properties during plasma-assisted ALD, by tuning the ion energy. More specifically, it shows that the phase composition of $TiO_2$ thin films can be tailored by substrate biasing, in addition to other parameters reported in the literature such as the reactant pressure, the deposition temperature, the substrate material and post-deposition

annealing [15-17]. Also the compositional properties of the $TiO_2$ films are affected by biasing, which allows for tuning the electrical, structural and optical properties of the films. In preliminary studies, effects of biasing on other metal-oxide systems have been confirmed as well. For $Al_2O_3$ and $Co_3O_4$ thin films deposited by plasma-assisted ALD, for example, we found that the GPC and the oxide-to-metal ratio were affected by substrate biasing. According to Takagi, changes in material properties generally obtained by increasing the substrate temperature can also be expected when the sample is subjected to energetic ions instead [6]. Physical mechanisms that might be activated or enhanced by the energetic ions include lattice atom displacement and subsurface implantation [6, 11, 18]. Since rutile $TiO_2$ is usually obtained at elevated substrate temperatures or after post-deposition annealing, substrate biasing might replace the need higher thermal processing loads. Another mechanism that might play a role is film stress induced by the physical impact of the energetic ions, which can result in a phase-transformation to a more thermally stable phase. The mechanisms behind the tunability of the material properties by substrate biasing will however need to be addressed in future studies. In order to obtain thin films with preferred material properties, the distribution of the ion energy can also expected to be important. However, when substrate-tuned biasing is employed, the ion energy can be broadly distributed around the average value of the ion energy. Consequently, for a given bimodal ion energy distribution the ions with the lower energies may induce beneficial effects, whereas the ions with higher energies could induce unwanted effects at the same time. With a better defined ion energy, the effects of biasing on thin film material properties might be more selective and more accurately controllable. A narrow distribution of the ion energy can, for example, be obtained by pulsed biasing - a method that uses a more complex bias signal applied to the substrate stage [19]. Finally, it is noted that the timing of substrate biasing can also be varied within the plasma pulse during ALD. For instance, the substrate biasing can be enabled only after the ALD surface reactions have taken place (typically after the initial second) such that the exposure to high energy ions can be considered an *in situ* film treatment executed every ALD cycle.

# Addendum

A number of additional experiments have been carried out using a Star-Ti as the precursor, to obtain more insights into the crystallization of the $TiO_2$ films. It has been found that the crystalline phase of $TiO_2$ deposited from Star-Ti as the precursor can also be tailored by substrate biasing. The films crystallize after a certain film thickness is reached,

an effect that may be related to stress in the films.

For these experiments, $Ti(Cp^{Me5})(OMe)_3$ [Star-Ti, purity > 99%, Air-Liquide] was used as the precursor, held in a stainless steel container which was heated to 78 °C and bubbled with Ar. All dose and purge times were set to 5 s and deposition took place at 300 °C for substrate bias voltages of 0 to -200 V. Substrate-tuned biasing was employed for voltages between 0 and -100 V, whereas 14 and 24 W RF substrate biasing was applied to obtain substrate bias voltages of -150 and -200 V, respectively. During deposition, the film thickness was monitored by *in situ* spectroscopic ellipsometry (SE). After deposition, ∼30 nm thick films were characterized by grazing-incidence X-ray diffraction (XRD) and X-ray reflectivity (XRR) measurements. For $TiO_2$ films varying in thickness from ∼7 up to ∼30 nm, deposited at 4 inch Si substrates and with substrate bias voltages of 0, -100 and -200 V, wafer-curvature tests were performed to determine the residual stress in the films.

The XRD spectra, shown in Fig. 7.4, illustrate that also for $TiO_2$ films deposited using Star-Ti as the precursor the crystalline phase can be tailored gradually from anatase to the rutile by increasing the substrate bias voltage from 0 to -200 V.

Figure 7.5 illustrates that the growth per cycle (GPC) increases abruptly after a certain number of cycles for films deposited at 0 to -200 V. The change in GPC occurred after ∼414, ∼290 and ∼90 cycles for bias voltages of 0, -100 and -200 V, respectively. The corresponding film thicknesses are ∼14.8, ∼11.2, ∼3.8 nm, respectively. The abrupt increase in GPC, which has been found for all the films, is expected to be due to crystallization of the films, which apparently happens when a critical film thickness is reached. Initially the growth per cycle (GPC) was approximately similar for all the films (values between 0.36 and 0.40 ± 0.05 Å). After crystallization, however, the GPC of the film deposited at -200 V increased to 0.60 ± 0.05 Å. This GPC is significantly higher than 0.53 ± 0.05 and 0.52 ± 0.05 Å found for the $TiO_2$ films deposited at 0 and -100 V, respectively.

For $TiO_2$ films deposited at 0, -100 and -200 V, mass densities of 4.0 ± 0.1, 4.0 ± 0.1, and 3.5 ± 0.1 g $cm^{-3}$ have been found by XRR. It is expected that the higher GPC for the film deposited at -200 V is due to its lower mass density.

In Fig. 7.6, the residual stress in $TiO_2$ films deposited on Si substrates is shown for films up to ∼30 nm, deposited with different bias voltages. For 0 nm $TiO_2$, the residual stress is 0 MPa per definition. The negative values found for the $TiO_2$ films indicate a compressive stress, induced by the impact of energetic ions [20]. The first datapoints are

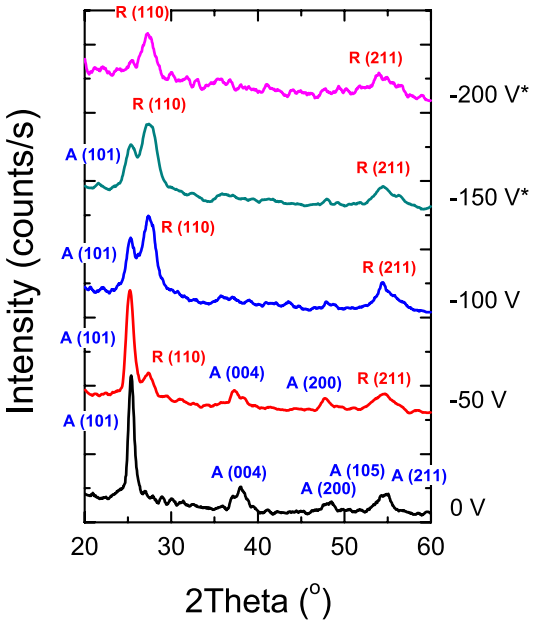



**Figure 7.4:** X-ray diffraction spectra for ∼30 nm thick $TiO_2$ films deposited at 300 °C. Peaks corresponding to the anatase and rutile crystalline phases are denoted with "A" and "R", respectively. Substrate-tuned biasing was employed for voltages between 0 and -100 V, whereas 14 and 24 W RF substrate biasing was applied to obtain substrate bias voltages of -150 and -200 V (labeled by asterisks).

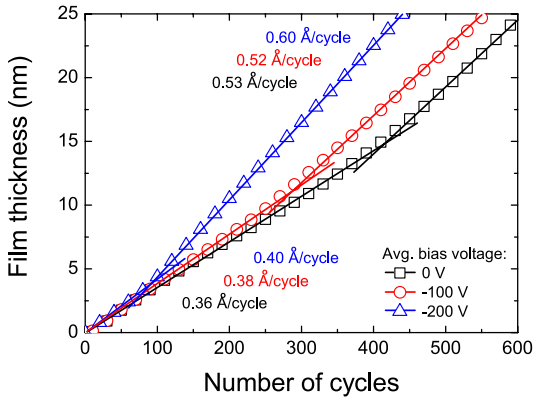



**Figure 7.5:** $TiO_2$ film thickness as a function of the number of cycles for films deposited at 300 °C. Substrate-tuned biasing was employed for 0 and -100 V, whereas 24 W RF substrate biasing was applied to obtain a substrate bias voltages -200 V.

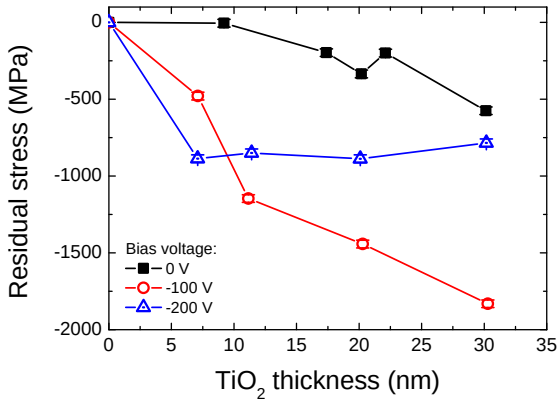



**Figure 7.6:** Residual film stress as a function of the average bias voltage for $TiO_2$ films deposited at 300 °C. Substrate-tuned biasing was employed for 0 and -100 V, whereas 24 W RF substrate biasing was applied to obtain a substrate bias voltages of -200 V.

plotted for a 9.7 nm film deposited at 0 V, a 7.1 nm film deposited at -100 V, and a 7.1 nm film deposited at -200 V. For these films, residual stress values of -5, -480, and -887 $\pm$ 25 MPA have been found, respectively. At the corresponding film thicknesses, the film deposited at -200 V is expected to be (partly) crystallized, whereas the films deposited at 0 and -100 V are amorphous. For films deposited at 0 and -100 V the stress increases with the film thickness, whereas for the -200 V sample the stress stays approximately equal. The latter effect is expected to be due to the lower mass density of the film deposited at -200 V, which relaxes a further increase of the stress.

It is plausible that the stress in the films, the critical thickness for crystallization and the crystalline phase are related, however additional experiments are required to further explain the effects that were observed.

# Acknowledgements

Dr. T. Fernández Landaluce, W. Keuning, M. J. F. van de Sande, J. J. L. M. Meulendijks, J. J. A. Zeebregts (all TU/e), and Dr. W. M. Arnold Bik (AccTec B.V.) are acknowledged for their assistance. SAFC Hitech Ltd. is thanked for supplying the precursor. This work is carried out within the Thin Film Nanomanufacturing (TFN) programme and is supported financially by the Dutch Technology Foundation STW.

# References


1. H. B. Profijt, S. E. Potts, M. C. M. van de Sanden, and W. M. M. Kessels, *J. Vac. Sci. Technol. A* **29**, 050801 (2011).
2. H. Kim, S. Woo, J. Lee, Y. Kim, H. Lee, I.-J. Choi, Y.-D. Kim, C.-W. Chung, and H. Jeon, *J. Electrochem. Soc.* **158**, H21-H24 (2011).
3. T. O. Kääriäinen and D. C. Cameron, *Plasma Process. Polym.* **6**, (2009).
4. E. A. Edelberg, A. Perry, N. Benjamin, and E. S. Aydil, *J. Vac. Sci. Technol. A* **17**, 506 (1999).
5. H. B. Profijt, P. Kudlacek, M. C. M. van de Sanden, and W. M. M. Kessels, *J. Electrochem. Soc.* **158**, G88 (2011).
6. T. Takagi, *J. Vac. Sci. Technol. A.* **2**, 382 (1984).
7. A. H. M. Smets, W. M. M. Kessels, and M. C. M. van de Sanden, *J. Appl. Phys.* **102**, 073523 (2007).
8. N. Kosku, H. Murakami, S. Higashi, and S. Miyazaki, *Appl. Surf. Sci.* **244**, 39 (2009).
9. Y. H. Lee, *Vacuum* **51**, 503 (1998).
10. W. Zhou, X. Zhong, X. Wu, L. Yuan, W. Shu,W. Li, and Y. Xia, *J. Phys. D: Appl. Phys.* **40**, 219 (2007).
11. L.M. Williams, and D.W. Hess, *J. Vac. Sci. Technol. A* **1**, 1810 (1983).
12. T. Hiramatsu, M. Furuta, H. Furuta, T. Matsuda,C. Li, and T. Hirao, *J. Cryst. Growth* **311**, 282 (2011).
13. J. S. Logan, *IBM J. Res. Dev.* **14**, 172 (1970).
14. D. Gahan, B. Dolinaj, and M. B. Hopkins, *Rev. Sci. Instrum.* **79**, 033502 (2008).
15. A. Sarkar, S. E. Potts, S. A. Rushworth, F. Roozeboom, M. C. M. van de Sanden, and W. M. M. Kessels, *ECS Trans.* **33**, 385 (2011).
16. J. Aarik, A. Aidla, V. Sammelselg, H. Siimon, and T. Uustar, *J. Cryst. Growth* **169**, 496 (1996).
17. S. K. Kim, W. -D. Kim, K. -M. Kim, C. S. Hwang, and J. Jeong, *Appl. Phys. Lett.* **85**, 4112 (2004).
18. Y. Lifshitz, S.R. Kasi, and J.W. Rabalais, *Phys. Rev. B* **41**, 10468 (1990).
19. P. Kudlacek, R. F. Rumphorst, and M. C. M. van de Sanden, *J. Appl. Phys.* **106**, 073303 (2009).
20. C. A. Davis, Thin Solid Films 226, 30 (1993).

Chapter 8

# General Conclusions and Outlook

In this dissertation work, a variety of aspects related to the plasma-surface interaction in plasma-assisted ALD have been addressed. The following general conclusions can be drawn from this study:

- The popularity of plasma-assisted ALD has increased rapidly in recent years, as manifested by the increasing number of recent publications about the topic, the large set of thin film materials that have been synthesized by the method, and the increasing number of ALD equipment manufacturers providing dedicated plasma-assisted ALD tools. The use of a plasma during ALD allows for more freedom in processing conditions and for a wider range of material properties compared with the conventional thermally driven ALD method. Reduced film conformality, plasma-induced damage and industrial scale-up of the deposition process are the most significant challenges related to plasma-assisted ALD. One promising application of plasma-assisted ALD is the deposition of ultra-thin films at room temperature. Both for plasma-assisted ALD and ozone-based ALD three criteria for viable deposition processes with acceptable cycle times at room-temperature have been established.

- Ion-induced damage is an aspect that requires attention, however it is not found to be necessarily a major issue during remote- and direct-plasma ALD under the deposition conditions typically employed. It is, however, relevant to have an understanding of how the ion energy depends on the type of plasma source, the reactor geometry, the operating power and the operating pressure. Under processing conditions usually employed, ion energies are several tens of eV at maximum. Depending on the growth-per-cycle of the process, the plasma exposure time required to reach saturation of the ALD cycle, and the ion flux, the energy brought by the ions can be one up to a few eV per atom deposited. This is typically sufficiently high to potentially stimulate the ALD surface reactions, e.g., through ligand de-

sorption and adatom migration. Vacuum ultraviolet (VUV) photons, present in the plasma, can degrade the electrical performance of electronic devices employing metal-oxide films deposited by ALD. Since these photons are (self-)absorbed by neutral gas species, this effect can be suppressed by operating at higher pressures.

- Using two substrate biasing techniques the ion energy has been enhanced up to hundreds of eV. With substrate-tuned biasing the impedance between the substrate stage and the ground is tuned using an external electrical circuit, which offers control over the substrate bias voltage without the need for an additional RF power source. Alternatively, with RF biasing a RF power source is connected to the substrate stage through a matching network. The impact of high energy ions has been investigated for three metal-oxide systems. For $Al_2O_3$ and $Co_3O_4$, the residual stress was tailored and the mass density was increased, respectively, using the impact of high-energy ions. For $TiO_2$, it has been demonstrated that the crystalline phase can be tailored gradually from the anatase to the rutile phase. As it is not trivial to obtain as-deposited rutile $TiO_2$ by plasma-assisted ALD, this effect may be of interest for a range of applications. Considering the results, it can be concluded that substrate biasing is a promising technique to tailor the material properties of thin films synthesized by plasma-assisted ALD. The fact that the plasma-surface interaction can be manipulated, in addition to the other plasma parameters, is the distinguishing factor with respect to thermal ALD.

The results and insights obtained in this work allow for the description of a number of directions for future research:

- As discussed in Chapter 2, one of the major challenges for plasma-assisted ALD is the conformal deposition of films in 3D structures of high aspect ratio such as trenches and vias. This is the result of surface recombination of radicals at surfaces, such that radicals are not able to reach deep into a trench or via. Future research could focus on collecting more experimental results on the conformality of ALD-deposited films in 3D structures, after which specific experiments might be designed that aim at improving the conformality, for instance by manipulating the plasma properties.

- With respect to precursors, it would be desirable to have an increased number of precursors available on the market with high vapor pressures (i.e. $\geq$ 5 Torr) at room-temperature. Consequently, heating or bubbling of the precursor would not be necessary and the risk of precursor condensation in the reactor and/or on

the substrate would be significantly reduced. For precursor manufacturers also opportunities exist to design precursors specifically for interaction with plasmas that allow, for example, for control over the resulting material properties by varying the plasma parameters and/or by using substrate biasing.

- Although this work mainly focused on ions, also the energetic vacuum ultraviolet (VUV) photons present in the plasma have been shown to interact with the material deposited. In Chapter 4, it was demonstrated that these VUV photons are able to break bonds near material interfaces. As an alternative to plasma-assisted ALD, only UV or VUV photons may be used as the reactant species to break the bonds of adsorbed precursor molecules. In order to decouple the contribution of radicals and ions, it is desired to only have VUV photons present near the substrate surface, which might be accomplished, for example, by using a noble gas plasma and by filtering the ions using magnetic fields. The VUV photons may also be generated in a separate reactor and transported to the ALD reactor through tubing and VUV-transparent windows. By using plasmas created in different gases, VUV photons with different energies can be generated, which might break different bonds in the precursor and, consequently, allow for control over of the resulting material properties. Alternatively, a monochromator can be used to filter the VUV photons by their energy.

- Future work on substrate biasing could, for example, focus on bias signals with higher frequencies or more complex waveforms that consequently result in narrower ion energy distributions. Alternatively, the bias signal can be ramped up or down during the plasma exposure step, the timing can be varied and different gases or gas mixtures can be used. Also in configurations other than remote plasma reactors, the use of (substrate) biasing can be of interest. For reactors with capacitively-coupled plasma sources, for example, biasing may be applied to one of the electrodes (or to the grid in the case of a remote "triode" configuration) to manipulate the plasma properties, the ion energy and/or the ion flux. In that respect, there is also a lot to learn from other plasma-processing techniques, such as plasma-enhanced chemical vapor deposition, plasma-enhanced chemical physical vapor deposition, and plasma etching. In these research fields there is a lot of knowledge and experience with techniques to manipulate the plasma properties and, consequently, the resulting material properties. When the advantages of substrate biasing during plasma-assisted ALD are demonstrated for a significant set of relevant materials, the industry might decide to implement the substrate biasing technique in commer-

cial reactors. From that moment onward, the use of the substrate biasing technique will be accessible to more researchers who could start investigating the influence of energetic ions on other material systems, accordingly.

These are just a few of the many future research directions that can be undertaken as a result of the work presented in this dissertation.

# Summary

## Plasma-Surface Interaction in Plasma-Assisted Atomic Layer Deposition

Atomic Layer Deposition (ALD) is a vapor-phase deposition technique in which ultra-thin films are synthesized by repeating two subsequently executed half-cycles. Due to its characteristic self-limiting surface reactions, ALD offers sub-nanometer precision of film growth, uniform deposition over large substrate areas and conformal deposition in structures of high aspect ratio. Plasma-assisted ALD is a variant to the conventional thermal ALD technique where the surface is exposed to a plasma during the second half-cycle. The use of a plasma allows for more freedom in processing conditions and for a wider range of material properties compared with the conventional thermally-driven ALD method. Although it has been known from plasma-based techniques that photons and ions can also play an important role during processing, their contribution has never been systematically addressed for the specific case of plasma-assisted ALD. In this dissertation work, the plasma-surface interaction in plasma-assisted ALD is investigated.

In the first part of this dissertation, the basics and status of plasma-assisted ALD have been discussed. A classification of plasma-capable ALD configurations has been made and examples for plasma-based processes of metal-oxide, metal-nitride and pure metal thin films prepared by plasma-assisted ALD have been used to illustrate its merits compared to thermal ALD. Several challenges of plasma-assisted ALD, such as plasma-induced damage and surface-recombination of radicals, have also been identified. Several reported emerging applications of plasma-assisted ALD have been reviewed. Since the deposition of thin films at low temperatures, and in particular at room temperature, is one of the most promising application areas of plasma-assisted ALD, special attention has been dedicated to this topic. Taking the deposition processes of $Al_2O_3$, $SiO_2$, and $TiO_2$ as examples, criteria for viable deposition at room-temperature using plasma-assisted ALD and ozone-based ALD have been identified.

The second part deals with the identification and evaluation of ions and photons during plasma-assisted ALD. The presence and importance of ions have been discussed for four reactor configurations commonly used during plasma-assisted ALD. It has been shown that the energy and flux of ions towards the substrate surface is mainly determi-

ned by the reactor configuration, the gas pressure, the plasma power, and the electrical potential of the substrate stage. Under processing conditions typically employed during plasma-assisted ALD, ion energies are up to several tens of eV and ion-induced damage is therefore not a major issue during most processes. The energy flux of the ions toward the substrate surface can however be sufficient to promote some beneficial physical effects such as enhanced ligand-desorption, adatom migration and displacement of lattice atoms. With respect to the optical emission of plasmas, it has been shown that energetic vacuum ultraviolet (VUV) photons can be present in plasmas, which are able to induce electrical defects at interfaces. By varying the gas pressure and the plasma power, however, the influence of ions and photons can be suppressed.

The third part of this dissertation discusses the exploitation of the presence of ions during plasma-assisted ALD using substrate biasing in order to affect the properties of metal-oxide films. The ion energy was enhanced by applying a substrate bias signal at radio frequency to the substrate stage in a reactor equipped with an inductively-coupled plasma source. Alternatively, substrate-tuned biasing was used where no additional power source is required and where the substrate potential can be varied by enhancing capacitive coupling using an external electrical circuit. It has been demonstrated that both biasing techniques are viable and that ion energies have been increased up to a few hundreds of eV. The influence of these high-energy ions on ALD-synthesized thin films was illustrated for $Al_2O_3$, $Co_3O_4$ and $TiO_2$ and it has been demonstrated that thin film properties can be tailored in terms of thin-film stress, composition, density and crystallinity when ion energies are carefully tuned.

To conclude, in this dissertation work important aspects of the plasma-assisted ALD technique have been elucidated leading to a better understanding of the fundamental and technological opportunities and limitations of the technique. The work will therefore contribute to the advancement and the acceptance of plasma-assisted ALD in science and technology.

# Samenvatting

## Plasma-Oppervlak Interactie tijdens Plasma-Geassisteerde Atoomlaagdepositie

Atoomlaagdepositie (ALD) is een gasfase depositiemethode waarbij extreem dunne lagen gedeponeerd worden door twee halfcycli continu te herhalen. Dankzij de typische zelflimiterende oppervlaktereacties biedt ALD sub-nanometer nauwkeurigheid van de materiaalaangroei, uniforme depositie op grote substraatoppervlakken en een perfecte stapbedekking in structuren met een grote diepte-breedte verhouding. Plasma-geassisteerde ALD is een variant op het conventionele thermisch-gedreven atoomlaagdepositieproces waarbij het oppervlak wordt blootgesteld aan een plasma tijdens de tweede halfcyclus. Door een plasma te gebruiken, wordt meer vrijheid verkregen op het gebied van proceseigenschappen en is er meer controle over de materiaaleigenschappen. Hoewel het bekend is dat ionen en fotonen een belangrijke rol kunnen spelen tijdens plasmaprocessen, is hun invloed nooit uitvoerig onderzocht voor het plasma-geassisteerde ALD proces. In het promotietraject waarvan dit proefschrift het resultaat is, is de interactie tussen plasma's en oppervlakken tijdens plasma-geassisteerde atoomlaagdepositie onderzocht.

In het eerste deel van dit proefschrift zijn de basiseigenschappen en de huidige stand van zaken met betrekking tot plasma-geassisteerde ALD bediscussieerd. Een overzicht van de verschillende soorten reactoren voor plasma-geassisteerde ALD is opgesteld en aan de hand van voorbeelden van processen voor depositie van metaaloxide, metaalnitride en pure metaallagen zijn de voordelen van plasma-geassisteerde ALD besproken. De mogelijke complicaties die kunnen optreden tijdens het depositieproces, zoals schade aan het oppervlak na blootstelling aan een plasma en oppervlakteverliezen van radicalen, zijn ook geïnventariseerd. Verder zijn enkele veelbelovende toepassingen van de depositiemethode besproken. Aangezien depositie op lage temperaturen, zelfs op kamertemperatuur, een veelbelovende toepassing is van plasma-geassisteerde ALD, is er extra aandacht besteed aan dit onderwerp. Aan de hand van depositieprocessen voor $Al_2O_3$, $SiO_2$ en $TiO_2$ lagen zijn de eisen voor een succesvol proces op kamertemperatuur met plasma-geassisteerde ALD of op ozon-gebaseerde ALD geïdentificeerd.

In het tweede deel van dit proefschrift is besproken welke ionen en fotonen aan-

wezig zijn tijdens het depositieproces. De rol van deze ionen en fotonen is besproken voor de vier reactorontwerpen die het vaakst gebruikt worden voor plasma-geassisteerde atoomlaagdepositie. Er is aangetoond dat de energie en fluks van ionen naar het substraattoppervlak worden bepaald door het ontwerp van de reactor, de gasdruk, het plasmavermogen en de elektrische potentiaal op de substraathouder. Voor veelgebruikte procescondities is de ionenenergie enkele tientallen elektronvolts waardoor schade als gevolg van ionen niet echt aan de orde zal zijn. De fluks van ionen met hoge energieën naar het materiaaloppervlak kan echter wel voldoende zijn om fysische mechanismen, zoals verwijdering van liganden en oppervlakteverplaatsing van al of niet chemisch gebonden atomen, te activeren. Wat betreft de optische emissie van plasma's is aangetoond dat vacuüm-ultraviolet (VUV) fotonen aanwezig kunnen zijn met voldoende energie om elektrische defecten te creëren op grensvlakken tussen verschillende lagen. De invloed van ionen en fotonen kan echter beperkt worden door de gasdruk en het plasmavermogen te veranderen.

In het derde deel van dit proefschrift is besproken hoe ionen kunnen worden ingezet om eigenschappen van metaaloxide lagen te beïnvloeden, door een biasspanning aan te leggen op de substraathouder. In een reactor uitgerust met een inductief-gegenereerd plasma is de ionenenergie vergroot met behulp van een radiofrequent (RF) spanningssignaal dat aangelegd is op de substraathouder. In een ander experiment is de potentiaal van de substraathouder ingesteld door de impedantie tussen aarde en de substraathouder te variëren, wat invloed heeft op de capacitieve koppeling van het plasma naar het substraat. Beide technieken zijn succesvol geïnstalleerd en de ionenenergie is vergroot naar enkele honderden elektronvolts. De invloed van ionen met hoge energieën is getest op $Al_2O_3$, $Co_3O_4$ en $TiO_2$ lagen en er is aangetoond dat de eigenschappen van dunne films, zoals de interne materiaalspanning, de samenstelling, de massadichtheid en de kristalfase, naar wens kunnen worden ingesteld wanneer de ionenenergie nauwkeurig wordt gevarieerd.

Het onderzoek wat beschreven is in dit proefschrift heeft belangrijke aspecten van plasma-geassisteerde ALD verduidelijkt en ervoor gezorgd dat er meer begrip is van de fundamentele en technologische mogelijkheden en grenzen van de techniek. Daarom draagt dit werk bij aan de ontwikkeling en omarming van de techniek in wetenschap en industrie.

# List of publications related to this work

1. S. E. Potts, H. B. Profijt, R. Roelofs, and W. M. M. Kessels, Chem. Vap. Dep., *to be submitted* (2013).
2. H. B. Profijt, M. C. M. van de Sanden, and W. M. M. Kessels, J. Vac. Sci. Technol. A 31, 01A106 (2013).
3. S. E. Potts, H. B. Profijt, R. Roelofs, and W. M. M. Kessels, ECS Trans. 50 (2012).
4. H. B. Profijt and W. M. M. Kessels, ECS Trans. 50 (2012).
5. H. B. Profijt, M. C. M. van de Sanden, and W. M. M. Kessels, Electrochem. Solid-State Lett. 15, G1 (2012).
6. H. B. Profijt, S. E. Potts, M. C. M. van de Sanden, and W. M. M. Kessels, J. Vac. Sci. Technol. A 29, 050801 (2011).
7. W. M. M. Kessels, S. E. Potts, H. B. Profijt, and M. C. M. van de Sanden, in "Atomic Layer Deposition of Nanostructures Materials", edited by M. Knez and N. Pinna (Wiley VCH, 2011)
8. H. B. Profijt, P. Kudlacek, M. C. M. van de Sanden, and W. M. M. Kessels, J. Electrochem. Soc. 158, G88 (2011).
9. G. Dingemans, N. M. Terlinden, D. Pierreux, H. B. Profijt, M. C. M. van de Sanden, and W. M. M. Kessels, Electrochem. Solid-State Lett. 14, H1 (2011).
10. H. B. Profijt, P. Kudlacek, M. C. M. van de Sanden, and W. M. M. Kessels, ECS Trans. 33, 61 (2010).

# Dankwoord

Hoewel alleen mijn naam op de voorkant staat, hebben velen een belangrijk bijdrage geleverd aan de totstandkoming van dit proefschrift. In dit hoofdstuk wil ik deze mensen bedanken.

Allereerst mijn promotor Erwin; bedankt voor de uitstekende begeleiding tijdens mijn promotie! Het is erg indrukwekkend hoe toegewijd en enthousiast jij met jouw vak bezig bent! Ik heb veel aan jouw kritische feedback gehad en ben erg tevreden met de resultaten die beschreven staan in dit proefschrift. Ook Richard, mijn tweede promotor, wil ik danken voor de vele adviezen en het vertrouwen. Verder dank ik ook de overige stafleden van PMP voor de adviezen en de goede sfeer binnen de groep; de technici voor de hulp in en rond het lab; Jeanne en Lianne voor de assistentie op administratief vlak; Cristian, Noemi en Wytze voor de goede samenwerking binnen het STW project; mijn kamergenoten (zowel in NLaag als in het TNO gebouw) voor de goede sfeer op kantoor; en al mijn collega's voor de gezelligheid op de groep, op borrels en op conferenties. Met name van Erik en Harm heb ik veel geleerd over de ALD-I, maar ook de overige mede-gebruikers de mooiste opstelling binnen onze groep wil ik danken voor de goede samenwerking. Robin, mijn complimenten voor het pionierswerk wat je binnen jouw afstudeerproject hebt verricht! Het is van grote waarde geweest voor Hst. 3 in mijn thesis en het toekomstige onderzoek naar nanopatterning binnen de groep. Stephen, bedankt voor de goede samenwerking aan het review-artikel en de room-temperature ALD paper (Hst. 2 en 3 in dit proefschrift).

At ASM America, I would like to acknowledge Eric, FredA, FredJ, Xichong, Brennan, Jack, Kristy, and Timo. Spending a couple of months in Phoenix was a great and very instructive experience! Starting January 2013 we will be colleagues, so perhaps we'll meet again in the (near) future.

Ik dank mijn vrienden voor de interesse in mijn onderzoek en de afleiding die de gezellige avonden en weekenden hebben gebracht. Thijs en mijn paranimfen Hugo en Richard dank ik voor de leuke vakanties en avonden in de kroeg. Ik denk ook met veel plezier terug aan de borrelavondjes en de weekendjes weg met mijn oud-studiegenoten. Ook de feestjes en skivakanties met de heren en dames van Residentie 7-2 zijn memorabel!

Mijn ouders wil ik danken voor hun onvoorwaardelijke steun tijdens mijn studie en promotie. Ook mijn overige familie- en schoonfamilieleden dank ik voor de vele gezel-

lige weekendjes en de interesse in mijn werk.

Josien, bedankt voor jouw geduld en steun. Ik weet dat ik je soms bijna tot wanhoop dreef door op elk vrij moment (thuis, bij familie, in de trein, etc) mijn laptop erbij te pakken om even te kijken hoe de depositie vorderde, of de metingen goed verliepen, of om nog even "snel" wat data uit te werken (wat vervolgens uren zou duren). Gelukkig hebben we lekker bij kunnen komen op Hawaii. Nu de promotie erop zit, is het tijd voor ons volgende avontuur. Ga je mee?

Harald Profijt
’s-Hertogenbosch, September 2012

# Curriculum Vitae

Harald Profijt was born on 30 June 1981 in Hoogeveen, The Netherlands. After finishing Atheneum at the Menso Alting College in Hoogeveen, he started studying Electrical Engineering at the University of Twente in Enschede in August 2000. During his studies, he spent four months at Université Joseph Fourier in Grenoble (France) to work on the diamagnetic levitation of micro magnets. After this internship, Harald started his MSc graduation project within the Transducers Science and Technology (TST) group. In August 2008 he graduated cum laude on magnetron-sputtered Co/Pt multilayers for the diamagnetic levitation of micro electro mechanical systems (MEMS). In December 2008 he started his PhD project in the Plasma and Materials Processing (PMP) group at Eindhoven University of Technology in Eindhoven. Harald's research on plasma-surface interaction in plasma-assisted ALD was awarded with the Coburn and Winters Award of the AVS Plasma Science and Technology Division in 2011. In the winter of 2012, he spent three months at ASM America in Phoenix (Arizona, USA) to work on plasma characterization in a commercial plasma-assisted ALD module. After his PhD project, Harald joined ASM Belgium (Leuven) in January 2013.